DYNAMIC LOADING OF TUBE BUNDLES DURING TWO-PHASE

BLOWDOWN

AN EXPERIMENTAL STUDY OF STEAM GENERATOR TUBE LOADING DURING A TWO-PHASE BLOWDOWN

BY OUAJIH HAMOUDA, B.ENG., M.A.SC.

A THESIS SUBMITTED TO THE SCHOOL OF GRADUATE STUDIES IN
PARTIAL FULFILMENT OF THE REQUIREMENTS FOR THE DEGREE
DOCTOR OF PHILOSOPHY

MCMASTER UNIVERSITY

McMaster University DOCTOR OF PHILOSOPHY (2015) Hamilton, Ontario (Mechanical Engineering)

TITLE: An Experimental Study of Steam Generator Tube Loading during a Two-Phase Blowdown

AUTHOR: Ouajih Hamouda, B.Eng., M.A.Sc. (McMaster University)

SUPERVISOR: Professor Emeritus Dr. David S. Weaver

NUMBER OF PAGES: xxv, 269.

LAY ABSTRACT

The design of nuclear plant systems requires that public safety be ensured for the worst-case imaginable accident scenarios. This means that radioactive materials produced by nuclear fission must be safely contained. If the main steam pipe from a nuclear steam generator were to break, the water in the steam generator would rapidly boil off in what is called a blowdown. Such an event could produce significant loading on the heat exchanger tubes. Should the tubes rupture, radioactive materials may breach reactor containment. Thus, knowing the tube loading during this hypothetical scenario is an important input for safe design. The goal of this research is to improve our understanding of the effects of this postulated accident on the transient loading of the tubes. A laboratory study was carried out to simulate the blowdown. The experimental results provided valuable insights and guidance for the development of improved design tools.

ABSTRACT

This research studies the effects of a postulated Main Steam Line Break accident in a nuclear plant on the transient loading of steam generator tubes. The problem involves complex transient two-phase flow dynamics and fluid-structural loading processes. A better understanding of this phenomenon will permit the development of improved design tools to ensure steam generator safety.

This Thesis presents the results of an experimental laboratory study of the transient loading of a sectional model of steam generator tubes during a simulated two-phase blowdown. The research was carried out in a purpose designed and built experimental facility. The thermodynamic phenomena were investigated through dynamic pressures and temperatures. The transient tube loads were directly measured using dynamic load cells. The working fluid was R-134a and the tube bundle was a normal triangular array with a pitch ratio of 1.36.

Preliminary testing indicated parasitic loading on the instruments and remedial actions were taken to ensure measurement accuracy. The success of the instrumentation development methodologies was validated in a series of single-phase blowdowns. Two-phase blowdown experiments were then conducted with various levels of liquid and numbers of tube rows. The results provided hitherto unknown information relating the nature of the fluid-structure interaction and flow development during a two-phase transient blowdown across a tube bundle.

The pressure drop across the tube bundle established the thermal hydraulic fluid behaviour in the pressure vessel and controlled the upstream fluid discharge from the system. The flow through the bundle was choked for the majority of the transient. The transient tube loading was explained in terms of the associated fluid mechanics and the maximum load was compared with existing models obtained under steady flow conditions. An empirical model was developed that enables the prediction of the maximum tube loads once the pressure drop is known.

ACKNOWLEDGEMENTS

TABLE OF CONTENTS

LIST OF FIGURES

xi

LIST OF TABLES

LIST OF ABBREVIATIONS

AC	Alternating Current		CFD	Computational Fluid Dynamics
AECB	Atomic Energy Control Board		CLAIR	Code for LOCA Analysis of Indian PHWRs
AECL	Atomic Energy of Canada Limited		CSE	Containment System Experiments
ASME	American Society of Mechanical Engineers		DAQ	Data Acquisition
ATHOS	Analysis of the Thermal Hydraulics of Steam Generators		DBA	Design Basis Accident
			DC	Direct Current
BARC	Bhabha Atomic Research Centre		DTC	Discharge Time Constant
BLCBE	Boiling Liquid Compressed Bubble Explosion		EPRI	Electric Power Research Institute
BLEVE	Boiling Liquid Expanding Vapour Explosion		FEM	Finite Element Methods
BWR	Boiling Water Reactor		FFT	Fast Fourier Transform
CANDU	Canada Deuterium Uranium		HEM	Homogeneous Equilibrium Model
CATHENA	Canadian Algorithm for Thermalhydraulic Network Analysis		HFM	Homogeneous Frozen Model
CEA	Commissariat à l'Énergie Atomique		LOCA	Loss-of-Coolant Accident

MSLB	Main Steam Line Break	TRAC	Transient Reactor Analysis Code
NEA	Nuclear Energy Agency	TRACE	TRAC / RELAP Advanced Computational Engine
NIST	National Institute of Standards and Technology		
NPP	Nuclear Power Plant		
NRC	Nuclear Regulatory Commission		
OECD	Organisation for Economic Cooperation and Development		
PHWR	Pressurised Heavy Water Reactor		
PWR	Pressurised Water Reactor		
RELAP	Reactor Excursion and Leak Analysis Program		
RTV	Room Temperature Vulcanisation		
SLB	Steam Line Break		
SOPHT	Simulation Of Primary Heat Transport		

LIST OF SYMBOLS

A Area [m^2]

a Transverse pitch ratio

b Longitudinal pitch ratio

Bi   Biot number

C Flow coefficient

c Speed of Sound [m/s]

c_P Specific isobaric heat capacity [J/kg·K]

d Diameter [m]

E Young's modulus [Pa]

Eu   Euler number

F Force [N]

f Frequency [Hz]

$F(t)$ Dimensionless discharge function

Fo   Fourier number

G Mass flux [kg/m^2·s]

g Standard gravitational acceleration [m/s^2]

h Heat transfer coefficient [W/m^2·K]

H Height [m]

h Specific enthalpy [J/kg]

Hg   Hagen number

J Nucleation rate [m^3·s]$^{-1}$

Ja   Jakob number

K Drift flux constant

k Geometric tube bundle constant

L Length [m]

m Mass [kg]

M_{mol} Molecular weight

p Pressure [Pa]

R Radius [m]

Re   Reynolds number

R_g Universal gas law constant [J/kg·K]

s Specific entropy [J/kg·K]

T	Temperature [K]	*Greek symbols*	
t	Time [s]		
u	Velocity [m/s]	α	Thermal diffusivity [m^2/s]
V	Volume [m^3]	γ	Specific heat ratio
w	Mass flow rate [kg/s]	ε	Void fraction
x	Thermodynamic quality	η	Choked pressure ratio
z	Number of tube rows	η	Nucleation kinetics exponential function
		θ	Angle of elevation [rad]
		κ	Thermal conductivity [W/m·K]
		λ	Wavelength [m]
		μ	Viscosity [Pa·s]
		ξ	Pressure drop coefficient
		ρ	Density [kg/m^3]
		σ	Stress [Pa]
		σ	Surface tension [N/m]
		τ	Time constant [s]
		υ	Poisson's ratio

Subscripts

0	Stagnation		r	Rise
a	Ambient		s	Solid
atm	Atmospheric		sat	Saturation
av	Average		t	Transverse
b	Bubble		T	Vessel
c	Choked		TP	Two-phase
cs	Cross-sectional		$trans$	Transition
D	Discharge		u	Upstream
d	Downstream			
eq	Equilibrium			
f	Fluid			
g	Vapour			
H	Homogeneous			
i	Internal			
l	Liquid			
n	Natural			
p	Projected			

DECLARATION OF ACADEMIC ACHIEVEMENT

This experimental laboratory research was undertaken at McMaster University by the author, Ouajih Hamouda, under the supervision of Professor Emeritus Dr David Weaver. The bulk of the work was performed under contract to the Canadian Nuclear Safety Commission (CNSC), Dr Jovica Riznic as Technical Representative, Contract No. 87055-11-0417 – R430.3.

The entire contents of this Thesis represent original research contributions that are a result of novel experiments carried out by the author. The assistance of Departmental Technicians is acknowledged elsewhere. Data analysis was performed entirely by the author, as was the preparation of this Thesis along with all associated diagrams and graphs. The author has presented some facets of this research at various peer-reviewed international conferences. The resulting publications are listed below.

1. Hamouda, O., Weaver, D., & Riznic, J. (2011). An experimental rig and investigation of steam generator tube loading during Main Steam Line Break. *Proceedings of the 14th International Topical Meeting on Nuclear Reactor Thermalhydraulics*, September 25-30, Toronto, ON.

2. Hamouda, O., Weaver, D., & Riznic, J. (2012). Preliminary calibration tests for an experimental study of steam generator tube loading during blowdown. *Proceedings of the Canadian Society for Mechanical Engineering 2012 International Congress*, June 4-6, Winnipeg, MB.

3. Hamouda, O., Weaver, D., & Riznic, J. (2013). Commissioning tests for an experimental study of steam generator tube loading during blowdown. *Proceedings of the ASME 2013 Pressure Vessels & Piping Division Conference*, July 14-18, Paris, France.

4. Hamouda, O., Weaver, D., & Riznic, J. (2014). An experimental study of steam generator blowdown tube loading: preliminary results. *Proceedings of the Canadian Society for Mechanical Engineering 2014 International Congress*, June 1-4, Toronto, ON.

5. Hamouda, O., Weaver, D., & Riznic, J. (2014). Instrumentation development and validation for an experimental study of steam generator tube loading during blowdown. *Proceedings of the ASME 2014 Pressure Vessels & Piping Conference*, July 20-24, Anaheim, CA.

6. Hamouda, O., Weaver, D., & Riznic, J. (2015). Transient loading on nuclear steam generator tubes during a two-phase blowdown. *Proceedings of the 25th CANCAM*, May 31 – June 4, London, ON

7. Hamouda, O., Weaver, D., & Riznic, J. (2015). An experimental study of steam generator tube loading during blowdown. *Proceedings of the ASME 2015 Pressure Vessels & Piping Conference*, July 19-23, Boston, MA.

In memory of Emna Temani (1954 – 2013)

CHAPTER 1. INTRODUCTION

In nuclear steam generators, primary side reactor coolant flows inside the heat exchanger tubes, heating the water outside of the tubes in the secondary shell side to produce steam. Steam generator tubes are exposed to aggressive thermal and mechanical loads during their normal operating life. The tube bundles vibrate when subjected to the flow of secondary side coolant, particularly in the U-bend region of vertical U-tube steam generators where the flow is across the tubes. These potentially destructive vibrations are minimised by the installation of anti-vibration bars that support the tubes. The anti-vibration bars are typically designed to have small clearances between the tubes and their supports to allow for manufacturing tolerances and assembly as well as thermal expansion during operation. As a result, the tubes vibrate against their supports and if the vibrations are significant, mechanical wear may occur. This reduces the tube wall thickness at the points of contact with the tube supports.

The degradation of the tube wall integrity during the lifetime operation of steam generators due to mechanical wear and corrosion lowers the design margin of safety against structural failure. Tube wall thinning is especially problematic in nuclear power plants because the tubes inside the steam generators represent the boundary between the irradiated primary side coolant (deuterium or heavy water, D_2O, in CANDU reactors) and the secondary side coolant (light water, H_2O). The primary side reactor coolant is at a higher pressure than the secondary side coolant and any leakage through defects or tube rupture can therefore lead to the escape of irradiated primary side coolant out of containment. A main concern of reactor safety is to ensure that radioactive materials produced by nuclear fission during operation are safely contained. The loss of the structural integrity of steam generator tubes is therefore of utmost importance and a sufficient design margin against tube failure must always be ensured.

In practice, tube wall thinning is regularly monitored and controlled during scheduled outages. Excessively worn tubes are taken out of service so that the steam generators continue to function reliably over their design life, if not longer. If the main steam line in a Pressurised Water Reactor (PWR) nuclear power plant were to break, the pressurised heated water in the secondary side of the steam generators would suddenly be exposed to surrounding atmospheric conditions. In the secondary side of CANDU steam generators, the operating conditions are typically around 4.69MPa and 260°C. The rapid reduction in pressure to atmospheric conditions would cause the water to flash to vapour, producing what is called a 'blowdown'. This results in a high-velocity two-phase steam-water discharge out of the steam generator through the main steam pipe. A layout of the main nuclear plant components affected by this postulated Main Steam Line Break (MSLB) scenario in a CANDU design is illustrated in Fig. 1-1.

A MSLB accident would produce a very high flow rate of steam due to the substantial drop in the pressure at the point of the break. Since the tubes of a
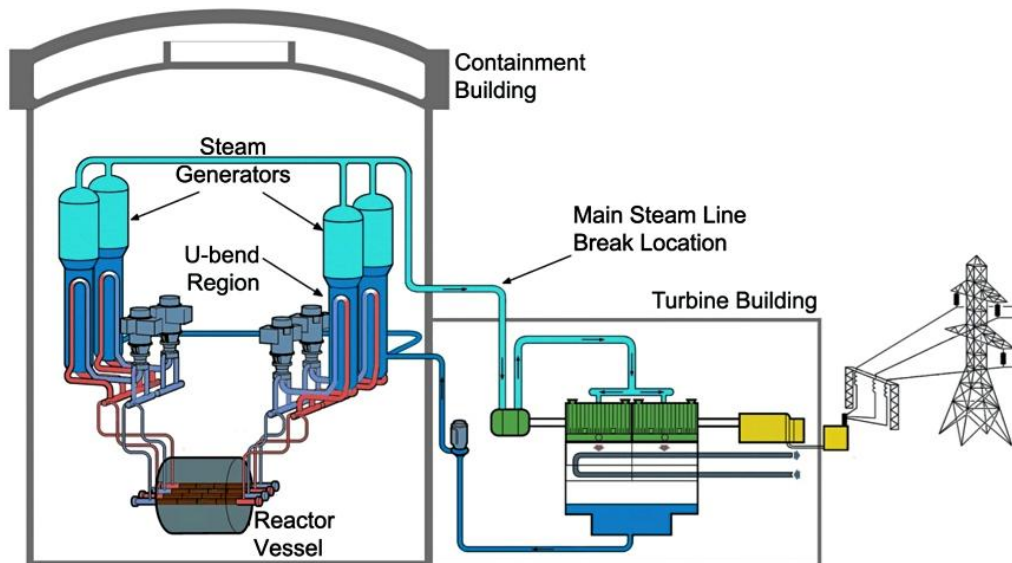
Figure 1-1. Main Steam Line Break (MSLB) accident scenario in a CANDU nuclear plant (adapted from AECL).

vertical U-bend type steam generator are oriented perpendicular to the direction of the flow in the U-bend region, they could be subjected to a significant and potentially dangerous transient hydraulic loading during a blowdown. The risk of structural tube failure is exacerbated if the tube wall thickness has been reduced due to long-term fretting wear and corrosion. If the structural integrity of the tubes is compromised, a leakage pathway is created that could possibly result in the escape of radioactive materials from reactor containment. Since this is unacceptable from a nuclear safety standpoint, it is essential that the structural integrity of the tubes be maintained. Thus, knowing the tube loading during such an event is an important input for safe design.

The transient fluid blowdown phenomenon has been the subject of much investigation in nuclear safety research, with particular focus on predicting the flow discharge properties. The problem is also encountered in the storage and transportation of liquefied gases, the design of refrigeration systems, desalination equipment, and autoclave leaching processes. The analysis of blowdown loading of steam generator tubes deals with complex interactions of rapid transient two-phase flow dynamics and fluid-structural loading processes that are very difficult to model physically or numerically. Hence, tube loading during a MSLB remains difficult to predict with any precision.

1.1. RESEARCH OBJECTIVE

The aim of this experimental study was to simulate a MSLB, investigate the physical phenomena causing the transient loading on a sectional model of steam generator tubes, measure the loading directly, and ultimately, to develop a predictive model for tube loading. The overall purpose of the research is to improve our understanding of the transient loading of steam generator tubes during a blowdown by providing physical insights and guidance for the development of modelling tools so that structural tube failures can be avoided.

Chapter 2 presents a review of the published literature. No predictive model is presently available that can be used to evaluate the dynamic loading of a tube bundle during a transient two-phase blowdown. This is due to a lack of experimental data and physical understanding of the phenomena.

A purpose-designed facility was built for this experimental investigation, which uses R-134a as the working fluid to simulate steam-water in a CANDU steam generator. The blowdown rig contains a CANDU design based model tube bundle in which transient load measurements were obtained. This represents the main experimental novelty of the study. The sectional tube bundle model is a normal triangular array with a pitch ratio of 1.36. Chapter 3 gives an overview of the experimental facility and the procedures employed. Chapter 4 discusses instrumentation problems discovered during commissioning, explaining why these occurred and describing the remedial procedures and corresponding instrumentation validation methodologies developed.

Chapter 5 provides a general description of the two-phase blowdown experiments carried out, accompanied by a discussion of the typical fluid transient thermal hydraulic phenomena observed. The tests were conducted with various levels of liquid R-134a and various numbers of tube rows in the test section. In Chapter 6, a parametric study of the experimental data is performed to develop a fundamental understanding of the transient two-phase flow phenomena and the mechanisms of dynamic tube loading. Chapter 7 explains the transient tube loading in terms of the associated flow physics. The maximum load is compared with existing models for tube loading obtained under steady flow conditions. An empirical predictive model of the blowdown load on the tube bundle is also developed based on the obtained experimental results. Chapter 8 presents a summary of the research findings, outlining the main contributions of this work.

CHAPTER 2. LITERATURE REVIEW

The two-phase blowdown phenomenon has received much attention over the past sixty years. For a comprehensive overview of flashing, depressurisation, vapour generation and growth, two-phase modelling, and other blowdown related research, the interested reader is referred to an excellent review by Pinhasi *et al*. (2005). The United States Nuclear Regulatory Commission (NRC) investigated the issue of steam generator tube vulnerability during a MSLB and concluded from dynamic response calculations that the predicted loads are not expected to pose a structural integrity risk in steam generator tubes (Reichelt, 2009).

The NRC study considered the thermal hydraulics of the initial stages of steam generator blowdown during which pressure waves propagate at acoustic velocities and did not include a detailed investigation of the loads developed because of the discharge flow present following the initial rapid transient effects. In addition, the analysis relied on calculations performed using one-dimensional thermal hydraulics codes (RELAP and TRAC-M), which do not account for three-dimensional cross-flow induced forces on the tubes. The problem continues to be the focus of some numerical investigations but, to the author's knowledge, no thorough experimental study has ever been performed. This chapter provides a brief overview of the relevant research progress made over the years, summarising the findings of the experimental and numerical studies available in the published literature.

2.1. EXPERIMENTAL STUDIES OF MSLB LOADING OF STEAM GENERATOR TUBES

Steam generator thermal hydraulics was the focus of several large-scale nuclear safety experimental programs in the 1970s, with emphasis placed on

modelling postulated critical Design Basis Accident (DBA) events. Large Steam-Line-Break (SLB) simulations were performed in scaled model facilities of typical commercial U-tube steam generators by Framatome in collaboration with CEA (Sireta, 1979), as well as by EPRI (Kalra & Adams, 1980). The purpose of the tests was to develop numerical capabilities to evaluate hydraulic loading on steam generator internals during blowdown transients.

The Framatome tests were performed on a scaled facility of a Model 51 steam generator with a total height of 3.5m, maximum cross-section of $0.2m^2$, and an outlet flow restrictor area of $13.6cm^2$ through which the MSLB was simulated. The transients were initiated from 'hot standby' (0% power) initial conditions with saturated liquid water at 7MPa. The experimental vessel was filled such that the stratified liquid free surface was initially located between the top of the tube bundle and the bottom of the steam separators before the blowdowns were initiated. Transient temperature and pressure measurements were collected and a peak pressure difference of about 70kPa was recorded at the uppermost tube support plate. It was concluded from this research that investigations that are more fundamental were required to study the initial transient stages of the blowdowns during which thermodynamic non-equilibrium effects were strongly influential.

The tests at EPRI were carried out on a 1:7 scale prototypical steam generator facility using Freon-11 as a working fluid. An in-line square tube bundle with 1:1 scale tube diameter was employed consisting of 76 U-tubes with 0.75-inch (1.905cm) outside diameter and 1.05-inch (2.667cm) tube spacing. The MSLB simulations were performed through a 4-inch diameter outlet nozzle ($81.1cm^2$ flow area) from subcooled liquid initial conditions of around 1013kPa and 82°C. Transient blowdown pressure and temperature measurements were obtained with a response time of 10ms and 500ms respectively. The results indicated a transient increase in the pressure drop across the steam separators, but no similar rise in pressure drop was recorded in the tube bundle. In addition, the build-up of back-pressure in a receiver dump tank of 2270L volume was found to

influence the transient depressurisation inside the modelled steam generator vessel significantly.

The Atomic Energy Control Board (AECB) carried out an experimental program (Forrest, 1995) using a different approach to determine the tolerance of steam generator tubes with various defects to high cross-flow velocities. Tube bundles containing 32 tubes in a triangular pitch array with 9 rows of 1.27cm outside diameter tubes and 0.95cm tube row spacing were placed in a water tunnel with a 50.8x13.2cm rectangular channel (670.56cm^2 flow area). High liquid cross-flow velocities were established with tube gap velocities of up to 3m/s. The tubes, of which some were pre-flawed, were tested at steady state up to failure (due to either a leak or complete severance) for a maximum duration of 10 minutes.

Typically, hydraulic loads on tubes in tube bundles are computed from pressure drop measurements using single-phase pressure drop relationships and two-phase flow corrections available in heat exchanger design guidelines (Shah & Sekulić, 2003; Zukauskas & Ulinskas, 1988). In the present study, it is expected that the employed sectional model of steam generator tubes would produce a realistic replication of the two-phase blowdown pressure drop in a commercial steam generator under postulated accident conditions. A significant amount of fluid resistance is imposed on the discharging flashing two-phase flow. Furthermore, a direct measurement of dynamic loading on the tubes is obtained in addition to the dynamic pressure measurements across the test section, which, to the author's knowledge, has never been done before.

2.2. NUMERICAL STUDIES OF MSLB LOADING OF STEAM GENERATOR TUBES

Numerical code simulations of transient events in nuclear systems typically rely on relatively simple models that divide the system into one-

dimensional flow paths. Such codes seldom contain three-dimensional flow modelling capabilities for predicting rapid transient two-phase cross-flow and radial flow conditions around steam generator tubes, which exist during blowdown. Steam generator computational codes usually model a general thermal hydraulic network without including the detailed local behaviour within each of the segments comprising the system. Confidence in the codes is developed through comparison of the numerical predictions with experimental data. For the past 40 years, computational methods have complemented results from scaled model experiments and prototypic tests for safety analysis and licensing purposes (Smith, 2010). In the late 1980s, various attempts were made to model the thermal hydraulics of Loss-Of-Coolant Accidents (LOCAs) and Steam-Line-Breaks numerically. The emphasis in the latter was on predicting the heat transfer characteristics and fluid-structural behaviour of the steam generator internal components.

A numerical simulation of a 100% MSLB from 'hot standby' initial conditions was performed on a 500MW U-tube PHWR (Pressurised Heavy Water Reactor) steam generator model (Saha *et al.*, 1993) using the Code for LOCA Analysis of Indian PHWRs (CLAIR), which is a two-fluid six-equation transient two-phase flow code comparable to TRAC, RELAP, and CATHENA. In order to simplify the analysis, the tube bundle was modelled as a single U-tube consisting only of two vertical pipes and no horizontal segment. The simulation was performed only for the first 1000ms of the transient and a peak pressure difference across the top tube support plate was reported to be just over 100kPa.

Based on this thermal hydraulic analysis, a numerical analysis of the structural loads following a MSLB on the CANDU type steam generator internals was performed (Bhasin *et al.*, 1993). The transient drag force on the tube bundle was computed by considering the outside wall friction on the entire bundle, modelled as a single tube, and the peak force was found to be 242.9kN. This value was divided by the total number of tubes in the actual steam generator, 2489

tubes, giving a maximum drag force per tube of 98N. The calculated maximum drag force in the steam separators was 314.8kN.

A numerical simulation of a complete SLB was also performed at EPRI for a Model-F steam generator using the ATHOS3-MOD1 thermal hydraulics code (Chappidi *et al.*, 1993). ATHOS is a three-dimensional code intended for the analysis of slow operational transients of re-circulating steam generators. The investigation was primarily concerned with the pressure imbalance across the pressure boundary represented by the tube walls due to the depressurisation of the steam generator. The drag pressure loading on the outer surface of the tubes was not directly addressed. Convergence problems were encountered with the ATHOS code as the simulations progressed towards 'dry steam' conditions and an extrapolation of the simulation results provided an estimated 107 seconds for the secondary side liquid to be depleted and steam generator dry-out to occur.

A similar study was performed by Ontario Hydro, which investigated tubes under transient blowdown conditions following a 100% MSLB (Sauvé *et al.*, 1996). A thermal hydraulic analysis of a Bruce 'B' CANDU steam generator was carried out to estimate the transient conditions in the U-bend using the computer code SOPHT. Instantaneous transient flow forces were then derived based on the calculated transient mass flux and pressure drop, which were obtained from the thermal hydraulic parameters: density, flow velocity, and void fraction. The transient simulation was initiated from 103% full power initial conditions, which is contrary to most other investigations in which 'hot standby' or 0% power initially subcooled liquid blowdown is generally considered to represent the worst case scenario for conservative modelling. A velocity correction factor was included in the analysis to account for slip flow between the vapour and liquid phases. The Reynolds number ranged between 10 and 10^5 during the transient blowdown.

The peak flow velocities, and therefore drag force, were established between 20 and 35 seconds following the initiation of the blowdown, as shown in Fig. 2-1. A peak velocity of about 6.8m/s was obtained, corresponding to a peak pressure drop of about 4.2kPa. The simulated velocities during this time segment show large sharp fluctuations of 1 – 7m/s and it is not clear what physical mechanisms could be responsible for such behaviour. The reason for the appearance of the oscillations was not addressed in the report and it may be that these were artefacts of numerical instabilities encountered at higher void factions. In order to derive the applied forces from the transient fluid parameters a two-phase drag coefficient was calculated based on empirical data obtained from bubbly air-water cross-flow over a single circular cylinder. The maximum drag coefficient was determined to be unity for high Reynolds numbers, and slightly higher than one for lower Reynolds numbers of about 100.

Under a TRAC-M (renamed TRACE) code development and validation program for the NRC (Beaton & Fletcher, 2003), code simulations were compared against experimental SLB tests (Mendler *et al.*, 1986) that were specifically
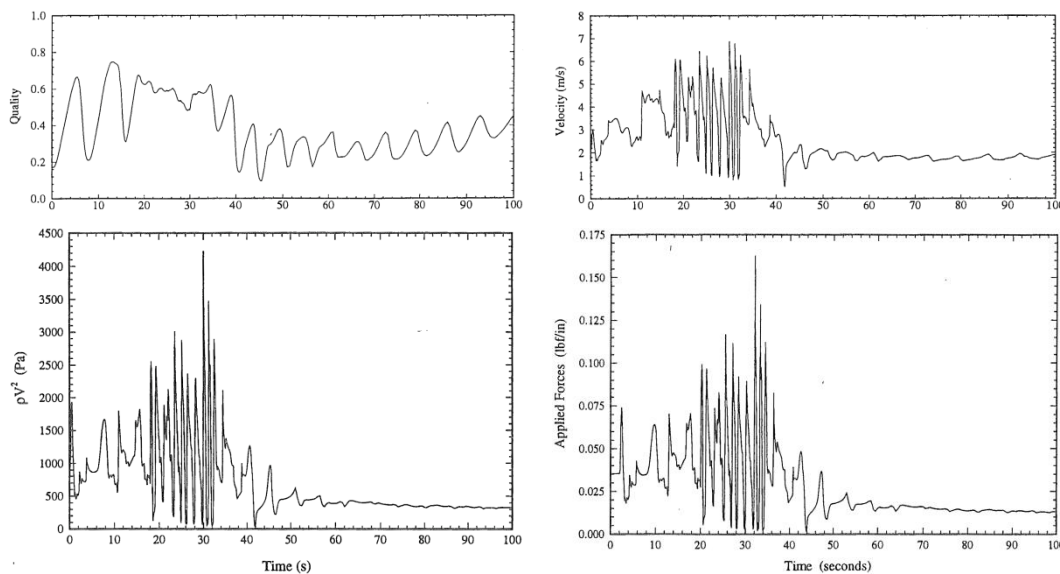
Figure 2-1. Bruce 'B' steam generator transient blowdown thermal hydraulics analysis (Sauvé *et al.*, 1996).

focused on thermal and hydraulic loads on steam generator internals. The experiments were performed in a large-scale Model Boiler (MB-2), which was a near prototypical 0.8% power-scaled facility of a Westinghouse Model F steam generator capable of generating up to 10MW. The MB-2 contained prototypical primary and secondary side temperatures, pressures, and mass flow rates, and was equipped with a tube bundle containing 54 U-tubes arranged in 4 columns and 13 rows. The 7m high tube bundle was constructed with the same material, dimensions (1.75cm tube outside diameter), and tube pitch (2.49cm square pitch array) as the original steam generator design.

Full 100% SLBs were simulated from 'hot standby' conditions by using a quick-opening valve that opens in less than one second. The outlet flow limiter was scaled using a 3.43cm throat diameter installed in a 7.62cm diameter steam line. The initial water levels ranged between 9.91 – 12.45m and the blowdowns were initiated from an initial secondary side pressure of around 7.591MPa to a break downstream pressure of around 99.3kPa. The U-tube bundle occupied a cross-section of 68.4x9.96cm and was wrapped in a rectangular channel placed inside the cylindrical shell of the boiler. This tube bundle channel flow was funnelled into the steam separator and riser sections, effectively isolating it from a region inside the boiler of stagnant 'dead space' represented by the volume outside the tube bundle channel and contained inside the outer shell. The downcomer was simulated by two pipes of 7.8cm inside diameter, which fed into the hot and cold leg openings of the wrapper box surrounding the tube bundle. The cross-sectional area of the pipes was selected to match a scaled representation of the actual downcomer annulus area in the Model F steam generator.

In the numerical simulations, the flow through the tube bundle was treated using a 'hydraulic diameter' variable, which allowed a pressure drop coefficient to be incorporated into one-dimensional flow paths between successive tube support plates. In the first 5 seconds of the transient experiments, a very fast two-phase level swell was observed, accompanied by an almost instantaneous

discharge of liquid. It was also observed that the flow in the downcomer during this initial period of the transient was reversed, such that the fluid at the bottom of the tube bundle region flowed back and upwards through the downcomer pipes rather than through the tube bundle, riser, and separator flow path. It was concluded in the numerical study that the relative losses in the downcomer and the separator towards the steam dome were such that the differential pressures did not change significantly, and therefore, that the experiments were not well suited to determine the ability of TRAC-M to predict transient differential pressure loadings on steam generator internals during MSLBs.

Another investigation by the NRC involved a detailed thermal hydraulic assessment of the loads in a generic Westinghouse PWR steam generator during a MSLB (Krotiuk, 2004) using the numerical code TRAC-M. Computer code simulations indicated that the largest forces occurred during a guillotine rupture of the steam line when the steam generator was initially in a 'hot standby' condition. The model implemented in the code simulations divided the steam generator into one-dimensional flow paths and was not capable of predicting radial flow conditions around the steam generator tubes. The loading on the steam generator internal components was determined based on the calculated thermal hydraulic conditions and the pressure difference was primarily attributable to friction losses.

Pressure drop coefficients, or hydraulic drag coefficients, were incorporated into the model as 'pressure drop correction multipliers' to account for irreversible form drag losses. The peak pressure differences across the tubes and the tube support plates were calculated using the same general pressure drop equation. The drag coefficient for a single tube was calculated using a correlation obtained for the corresponding geometry from a hydraulic resistance handbook (Idel'chik, 1996). A pressure loss coefficient of 1.1 was used for the tube support plates, which was conservative relative to the calculated pressure loss coefficient of 0.96 for flow through a thick perforated plate. A correction for two-phase

pressure drop was incorporated through a multiplier of 1.2 and an additional multiplier of 1.5 was included to account for uncertainties in the modelling.

The simulation results suggested that the largest loads were caused by thermal hydraulic effects related to the propagation of the initial depressurisation wave at acoustic velocity immediately following the sudden pipe break. Flow-induced loads that develop because of the 'quasi-steady' flow established after the initial rapid transient effects were judged to be smaller than the loads that arise during the initial stage of the transient. Consequently, the detailed TRAC-M investigation was only performed for the initial stage of the MSLB transient and no extensive analysis of the 'quasi-steady' loading on the steam generator internals was carried out. The peak pressure difference across the primary steam generator tubes at the U-bend was found to be 7.2kPa. A higher peak pressure difference of 59.1kPa was obtained across the top tube support plate, with a peak mass flow rate of 24,000kg/s.

The TRAC-M calculations were also compared to analytical calculations performed using predictive models for critical discharge from pressurised vessels (Moody, 1990). The calculation gives the instantaneous pressure difference across the tube support plate produced by the rarefaction wave travelling from the break location when it arrives at the tube support plate. The pressure directly above the tube support plate is lowered while the pressure directly below the tube support plate remains at the original pressure. The amplitude of the depressurisation wave entering the steam generator following the MSLB was found by determining the maximum choked flow rate and the corresponding discharge pressure at the break location. This was obtained from the steam generator volume, the initial fluid mass, the initial stagnation pressure, the initial stagnation enthalpy, and the break line diameter and area. Friction losses and pressure wave reflections were ignored and the pressure difference was calculated to be 62.1kPa.

In order to evaluate the behaviour of the cross-flow in the tube bundle region numerically, a three-dimensional fluid model must be applied to the transient discharge flow during the steam generator blowdown. In the NRC report, questions were raised concerning the potential accuracy of results obtained from a complete transient analysis, and specifically whether any existing thermal hydraulics codes such as TRACE and RELAP are able to accurately predict the behaviour of transient liquid boiling under relatively low pressure conditions. Oscillations in the data were observed as the void fractions progressed towards higher values and these instabilities were attributed to numerical conditions resulting from inaccuracies in the fluid-thermal correlations in the code. It was concluded that before the accuracy of such predictions can be accepted, the ability of thermal hydraulics codes to predict 'quasi-steady' thermal hydraulic steam generator behaviour correctly must be properly verified in advance.

During large-diameter SLBs, the steam generator restrictor is expected to choke the outlet flow, isolating the steam generator from any pressure fluctuations in the steam line. Furthermore, flow path resistances in the steam generator and two-phase flow established during a MSLB would mitigate the propagation of pressure waves from the steam line towards the tube bundle region. A summary of the results obtained during the simulated effects of MSLBs on steam generator internal components is presented in Table 2-1.

A variety of steam generator internal components was investigated with a wide range of analysis methodologies. Pressure loss coefficients were typically included, from which the drag load was computed. The sudden 'acoustic' hydrodynamic forces associated with the propagation of pressure waves were modelled according to a step change in pressure across the associated structural boundaries. Flow-induced vibration was studied by simulating the flow properties and using the computed forces as input for numerical structural models. In none of these studies was the hydraulic drag on the tube bundle due to the high-velocity transient two-phase cross-flow directly addressed.

Table 2-1. Summary of simulated MSLB pressure loads on steam generator internals.

MSLB research project	Year	Method of investigation	Test conditions	Peak pressure loading	Steam generator component	Physical loading mechanism
Framatome / CEA	1978	Scaled experiment	Saturated liquid H_2O (7MPa)	68kPa	Top tube support plate	Fluid-structural loading
EPRI	1980	Scaled experiment	Subcooled liquid F11 (1.01MPa)	1.1kPa	Steam separators	Fluid-structural loading
BARC	1993	CLAIR simulation	Subcooled liquid H_2O (5.99MPa)	98N (drag per tube)	Entire tube bundle	Tube wall friction
Ontario Hydro	1996	SOPHT simulation	Saturated liquid H_2O (4.6MPa)	4.2kPa	U-bend tubes	Flow-induced vibration
NRC	2004	TRAC-M simulation	Subcooled liquid H_2O (5.47MPa)	7.2kPa	U-bend tubes	Acoustic load
NRC	2004	TRAC-M simulation	Subcooled liquid H_2O (5.47MPa)	59.1kPa	Top tube support plate	Acoustic load
NRC	2004	Moody analytical calculation	Saturated steam H_2O (5.5MPa)	62.1kPa	Top tube support plate	Acoustic load

2.2.1 COMPUTATIONAL FLUID DYNAMICS MSLB SIMULATIONS

The application of Computational Fluid Dynamics (CFD) codes in nuclear safety analysis is not as well established as numerical system codes. CFD codes offer the advantageous capability to incorporate complex geometries and three-

dimensional flow effects, which are not properly predicted by one-dimensional system codes. However, the huge degree of sophistication intrinsic to transient two-phase flow phenomena makes CFD codes difficult to use in the evaluation of nuclear accident events. A comprehensive assessment of the state of affairs in terms of CFD applicability in nuclear safety simulations is provided by the OECD/NEA (Smith, 2010).

A coupled CFD / FEM (Finite Element Modelling) study was carried out to simulate a blowdown experiment performed at FZK in Germany (Wolf, 1982). Single-phase predictions with fluid-structure interaction agreed with experimental data for the initial stages after the break before phase change took place. Transient two-phase phenomena then begin to dominate, for which the simulations did not produce reliable results. A CFD analysis of a MSLB in a BWR (Boiling Water Reactor) was carried out at Forsmark NPP in Sweden (Tinoco, 2002). The instantaneous forces obtained were approximately twice those previously estimated from simpler methods and no experimental validation of the results was available.

The Korean Institute of Nuclear Safety instigated a CFD study of transient pressure in the main steam line of a PWR plant (Yu & Jo, 2007) following an incident at an operating plant in which a pressure relief valve was suddenly opened by accident. The event resulted in 7.115MPa steam being blown off to the atmosphere, which damaged some of the plant piping system components. The force caused by the rate of change of momentum in the main steam line due to the sudden change in the mass flow rate propelled a 3.3m pipe elbow into a refuelling water storage tank 50m away.

Using similar theoretical modelling principles as those established in the previous CFD investigation, the transient thermal hydraulic response of a steam generator secondary side to a MSLB was analysed (Jo & Moody, 2015) with the steam modelled as a real gas. The results of the CFD model suggested that the

steam in the region inside the steam generator above the tube bundle accelerates to a peak velocity of about 18m/s during a MSLB. By comparing this to normal operational velocities in the U-bend of around 2m/s, it was concluded that the hydraulic loading on the tubes could increase by a factor of nine.

2.3. CURRENT STATE OF KNOWLEDGE

In published accounts dealing with the investigation of the transient effects of MSLBs on tube bundles, the issue of fluidelastic instability vibrations occurring due to the increase in fluid velocity is sometimes raised. Fluidelastic instability happens in a tube bundle when the threshold critical velocity is met. The flow energy is then transferred at a sufficiently slow rate to the tubes such that a significant number of seconds is required for damaging vibration levels to be established. Once these vibrations begin, a considerable amount of time is needed for through wall wear or fatigue failure to occur, which can be as little as a few hours in extreme cases. Given that the transient loading duration during a steam generator MSLB is not more than a couple of minutes at most, fluidelastic instability is not likely to be a concern. The main fluid loading mechanism to be investigated and predicted is the transient drag load due to the substantial rise in the pressure drop across the tubes.

Mechanical tube loading during two-phase fluid blowdown involves the complex coupling of rapid transient two-phase flow dynamics and three-dimensional fluid-structural loading processes, which are very difficult to model physically or numerically. The difficulties are essentially associated with the accurate modelling of the physical nature of the liquid and vapour interfaces. These can exhibit very complex mechanics, the prediction of which is beyond current numerical capabilities. For instance, the velocities of the liquid and vapour velocities are often assumed equal, or in some cases, slip is accounted for through some physical or empirical relationship. In reality however, the mechanical

interactions between the two phases may be very complicated due to transient density variations, interfacial drag forces, and non-uniform pressure distributions along the interfacial boundaries. Similarly, the interfacial area concentration in a two-phase fluid depends on the phase change behaviour due to the transfer of heat and mass between the two phases.

During a two-phase blowdown, new interfaces can be created by bubble nucleation and existing interfaces can be destroyed by bubble coalescence. The problem of transient vapour bubble growth involves the complex modelling of a non-linear moving boundary. Simplifying assumptions such as spherical bubble symmetry, constant bubble concentration, and evenly dispersed non-coalescing bubbles are often employed to enable the development of numerical solutions (Pinhasi *et al.*, 2005). The two-phase flow patterns depend on the structural boundaries of the flow and the rapidity of the transient, in which a complete phase transformation of a significant amount of liquid to vapour occurs in the time scale of about 1 second, which adds to the above complexities.

The development of reliable tools for the prediction of hydraulic loading on tube bundles during large-break scenarios remains challenging. To the author's knowledge, there are no published accounts that accurately simulate two-phase transient blowdown pressure drop across tube banks or provide detailed measurements of tube loading during such events. Steam generator tube loading during a MSLB accident therefore remains difficult to predict with any precision.

CHAPTER 3. EXPERIMENTAL FACILITY

A purpose built experimental facility was designed and constructed to perform the simulations of a steam generator blowdown for this study. The system consists of four main components. The steam generator conditions are simulated by a vertical pressure vessel holding static liquid at the bottom and a test section with a sectional model of a typical tube bundle at the centre. The sudden pipe break is simulated at the top end by a rupture disc. The discharged fluid collects in a large vacuum reservoir placed above the disc, designed so that its pressure does not rise sufficiently during a blowdown experiment to control the process adversely. The following sections present an overview of the experimental facility and operating procedure. Design details of the facility are in Appendix A.

3.1. WORKING FLUID

The working fluid is refrigerant R-134a, which boils at near standard temperature and pressure and dynamically scales steam-water reasonably well for the purposes of this study. Experiments that are performed with water at typical steam generator conditions require large-scale facilities that are expensive to build and operate because of the high pressures involved and the significant amount of heat energy required. Modelling fluids with lower boiling points and latent heats of vaporisation than water are often used in thermal hydraulics tests to reduce the costs and technical difficulties. Using R-134a in this study greatly simplified the required experimental facility and decreased the associated costs.

By using R-134a, the experiments could be performed at near ambient laboratory conditions. The moderately low pressures meant that it was possible to use thin rupture discs, which open predictably and completely without introducing any blockage to the flow area at the rupture point. Additionally, since the

saturation temperature of R-134a is close to ambient conditions, it was relatively easy to maintain uniform initial temperatures without any thermal insulation. Direct visual liquid observation during the rapid blowdown event was also facilitated by performing the experiments at ambient temperature conditions.

In the fluid-to-fluid modelling of thermal hydraulics experiments, the flow field geometries, thermodynamics, and hydrodynamics should be scaled for both fluids. The loading on steam generator tubes during a blowdown is basically a fluid drag force and is expected to scale with the dynamic pressure head. Thus, fluid density and velocity are important scaling parameters. In two-phase flows, the ratio of liquid to vapour densities is important. R-134a has a density ratio of 35 at a temperature of 26°C and a pressure of 690kPa, which is very close to the water-steam density ratio of 34 at steam generator operating conditions of 257°C and 4.5MPa. The tube diameter and pitch ratio for the sectional model tube bundle used in these experiments were designed in compliance with geometric scaling requirements. The model is typical of CANDU steam generator designs and essentially has full sized tubes with the full-scale pitch ratio.

3.2. DESIGN OF EXPERIMENTAL APPARATUS

An illustration of the experimental apparatus is shown in Fig. 3-1 and a photograph of the facility is provided in Fig. 3-2. The total height of the pressure vessel from its base to the rupture disc is 1.49m and its cross-sectional area is 186cm^2. The height can be changed to 1.26m by inverting the pressurised liquid reservoir at the bottom, which is divided by a blank flange into two compartments with different volumes. The test section has the same cross-sectional area as the rest of the pressure vessel. The test section geometry is 138mm square and consists of a tube bundle of 12.7mm diameter tubes in a normal triangular array with a pitch ratio of 1.36 and 8 tubes per row. Boundary effects are minimised in the sectional bundle by using half tubes at the side walls.
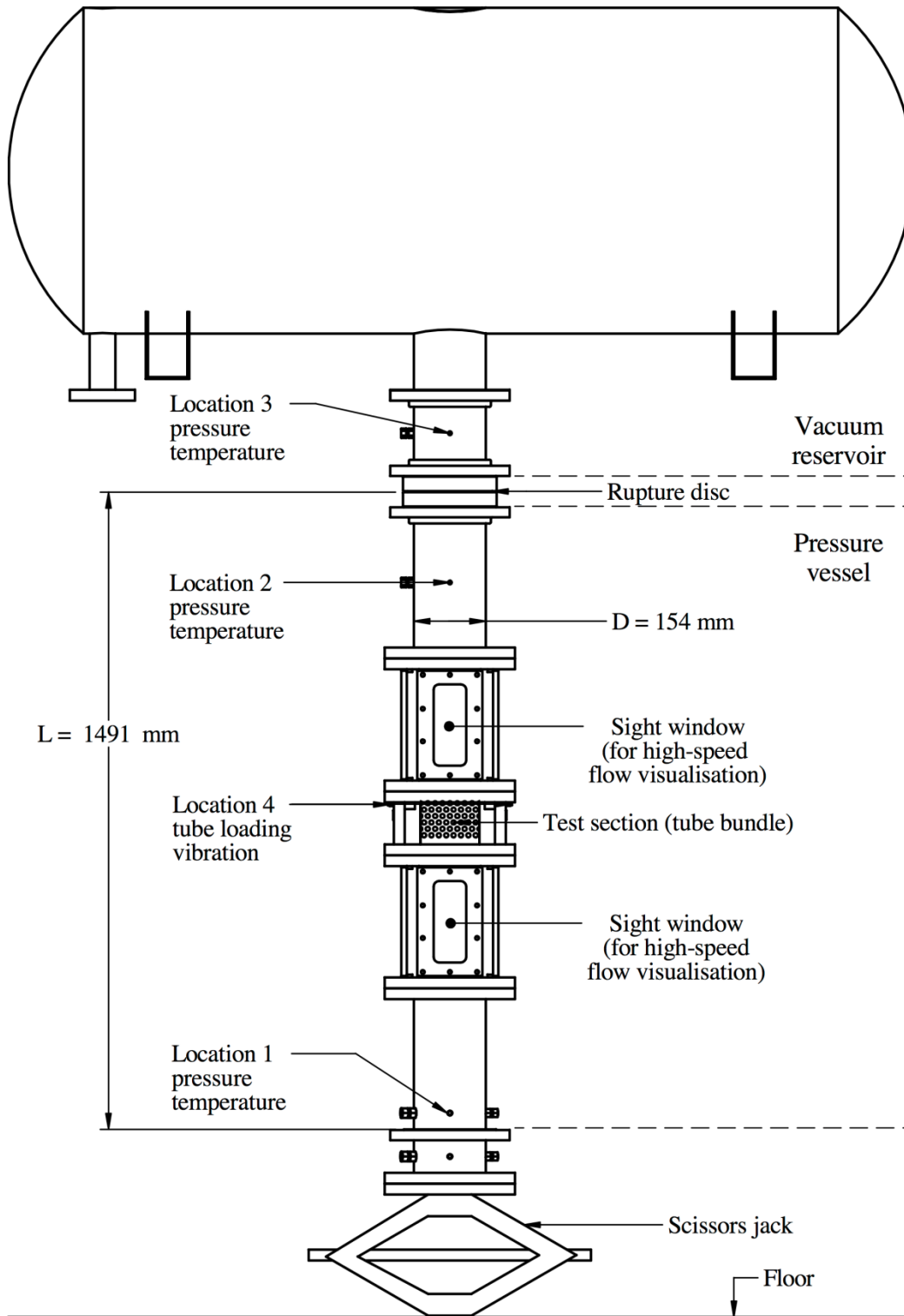
Figure 3-1. Experimental apparatus for simulating a steam generator blowdown.

Figure 3-2. Photograph of the experimental facility.

The simulation of a sudden guillotine pipe-break requires that the pressure relief be produced very rapidly with the pressure vessel cross-sectional area fully exposed to the downstream pressure. Rupture discs were chosen for this study since they open completely and predictably in a few milliseconds, without any obstruction to the flow, at a prescribed pressure difference of around 584kPa. Transient temperatures and pressures were measured upstream and downstream of the test section (locations 1 and 2 in Fig. 3-1 respectively) as well as downstream of the rupture disc (location 3 in Fig. 3-1) during the blowdown experiments. Fluid loading was obtained by summing the measurements of four piezoelectric load cells located on the corners of the test section (location 4 in Fig. 3-1). Vertical axis vibrations were also measured at the test section. Sight glass windows were placed above and below the test section so that the blowdown fluid mechanics could be visually monitored using two synchronised digital high-speed cameras.

3.3. EXPERIMENTAL PROCEDURE

A schematic diagram of the experimental apparatus is shown in Fig. 3-3. For each experiment, a rupture disc was inserted and the entire system above and below the rupture disc was drawn to a vacuum to purge any gases and create the necessary low pressure downstream of the rupture disc. A vacuum level of about 99.9% (70Pa) was established using a 250W rotary vane pump. The vacuum pump was operated intermittently to prevent overheating. The complete purging of the vacuum reservoir typically lasted for a few days.

The fluid reservoir was then charged with R-134a until the desired liquid level and pressure were achieved. Factory sealed R-134a bottles with a net weight of 13.6kg were used to deliver working fluid into the pressure vessel. These were fitted with liquid and vapour supply valves. The pressure differential between the pressurised R-134a supply and the experimental vessel was sufficient to drive the
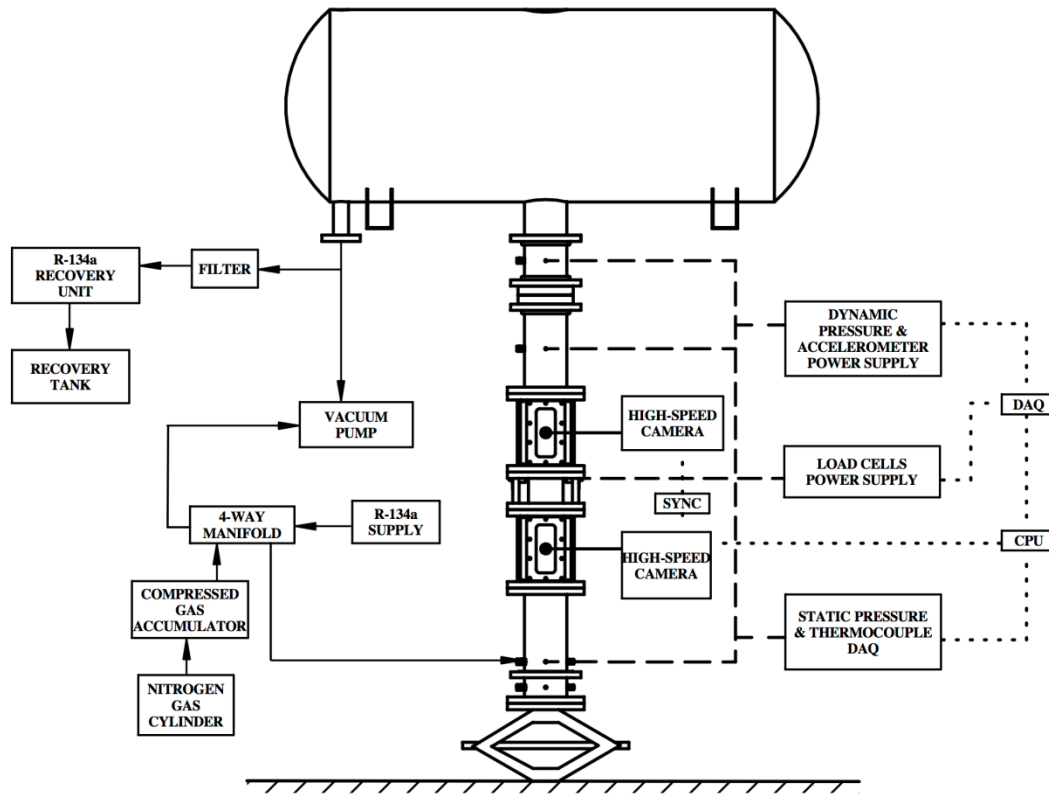
Figure 3-3. Schematic diagram of the experimental apparatus.

fluid into the reservoir without the need for any mechanical pumps. For large volumes of liquid, ambient cooling of the experimental facility and warm water bath heating of the R-134a supply facilitated the pressure vessel charging process. The amount of fluid charged into the pressure vessel was monitored using a digital R-134a scale and the reservoir pressure was monitored using static pressure sensors. The typical time required to reach satisfactory initial conditions at steady state was on the order of several hours for each experiment.

The final increase in pressure required to begin the transient blowdown was obtained using a nitrogen (N_2) gas pressure supply. The pressurised N_2 cylinder was connected to a compressed gas accumulator consisting of two chambers separated by an elastomeric diaphragm. This permitted the R-134a pressure to be finely controlled without introducing any foreign contaminant to

the system. The burst pressure for each rupture disc was between 555 – 613kPa (±5% manufacturer specified tolerance) so the precise rupture point could not be determined in advance. Thus, all of the instruments including the cameras were set to continuously capture and buffer the data before disc rupture and a number of pressure boost trials were performed until the disc ruptured. Ambient heating of the experimental facility during this stage facilitated the process by steadily increasing the static pressure of the R-134a, thereby decreasing the time required to achieve disc rupture.

When the rupture disc bursts, it emits a pressure wave that propagates towards the dynamic pressure transducer above the disc (location 3 in Fig. 3-1). The wave propagation time between the two points is about one millisecond. The arrival of this wave at the sensor point was set to trigger the logging process. This way, signal recording began almost immediately following the instant of rupture without any loss of data. This enabled the reliable acquisition of the rapid transient signals for the entire duration of the blowdown experiment, which was typically over in about one second. Once the experiment was complete, the working fluid was recovered using a positive displacement compressor, which draws the system contents down to a vacuum level of 51kPa. A filter was installed in the recovery line to remove foreign particles and dissolved moisture. The recovered R-134a was stored in 22.7kg tanks and reused in subsequent tests.

Following the purging of the system, the rupture disc was removed and replaced. The entire blowdown rig was supported on a stiff steel support structure such that the pipe from the vacuum tank to the fluid reservoir was suspended above the floor with sufficient space to insert a scissors jack at the bottom of the rig, as shown in Fig. 3-1. This jack was loaded against the pressure vessel so that the vertical transient load from the blowdown was carried largely by the floor rather than the vacuum tank. The scissors jack also facilitated the process of replacing the rupture discs by supporting the weight of the assembly below the disc and allowing it to be raised and lowered as required.

CHAPTER 4. INSTRUMENTATION DEVELOPMENT AND VALIDATION

The experimental investigation of the transient loading of a tube bundle by a suddenly accelerated fluid during a blowdown requires reliable measurements of dynamic pressures, temperatures, and loads. A number of challenges were encountered with the use of off-the-shelf instruments in this study. These were associated with the rapidity of the blowdown phenomenon, the significant transient temperature changes involved, and the shock loading produced with the initiation of the experiments.

The sudden opening of the rupture disc and the resultant rapid pressure relief of the pipe section upstream subjected the experimental facility to a significant axial shock loading. This produced transient structural responses due to the propagation of stress waves and vibrations. As a result, shock and vibration induced artefacts were apparent in the dynamic measurements of pressure and tube loading. Commissioning tests also showed that the sudden drop in temperature contributed to the degradation of the dynamic pressure sensor signals. In some cases, the data was compromised to the point that the output signals were of little quantitative value.

Rather than accepting the results as they were, it was considered important in this experimental investigation to identify the underlying causes of the instrumentation problems and address them correctively. The objective was essentially to remove the problematic effects from the signals as much as possible. This required a re-evaluation of all of the instruments: static and dynamic pressure transducers, thermocouples, and load cells. A program of instrumentation development was initiated to generate a reliable measurement capability for the current blowdown experiments.

The instrumentation development stage of this research consisted of a series of single-phase compressed N_2 gas blowdowns that were performed under similar initial conditions as the full-scale two-phase experiments. These commissioning tests enabled the evaluation and validation of the instrumentation and data collection system. Corrective actions were implemented to improve instrumentation reliability and resolve erroneous signals caused by undesired external effects. The success of the remedial measures was assessed by examining the sensor outputs under various input conditions. The following sections outline the design strategies and tests carried out to establish confidence in the pressure, temperature, and load data collection and instrumentation system.

4.1. PRESSURE INSTRUMENTATION DEVELOPMENT

The dynamic pressure sensors chosen for this study were high-sensitivity piezoelectric dynamic pressure transducers supplied by Dytran (models 2200 and 2300) with a range of 690kPa or 1720kPa and a nominal sensitivity of 2.9mV/kPa or 7.25mV/kPa depending on the model. Piezoelectric quartz transducers of this type are well suited for measuring transient blowdown pressures since they respond very rapidly with rise times of microseconds. They do not measure static pressures however. For the static pressure measurements, silicon-based strain gage pressure sensors supplied by Measurement Specialties (model U5100) were used. These measure down to zero absolute pressure and were therefore appropriate for the entire range of experimental conditions from the vacuum point to the maximum design pressure of 690kPa. The accurate measurement of transient blowdown pressures was one of the biggest challenges encountered in this study.

An example of erroneous pressure signals obtained during a preliminary commissioning test is shown in Fig. 4-1. Spurious artefacts are apparent in the first few milliseconds of the signal, where $t = 0$ represents the instant of disc

27

rupture. The large-amplitude high-frequency fluctuations cannot be explained physically by transient fluid pressure phenomena. The pressure amplitude also drops below absolute zero, which is physically impossible.

Several factors may have contributed to these measurement distortions. The main problem is that the blowdown produces transient thermal variations and mechanical vibrations in addition to the rapid changes in pressure. These concurrent effects can potentially compete with the desired pressure measurements in the signals. The vibration and temperature effects induce structural strains in the stainless steel body of the pressure transducer, which may affect the piezoelectric crystal inside. A response of the piezoelectric crystal to these undesired inputs would obscure the true pressures and result in erroneous pressure measurements. Although less likely, any flexure or displacement of the sensor lead wires during the blowdown can also create distortions in the signal output.

When a rarefaction pressure wave passes along a pipe, the relief on the internal pressure causes the pipe to suddenly contract in diameter and similarly, a
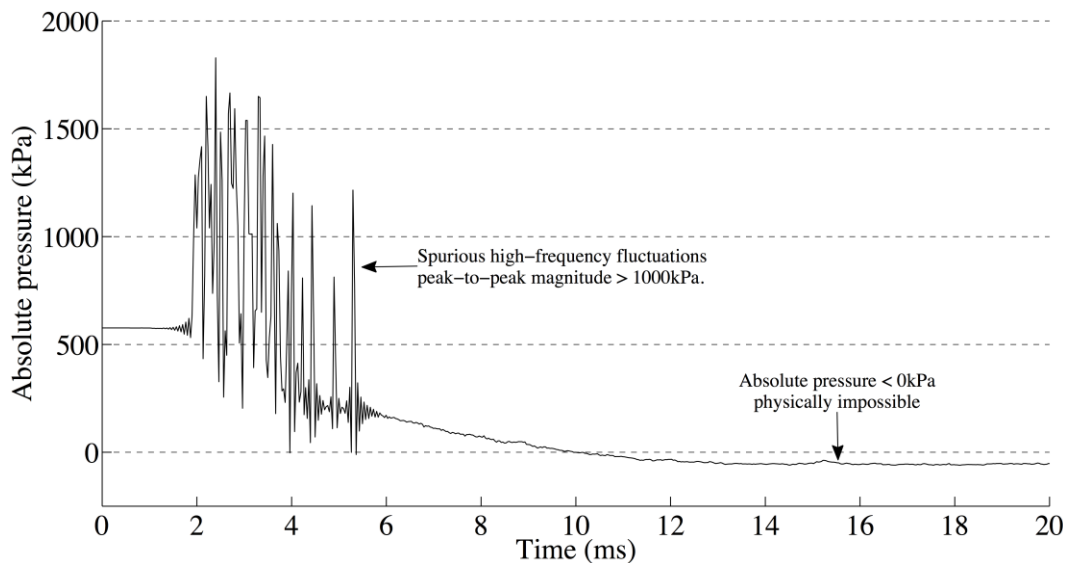
Figure 4-1. Sample erroneous transient pressure measurement during commissioning.

compression pressure wave would produce a sudden pipe expansion. These rapid pipe wall movements can subject pressure transducers mounted onto the pipe to significant accelerations. The dynamic pressure transducers chosen for this study are acceleration compensated by design. The integrated acceleration compensation acts in the axial direction of the sensors to minimise the effects of vibration in the measurements. As such, it was expected that the sensors would only be sensitive to transient pressure variations and would not pick up vibration signals from the rig during the blowdowns. The high-frequency 'ringing' observed in the pressure signal shown in Fig. 4-1 immediately following the opening of the rupture disc raised the question of whether the acceleration compensation in the sensors was capable of handling the vibration magnitudes generated in these experiments.

The breathing mode frequency of the pipes in the experimental facility, f_n, was estimated to be 5.3kHz according to Eq. (4-1) (Blevins, 1979),

$$ f_n = \frac{1}{2\pi R} \sqrt{\frac{E}{\rho(1-\upsilon^2)}} \, , \qquad (4\text{-}1) $$

where R is the cylinder radius, E is the modulus of elasticity, ρ is the density of the pipe shell material, and υ is the Poisson's ratio. The 5.3kHz frequency determined for the axisymmetric pipe breathing mode is of the same order as the frequency of the fluctuations observed in the dynamic pressure signals in Fig. 4-1. This suggests that radial pipe vibrations generated by the opening of the rupture disc might be responsible for the high-frequency high-amplitude 'ringing' observed in the pressure signals.

The vibrations can cause the piezoelectric quartz element and other components inside the pressure transducers to act as seismic masses. These inertial effects act in the direction parallel to the measurement axis. It appears that the alleged acceleration compensation performance of the sensors was

unsatisfactory for these experiments, the result being that the measurements were significantly degraded by the signal fluctuations caused by pipe vibrations. It seems that the transducer calibration may also be affected since the pressure amplitude drops below 0kPa vacuum, which is physically impossible.

There are many examples of published bodies of work with similar vibration-induced artefacts visible in dynamic pressure measurements. These are usually encountered in experimental studies dealing with steep large-amplitude pressure variations such as those that may occur during water-hammer, compressed gas detonation, pressurised vessel explosions, emergency liquefied natural gas transfer release, and pressurised pipe break (blowdown) accidents (Kang *et al.*, 2011). Even though the readings can sometimes be physically meaningless (such as the negative absolute pressure amplitude in Fig. 4-1), it seems that such pressure oscillation artefacts are generally either averaged or ignored (Chao & Shepherd, 2004).

For instance, periodic pressure fluctuations were observed in the results of a series of Containment System Experiments (CSE) performed to assess pressurised water reactor transients (Allemann *et al.*, 1970). The pressure signal oscillations were significant and occurred at a frequency of about 1kHz. The phenomenon was mainly attributed to trapped acoustic waves in the pressure taps connecting the instruments to the pressure vessel. In addition to these oscillations seemingly caused by the pipe tap connections, high-frequency fluctuations were also observed in pressure signals from sensors situated inside the vessel, in direct contact with the fluid, without any connecting tubes in between. These could not be explained physically and were most likely caused by structural vibrations. Figure 4-1 demonstrates that when such signal 'ringing' occurs, the remainder of the measurement could be distorted. Consequently, the overall quantitative reliability of the measurements cannot be guaranteed.

The response of piezoelectric pressure transducers can also be affected by exposure to rapid temperature changes that produce thermal gradients in the sensor body. If the thermal deformations are large enough to exert a physical load on the quartz crystal inside the sensor, then the pressure transducer registers a thermal output response, even if the pressure were to remain constant. In some cases, the thermal shock can cause a significant divergence of the transducer response from the desired pressure measurement. The problem has been encountered in two-phase pipe blowdowns (Winters & Merte, 1979) and internal combustion engine applications (Lee *et al.*, 2005), and is acknowledged by manufacturers of the piezoelectric transducers.

During a two-phase blowdown, the suddenly depressurising fluid simultaneously undergoes a significant transient drop in temperature. The transient temperature reduction observed in preliminary commissioning tests in this study was as large as 80°C in some cases. This subjects all of the components of the experimental facility, including the pressure sensors, to a rapid thermal shock that can result in erroneous pressure signals. Dynamic pressure transducer specifications provided by the manufacturers include a steady-state thermal drift correction coefficient. However, there is no manufacturer documentation available on the effect of abrupt temperature changes on pressure measurements.

Pressure measurements obtained during commissioning suggested that the transient mechanical and thermal effects caused by the initial blowdown pressure release consistently corrupted the dynamic pressure transducer signals. Contrary to some other published accounts in which no attempt was apparently made to correct or eliminate the resultant erroneous sensor readings, it was considered important in the present study to resolve all of the spurious artefacts in the signals. Since these effects cannot be easily quantified, they must be anticipated and minimised in order to establish measurement credibility and ensure reliable data collection.

4.1.1 VIBRATION AND THERMAL ISOLATION

Vibration isolation is a technique by which the undesirable effects of mechanical vibration are minimised. The magnitude of the vibration response can be significantly lowered by reducing the transmission of the excitation forces to the vibrating system. In practice, elastomeric suspension is commonly used for vibration isolation applications, which also adds damping. For this study, vibration isolation devices for the dynamic pressure transducers were custom designed, manufactured, and tested for accurate and reliable dynamic pressure measurement capability.

The design strategy was to embed the vibrating mass (pressure transducer) in a flexible material (isolator) attached to the vibration source (pipe wall) so that lower amplitudes of system dynamic response would be obtained for specific excitation conditions. The transducer mass vibrates at the natural frequency of the system and the required 'isolator' stiffness was selected to provide sufficient force transmission reduction. Since a low system natural frequency is desired, the support stiffness must be low and the vibrating mass must be relatively large.

A vibration isolation design was developed by moulding an elastomeric material, which provides the soft support, between the pressure transducer and the pipe wall. The pressure transducer is mounted in a custom manufactured brass ring to increase the mass of the vibrating system. RTV silicone is moulded between this ring and a brass housing, which is mounted onto the pipe wall. A photograph of the vibration isolator design and an illustration of the mounting orientation are shown in Fig. 4-2. The device is fixed in the pipe walls with the pressure sensing face flush with the inside walls of the pipe. This was important in order to capture the dynamic pressures of the propagating waves accurately following the opening of the rupture disc. Details of the vibration isolation device are provided in Appendix B.1.
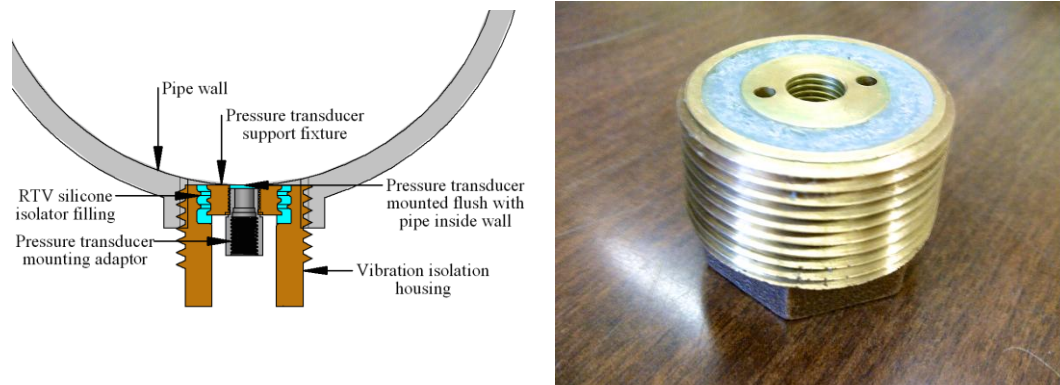
Figure 4-2. Prototype device for pressure transducer isolation.

Erroneous measurements caused by thermal loading were also addressed and corrective measures for these were developed and implemented. The thermal shock phenomenon was tested by dipping the pressure transducers from room temperature into a container of ice water and observing the output response. Theoretically, a pressure sensor that is gently dipped from room temperature into a pool of colder liquid should not indicate any significant change in pressure. The process is essentially isobaric, assuming that the hydrostatic pressure is negligible, and any detectable signals emitted from the sensor would therefore be artefacts of thermal shock. The static pressure sensors, which are digitally temperature-compensated, were tested in this way and no visible thermal-induced response was registered. The output response of the dynamic pressure transducers however showed substantial susceptibility to thermal shock.

Different ways of minimising the temperature effects were investigated and it was found that the application of a 2mm layer of thermal insulation (RTV silicone, grade 108) on the pressure sensing face of the sensors was most effective. The effects of sudden temperature changes on the dynamic sensors were compared with and without insulation coatings. A sample comparison is shown in Fig. 4-3, which plots spurious pressure signals against the logarithm of time. The spurious pressure signal amplitude caused by the thermal input in the exposed pressure transducer is 120kPa. This represents almost 20% of the sensor full

measurement range for a temperature drop of about 20°C. Importantly, this peak in thermal response begins within a few milliseconds of immersion. The effect of the insulation was to increase the time taken for the transducer to be affected by the thermal shock substantially (by as much as two orders of magnitude) as well as to reduce the spurious pressure amplitude. The effect of delaying these thermal effects is important since the dynamic pressures of interest are typically measured in the first tens of milliseconds in the blowdown experiments.

The transient temperature profile of a 2mm layer of insulation dipped into a liquid at 0°C from room temperature can be predicted from an unsteady one-dimensional heat conduction analysis. The boundary conditions are ambient fluid temperature (0°C) on the cold side and perfect insulation on the hot side (pressure sensor face). The temperature variation inside the layer is characterised by the Fourier number, Fo, and the Biot number, Bi, defined in Eqs. (4-2) and (4-3) respectively,
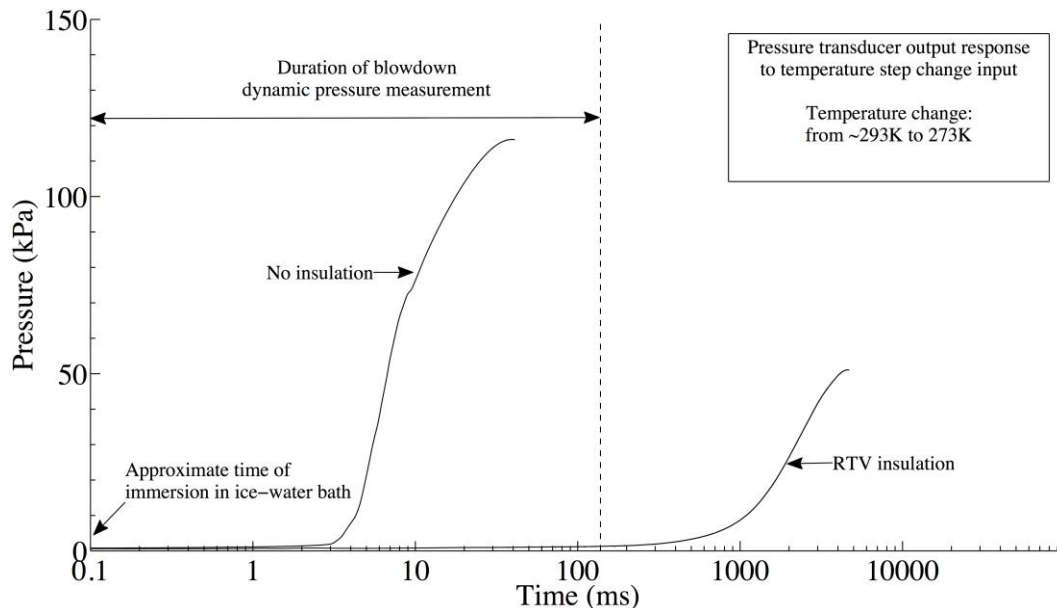
Figure 4-3. A comparison of the output response of the dynamic pressure transducers dipped gently into a container of ice water with and without a layer of insulation coating applied.

$$\text{Fo} = \frac{\alpha t}{L^2} \, , \tag{4-2}$$

$$\text{Bi} = \frac{hL}{\kappa} \, , \tag{4-3}$$

where α is the thermal diffusivity, t is the characteristic time, L is the characteristic length, h is the average local heat transfer coefficient, and κ is the thermal conductivity.

The instantaneous temperature at any given position along the length of the insulation layer can be determined from the unsteady heat conduction solution. The thermal diffusivity of the RTV insulation layer was determined to be $1.4 \times 10^{-7} \text{m}^2/\text{s}$. The time required for the temperature at the hot end of the layer to drop by $0.2°\text{C}$ was solved numerically for water ($\kappa = 0.6 \text{W/m·K}$) and R-134a ($\kappa = 0.09 \text{W/m·K}$). The Biot number was found to be 11.7 for water and 7.1 for R-134a, and the time delay was determined to be about 2.1s for water and 2.2s for R-134a. The estimated times are greater than the transient durations of the blowdown experiments in this study, which establishes further confidence in the insulation performance of the RTV silicone layer for the purposes of this research.

The stiffness of the piezoelectric pressure transducers is generally specified by the manufacturers to be around 80MN/m. The RTV silicone insulation layer stiffness, k, can be estimated based on the coated surface area of the pressure transducer, A, the elastic modulus, E, and the coating layer thickness, L, according to Eq. (4-4),

$$k = \frac{AE}{L} = \frac{0.25\pi \left(0.009\right)^2 \cdot 1.16 \times 10^6}{0.002} = 37 \text{ kN/m} \, . \tag{4-4}$$

The calculation indicates that the axial stiffness of the thermal insulation layer is about three orders of magnitude smaller than the stiffness of the pressure

transducer. Therefore, the effect of the former on the sensitivity of the latter is expected to be negligible.

The speed of sound in RTV silicone is about 1000m/s whereas it is only about 530m/s in liquid R-134a at 20°C. It takes about 2μs for a pressure wave to travel across the 2mm layer of RTV silicone. Since the pressure wave acoustic velocity is higher in the RTV silicone than in the surrounding fluid, pressure waves are transmitted to the pressure transducer without any phase distortions in the pressure signals. Hence, by insulating the sensors using a thin layer of RTV silicone, the sensor thermal output response is delayed sufficiently and the measurements obtained are expected to be reliable and accurate before heat transfer produces any degradation in the signals. The vibration isolator device shown in Fig. 4-2 was designed so that the pressure transducers could be installed with a 2mm recess at the measurement point, which was filled with RTV silicone for thermal insulation.

A sample set of signals obtained at the point directly above the rupture disc (location 3 in Fig. 3-1) during a N_2 gas blowdown test is shown in Fig. 4-4. The measurements were provided by each of a static pressure sensor, a dynamic pressure transducer installed directly in the pipe, and a dynamic pressure transducer that was vibration isolated using the device shown in Fig. 4-2. The radial positioning of the sensors and their proximity is such that the pressure signals should essentially be the same. Some phasing discrepancy may be expected due to the opening pattern of the rupture disc and the three-dimensional spatial distribution of the initial pressure wave propagating from the rupture point.

The results demonstrate that the output signal of the un-isolated sensor contains a sharp dip in pressure 2 – 3ms after blowdown initiation, which is probably caused by vibrations in the pipe walls. This undesired response is consistent with previous commissioning results in which the mechanical effects were unaccounted for. Additionally, the pressure amplitudes following this sharp
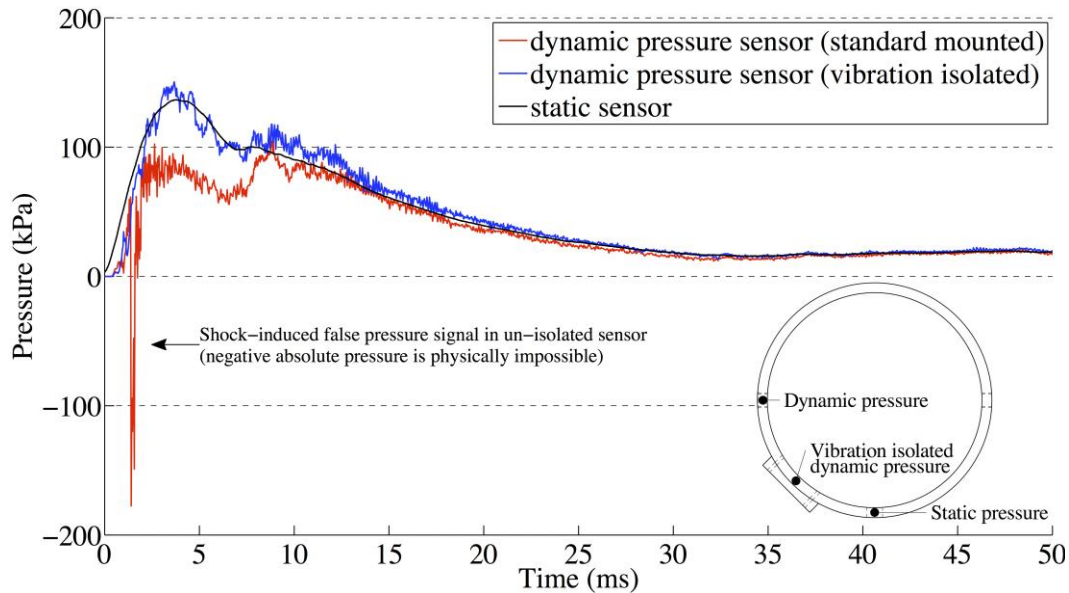
Figure 4-4. Vibration isolated dynamic pressure during N_2 commissioning test.

decrease in the pressure do not agree with the pressures measured by the other sensors for about $5 - 10$ms. This suggests that a sensor providing erroneous signals induced by undesired effects may suffer from a loss of accuracy that cannot be determined beforehand. The importance of addressing the spurious artefacts in the measurements is clearly demonstrated in these results.

The pressure signals collected from the other two sensors in Fig. 4-4 show good agreement. The vibration isolated pressure transducer captures the local pressure perturbation details, while the overall pressure amplitudes match the static sensor measurements. Based on the matching pressure amplitudes, it also appears that the thermal shock effects were effectively resolved. Thus, the dynamic pressure measurements were rendered quantitatively reliable for the initial stages of the transient blowdowns involving rapid wave propagations and dynamic pressure variations. After a time delay of about 25ms due to the slower response time, the static sensor provides an accurate average pressure trace for the remaining duration of the transient.

From these results, confidence was established that the mechanically induced artefacts were successfully removed by using custom designed and manufactured vibration isolation devices. Moreover, the application of a thin surface coating of RTV silicone insulation seemed to eliminate the thermal shock effects in the pressure measurements.

4.1.2 PRESSURE DATA REDUCTION

The dynamic pressure transducers were chosen based on their specified high-frequency response of up to 200kHz. This allows for accurate measurements of rapid pressure variations in the first few milliseconds following disc rupture. Given that these piezoelectric sensors do not measure steady-state pressures, static pressure sensors were used to monitor and establish the vessel pressures and initial conditions in the preparatory stages of the experiments. Interestingly, it was discovered that the static sensors also offered some dynamic capabilities.

The static sensor manufacturers quoted a response time constant of 160μs in a private communication, which gives a signal rise time of about 0.8ms. This is about two orders of magnitude slower than the dynamic pressure transducer response. Thus, the static pressure sensor output signals are low-pass filtered measurements of the average transient pressures, and do not contain the details of the dynamics that occur in fractions of milliseconds. The sensors are digitally temperature compensated by an integral temperature sensor through an internal signal conditioner, which is MEMS-based (Micro-Electro-Mechanical Systems) with a temperature range of -40°C to 125°C.

Figure 4-5 shows transient pressure measurements obtained below and above the rupture disc (locations 2 and 3 in Fig. 3-1 respectively) in a N_2 gas blowdown test. A dynamic pressure transducer and a static pressure sensor were installed at each of the pressure measurement points along the blowdown pipe. The transient measurements were acquired from both the dynamic and static

pressure sensors. The individual dynamic and static signals at the two locations are shown on the left of Fig. 4-5. The measurements agree fairly well for the majority of the duration shown, which suggests that two-dimensional effects across the pipe cross-sectional area are insignificant.

The complete pressure measurement for the entire blowdown duration is shown on the right of Fig. 4-5. This was obtained by combining the two sets of simultaneous pressure measurements, starting from the initial rapid transient stage until equilibrium steady state. The dynamic pressure transducers provided the rapid pressure wave propagation and phase information. The relatively slower quasi-steady transient pressure profile was completed by the static pressure sensor measurements. This was necessary because of the drift that occurs in the dynamic sensors when the pressure changes are slow.

Since the static pressure sensors were not originally intended to measure transient blowdown pressures, the data collection system used for the static
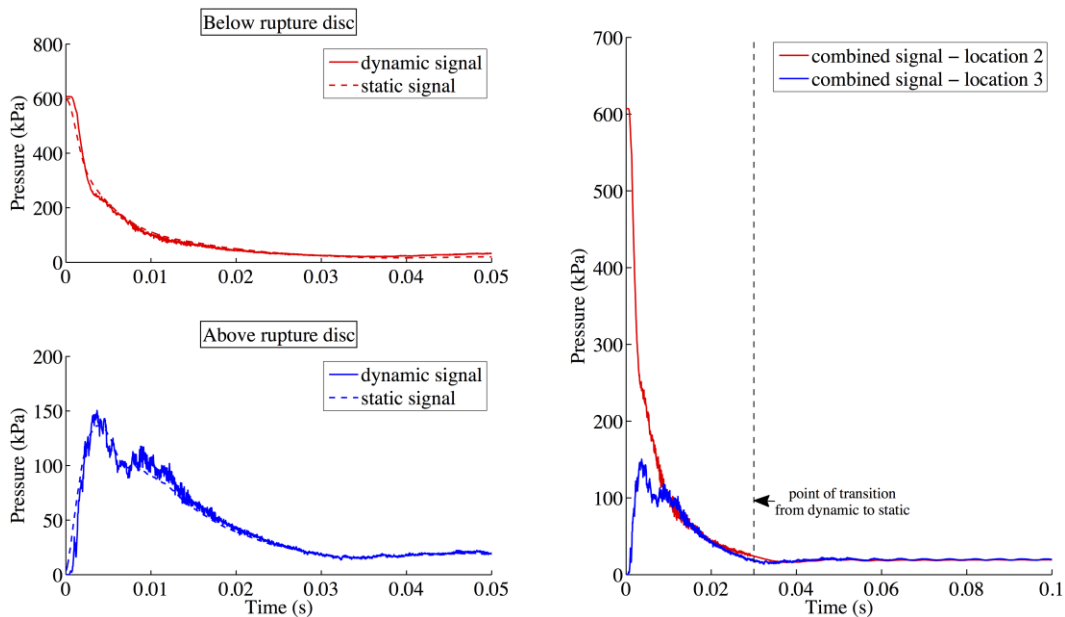
Figure 4-5. Transient pressure during a N_2 commissioning test: individual dynamic and static output signals (left), combined pressure signal (right).

pressure sensors was separate from that used for the dynamic sensors. Considerable care was therefore taken to ensure that the measurements were all accurately synchronised by a hardware-timed clock shared simultaneously between all of the measurement channels. This prevented phase distortion in the signals by providing time-synchronised measurements across all of the data acquisition channels at a sampling rate of 30kHz. The pressure sensors were all calibrated simultaneously in a plenum device that is opened and shut by an electrically controlled quick-acting solenoid valve. This provided repeatable measurements for controlled dynamic step pressure changes as well as constant pressures. Details of the pressure calibration are provided in Appendix B.1.1.

4.1.3   PRESSURE VALIDATION

Aside from eliminating the cost and logistics of handling R-134a, carrying out commissioning tests using single-phase compressed N_2 gas also provides experimental results for which the theory is well understood and predictive mathematical tools are readily available. The theoretical modelling of the transient pressures was easily tractable and reasonably accurate for the N_2 blowdowns, and the results could therefore be used to evaluate the instrumentation and data collection system. Once instrument credibility is established, tests can be performed for which the outcome is not known, with confidence that the output signals are a true representation of the desired phenomena.

The mass flow rate of a compressible gas initially at a uniform stagnation pressure and suddenly released to lower ambient pressure surroundings through a discharge plane can be derived from the continuity equation. The analysis is greatly simplified by assuming isentropic and adiabatic discharge through a perfect nozzle and treating the N_2 as an ideal gas. The corresponding one-dimensional flow at the exit plane during the blowdown of a pressurised gas vessel can be expressed according to Eq. (4-5) (Moody, 1990),

$$w^2 = G^2 A^2 = A^2 \left[\frac{2\gamma}{\gamma-1} \right] \rho_0 p_0 \left(\frac{p}{p_0} \right)^{\frac{2}{\gamma}} \left[1 - \left(\frac{p}{p_0} \right)^{\frac{\gamma-1}{\gamma}} \right],$$ (4-5)

where w is the mass flow rate, G is the mass flux, A is the flow area, γ is the ideal gas specific heat ratio, ρ_0 is the gas density, p_0 is the gas pressure, and p is the exit pressure. If the difference between the vessel pressure and the ambient pressure is sufficiently large, the flow will be choked. Choking occurs when the ratio of the ambient downstream pressure to the upstream vessel pressure is less than the choked pressure ratio, η. This can be determined from Eq. (4-6),

$$\eta = \frac{p_c}{p_0} = \left(\frac{2}{\gamma+1} \right)^{\frac{\gamma}{\gamma-1}},$$ (4-6)

where p_c is the critical (choked) pressure at the exit plane. When the flow is choked, the mass flow rate of the gas discharge is maximum and depends only on the upstream conditions in the vessel. The choked velocity of the gas is equal to the speed of sound, and the choked or critical mass flow rate is given by Eq. (4-7),

$$w_c = -A_D C_D \left[\gamma p_0 \rho_0 \left(\frac{2}{\gamma+1} \right)^{\frac{\gamma+1}{\gamma-1}} \right]^{\frac{1}{2}},$$ (4-7)

where A_D is the discharge area and C_D is the discharge coefficient. The discharge coefficient is typically used to account for non-isentropic losses due to factors such as orifice geometry restrictions. In the present analysis, isentropic discharge was assumed and the coefficient was set to unity. The instantaneous mass remaining in the vessel can then be calculated from Eq. (4-8),

$$m(t) = m_0 \left[F(t) \right]^{\frac{2}{\gamma-1}},$$ (4-8)

where m_0 is the initial mass of gas in the vessel and $F(t)$ is a time-dependent function (Fthenakis, 1993) defined by Eq. (4-9),

$$F(t) = \left[1 + \frac{w_{0,c}(\gamma - 1)}{2m_0} t \right]^{-1},$$

(4-9)

where $w_{0,c}$ is the initial critical mass flow rate. The instantaneous discharge flow rate, pressure, temperature, and density can be derived from Eq. (4-8) and the respective relationships are shown in Eqs. (4-10), (4-11), (4-12), and (4-13),

$$w(t) = w_0 \left[F(t) \right]^{\frac{\gamma + 1}{\gamma - 1}},$$

(4-10)

$$p(t) = p_0 \left[F(t) \right]^{\frac{2\gamma}{\gamma - 1}},$$

(4-11)

$$T(t) = T_0 \left[F(t) \right]^2,$$

(4-12)

$$\rho(t) = \rho_0 \left[F(t) \right]^{\frac{2}{\gamma - 1}},$$

(4-13)

where T is the gas temperature. The equations presented above apply only when the flow is choked. When the pressure in the vessel drops to the point that the downstream to upstream pressure ratio is above the choked pressure ratio, the flow at the discharge plane becomes subsonic. The time required for the discharge flow to transition from choked to subsonic can be determined from Eq. (4-14),

$$t_{trans} = \frac{2m_0}{(\gamma - 1)w_0} \left[\frac{1}{\sqrt{\frac{\gamma + 1}{2}} \left(\frac{p_a}{p_0} \right)^{\frac{\gamma - 1}{2\gamma}}} - 1 \right],$$

(4-14)

where p_a is the ambient pressure. The subsonic discharge mass flow rate is given by Eq. (4-15),

$$w = -A_D C_D \left[\left(\frac{2\gamma}{\gamma - 1} \right) p_0 \rho_0 \left(\frac{p_a}{p_0} \right)^{\frac{2}{\gamma}} \left[1 - \left(\frac{p_a}{p_0} \right)^{\frac{\gamma - 1}{\gamma}} \right] \right]^{\frac{1}{2}}. \qquad (4\text{-}15)$$

The mass remaining in the vessel can be determined by subtracting the mass discharged over any given length of time and the gas density can be determined according to Eq. (4-16),

$$\rho(t) = \frac{m(t)}{V}, \qquad (4\text{-}16)$$

where V is the vessel volume. The pressure and temperature of the gas can be determined according to the ideal gas law. This analysis procedure implicitly assumes that the gas does not condense during depressurisation and that the pressure in the discharging vessel is uniform.

A theoretical prediction of the gas blowdown pressure is compared against the actual pressure measured at the bottom of the pressure vessel (location 1 in Fig. 3-1) during a N_2 blowdown test in Fig. 4-6. The theoretical transient pressure is based on the analysis procedure presented above using the initial experimental pressure and temperature, the vessel volume, and the assumption of isentropic, adiabatic, ideal gas discharge through a perfect nozzle with the same flow area as the rupture disc. The analysis assumes uniform conditions inside the pipe and does not account for the pressure gradient along the pipe axis, unsteady wave propagation effects, or local pressure perturbations. The prediction in Fig. 4-6 is therefore only an estimate of the real transient pressure.

Despite these simplifications, the measured pressure amplitude and the rate of the depressurisation agree fairly well with the theoretical prediction. The theory predicts a slightly steeper initial depressurisation rate since the flow is modelled as instantly choked and the inertia of the gas as it accelerates from the initial stagnant conditions is not accounted for in the model. A close-up of the
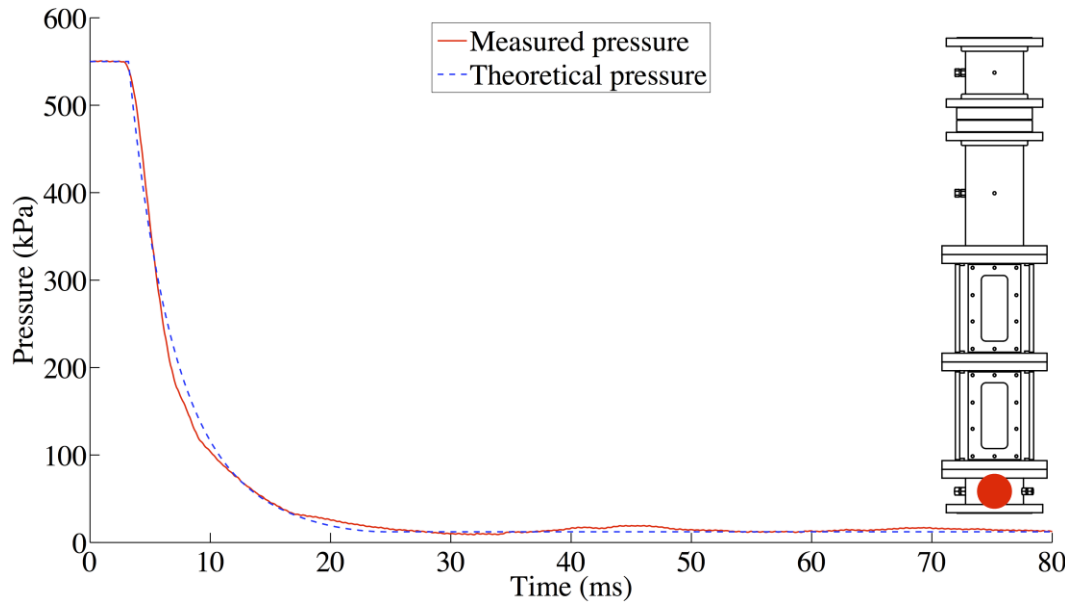
Figure 4-6. Comparison of theoretical N_2 vessel discharge pressure with actual blowdown measurement.

pressures converging towards steady-state conditions is shown in Fig. 4-7. The final static pressure can be estimated by assuming that the gas expands isothermally in the vacuum reservoir. This is supported by thermocouple measurement observations that indicated no discernible change in temperature in this region. The final static pressure calculated according to Eq. (4-17) is

$$p_{final} = p_0 \frac{V_{vessel}}{V_{total}} = 550 \times \frac{0.021}{0.934} = 12 \text{ kPa} . \qquad (4\text{-}17)$$

The measured static pressure of 14kPa at the end of the blowdown is within 2kPa of the theoretical prediction, which validates the static equilibrium pressure measurement. The oscillations in the measured pressure towards the end of the blowdown are caused by wave acoustics, which are not predicted by the vessel blowdown theory. The period of oscillation is about 25ms. The fundamental wave frequency of the first harmonic, f_n, can be determined for a pipe closed at one end and open at the other from Eq. (4-18),
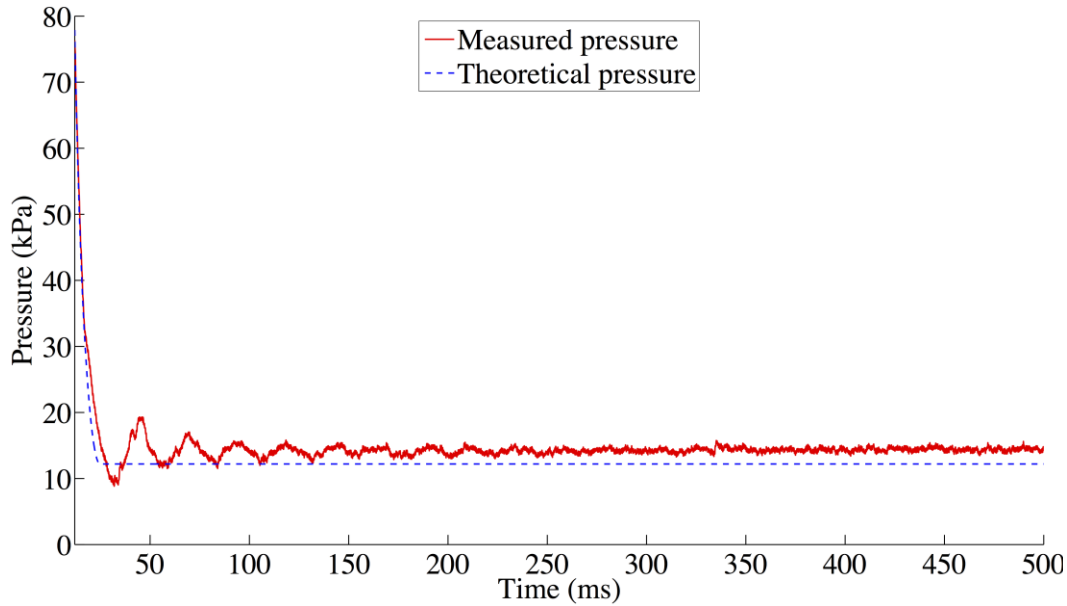
Figure 4-7. Comparison of theoretical N_2 steady-state equilibrium pressure with actual blowdown measurement.

$$f_n = \frac{c}{\lambda} = \frac{c}{4(L+0.4d)} = \frac{334 \text{ m/s}}{4 \times 1.995 \text{ m}} = 42 \text{ Hz}, \qquad (4\text{-}18)$$

where c is the acoustic velocity, λ is the acoustic wavelength, and L is the effective length of the pipe. The measured oscillation frequency was $1 \div 0.025\text{s} = 40\text{Hz}$, which is about the same as the frequency calculated from Eq. (4-18). In addition to the modelling assumptions, instrument uncertainties produce some discrepancy between the theoretical and measured pressures. Overall, the comparison with the theoretical predictions satisfactorily validates the transient pressure measurements over the full duration of the blowdown.

Following the sudden opening of the rupture disc, the pressurised gas is exposed to a downstream region of lower pressure. The propagation velocity of the initial rarefaction wave in the pressurised pipe can be determined based on compressible gas dynamics theory. Simple one-dimensional steep-fronted planar waves propagating at acoustic velocity along the length of the pipe are assumed

45

and head losses and viscous effects are ignored. The gas properties are assumed radially uniform along the pipe flow axis. The temperature is also assumed to remain above the saturation temperature during the blowdown, such that there is no liquid condensation. The acoustic propagation velocity, c, can be calculated from Eq. (4-19),

$$c = \sqrt{\gamma R_g T} = \sqrt{\frac{\gamma p}{\rho}}, \qquad (4\text{-}19)$$

where R_g is the specific gas constant. Alternatively, the wave velocity can be calculated by incorporating the effects of the pipe wall elastic deformation as given by Eq. (4-20) (Tijsseling, 1996),

$$c = \sqrt{\frac{\gamma R_g T}{1 + \dfrac{d\rho\gamma R_g T}{EL}}} = \sqrt{\frac{\gamma p}{\rho\left(1 + \dfrac{d\gamma p}{EL}\right)}}, \qquad (4\text{-}20)$$

where d is the pipe inside diameter, ρ is the gas density, E is the elastic modulus of the steel pipe, and L is the nominal pipe wall thickness. Equations (4-19) and (4-20) both give a wave propagation velocity of 350m/s in N_2 gas at 21°C. This is typical for gas-filled pipes where the fluid-structure interaction is insignificant because the gas density is negligible compared to the solid steel pipe density.

Figure 4-8 presents dynamic pressures measured following the initiation of blowdown in a N_2 gas commissioning test. The measurement locations are indicated on the right. The graph shows the pressure measurements immediately after rupture on a logarithmic time scale, compared against the predicted timings of pressure wave propagation. The logarithmic scale was chosen to emphasise the transient measurements obtained in the initial stages of the experiment. All graphs in this Thesis in which the initial transient stages are important will be presented on logarithmic time scales. The calculated propagation timings are computed based on the pressure wave velocity of 350m/s and the distance travelled to the

corresponding pressure measurement point. The timings of the arrival of the pressure waves at the measurement locations agree very well with the theoretical predictions. The results confirm that the pressure transducers accurately capture the passage of the waves, which validates the dynamic pressure measurements as well as the signal capture and synchronisation system.

In the first few milliseconds following rupture, when the rates of pressure change are rapid, the dynamic pressure transducers provide accurate measurements. The high-amplitude noise of the pressure transducers was eliminated using shock absorbing and vibration isolating adapters. A thin surface coating of RTV silicone insulation was effective in eliminating the thermal shock effects. As steady conditions are approached towards the end of the blowdown, the static pressure sensors provide reliable pressure measurements. The measurements of both sensors are combined to obtain the full pressure trace.

The results of the single-phase commissioning tests showed that the pressure measurements compared reasonably well with theoretical predictions.
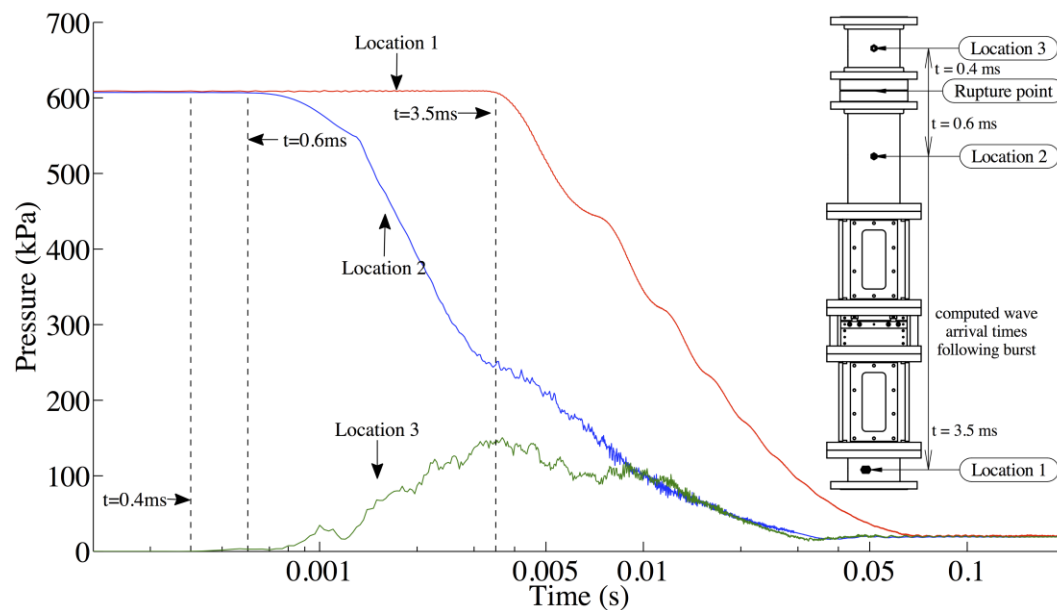
Figure 4-8. Comparison of computed wave propagation timings with blowdown pressure measurements.

The maximum pressure measurement uncertainty was estimated to be ±17.2kPa, with most of the uncertainty attributed to the manufacturer quoted non-linearity of the dynamic pressure transducers. The frequency response of the sensors was established to be within 90% accuracy in the 7Hz – 2.6kHz range for the dynamic sensors and in the 0Hz – 0.2kHz range for the static sensors. Details of the uncertainty analysis and sensor dynamic response characteristics are provided in Appendix sections C.1 and C.4.3 respectively.

4.2. TEMPERATURE INSTRUMENTATION DEVELOPMENT

Sheathed exposed-junction fine wire Chromel-Constantan thermocouples supplied by Omega (model EMQSS-010-6) were used to provide temperature measurements in this study. The diameter of the thermocouple fine wire is 25μm, which was chosen for fast temperature response. The thermocouples are protected by 15.24cm long 0.25mm diameter stainless steel sheaths and were mounted with the exposed junction protruding slightly beyond the inside pipe walls.

A significant challenge associated with the installation of this thermocouple design was creating a seal at the blowdown pipe walls, due to the fragility of the exposed junction and thermocouple sheath. The seal was implemented using custom-machined Teflon ferrules and the details of the sealing methodology are provided in Appendix B.2. Despite being subjected to rapid and substantial changes in fluid flow rate in the blowdown experiments, all of the thermocouples remained intact and performed reliably throughout the experimental phase of this research.

4.2.1 TEMPERATURE DATA REDUCTION

The thermocouple signals were digitally filtered using a zero-phase 2kHz low-pass filter that processes the input data in both the forward and reverse directions. This reduces noise in the signal while preserving the phase. The

transient temperatures were acquired at the same points along the blowdown pipe as the transient pressure measurements. This enabled the evaluation of the fluid thermodynamic properties. A single-component two-phase fluid mixture at thermal equilibrium will exist at its saturated thermodynamic state. The saturated fluid temperature and pressure measurements can be compared to the computed saturated vapour pressure, p_{sat} (in kPa), which is based on the temperature, T (in K), according to Eq. (4-21) (Huber & Ely, 1994),

$$
\begin{aligned}
\log_{10} p_{sat} = 40.7 - \frac{2363}{T} - 13.07 \log_{10} T + 0.0076T \\
+ 0.2343 \left(\frac{376.1 - T}{T} \right) \log_{10} \left(376.1 - T \right).
\end{aligned}
\tag{4-21}
$$

Alternatively, the saturation temperature, T_{sat}, can be computed from the measured pressure, p, according to Eq. (4-22),

$$
T_{sat} = \frac{2094}{14.41 - \ln p} + 33.06 .
\tag{4-22}
$$

Details of the thermocouple calibration are provided in Appendix B.2.1.

4.2.2 TEMPERATURE VALIDATION

A local temperature measurement is plotted in Fig. 4-9 against the computed saturation temperature based on the pressure measured below the rupture disc (location 2 in Fig. 3-1) in a two-phase blowdown test. Overlapping measured and computed temperatures indicate saturated thermodynamic fluid conditions. The measured temperatures and computed saturation temperatures agree closely for the majority of the transient duration. The readings were obtained in the region of the pressure vessel initially filled with pressurised vapour R-134a. The agreement between the two independent measurements validates the data collection system.
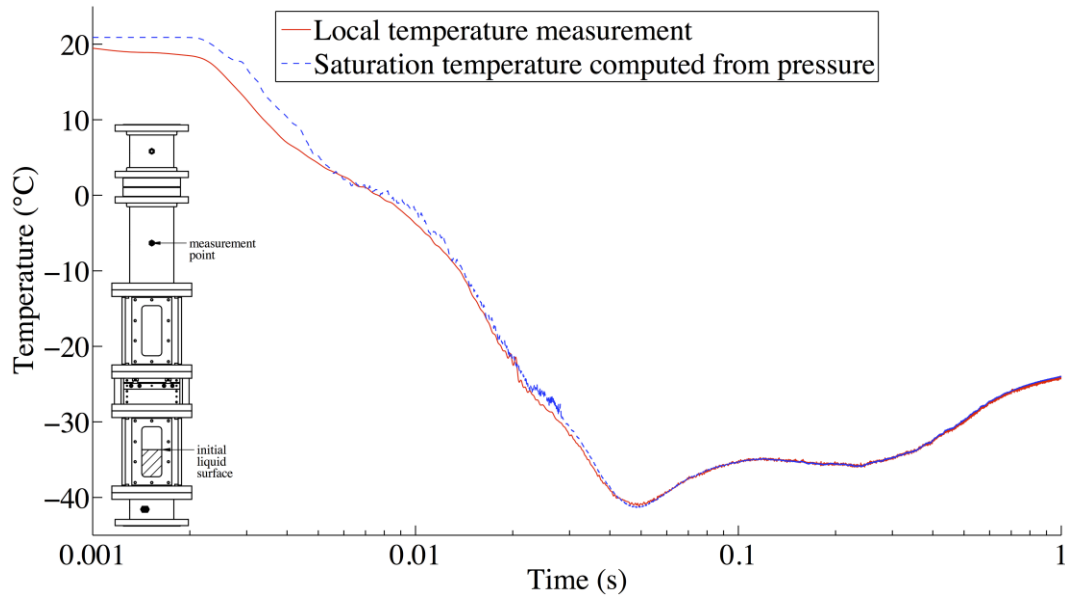
Figure 4-9. Validation of a temperature measurement through a comparison of the measured local temperature and the computed saturation temperature from the measured pressure.

When a fluid is superheated, its temperature would be higher than the theoretically predicted saturation temperature computed from an instantaneous pressure measurement. The initial temperature in Fig. 4-9 was lower than the computed saturation temperature, which represents subcooled conditions. This is due to the relatively cold temperature of the vessel walls, which caused condensed liquid films to form along the inside pipe walls near the thermocouple junction. Upon blowdown initiation, the vapour temperature rapidly went towards saturated thermodynamic conditions. The two curves converged about 5ms into the transient. The saturated thermodynamic condition persisted at this measurement location for the remainder of the transient.

At the end of the transient blowdown, a small amount of residual liquid collects at the bottom of the pressure vessel. The liquid boils and the conditions in the pressure vessel at this point are in thermodynamic saturated equilibrium. A quantitative measure of the uncertainty in the independent temperature and pressure measurements can therefore be obtained by comparing the readings with

the computed estimates. Figure 4-10 presents the same measurements that were shown in Fig. 4-9, between 1 and 3 seconds after disc rupture.

The temperatures from the independent measurements agree with each other to within 0.5°C and the pressures are within 2kPa of each other. The uncertainty of the temperature measurements was estimated to be ±0.9°C. The response time of the thermocouple depends on the heat transfer properties of the surrounding fluid and is difficult to quantify with precision. The dynamic response of the thermocouple measurement shown in Fig. 4-9 appears to match that of the dynamic pressure transducer. Details of the measurement uncertainty and frequency response are in Appendix sections C.2 and C.4.3 respectively.

4.3. LOAD INSTRUMENTATION DEVELOPMENT

The accurate measurement of the dynamic fluid load on the tube bundle proved to be one of the main challenges of this experimental study.
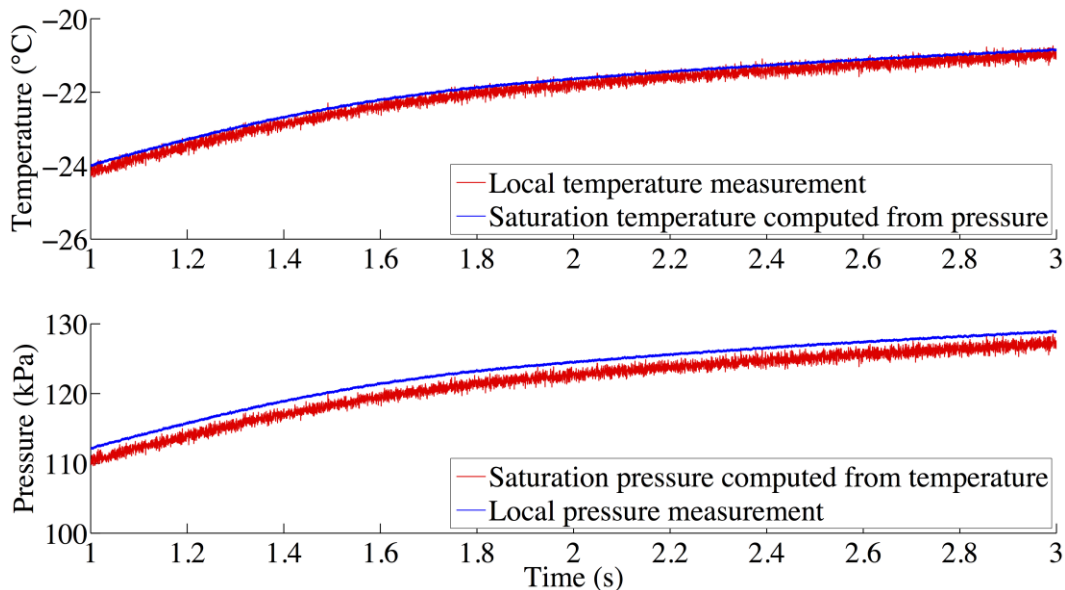
Figure 4-10. Comparison of the measured and computed saturation temperatures and pressures during post-blowdown equilibrium conditions.

Commissioning tests showed that there were many obstacles associated with the transient load measurement system. Figure 4-11 gives an example of the dynamic load measured on the tube bundle in a preliminary commissioning test. The transient pressure drop measured along the length of the blowdown pipe (across the tube bundle) between the bottom of the pressure vessel (location 1 in Fig. 3-1) and the exit region above the rupture disc (location 3 in Fig. 3-1) is also provided.

The pressure drop is initially 573kPa when the rupture disc is closed, and drops to zero after the blowdown is complete and the pressures in the vessel equalise. The load measurement is the instantaneous summation of four piezoelectric load cell signals. Almost immediately after rupture ($t = 0^+$) the effects of the initial shock loading on the sensors are manifested through a steep dynamic load change followed by large-amplitude oscillations. The significant periodic signal fluctuations continue for much of the duration of the blowdown.

Figure 4-12 shows the vibration measurements obtained using an accelerometer mounted on the test section lower steel flange during the
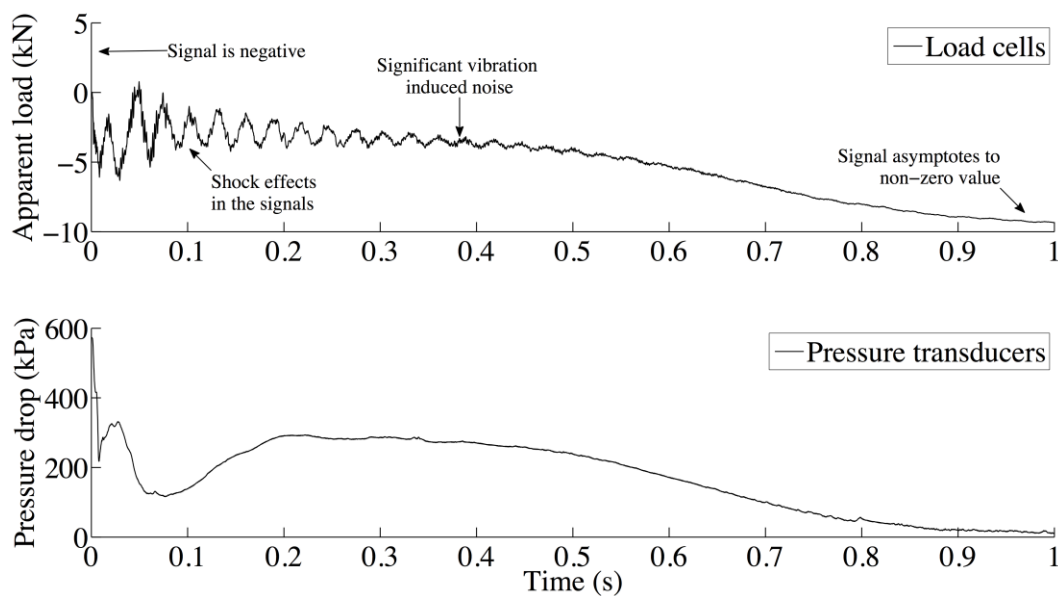
Figure 4-11. Spurious dynamic load measurements on the tube bundle during commissioning.

commissioning test of Fig. 4-11. Also shown are FFT plots of the dynamic load and vibration signals, both of which contain similar frequency content with a primary natural frequency of 35Hz. Thus, the 35Hz oscillations in the load signals were determined to be vibration signals occurring at the lowest axial natural frequency of the test section. Since the oscillations in the signals are understood to represent the test section fundamental axial mode of vibration, as confirmed by the accelerometer measurements, one might simply ignore them and take the mean value of the signal as the tube loading.

Qualitatively, after the first 0.2s of the transient, the trend in the mean load signal shown in Fig. 4-11 follows that of the pressure drop measured across the tube bundle. However, looking at the tube loading measurements, the measured signal is negative when the upward drag load on the tubes should register as positive. The direction of the loading is opposite to that expected. There also appears to be a significant shift of the static zero load signal at the beginning of
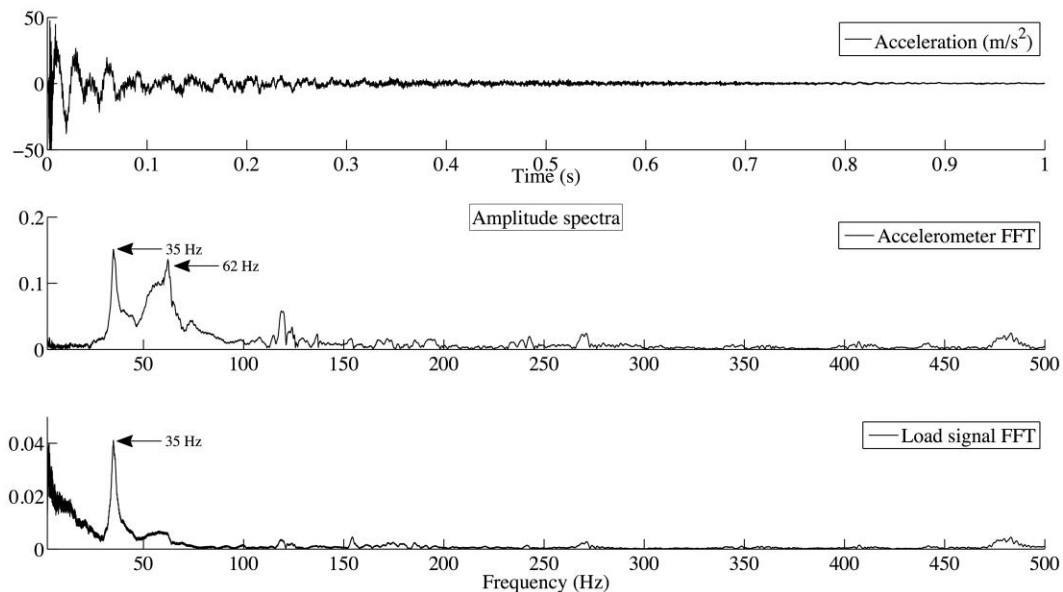
Figure 4-12. FFT analysis of accelerometer and load signals.

the measurement. The measured load must converge to zero at the end of the blowdown under no loading, but the signal asymptotes to about -9.3kN instead.

The symptoms observed in the load signals suggest that large shock-loads associated with the sudden blowdown initiation severely degraded the performance of the piezoelectric load cells. The inertial effects produced by the vibration of the experimental facility further distorted the load signals by introducing large-amplitude periodic oscillations in the signals. The mean dynamic loads remained unexplainable in terms of fluid drag phenomena, and a proper investigation of tube bundle loading could not be carried out.

The magnitude of the sudden axial load on the rig can be estimated by determining the force, F, exerted on the pipe when the rupture disc suddenly opens. Figure 4-13 presents a simplified free-body diagram of the experimental blowdown pipe. The diagram shows the forces before rupture ($t = 0$) and after a time Δt has elapsed, equivalent to the time required for a stress wave to travel the distance between the rupture disc and the load cells. The pressure vessel is modelled as a uniform pipe with a cross-sectional area A_i of 186.4cm^2.

The pipe reservoir is initially filled with stagnant pressurised R-134a at a pressure p_i of 600kPa. The region downstream of the rupture disc is initially in a vacuum, with p_∞ approximated as 0kPa. The cylindrical pipe section below the rupture disc is subjected at the bottom end to an internal pressure p_i and an external pressure p_{atm}. The net pressure differential on the pipe, Δp, is the difference between the internal pressure and the atmospheric pressure, as shown in Eq. (4-23),

$$\Delta p = p_i - p_{atm}. \tag{4-23}$$

A force must counteract this pressure difference in order to satisfy equilibrium, and the two forces must be equal for the cylinder to remain in static equilibrium. When a closed cylinder is subjected to an internal pressure, three
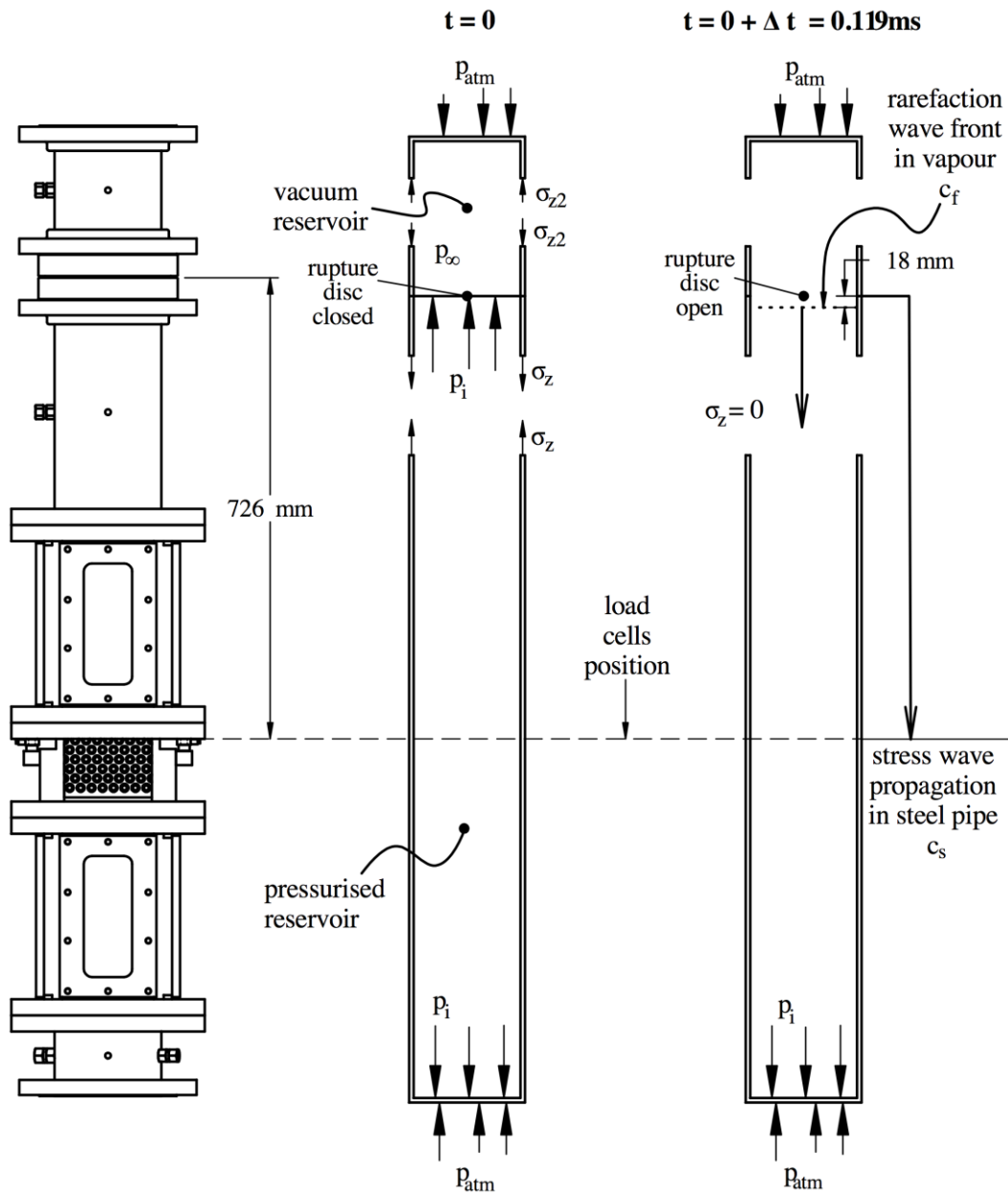
Figure 4-13. Longitudinal thrust shock loading due to sudden disc rupture.

mutually perpendicular principal stresses are created in the cylinder walls. These are the circumferential stress, the radial stress, and the longitudinal stress. The radial forces applied outwards on the pipe walls by the internal pressure produce the circumferential stresses. Similarly, at the closed pipe ends, the static pressure

force stretches the pipe walls and develops longitudinal stresses along the axis of the pipe.

When the inside diameter is more than 20 times the pipe wall thickness, the pipe can be assumed as 'thin-walled'. In this case, the circumferential and longitudinal stresses across the pipe wall are constant and the radial stress is negligible compared to the two other principal stresses. The Schedule-40 steel pipes employed in the current experimental facility have an inside diameter of 15.4cm and a nominal thickness of 0.71cm. The diameter to thickness ratio is 21.7, which is greater than 20 and therefore qualifies the pipe to be modelled as a thin-walled cylinder. Prior to disc rupture, the net internal pressure force is equal to the longitudinal stress force as given by Eq. (4-24),

$$\Delta p A_i = \sigma_z A_t , \tag{4-24}$$

where σ_z is the longitudinal stress, A_i is the inside cross-sectional pipe area, and A_t is the steel transverse area of the pipe.

Following the instantaneous disc rupture, the removal of the pressure boundary between the pressurised and vacuum regions relieves the longitudinal stress in the pipe wall ($\sigma_z = 0$), which was balancing the pressure load at the bottom. Thus, a rarefaction stress wave propagates down the pipe at the speed of sound in steel, c_s, which is about 6100m/s. This reaches the location of the load cells, a distance L_s of 0.726m away, in a time Δt, calculated in Eq. (4-25),

$$\Delta t = \frac{L_s}{c_s} = \frac{0.726 \text{ m}}{6100 \text{ m/s}} = 0.119 \text{ ms} . \tag{4-25}$$

In this time, the distance L_f travelled by the rarefaction wave along the axis of the pipe through the vapour medium, at a sonic velocity c_f, is given by Eq. (4-26),

$$L_f = c_f \Delta t = 150 \text{ m/s} \times 0.119 \text{ ms} = 18 \text{ mm} . \tag{4-26}$$

Since the speed of propagation of the stress wave in steel is much faster than the rarefaction wave in vapour, the pressure in the pipe at the load cells has not yet changed when the balancing stress in the pipe has disappeared. The resulting unbalanced 'shock load', F, can be estimated by Eq. (4-27) as

$$F = \Delta p \cdot A_i = (600 - 100) \text{ kPa} \times 186.4 \text{ cm}^2 = 9.32 \text{ kN} . \qquad (4\text{-}27)$$

Hence, the sudden axial force exerted on the rig is estimated to be about 9.32kN, which is equivalent to a shock loading of about 0.95 tonnes. Due to this sudden shock loading on the load cells, preliminary attempts to measure the transient tube bundle loads were unsuccessful. The load cell signals were apparently saturating immediately following blowdown initiation, producing overall transient measurements that were not useful.

The shock-induced response in the load cell signals shown in Fig. 4-11 appears almost immediately after the rupture disc opened, in about $0.1 - 0.2$ms. The calculated timing of the propagation of the stress wave from the point of the rupture disc to the load cells of 0.119ms is in agreement with these measurements. This lends further support to the interpretation that the registered response in this period is not due to fluid acoustic phenomena, but rather an artefact of the structural stress wave propagation in the pipe walls. Interestingly, the estimated shock loading on the rig from Eq. (4-27) is the same as the 9.3kN amplitude to which the signals were observed to asymptote at the end of the blowdown.

By observing that the load distribution following the initial shock matches the trend of the pressure drop and therefore seems logical, it appears possible that the axial shock loading distorted the load cell signals and displaced the original datum from which the measurements were obtained. The overall load signal may have been shifted by the amount of the steady state zero load signal, which was about 9.3kN. It is therefore plausible, based on explainable physics, that by simply shifting the whole measured load signal upwards by 9.3kN, a true dynamic

measurement of the blowdown drag load would be presented. However, even though the signal trends agreed with pressure drop measurements, the effect of the shock load renders the load cell output to be of no reliable quantitative value.

The extent of signal distortion due to shock-induced loading of the original test section design during commissioning was such that the measured dynamic loads could not be directly related to the fluid drag loading phenomena being investigated. In order to determine the transient drag force on the tube bundle accurately in the presence of the shock loading, it was important to isolate the test section mechanically such that the shock loading does not induce significant signal distortion.

An experimental program was developed and initiated to overcome the shock loading problems and validate the measurement system for dynamic tube loading. Dynamic loads were acquired for various blowdown configurations: with and without the tube bundle installed, using single-phase and two-phase fluids, and with a range of initial fluid volumes. These tests allowed the structural and hydraulic forces on the test section frame during blowdown to be evaluated, which enabled the reliability of the measurement system for the dynamic tube loading to be established.

4.3.1 SHOCK ISOLATION DESIGN

The load cells chosen to measure the dynamic load on the tube bundle were piezoelectric quartz washer-type force transducers supplied by PCB (model 202A) with a measurement range of 44.5kN and a nominal sensitivity of 112mV/kN. The stiffness of each load cell is about 5kN/μm, which is comparable to a solid piece of steel of similar dimensions. The purpose of the test section design was to transfer the dynamic fluid load on the tube bundle entirely through the load cells situated in the exterior of the pressure vessel. An illustration of the load measurement methodology is provided in Fig. 4-14.
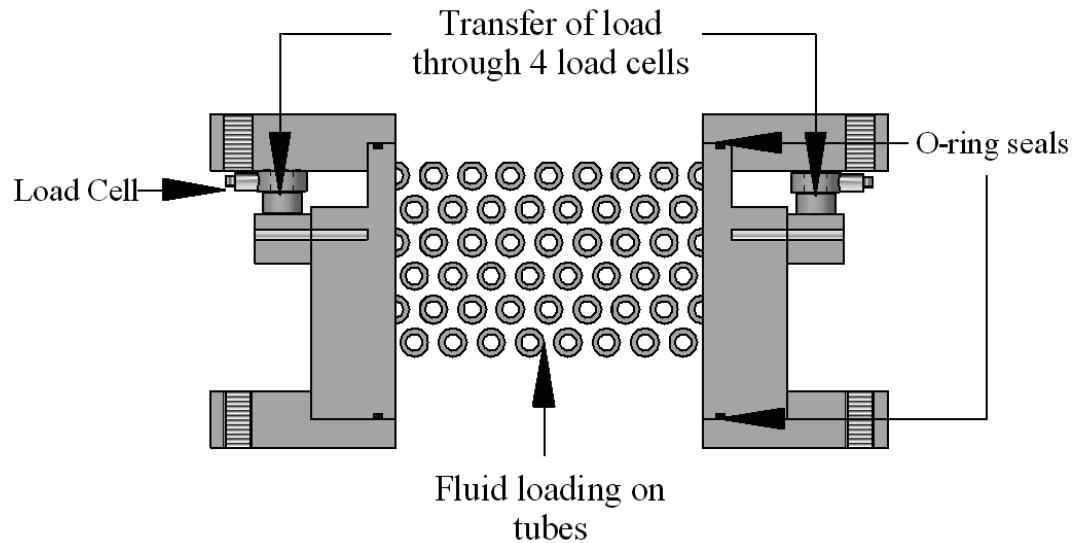
Figure 4-14. Load measurement design.

The load cells needed to be sealed from the internal fluid reservoir to ensure that they would not be not exposed to R-134a. A sufficiently soft seal was required so that the tube bundle was mechanically isolated and the entire dynamic fluid load was transferred exclusively through the load cells. O-rings were placed between the steel pressure vessel flanges and the tube bundle frame for fluid sealing and mechanical load isolation. The expectation was that the fluid drag load would be completely transmitted through the load cells only. If any of the loading on the tubes is transferred anywhere other than at the load cells, the readings would be incorrect. Therefore, it was particularly important in this design that the load was not transferred at the O-rings.

In order for the design to perform satisfactorily, the O-rings must isolate the tube bundle frame from any extraneous loading that may interfere with the measurements. Preliminary measurements of dynamic loads on the tube bundle during blowdown indicated parasitic loading on the load cells. The only logical explanation found for the erroneous transient load results was the presence of alternate mechanical load paths. These produced shock loading on the load cells and resulted in undesirable effects in the signals. Design changes were therefore

needed to ensure accurate load measurement and the test section was modified to correct these issues. In particular, the detrimental initial shock effects and load cell cross-sensitivity needed to be resolved.

Following several design iterations intended to address the above issues, a successfully modified test section design was devised. Among other design changes, the original O-rings, for which the geometrical tolerance was smaller than the structure could tolerate in the form of shock loading, were replaced by thicker O-rings. The high stiffness of the load cells coupled with the relatively negligible stiffness of the newer O-rings used to seal the test section allowed practically the entire load applied onto the tubes during the transient blowdown to be registered by the sensors. Details of the design methodology for shock load elimination are provided in Appendix B.3.

One of the features of the modified test section design was that the tube bundle could readily be removed and replaced either by a tube bundle of a different geometry, or by blank solid walls. When the blank test section walls were inserted in the region formerly occupied by the tube bundle, the obstruction to the blowdown flow was removed. The pressure vessel then essentially becomes a hollow pipe with a uniform cross-sectional flow area. An experiment that is carried out with blank test section walls and a significant volume of liquid would validate the response of the load cells to a virtually non-existent drag load. The shock loading on the rig remains the same, but since there are no tubes in the test section and therefore no restriction to the flow, the drag loading measurement should be almost zero. The only source of loading is friction along the length of the test section walls, which is negligible.

Blowdown tests were performed with varying volumes of liquid R-134a and with the tube bundle removed from the test section in order to evaluate the modified test section design and load cell response to the zero load conditions. Figure 4-15 shows dynamic load measurements obtained from two tests

performed with the tube bundle removed from the test section. The measurements show relatively large immediate shock loads in the original design configuration and minimal output from the modified shock-isolated configuration. This demonstrates the successful elimination of the undesired shock effects in the load cell signals using the modified test section design. Thus, by adapting the design to achieve improved performance under blowdown conditions, mechanical shock effects in the measurements were effectively resolved.

4.3.2 LOAD DATA REDUCTION

The load cell signals were monitored individually and the sum of the four signals was used for the total transient drag load on the tubes. The individual load cell signals provide information on the cross-sectional load distribution on the tube bundle, whereas the total signal provides the amplitude of loading on the tubes. A sample set of blowdown load signals acquired from the four individual
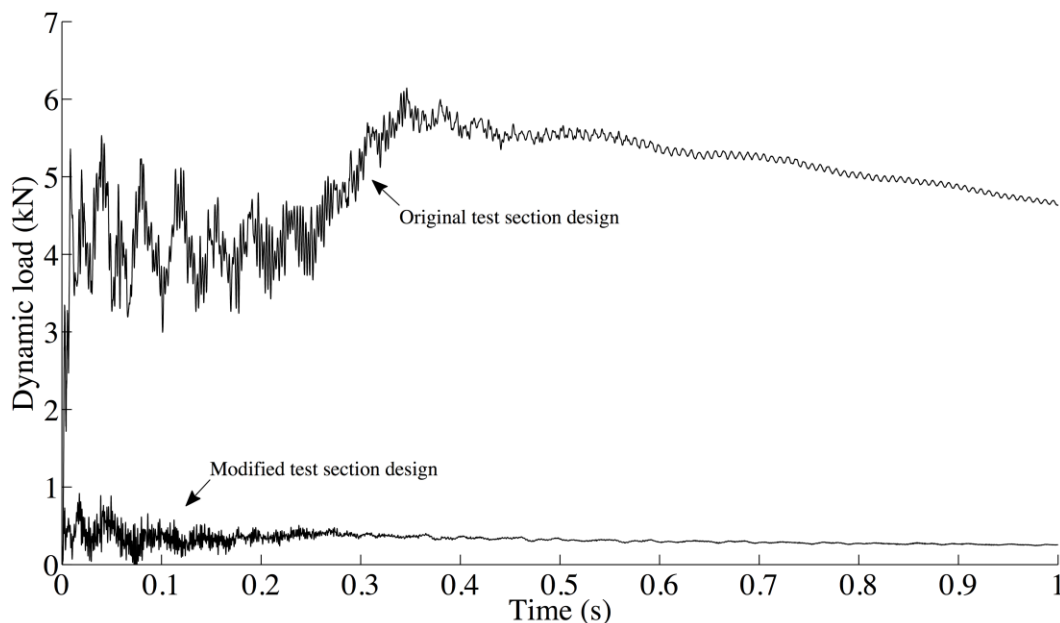
Figure 4-15. Zero load comparison of original and modified test section designs with blank test section walls.

load cells is shown in Fig. 4-16. The maximum difference of about 30mV between the individual signals is attributable to the non-uniform distribution of the fluid load on the tube bundle and the variability in the individual sensitivity of the sensors, which is specified by the manufacturer to be between ±10% and ±20%. In the context of the experimental drag loads measured, only the total summed signal is required to determine the dynamic loading on the tube bundle.

The uniform distribution of the total load across the four load cells, which was consistently observed for multiple blowdown experiments, provides confidence in the load measurement design. The total load on the tube bundle was calibrated dynamically by suspending known weights from the tube bundle using strands of high-strength braided wire. The suspension wires were cut suddenly to produce a controlled and repeatable dynamic unloading of the tubes. The dynamic load input triggers a step response in the load output signal, the amplitude of which was recorded for several calibration weights of up to 40kg. Details of the load calibration procedure are discussed in Appendix B.3.1.
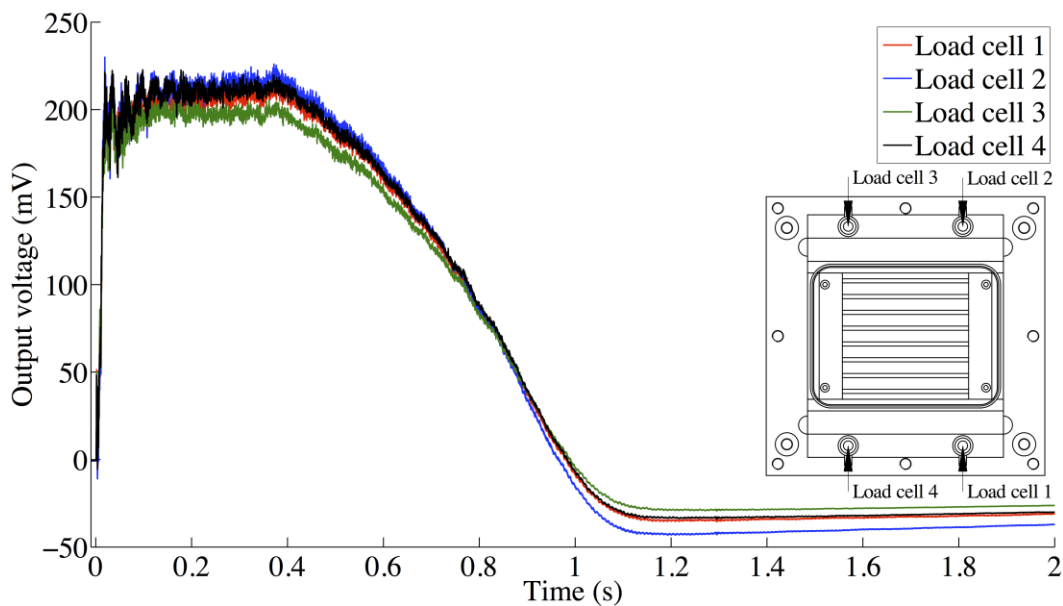
Figure 4-16. Decomposition of total load into individual load cell output signals.

The periodic oscillations in the load cell measurements are caused by the structural rig dynamics. When the four signals are summed, the frequency of the signal oscillation represents the vertical mode of vibration of the test section assembly. The mode frequencies in the load signals were supported by accelerometer measurements obtained at the test section. Figure 4-17 shows vibration and overall tube loading measurements, which display similar frequency content. An FFT plot of the accelerometer signal indicates that the primary natural frequencies in the signals are 59Hz and 121Hz.

The oscillations in the signals occurring at the natural frequencies can be removed from the overall tube load measurement to provide a mean transient trace of the dynamic load on the tube bundle. The load signal on the left hand side of Fig. 4-17 is shown before any digital filtering was performed, and on the right hand side after processing the signal using a 2kHz low-pass filter and narrow selective frequency stop-band filters. The filtered signal represents the mean tube
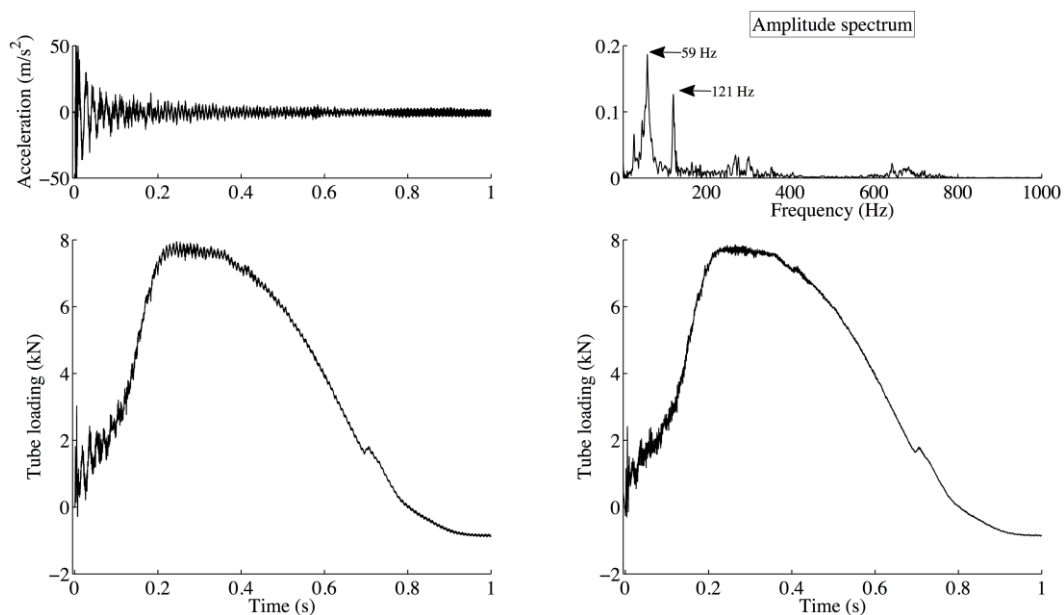
Figure 4-17. Digital load signal filtering procedure: vibration signal (top-left), vibration FFT plot (top-right), original load signal (bottom-left), and filtered load signal (bottom-right).

load measurement with the amplitude and phase preserved. The load measurements obtained in this study were all digitally processed in this manner.

When a piezoelectric sensor is subjected to a sudden step impulse input, an immediate output response is registered after which the signal begins to decay towards zero. If the step input is held constant for a certain amount of time and then removed, the final output signal will drop below the original base-line reference zero point by the same amount that the signal had discharged during the time when the input was held constant. The Discharge Time Constant (DTC) determines the output response of the data collection system during the static stage of the measurement (when the input is held constant).

The DTC of the piezoelectric load cells employed in this study is about 2000s, which is long enough to allow the load measurements to be performed over a very wide frequency range, from quasi-static to 40kHz. The frequency response of the load measurement system was analysed to determine its validity over the frequency range of interest in the current experiments. It was established that the low-frequency response of the data capture system was limited by the electronic power supply and signal conditioning system, yielding an overall DTC of about 4.43 seconds. The frequency response characteristics of the load cells and all of the associated components of the data acquisition system are discussed in detail in Appendix C.4.

In Figs. 4-16 and 4-17, it can be observed that the load signal drops below the zero reference point at the end of the blowdown transient. This negative load amplitude is equal to the value of the signal that had decayed from the original positive dynamic load. Generally, the loss in the output signal during the initial 20% of the DTC is linearly related to the time elapsed. That is, with a DTC of about 4.43s, 10% of the load signal decays 0.443s following a sudden step input. The signal discharges an additional 10% of the impulse input over the next

0.443s. Eventually, the signal decays towards the zero reference point once equilibrium is established, which occurs after about five DTCs.

On the left of Fig. 4-18, the load signal discharge in the current experiments is shown to be linearly related to the duration of the blowdown transient. The dashed line plots the relationship between the signal decay and the DTC, and it is observed that about 10% of the signal drops below the reference zero for every additional 443 milliseconds of the transient. The signals all eventually asymptote back to the zero baseline, as shown in the central graph of Fig. 4-18. This is expected to take 5 times the DTC of 4.43s, which is about 22s.

By observing that the amplitude of the signal discharge is linearly proportional to the duration of the transient signal, a linear correction that shifts the decaying portion of the signal upwards can be implemented. The linear relationship is given by the dashed line shown in Fig. 4-18, and was used to correct the signal offset for all of the load measurements such that the transient
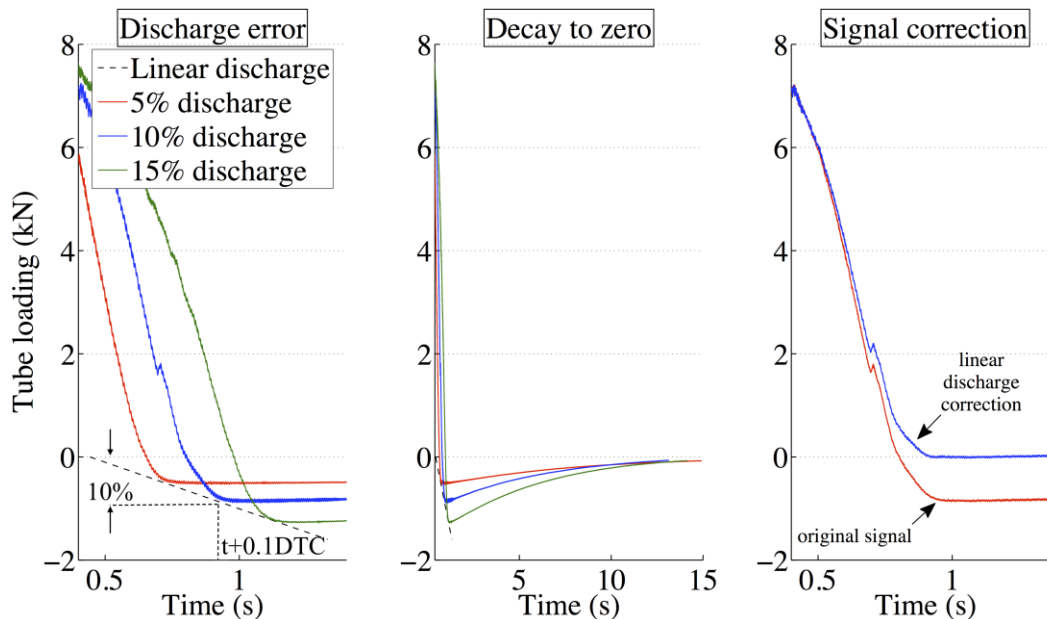
Figure 4-18. Tube bundle load signal discharge correction: discharge error at the end of the transient (left), long-term decay back to zero (centre), linear discharge signal correction (right).

load always begins and ends at the zero baseline reference. An example result of this digital data correction procedure is shown on the right of Fig. 4-18.

4.3.3 LOAD VALIDATION

The fluid drag load exerted on a tube bundle is directly proportional to the pressure drop across the tubes. Since the transient pressure difference across the tube bundle was measured in the present experiments, a quantitative validation of the load signals could be obtained by comparing the trends of the signals from the load cells against those from the pressure transducers. Figure 4-19 shows a two-phase blowdown load signal obtained using the modified test section design, which was digitally processed according to the procedures described in the preceding section. The signal is compared against the transient pressure drop measured across the tube bundle. The good agreement between the two trends demonstrated in Fig. 4-19 was consistently observed for all of the blowdown experiments performed in this study.

The initial peak in the first 50ms of the transient pressure drop measurement is related to the acceleration of the liquid above the tubes towards the rupture disc. The dynamic change in the rate of the fluid momentum in this region of the pressure vessel downstream of the tube bundle has a marginal influence on tube loading, and little load is measured during this time. Following these initial unsteady downstream effects, the pressure drop across the tube bundle consists mainly of the pressure loss of the upstream fluid as it accelerates through the tube bundle towards the discharge region.

Transient fluid loading on the tube bundle continues to be measured for the remainder of the transient. The distribution of the drag loading on the tube bundle after the initial 50ms is observed to follow the trend of the measured pressure drop very well. If the pressure sensors were located closer to the tube bundle, then the pressure difference would be measured strictly across the inlet
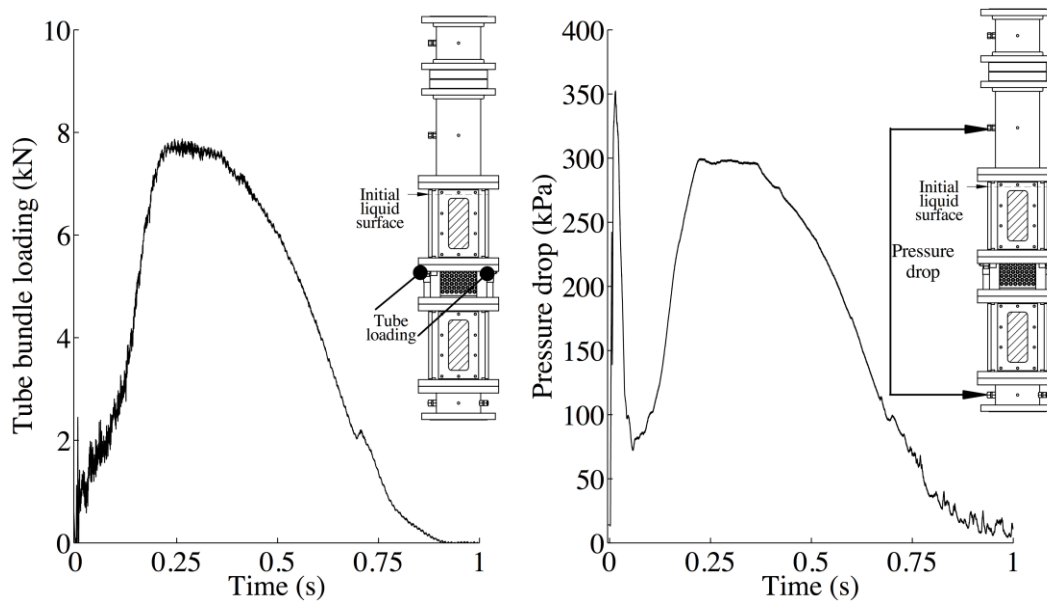
Figure 4-19. Comparison of the transient tube bundle loading and pressure drop trends showing that all measurement issues have been resolved.

and exit of the tube bundle, and no downstream fluid acceleration effects would be observed in the pressure signals.

The results demonstrate that the spurious measurements caused by sudden blowdown shock loading have been effectively eliminated. Confidence was established in the load measurements by verifying that the individual load signals were uniformly distributed and that the overall load on the tube bundle matched the measured pressure drop trends very well. Hence, by anticipating and mitigating the negative effects of the shock loading on the measurements, problematic issues in the signals were successfully addressed and the dynamic loads measured could be related to the desired fluid drag loading phenomena.

The uncertainty in the load measurements was estimated to be ±0.4kN, with most of the uncertainty attributed to the manufacturer specified linearity of the sensors. The maximum amplitude of the combined load cell measurements in this study were only about 5% of the full measurement span. The linearity of the

sensors in this range is therefore expected to be better than the manufacturer quoted linearity over the full measurement range of the sensors. It follows that the linearity of the load cells during calibration was found to be better than specified by the manufacturers, with a maximum measurement deviation of about ±0.03kN. Details of the uncertainty analysis performed for the quasi-steady and dynamic measurements are provided in Appendix C.3.

4.4. INITIAL CONDITIONS

The initial steady-state R-134a fluid conditions inside the pressure vessel must be accurately determined in order to analyse the transient fluid depressurisation following the sudden opening of the rupture disc. The initial fluid properties such as the speed of sound and the fluid volume in the pressure vessel can be established once the initial R-134a thermodynamic properties are determined. While charging R-134a into the pressure vessel, the only available indication of the R-134a inventory inside the pressurised reservoir was via the visual observation of the liquid level through the glass windows. In order to determine the fluid inventory quantitatively and reliably, the R-134a supply cylinder was placed on a digital scale supplied by Yellow Jacket (model 68802) throughout the charging process in every experiment.

The readout on the scale displayed the mass of R-134a discharged from the supply bottle into the experimental pressurised reservoir system. Knowing the reservoir volume and the liquid and vapour pressures and temperatures, the partial concentration of the liquid and vapour phases can be determined from the total mass of R-134a discharged into the reservoir. By assuming a quiescent pool of liquid below a uniform region of saturated vapour, the corresponding volumes of the liquid and vapour domains in the pressure vessel can be established. Once the fluid properties and the height of the liquid surface are known, the subsequent transient phenomena that begin with blowdown initiation can be investigated.

4.4.1 CALCULATION OF THE INITIAL LIQUID VOLUME

The pressures and temperatures of the liquid and vapour phases were assumed to be uniformly distributed throughout their respective domains and a uniform density was computed based on the measurements at the sensor locations. The liquid density was determined from the pressure and temperature measurements and the vapour density was determined by assuming a saturated vapour state corresponding to the pressure measurement. The temperature readings in this region were slightly lower than the saturation temperatures of the vapour, influenced by heat transfer from the colder pipe surroundings and liquid condensation on the inside pipe walls.

The densities were determined from the National Institute of Standards and Technology (NIST) database with an uncertainty of 0.05%. The range of initial liquid and vapour densities in the experiments varied between 1222 – 1248kg/m^3 and 26.1 – 29.4kg/m^3 respectively. From the liquid and vapour densities, ρ_l and ρ_g, the initial volume of liquid in the pressurised reservoir, V_l, can be calculated according to Eq. (4-28),

$$V_l = \frac{m_T - \rho_g V_T}{\rho_l - \rho_g},$$
(4-28)

where V_T is the total volume of the pressure vessel below the rupture disc and m_T is the total mass of R-134a introduced into the system. The initial liquid surface height from the bottom of the reservoir, H_l, can be readily evaluated by dividing the liquid volume, V_l, by the cross-sectional area of the vessel, A_{cs} (186cm^2), as shown in Eq. (4-29),

$$H_l = \frac{V_l}{A_{cs}}.$$
(4-29)

A compressed gas accumulator with a total volume of $0.0028m^3$ was used to pressurise the fluid below the rupture disc and trigger the blowdowns. The accumulator contains an elastic diaphragm, which separates the compressed gas driver from the pressurised fluid R-134a in the system. During pressurisation, the introduction of compressed N_2 gas into the driver section of the accumulator results in the expansion of the elastic diaphragm. This compresses the R-134a in the receiver section, steadily drives it out of the accumulator, and boosts the pressure in the experimental reservoir below the rupture disc. At some point during this process, usually after most of the R-134a in the accumulator has been driven out, the pressure required to burst the rupture disc is attained.

For the purposes of calculating the initial conditions in the pressure vessel, the volumes of the accumulator and the connecting lines were ignored. The assumption was that the accumulator is almost completely filled with compressed N_2 gas at the point when the blowdown begins, which was supported by experimental experience gained during testing. In the worst-case scenario, the accumulator is completely filled with liquid R-134a, and the initial liquid volume in the reservoir is $0.0028m^3$ less than the calculated value. This volume of fluid enters the pressure vessel during the blowdown experiment and must therefore be included in the total fluid volume calculation for each test.

Different reservoir volumes were used in the experiments depending on the length of the pressure vessel section below the rupture disc. The volume occupied by the solid tubes in the tube bundle was accounted for in the calculation of the initial conditions. The pressures in the regions occupied by the liquid and vapour phases were initially different due to the liquid hydrostatic head and the additional compression provided by the N_2 gas pressurisation system. The liquid height based on the initial volume calculations was consistent with the hydrostatic pressure head based on the collected pressure and temperature data. The discrepancy between the two due to the effect of the additional pressure boost was between 0.7 – 4.5kPa.

The estimated uncertainties associated with the initial pressure, temperature, and mass measurements were ±3.0kPa, ±0.9°C, and ±18g respectively. The maximum uncertainties in the initial liquid volume and height calculations were estimated to be ±0.68L and ±3.7cm respectively. Since the amount of R-134a in the accumulator at the time of disc rupture could not be precisely determined, there was an additional estimated initial liquid height uncertainty of about ±7.5cm. A list of the initial conditions for all of the blowdown experiments performed is provided in Appendix D. The tests are arranged from smallest to largest percentage fill of the pressure vessel, which can be divided into four main categories: minimum (3 – 10%), small (21 – 24%), moderate (39 – 56%), and large (63 – 67%).

4.4.2   CALCULATION OF THE RUPTURE DISC OPENING INSTANT

It is important to establish a precise and repeatable method of determining the instant of blowdown initiation given the significance of the phenomena that occur in the first few milliseconds. The procedure developed for establishing the instant that the rupture disc opens ($t = 0$) was based on the initial thermodynamic conditions of the R-134a in the pressure vessel below the rupture disc. When the rupture disc opens, compression and rarefaction waves propagate upwards and downwards respectively, originating at the point of the rupture disc.

A positive rise in pressure is signalled by the arrival of the compression wave above the disc (downstream) and a negative pressure wave is signalled below the rupture disc (upstream). The compression wave, which travels upwards towards the vacuum reservoir, is used to determine the time $t = 0$. This is because the propagation of the wave through the vacuum reservoir occurred at a velocity that was consistent for all of the experiments, making this method universally applicable to all of the tests that were performed.

The velocity of propagation of the wave, which is equivalent to the speed of sound from Eq. (4-19), can be determined from the initial thermodynamic state of the saturated vapour in the pressure vessel. The calculated velocity for the full range of initial experimental conditions was about 145m/s. This velocity, together with the distance of the pressure transducer from the rupture disc (138mm) sets the time required for the pressure wave to travel between the two points. Thus, the instant of rupture disc opening ($t = 0$) was established to occur a time $\Delta t = 0.95$ms before a rise in pressure was detected in the transducer signal. Since the instrument outputs were all hardware synchronised, this method allowed the time $t = 0$ to be accurately established for all of the simultaneous measurements.

Figure 4-20 shows a sample pressure signal obtained for test T02 at location 3 above the rupture disc (refer to Fig. 3-1). The instant of the opening of the disc was set to occur at $t = 0$, which is 0.95ms before the pressure rise was identified in the signal. The signal noise is about ±0.03kPa and the observed signal rise is of the order of 0.3kPa. Since the opening pattern of the disc produces a pressure wave front that is not a perfect square wave, the pressure signal in the boundary layer of the flow channel does not show an ideal step rise in pressure. The slope of the rising pressure signal increases sharply about 0.5ms after signal detection.

The trend of the rise in pressure was observed to be very consistent across all of the experiments, confirming the uniformity and repeatability of the disc opening pattern. The time for the complete opening of the rupture discs was estimated to be about 3ms. The wave speed calculation, sampling resolution, and transducer diameter result in an uncertainty in the calculation of $t = 0$. The maximum wave speed uncertainty according to the NIST guidelines was estimated to be ±0.073m/s. The 30kHz sampling rate error was ±0.033ms, and the pressure wave, travelling at 145m/s, traverses the face of the 5.5mm diameter transducer in about 0.038ms. The combined uncertainty was estimated to be
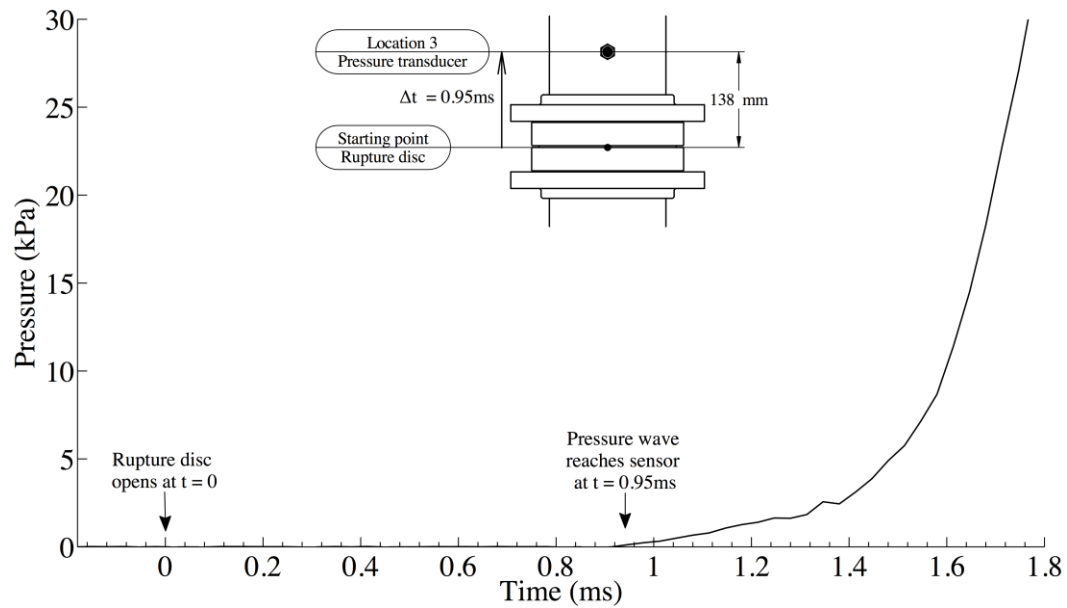
Figure 4-20. Rupture disc opening instant at time $t = 0$ (test T02).

±0.05ms, which is about 5.3% of the duration of the wave propagation from the rupture disc to the transducer location.

CHAPTER 5. BLOWDOWN TRANSIENT THERMAL HYDRAULIC PHENOMENA

A general description of the two-phase flow phenomena that were observed in the blowdown experiments performed for this research are described in this chapter through a selection of illustrative examples. A number of experiments were performed with varying initial volumes of liquid R-134a ranging from 0.8 – 15.4L (3 – 67% of the pressurised reservoir volume) to determine the effect of the initial liquid volume on the tube loading and blowdown processes. The number of tube rows was varied from zero to six rows. In all, data were collected for 12 experiments. An understanding of the main thermal-hydraulic phenomena observed in the experiments enables the attendant effects on the dynamic structural loading of a tube bundle subjected to transient two-phase cross-flow to be identified.

The particular graphs used are from a variety of 'typical' tests that best clarify the pertinent fluid mechanics. While the details such as event timings and dependent parameter amplitudes varied significantly with the initial liquid levels and numbers of rows in the bundle, the general phenomenological behaviour observed was common to all of the tests. The initial steady-state thermodynamic fluid properties were similar in all of the experiments. The initial liquid R-134a pressure and temperature ranges were 554 – 616kPa and 287 – 294K (14 – 21°C) respectively. The complete set of experimental data is provided in Appendix E.

5.1. GENERAL OVERVIEW OF BLOWDOWN TRANSIENTS

A sample set of transient pressures measured in blowdown test T08 at the three sensor points along the pipe are shown in Fig. 5-1. This test was performed with six rows of tubes in the test section and 52% of the pressure vessel filled

with liquid R-134a. The pressure sensors at locations 1 and 2 below the rupture disc were in the regions initially filled with subcooled liquid and saturated vapour respectively. Initially, the liquid was at 581.6kPa and 18.3°C and the vapour was at 570.2kPa and 18.7°C. Location 3 above the rupture disc was initially in a vacuum. The general transient behaviour observed is typical of all the two-phase blowdown experiments carried out. The pressure amplitudes and event durations varied from test to test due to changes in the initial conditions, the pressure vessel dimensions, and the number of rows of tubes in the test section.

The transient pressure traces show distinct features that can be split into three main segments, which in test T08 are observed to occur between 0 – 10ms, 10 – 600ms, and from 600ms onwards. In the first 10 milliseconds of the test, pressure waves originate at the point of the rupture disc and propagate rapidly at the speed of sound. This is followed by a period of vigorous phase transition in which the ratio of vapour to liquid in the pressure vessel increases rapidly. At the same time, the two-phase fluid mixture is discharged through the open rupture
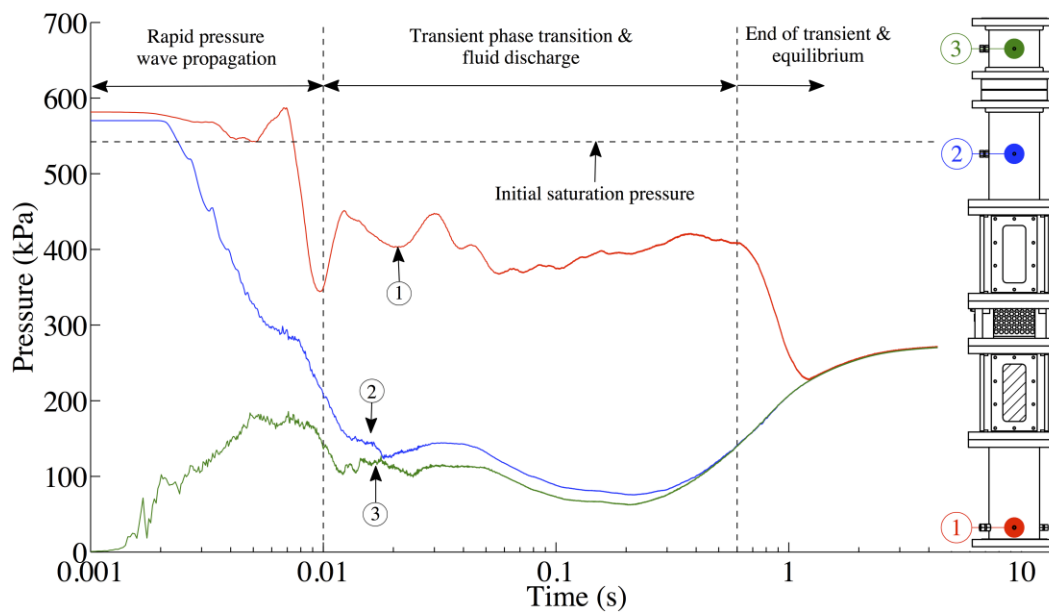
Figure 5-1. Sample transient blowdown pressures (test T08).

disc due to the pressure difference between the pressure vessel and the vacuum tank. At about 600ms, the pressures everywhere in the system begin to equalise until equilibrium conditions are established, signalling the end of the transient.

When the rupture disc opens, the fluid is suddenly exposed to the downstream vacuum reservoir. The pressure relief is transmitted upstream of the rupture disc (towards the bottom of the vessel) as a rarefaction pressure wave. The liquid's inertia limits its initial flow rate. The rapid rates of depressurisation (or pressurisation at location 3) observed are typical of large-amplitude pressure waves propagating at the acoustic velocity. The time delay to depressurisation does not begin at the sensor points until the rarefaction wave arrives, and can be computed from the sonic velocities in the vapour and liquid. This explains the difference seen in times for the depressurisation to begin at the points above and below the tube bundle.

The small pressure variations measured at location 1 below the tube bundle between 2 – 8ms (before the arrival of the rarefaction pressure wave) are associated with fluid-structure interactions between the stagnant liquid pool and the steel pipe. These are caused by the pressure vessel vibrations and shock loading along the pipe walls immediately following disc rupture. The stress waves propagate through the steel at about 6100m/s, which is more than 40 times greater than the propagation speed in vapour R-134a. This explains the appearance of pressure fluctuations in the liquid before depressurisation, and their attenuation following the formation of compressible vapour.

At about 7ms, the liquid pressure drops below its initial saturation pressure of 542kPa. The rapid pressure decrease is halted by the initiation of phase transition from liquid to vapour at about 9ms. The ensuing vigorous generation of vapour produces a recovery in the pressure amplitude to a value that remains substantially lower than the initial saturation pressure. The two-phase fluid mixture simultaneously flashes and accelerates through the tube bundle and the

pressure difference across the bundle remains nearly constant until about 0.4s into the blowdown. The void fraction in the pressure vessel continues to increase until the majority of the liquid has boiled off. Once the vessel liquid inventory is essentially depleted, about one second into the blowdown, the system pressures equalise at the pressure of the accumulated vapour R-134a in the vacuum reservoir.

5.2. DESCRIPTION OF VISUAL BLOWDOWN FLUID DYNAMICS

Flow visualisations were captured in test T08, for which the transient pressures were presented in the preceding section, using two synchronised digital high-speed cameras. The images were taken at the sight windows above and below the test section (refer to Fig. 3-1) and were synchronised to the data acquisition system. By obtaining high-speed images of the transient flow, the behaviour of the two-phase fluid mixture as it enters and exits the tube bundle can be monitored. This provides valuable insights into the mechanisms of phase transition, vapour growth, and transient fluid regime development. A fundamental understanding of the governing flow phenomena can then be developed by relating the visual phenomena to the physical measurements.

High-speed image sequences of the transient two-phase flow pattern development are shown above and below the tube bundle in Figs. 5-2 and 5-3 respectively. The images are presented along with the corresponding transient pressures measured at the nearest transducer locations. Figure 5-2 shows the saturated vapour region and the pressure measurement at location 2. Figure 5-3 shows the subcooled liquid domain and the pressure at location 1. The images depict the general flow phenomena observed in most of the two-phase blowdown tests carried out, starting from the opening of the rupture disc until the completion of the blowdown transient. The time $t = 0$ refers to the instant when the rupture disc opens, which was set to frame 0000.
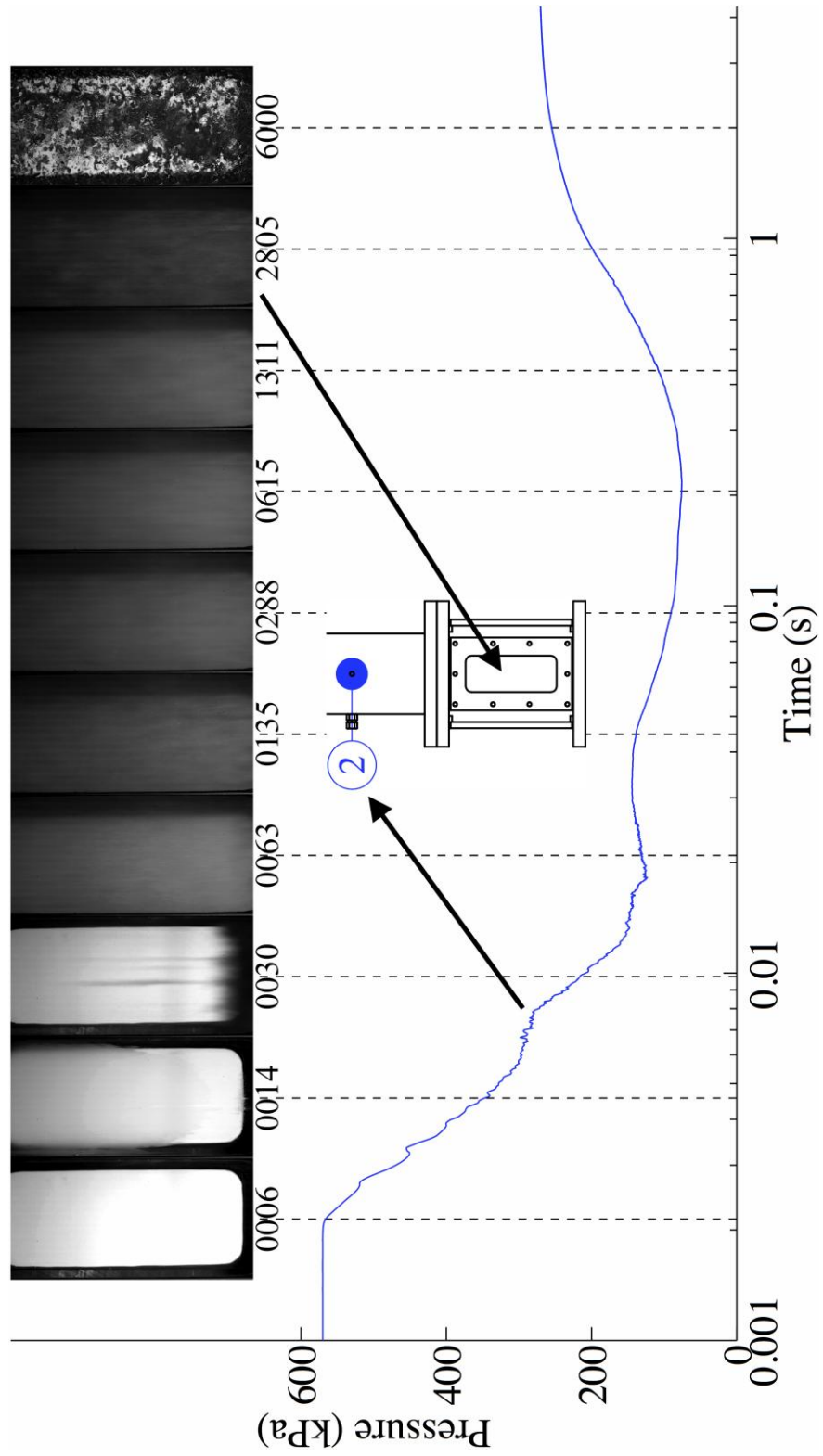
Figure 5-2. Synchronised high-speed images and transient pressure measured at location 2 (test T08).
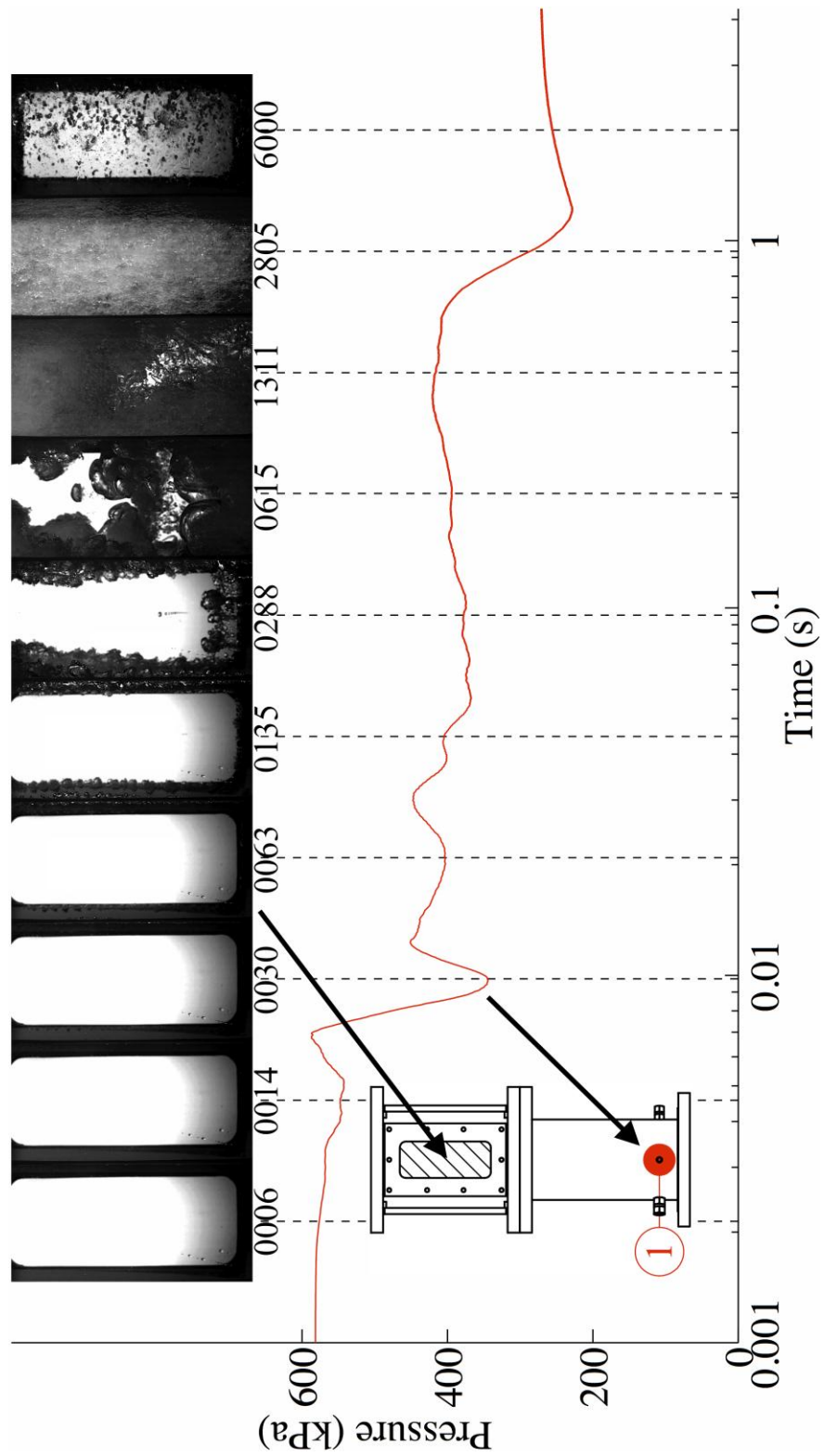
Figure 5-3. Synchronised high-speed images and transient pressure measured at location 1 (test T08).

The 4-digit numeric labels below the images in Figs. 5-2 and 5-3 represent the frame numbers. The images were filmed at a rate of 3000fps and each increment of three frames represents 1ms of elapsed time. 500W halogen spotlights were used to direct light into the windows through the transparent liquid and vapour media and into the camera lenses. The liquid surface in test T08 was between the two windows. The images show the regions initially completely occupied by pressurised vapour (above) and liquid (below). In some tests, the liquid level was visible through the windows and the liquid-vapour interface appeared as a dark line in the images. The liquid-vapour interfaces are opaque and therefore block the transmission of light through the windows. A shadow is cast that appears as a darker shade than the surrounding lit regions in the images. In order to film the interfaces adequately, additional spotlights were used to provide front lighting, which reflects off the liquid-vapour interfaces back into the lenses. This must be dim in order not to saturate the image brightness.

Between frames 0006 and 0014 in Fig. 5-2 ($t = 2 - 4.7$ms), a rarefaction wave that had originated at the rupture disc passes along the viewing section downwards towards the bottom of the pressure vessel. The associated rapid reduction in pressure condenses the saturated vapour. This explains the faintly discernible condensed liquid, which appears blurry at the bottom of frame 0014. A two-phase mixture that is accelerating upwards appears at the bottom of frame 0030 ($t = 10$ms). By frame 0063 ($t = 21$ms), the two-phase mixture covers the entire viewing area. As the transient progresses from $t = 45$ to $t = 437$ms (frames $0135 - 1311$) the two-phase mixture continues to be visible in the corresponding images.

The flow patterns during this period are difficult to distinguish due to the significant amount of light obstruction and degradation in the image quality. Around $t = 935$ms in Fig. 5-2 (frame 2805) the flow was observed to decelerate. The pressure increases monotonically during this time. Liquid films and small droplets falling by gravity are observed in frame 6000, 2 seconds after blowdown

initiation. This occurs following the completion of the transient, once the pressures in the reservoir have equalised.

The dark frames can be digitally manipulated for increased brightness in order to glean more information from the images. The result is shown in Fig. 5-4. This method of digital image enhancement facilitates the interpretation of the flow physics. The images seem to show a homogeneous two-phase fluid distribution. Despite the photographic challenges associated with such an extremely rapid transient and a significant change in the void fraction (from 0% to 100% in about 1 second), viewing these images as an animated film provides meaningful information about the flow mechanics and the two-phase mixture heterogeneity or uniformity. The high-speed images presented in this Thesis were all digitally enhanced for improved image quality.

In Fig. 5-3, there is no visible change in the liquid from the original conditions until frame 0030 (t = 10ms). During this time, a flashing two-phase mixture was already observed in the region above the tube bundle. This demonstrates the extremely rapid nature of the transient phase transition phenomena that occur in the initial stages of these blowdown experiments. Some vapour generation is observed in frame 0063 (t = 21ms) in the peripheries of the

| 0135 | 0288 | 0615 | 1311 | 2805 |
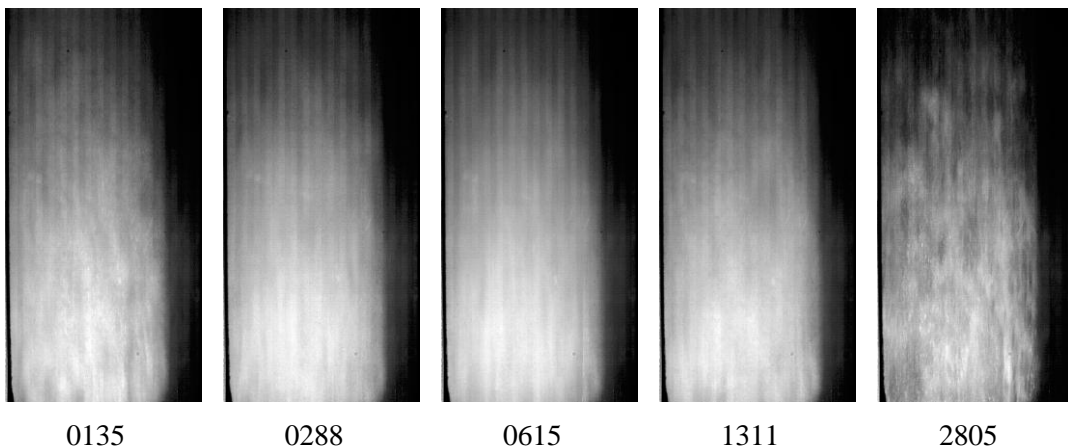
Figure 5-4. Digitally enhanced image brightness for frames 0135 – 2805 (t = 45 – 935ms, test T08).

image. The bubble growth is more visible in frame 0135 (t = 45ms) and in frame 0288 (t = 96ms) the bubbles continue to occupy a larger portion of the viewing area. In addition, rising bubbles originating from below the window appear at the bottom of the image. The darker regions in these images represent the expanding two-phase plumes.

The images in the first 200ms of the transient show vigorous liquid boiling, which creates densely populated vapour clouds. The high interfacial concentration between the two phases is clearly visible in frame 0615 (t = 205ms) in which the bottom half of the image is almost entirely occupied by bubbles and vaporised plumes. At the same time, the liquid bulk in the top half of the image appears to remain largely unperturbed. By frame 1311 (t = 437ms) the interfacial concentration increases to the extent that most of the light transmitted through the window is blocked. The flow continues to develop non-uniformly as it discharges upwards and most of the liquid has already boiled off in frame 2805 (t = 935ms). The transient is complete in frame 6000 (t = 2s) and falling liquid is visible on the glass surface as well as in the centre of the vessel cross-section.

The velocity of distinct fluid interfaces such as dispersed bubbles or entrained droplets can be estimated by digitally imposing a scaled grid on the viewing area and visually tracing the time-stamped flow. An example of this methodology is presented in Fig. 5-5. The image sequence shows rising bubbles shortly after blowdown initiation, filmed below the test section in test T02. The grid super-imposed on the images is 10mm square and the frames are shown in 10ms time-steps. The darker regions on the sides represent expanding two-phase plumes and the inside lighter region is the relatively undisturbed liquid. A group of rising vapour bubbles is observed in the centre of the images. From the distance covered (about 35mm) in the elapsed time of 30ms, the bubble velocity was estimated to be about 1.2m/s.
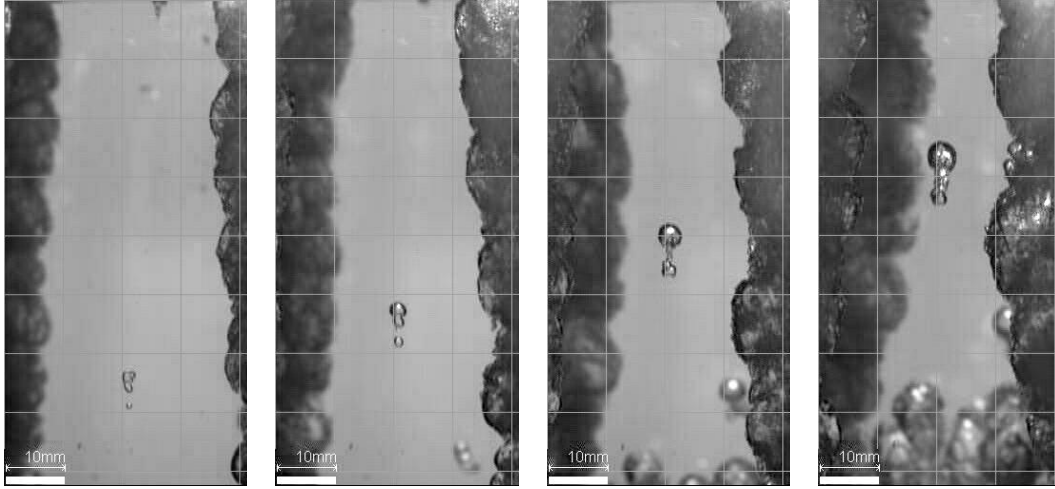
Figure 5-5. High-speed images of rising bubbles during blowdown (10ms time-step, test T02).

The velocity of a single rising bubble, u_b, can be determined from the drift flux relative velocity of vapour in a low void fraction fluid according to Eq. (5-1) (Whalley, 1987),

$$u_b = K \left[\frac{\sigma g \left(\rho_l - \rho_g \right)}{\rho_l^2} \right]^{\frac{1}{4}}, \tag{5-1}$$

where K is an empirical constant, σ is the surface tension, g is the acceleration due to gravity, and ρ_l and ρ_g are the liquid and vapour densities respectively. Various values for K are presented in the literature: 1.18 (Wallis, 1969), 1.41 (Ishii & Zuber, 1979), and 1.53 (Collier & Thome, 1994). The corresponding rising bubble velocities predicted from Eq. (5-1) are 0.11m/s, 0.13m/s, and 0.14m/s respectively. The bubble velocity estimated from Fig. 5-5 is under-predicted by a factor of 10. This is because the models were developed for vapour bubbles in a hydrostatic pressure field. The significant pressure gradients established during the initial transient blowdown stages result in a relatively high bubble velocity.

The images are useful for evaluating the transient flow velocity below and above the tube bundle. The two-phase fluid velocity is related to the pressure drop

across the tube bundle and its evaluation assists in developing an understanding of the two-phase transient tube bundle loading. For illustration purposes, Fig. 5-6 shows the flashing two-phase front discharging from the tube bundle in test T04 immediately after the initial rarefaction wave has passed. A 10mm square grid is super-imposed on the images, which are provided in 2.7ms increments.

Growing two-phase plumes are visible at the sides. The vapour expands into the bulk liquid and accelerates past the apparently static liquid. The flashing two-phase mixture downstream of the tube bundle enters the bottom of the image in the second frame and travels a distance of about 75mm in 8ms with an estimated average velocity of 9.4m/s. Hence, the observed flow development can be related to the transient measurements by monitoring the fluid velocities. This allows a fundamental interpretation of the governing flow phenomena during transient two-phase tube loading to be developed.

5.3. PRESSURE WAVE PROPAGATION

Under steady-state conditions before blowdown initiation, the pressure vessel contains distinct liquid and vapour domains. The liquid free surface forms the interface between the two phases. When the rupture disc opens, fluid depressurisation begins and the pressure relief is transmitted along the upstream
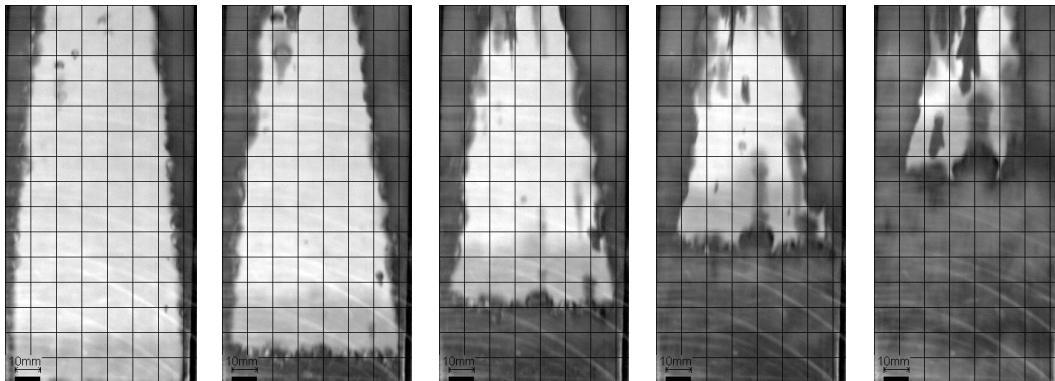
Figure 5-6. Flashing two-phase mixture front downstream of the tube bundle (2.7ms time-step, test T04).

pressurised pipe section as a rarefaction wave. The wave propagates away from the rupture disc towards the bottom of the vessel. The initial wave propagation occurs through the saturated vapour region below the disc. Following the arrival of the rarefaction wave at the liquid surface, it propagates through the subcooled liquid. The transmission of the wave through this liquid-vapour interface is accompanied by complex partial wave reflection phenomena.

The transient pressures obtained in tests T05 and T07 at locations 1 and 2 (refer to Fig. 3-1) in the first 10ms following rupture are compared in Fig. 5-7. In both tests, the rarefaction wave travels a distance of 211mm from the rupture disc to the measurement station at location 2, under similar thermodynamic conditions (saturated vapour). The wave propagation velocity was computed from the experimental data as 132.6 ± 5.1 m/s. Although the pressure at location 2 appears to decrease at about 2ms, the wave arrival time was identified on close inspection as 1.7ms for both tests. The apparent 0.3ms delay is due to the shape of the wave front, which does not produce an immediate step decrease in the pressure. Similar behaviour is shown in Fig. 5-1, where the wave was set to arrive 0.9ms after rupture at location 3 but appears to be 1.2ms. The rarefaction wave steepness was identical for both tests, demonstrating the excellent reproducibility of the disc opening behaviour in these experiments.

There are many documented examples of rapid fluid depressurisation experiments in the literature in which the break characteristics were found not to be consistently uniform. Thick glass diaphragms that were used to contain water at prototypical reactor pressures and temperatures (Edwards & O'Brien, 1970) were observed to leave non-yielding obstructions, which significantly reduced the effective discharge flow area. Cellulose triacetate membranes that were shattered by an external piercing mechanism were found to deflect non-reproducibly before rupturing, resulting in various pressure wave magnitudes and durations (Winters & Merte, 1979). A melting wire mechanism was also found to cause reproducibility problems especially when poor wire contact caused non-uniform
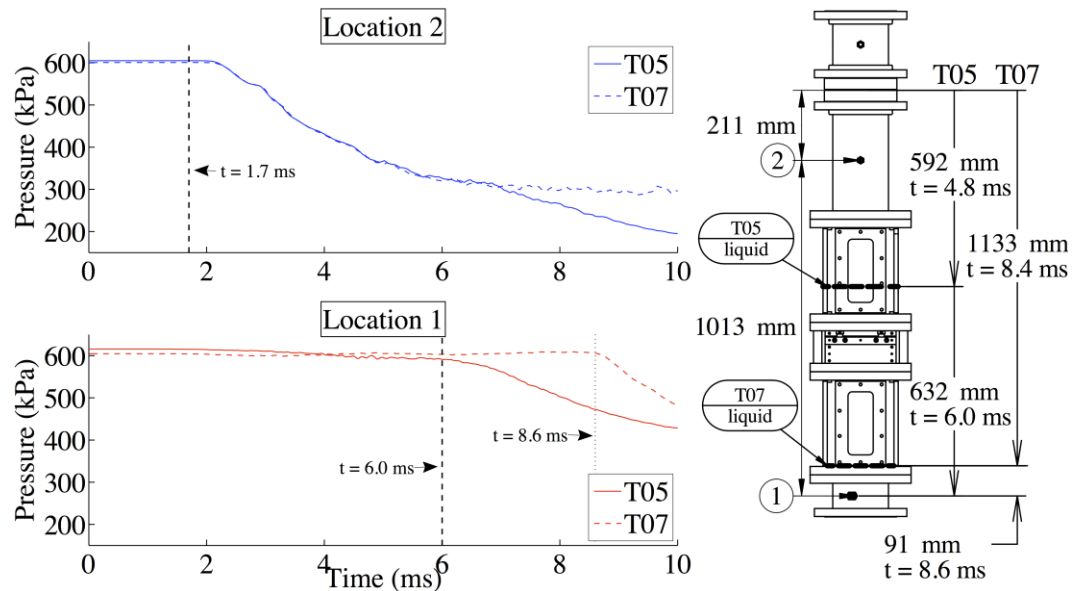
Figure 5-7. Rarefaction wave propagation in tests T05 & T07 at locations 1 & 2.

heating, which resulted in partial membrane tears instead of clean breaks (Deligiannis & Cleaver, 1996). Thick rupture discs used in scaled blowdown experiments were found to leave non-yielding obstructions that considerably reduced the discharge break area (Kang *et al.*, 2011). None of these problems was encountered in the present study. The thin high-quality rupture discs used consistently showed uniform opening characteristics.

In single-phase compressible gases, the acoustic velocity of compression and expansion waves is the same and can be calculated from Eq. (4-19). However, a de-compressive disturbance in saturated vapour may result in liquid condensation, which affects the wave front propagation velocity. The theoretical speed of sound in vapour R-134a at standard temperature conditions is 145m/s. The measured velocity of the rarefaction waves in the present tests, verified by the calculated timings shown in Fig. 5-7, was about 130m/s. The phase change accompanying the wave propagation through saturated vapour resulted in a slightly reduced acoustic velocity.

86

The respective liquid level heights from the bottom of the reservoir are 670mm and 129mm in tests T05 and T07. In test T05, the rarefaction wave travels 592mm through vapour and 632mm through liquid before arriving at location 1, whereas in test T07, the propagation occurs through 1133mm of vapour and 91mm of liquid. The speed of sound in liquid R-134a is about 542m/s, which is 4 times faster than in vapour. The rarefaction wave therefore takes longer to travel to location 1 in test T07, when the liquid level is lower, compared to test T05. Test T05 was performed with six rows of tubes in the test section, while the tubes were removed in test T07. Interestingly, the tube bundle does not seem to have any discernible influence on the propagation of the rarefaction waves as evidenced by the measured wave velocities.

The maximum possible reduction in the pressure of the vapour following the opening of the rupture disc, Δp, can be estimated by assuming that the vapour is discharged at its maximum possible velocity, which is the speed of sound. The relationship is given by Eq. (5-2),

$$\Delta p = \rho \cdot \Delta u \cdot c = \rho \cdot c^2 , \qquad\qquad (5\text{-}2)$$

where Δu is the change in velocity from zero to sonic, ρ is the density, and c is the speed of sound. The density of saturated R-134a vapour at 300kPa is 14.8kg/m^3 and the speed of sound is about 146m/s. From Eq. (5-2), the estimated pressure drop is 315kPa, which agrees with the pressure drop observed in Fig. 5-7 for test T07 at location 2. Hence, the vapour discharge is choked.

During these early stages of the transient, no phase change has occurred yet at the rupture disc point. While the pressure remains steady at an amplitude of about 300kPa in test T07, it only remains at 300kPa for about 1.5ms in test T05 and then drops further about 7ms after the disc opens. This is due to the smaller initial amount of single-phase vapour above the liquid region, which discharges more rapidly and promotes a faster transition to subsonic discharge conditions.

The condensation effect caused by the propagation of the rarefaction wave through the saturated vapour domain was visible in the high-speed flow visualisations. A high-speed image sequence taken through the upper window in test T06 is shown in Fig. 5-8. The arrow tips trace the condensation wave front, providing a reasonable estimate of the rarefaction wave position with respect to time. The phase change is difficult to see in the still images and is better identifiable in animated image sequences. In the images shown, the blurriness behind the wave front, which is most visible near the top and sides of the frames, represents condensed liquid. The 'condensation' wave front travels a distance of about 180mm in four frames, which is 1.33ms. The corresponding estimated speed of the rarefaction wave traced in the images is about 135m/s. This estimated velocity is similar to the velocity computed from the pressure signals, which confirms the quality of the data and the adequacy of the high-speed images for obtaining quantitative velocity estimates.

The speed of sound in a two-phase medium cannot be determined by simple thermodynamic state properties as in single-phase fluids. In fact, analytical descriptions of wave propagation phenomena in two-phase flows do not exist, apart from the simplified extreme cases of perfect homogeneous equilibrium, or 'frozen' conditions, where the mass, momentum, and energy transfer terms between the two phases disappear (Städtke, 2006). In a two-phase mixture, the
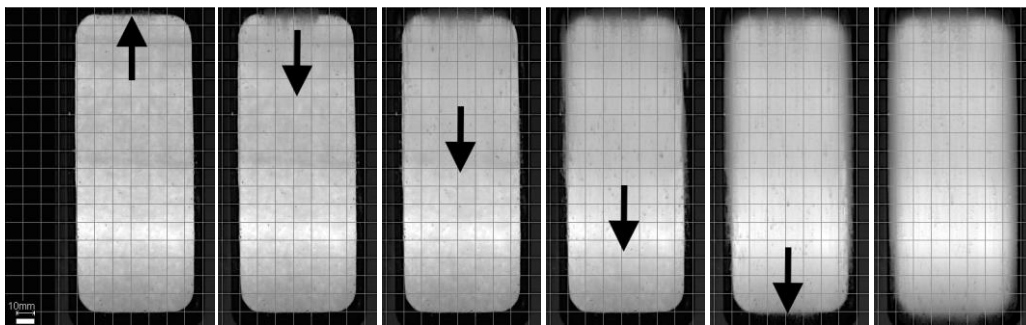
Figure 5-8. Propagating 'condensation' wave front (0.33ms time-step, test T06).

speed of sound depends on the flow regime, the frequency of the pressure wave, whether it is a pulse or continuous wave, and the nature of the disturbance (compressive or de-compressive). The computed velocity estimates in Fig. 5-7 are therefore only valid for a brief period directly following disc rupture, during which the fluid states are in single-phase. The rapid dynamic vapour generation that ensues substantially changes the speed of sound.

The average density of a homogeneous two-phase fluid mixture, ρ_H, is defined by Eq. (5-3) (Pinhasi *et al.*, 2005),

$$\rho_H = \left(\frac{x}{\rho_g} + \frac{1-x}{\rho_l} \right)^{-1} , \qquad (5\text{-}3)$$

where x is the thermodynamic quality, and ρ_g and ρ_l are the vapour and liquid densities respectively. If the quality remains constant, the homogeneous two-phase speed of sound, c_H, is related to the void fraction, ε, according to Eq. (5-4),

$$c_H = \left(\frac{\rho_H \varepsilon}{\rho_g c_g^2} + \frac{\rho_H (1-\varepsilon)}{\rho_l c_l^2} \right)^{-\frac{1}{2}} , \qquad (5\text{-}4)$$

where c_g and c_l are the vapour and liquid sonic velocities respectively. The homogeneous two-phase speed of sound computed from Eq. (5-4) for R-134a at 584kPa is plotted against the void fraction in Fig. 5-9. The homogeneous sound velocity is typically lower in the two-phase mixture than in the pure liquid and vapour phases.

Pressure oscillations in the signals at the bottom measurement station almost immediately following disc rupture were commonly observed in the present blowdown experiments. Sample pressure fluctuations measured in three different tests are presented in Fig. 5-10. The fluctuations begin about 1ms after the rupture disc opens. At this point in time, the rarefaction wave has only travelled about 14cm away from the rupture disc. The sound velocity in the steel
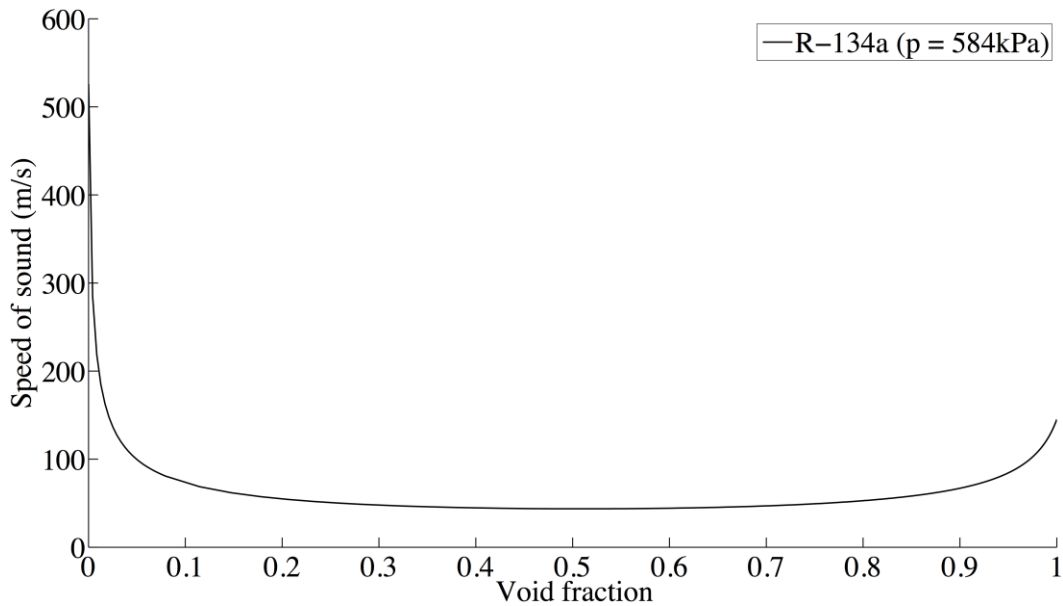
Figure 5-9. Computed speed of sound for a two-phase homogeneous R-134a mixture at 584kPa.

pipes is about 6100m/s, which is more than 40 times faster than in vapour R-134a. It seems therefore that vibrations induced in the pipe by the opening of the rupture disc propagate ahead of the fluid pressure waves and produce some interactions between the pipe and the stagnant liquid. This produces pressure disturbances in the liquid R-134a, which appear as fluctuations in the pressure transducer signals about 5 – 15ms after rupture.

The axial vibrations were measured in the experiments and FFT plots of the accelerometer signals are provided for tests T04, T08 and T09 in Fig. 5-11. The natural frequency of vibration in the vertical direction was about 60Hz. The period of the fluctuations in Fig. 5-10 is about 15ms, which gives a cycle frequency of about 65Hz. The closeness of the two frequencies supports the interpretation of the oscillations in the signals as being caused by fluid-structure interactions between the vibrating pressure vessel and the static pressurised liquid.

Following the transient depressurisation, the generation of vapour increases the compressibility of the R-134a. The vapour phase growth is very
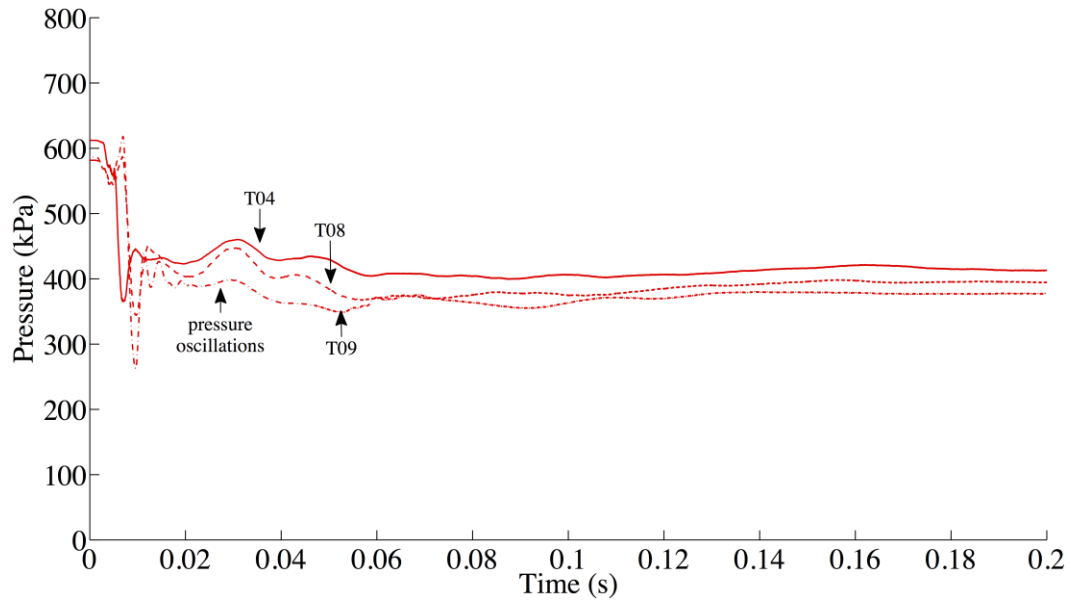
Figure 5-10. Pressure fluctuations at location 1 (tests T04, T08 & T09).

rapid and develops at the pipe walls, near the pressure transducers. This increase in fluid compressibility results in the attenuation of the pressure fluctuations, which explains the broadening of the oscillations after about 45ms and their subsequent disappearance in Fig. 5-10. The damping of the oscillations occurs at about the same time during which rapid vapour generation was observed in the high-speed images (refer to Fig. 5-3). The fluctuations do not seem to have any observable effect on the transient pressure amplitudes that follow. These are mainly influenced by the reservoir volume, the amount of liquid fill, the rate of phase change and vapour growth, and the two-phase discharge rate through the test section.

5.4. VAPOUR CHOKING

When the rupture disc opens, the pressure vessel contains separate liquid and vapour phase domains and the initial discharge is single-phase vapour. Since the pressure ratio between the pressure vessel and the downstream reservoir
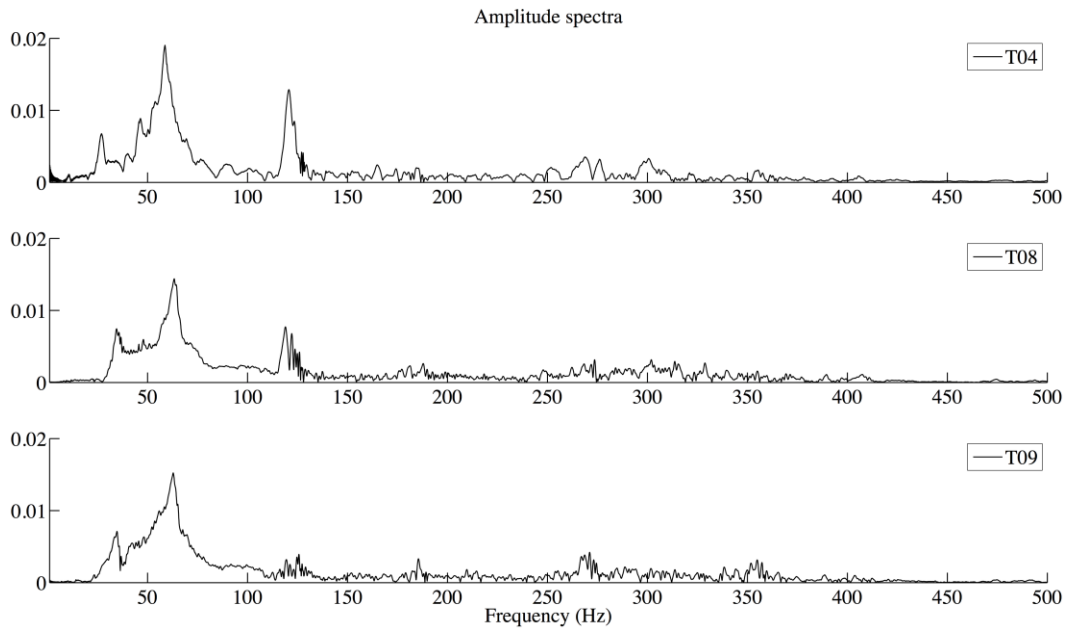
Figure 5-11. FFT plots of vessel vibrations in tests T04, T08 & T09.

(initially in a vacuum) is very high, the accelerating vapour phase rapidly becomes choked. Flow choking occurs when the fluid velocity is equal to the speed of sound, at which point small flow disturbances cannot propagate upstream and any further reduction in downstream pressure has no effect on the flow rate.

The critical (or choked) flow condition establishes the maximum possible discharge mass flow rate. When choking occurs, the ratio of the pressure at the choked plane to the upstream pressure (the critical pressure ratio) assuming isentropic ideal gas is defined by Eq. (4-6). For vapour R-134a at 20°C, the specific heat ratio is 1.2 and the critical pressure ratio is 0.56. Therefore, vapour R-134a discharge at 20°C will be choked as long as the upstream pressure is at least 1.8 times the downstream pressure.

The transient pressures in test T07 at locations 2 and 3, upstream and downstream of the rupture disc respectively, are shown in Fig. 5-12. The initial single-phase vapour discharge can be determined by modelling the unsteady compressible flow behaviour upon the initiation of a large-amplitude one-

dimensional disturbance (sudden pipe break) in a uniform pipe. The initial mass flux, G, is given by Eq. (5-5) (Moody, 1990),

$$G = \rho u = \rho_0 c_0 \left(\frac{2}{\gamma+1} \right)^{\frac{\gamma+1}{\gamma-1}} , \qquad (5\text{-}5)$$

where ρ is the vapour density, u is the vapour velocity, ρ_0 is the initial density, γ is the specific heat ratio, and c_0 is the initial vapour speed of sound, defined according to Eq. (5-6),

$$c_0 = \sqrt{\frac{\gamma p_0}{\rho_0}} , \qquad (5\text{-}6)$$

where p_0 is the initial pressure of the vapour. From the initial pressure of 600.7kPa, the initial discharge mass flux was computed to be 1,549kg/m²s. The corresponding discharge mass flow rate through the rupture disc is 28.3kg/s.
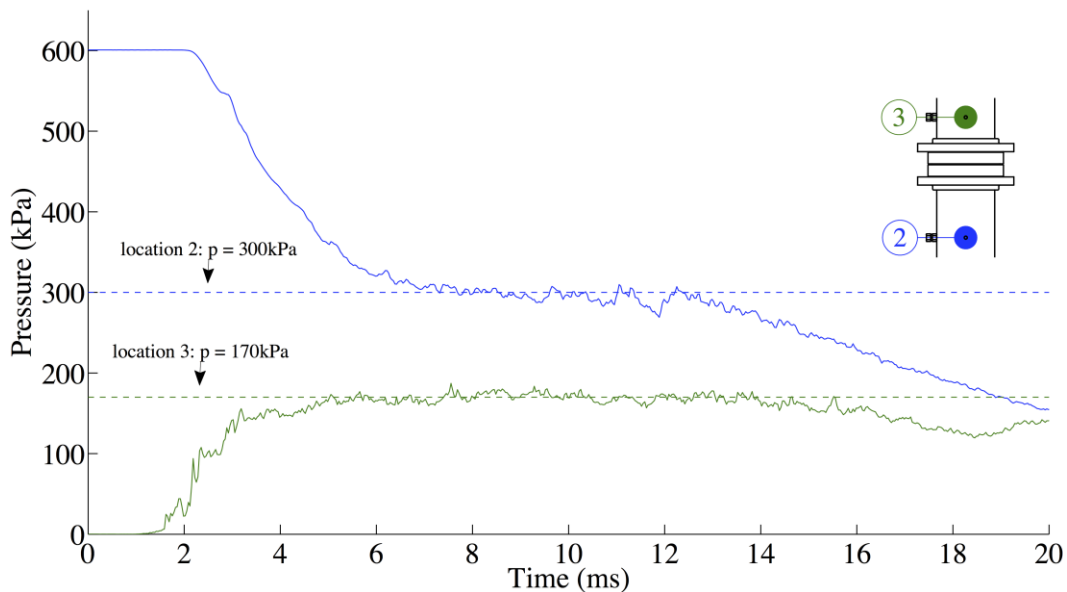
Figure 5-12. Pressure measurements at locations 2 & 3 showing brief choked single-phase vapour discharge through the rupture disc (test T07).

In the first 12ms, the pressure upstream of the disc drops to about 300kPa and the downstream pressure increases from vacuum to about 170kPa. This gives a pressure ratio of 0.57, sufficiently close to the computed critical pressure ratio of 0.56 to suggest that the vapour R-134a discharge is choked during this time. This also explains why the pressure difference remains approximately the same for about 4ms. The steady critical mass flux during this time was determined based on the upstream pressure of 297.5kPa from Eq. (4-7) as 1,253kg/m^{2}s, which corresponds to a critical mass flow rate of 22.9kg/s. The steady choked flow rate is lower than the initial discharge flow rate since the pressure has decreased. Both pressures then begin to decrease, indicating that the discharge flow becomes subsonic at about 12ms.

5.5. PHASE TRANSITION

In all of the tests performed, the pressure measurements in the liquid region (location 1 in Fig. 3-1) indicated that the initial rapid depressurisation of the liquid R-134a proceeded to a minimum pressure that was lower than the initial saturation pressure, as shown in Fig. 5-1. Following the minimum pressure point, the pressure recovered to a pressure amplitude that typically remained steady for several hundred milliseconds. The recovery in the pressure amplitude is caused by the rapid expansion and growth of the vapour phase. The vapour generation is delayed and occurs in superheated liquid after the pressure drops below the saturation point. The amplitude to which the pressure recovers remains below the initial liquid saturation pressure. This behaviour was also observed in blowdown experiments documented in the published literature (Edwards & O'Brien, 1970; Winters & Merte, 1979).

High-speed flow pattern visualisations provided interesting insights into the physical mechanisms of vapour generation and growth in the liquid immediately following the rapid depressurisation. An image sequence of the rapid

vapour growth seen through the lower window, filmed in test T11 at 3000fps, is shown in Fig. 5-13. Also shown is the transient pressure at location 1 below the window. Test T11 was performed with three rows of tubes in the test section and with 53% of the vessel filled with liquid R-134a initially at 595.6kPa and 15.9°C.

The vapour generation behaviour shown was consistently observed in all of the experiments in which high-speed flow visualisations were obtained. The images show that the generation of vapour occurs mainly at the solid-liquid vessel wall boundaries. The expanding bubbles develop on both sides of the glass windows, which are housed in steel frames, as well as below the windows in the bottom steel reservoir. The vapour that is generated grows radially into the liquid bulk and rises upwards towards the vacuum reservoir. After about 0.25s, the two-phase mixture covers most of the viewing area. The dark regions in frames 0629 and 0780 indicate that the void fraction is significantly increased by about 200ms.

The study of bubble nucleation in superheated liquids is well established in the field of boiling heat transfer (Carey, 2008). The mechanisms of bubble
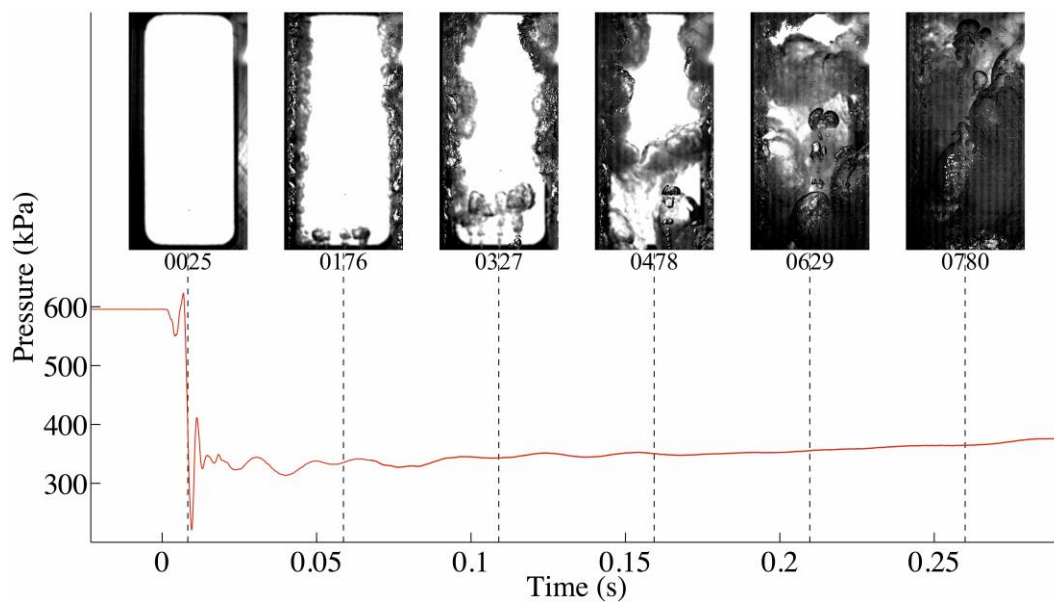
Figure 5-13. High-speed visualisation of vapour growth with pressure measurement (test T11).

nucleation are related to the degree of liquid superheat and are classified into two types: homogeneous and heterogeneous. In a perfectly homogeneous system, nucleation arises spontaneously in the liquid bulk due to molecular interactions and density fluctuations. Heterogeneous nucleation takes place at liquid-vapour interfaces and liquid-solid boundaries where the bubble nucleation activity is promoted by system imperfections such as cavities in rough surfaces, fluid impurities, dissolved gases, and foreign particles suspended in the liquid.

The level of superheat required for homogeneous nucleation to occur in a superheated liquid can be determined by considering the kinetics of bubble formation. The kinetic limit of superheat predicts the theoretical point at which spontaneous and random density fluctuations arising from molecular interactions result in the formation of small vapour embryos. By assuming a nucleation rate of vapour nuclei, J, as being representative of 'spontaneous nucleation', the temperature at which pure liquid substances undergo homogeneous nucleation can be predicted from Eq. (5-7) (Carey, 2008),

$$J = 1.44 \times 10^{40} \left[\frac{\rho_l^2 \sigma}{M_{mol}^3} \right]^{\frac{1}{2}} \exp \left\{ \frac{-1.213 \times 10^{24} \sigma^3}{T_l \left[\eta p_{sat}(T_l) - p_l \right]^2} \right\}, \qquad (5\text{-}7)$$

with the threshold value of $J = 10^{12} \text{m}^{-3}\text{s}^{-1}$, where ρ_l is the liquid density, σ is the surface tension, M_{mol} is the molecular weight, T_l is the liquid temperature, $p_{sat}(T_l)$ is the saturation pressure at the liquid temperature, p_l is the liquid pressure, and η is calculated from Eq. (5-8),

$$\eta = \exp \left[\frac{p_l - p_{sat}(T_l)}{\rho_l R_g T_l} \right], \qquad (5\text{-}8)$$

where R_g is the ideal gas constant per unit mass. Equation (5-7) can be applied directly to the present R-134a blowdown experiments as well as secondary side operating conditions in steam generators, in order to determine whether there is

sufficient liquid superheat available to promote homogeneous bulk nucleation during a sudden depressurisation.

The minimum liquid R-134a pressure that was observed in test T11 during the initial rapid depressurisation stage shown in Fig. 5-13 was 221kPa. The corresponding R-134a equilibrium saturation temperature is -7.5°C. In order for homogeneous nucleation to occur at this pressure, the initial R-134a liquid temperature estimated from Eq. (5-7) is about 61°C. In the present blowdown tests, the initial liquid temperature was never greater than 21°C, which is 40°C short of the calculated superheat required. This indicates that the conditions in these experiments were not favourable for homogeneous nucleation in the liquid bulk, which is in agreement with the nucleation patterns observed.

In an operating steam generator, the maximum theoretical initial water superheat possible during blowdown to atmospheric conditions occurs if the liquid pressure is assumed to fall very rapidly to atmospheric pressure (101.3kPa). By assuming that the pressurised secondary side liquid is suddenly dropped to atmospheric pressure, the required superheated liquid temperature for homogeneous nucleation calculated from Eq. (5-7) is 305°C, which is higher than the typical 260°C operating temperature in the secondary side of a CANDU steam generator. Therefore, even under conservative assumptions, homogeneous nucleation is unlikely to occur in the secondary side of a steam generator during blowdown. These predictions confirm that the current experiments adequately replicate the phenomena that would occur in a full-scale CANDU steam generator during a postulated Main Steam-Line-Break.

The role of surface roughness in heterogeneous nucleate boiling has been widely researched and is well recognised (Carey, 2008). The surface roughness governs the active nucleation site density, which influences the number of bubbles that form during boiling. Blowdown experiments performed in smooth acrylic vessels have shown that the pressures recover to lower amplitudes compared to

steel vessels, and that the blowdown durations are longer (Deligiannis & Cleaver, 1996). The increased presence of nucleation sites on the steel surfaces promotes a more vigorous phase transition resulting in greater superheat relief. This produces higher pressure amplitudes and shorter blowdown durations. In the present experiments, there was no evidence of nucleation on the quartz glass window surfaces.

A high-speed image sequence of a commissioning blowdown test filmed through a vertical glass tube 12.7mm in diameter is presented in Fig. 5-14. The test was performed at a reduced pressure of about 310kPa with subcooled R-134a at a saturation temperature of about 0°C. Details regarding this and a series of other commissioning tests are presented elsewhere (Hamouda, 2011). The initial formation and growth of the vapour phase in the liquid was restricted to a single bubble plug that originated at the bottom closed end steel cap. No nucleation occurred on the glass tube wall. From the images, the bubble plug was estimated to accelerate to a velocity of about 0.67ms in the final few frames.

The terminal velocity of a rising bubble plug, u_p, can be theoretically predicted from Eq. (5-9) (Whalley, 1987),

$u = 0$m/s $u = 0.36$m/s $u = 0.52$m/s $u = 0.53$m/s $u = 0.62$m/s $u = 0.67$m/s
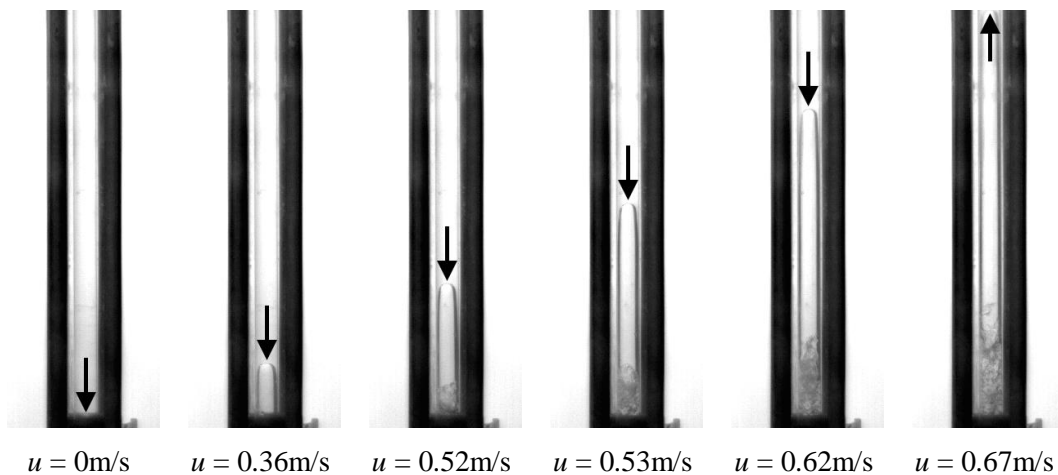
Figure 5-14. Bubble plug in vertical glass tube blowdown (commissioning test, 78.5ms time-step).

$$u_b = 0.35\sqrt{\frac{gd\left(\rho_l - \rho_g\right)}{\rho_l}} \; , \qquad\qquad (5\text{-}9)$$

where g is the gravitational acceleration, d is the tube diameter, and ρ_l and ρ_g are the liquid and vapour densities respectively. The estimated velocity from Eq. (5-9) was 0.12m/s. Similar to the rising bubble case observed in Fig. 5-5, the theoretical model predicts a much smaller velocity than was observed in the blowdown experiment. The transient pressure fields in the initial stages of the blowdowns promote a faster bubble rise towards the vacuum reservoir.

Another feature observed in the flow visualisations was vapour growth at pre-existing liquid-vapour interfaces. A compressed gas accumulator was used to pressurise the vessel and begin the blowdowns. This sometimes caused compressed R-134a gas bubbles to be pushed into the bottom of the liquid region in the pressure vessel through the connecting lines. A high-speed flow visualisation depicting the occurrence of this phenomenon is shown in Fig. 5-15. The image sequence was filmed through the lower window in test T05.

The first couple of frames filmed before the opening of the rupture disc show a group of R-134a gas bubbles that had been introduced into the pressure vessel through the pressurising line. The bubbles grow rapidly upon blowdown initiation. The liquid-vapour interfaces promote much greater bubble growth than the pressure vessel walls. The physical explanation for this behaviour is that the bubbles provide a larger surface area for heat transfer from the superheated liquid across the vapour interface, promoting a greater rate of vapour expansion.

A comparison of the vapour phase growth in pure single-phase liquid (T09) and bubbly two-phase fluid (T12) is shown in Fig. 5-16. The images are presented in 50ms time-steps with a super-imposed 10mm square grid. The rate of vapour growth is observed to be higher in test T12. The viewing section is comprised entirely of a two-phase mixture by the fifth frame at which point it
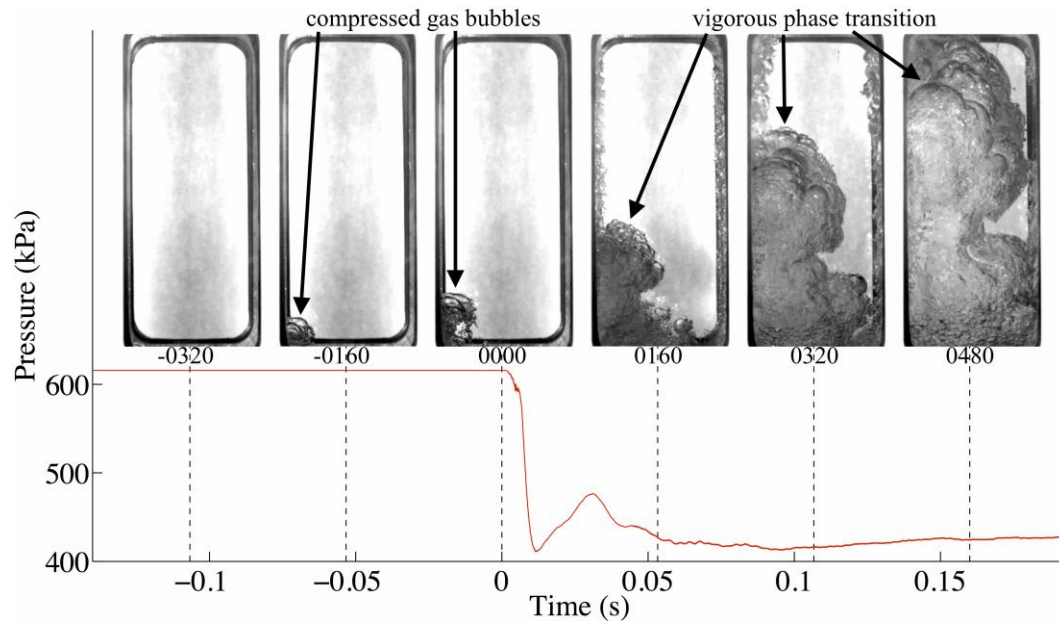
Figure 5-15. High-speed images of pre-existing bubbles that promote vigorous phase transition following blowdown initiation (test T05).

becomes difficult to distinguish individual bubbles. In test T09, the individual bubbles can be more easily identified. The average rising velocity of the bubbles towards the end of the image sequence was estimated to be about 0.9m/s. The predicted velocity from Eq. (5-1) is 0.1m/s, which under-predicts the bubble rise velocity by a factor of almost 10.

A group of small bubbles developed independently in test T09, visible near the centre of the image in the 2nd and 3rd frames. Although the bubbles appear to be nucleating spontaneously in the liquid bulk, such behaviour might possibly result from heterogeneous nucleation on suspended microscopic particles or micro-bubbles of non-condensable foreign gas in the liquid. These would not be distinguishable in the images due to the resolution limitations. Based on these observations, it may be inferred that a steam generator MSLB would result in vigorous vapour generation at sizeable surface imperfections in the liquid-metal boundaries, suspended foreign particles in the secondary side water, and any pre-existing liquid-vapour interfaces in the liquid bulk.
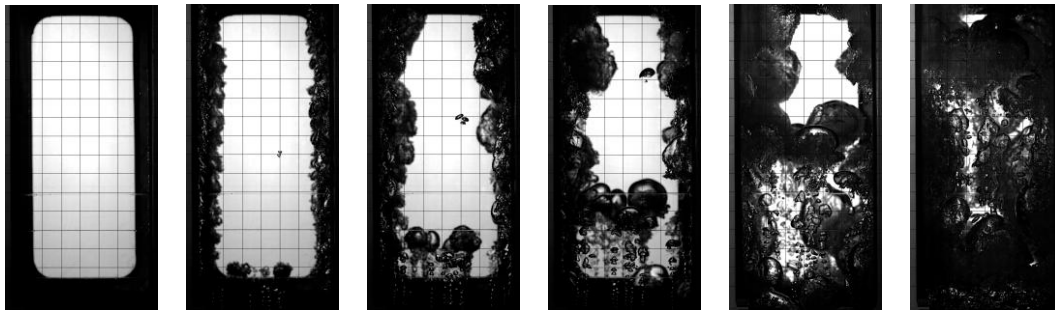
(a) Test T09: nucleation in quiescent liquid pool.
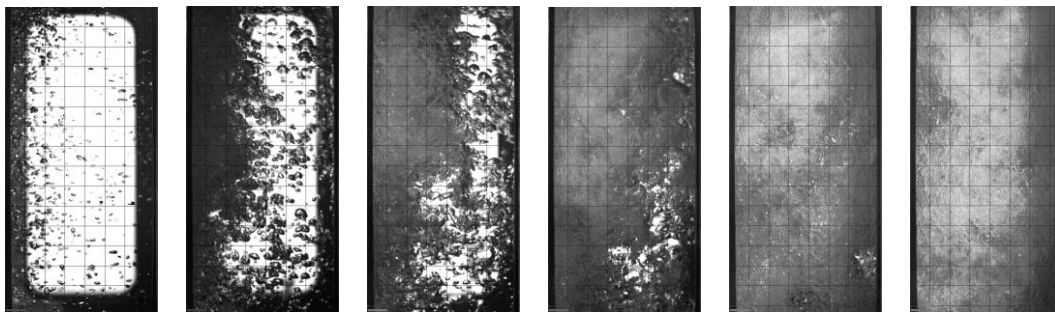
(b) Test T12: growth of pre-existing compressed gas bubbles.

Figure 5-16. High-speed flow visualisation of bubble growth, (a) test T09, (b) test T12 (50ms time-step).

The rate of growth of very small bubbles is limited by the rate at which the expanding vapour can accelerate the surrounding liquid. Heat transfer from the liquid during this stage is very fast and the process is controlled by fluid inertia. The bubble diameter grows linearly with time. In the later stages of the bubble growth, once the superheat in the boundary layer of the bubble has been significantly depleted, the rate of growth becomes dominated by the rate of heat diffusion from the liquid. Fluid inertia is negligible for bubbles of sufficiently large diameter and the rate of growth is approximately proportional to the square root of time.

The bubble radius at which the transition occurs between inertia-controlled and thermal-controlled bubble growth in a superheated liquid at a constant ambient pressure, R_{trans}, can be estimated from Eq. (5-10) (Carey, 2008),

$$R_{trans} = \frac{\left(\dfrac{12\kappa_l}{\pi\rho_l c_{pl}}\right)\text{Ja}^2}{\sqrt{\dfrac{2\left[T_a - T_{sat}\left(p_a\right)\right]h_{lg}\rho_g}{\rho_l T_{sat}\left(p_a\right)}}}, \tag{5-10}$$

where κ_l is the liquid thermal conductivity, ρ_l is the liquid density, c_{pl} is the liquid specific isobaric heat capacity, T_a is the ambient liquid temperature, $T_{sat}(p_a)$ is the saturation temperature corresponding to the ambient liquid pressure, h_{lg} is the latent heat of vaporisation per unit mass, ρ_g is the vapour density, and Ja is the Jakob number defined in Eq. (5-11),

$$\text{Ja} = \frac{\rho_l c_{pl}\left[T_a - T_{sat}\left(p_a\right)\right]}{\rho_g h_{lg}}. \tag{5-11}$$

The estimated bubble transition radii for tests T02 (shown in Fig. 5-5) and T09 (shown in Fig. 5-16a) were 1.8μm and 0.3μm respectively. Since the identifiable bubbles in the flow visualisations were several orders of magnitude larger, the bubble growth regime may be safely assumed to be mainly governed by the rate of heat diffusion from the surrounding liquid to the vapour bubbles. The bubble radius as a function of time, $R_b(t)$, for the thermally-controlled bubble growth regime can be estimated according to Eq. (5-12) (Carey, 2008),

$$R_b\left(t\right) = 2\sqrt{\frac{3}{\pi}}\text{Ja}\sqrt{\frac{k_l}{\rho_l c_{pl}}t}. \tag{5-12}$$

A comparison of the measured bubble radii from the flow visualisations and the theoretical growth rate starting at the initial bubble radius ($t \approx 50\text{ms}$) is shown in Fig. 5-17. Various bubble diameters were traced (refer to Figs. 5-5 and 5-16) and the theoretical curves were determined from Eq. (5-12) using the ambient pressures of 275kPa and 380kPa in tests T02 and T09 respectively. These pressures were measured at location 1 and were observed to remain steady for the

time segments shown in Fig. 5-17. The bubble growth was significantly under-predicted by the theoretical model, especially towards the later stages when the bubbles reached considerable sizes.

This discrepancy may be due to the assumption of constant ambient pressure, which does not account for the transient pressure fields established during the blowdown. Additionally, the models were developed assuming that the heat diffusion occurs mainly by conduction through the bubble boundary layer. Convection effects due to bubble slip may result in more heat transferred to the vapour bubbles. Furthermore, bubble coalescence may have resulted in bubble radius measurements that were larger than the actual radii of the individual bubbles. Overall, it appears that the bubble velocity and growth during the transient blowdown are significantly under-predicted by the theoretical pool boiling models available in the literature.

In test T06, the liquid surface separating the pressurised liquid at the bottom of the vessel and the saturated vapour below the rupture disc was filmed
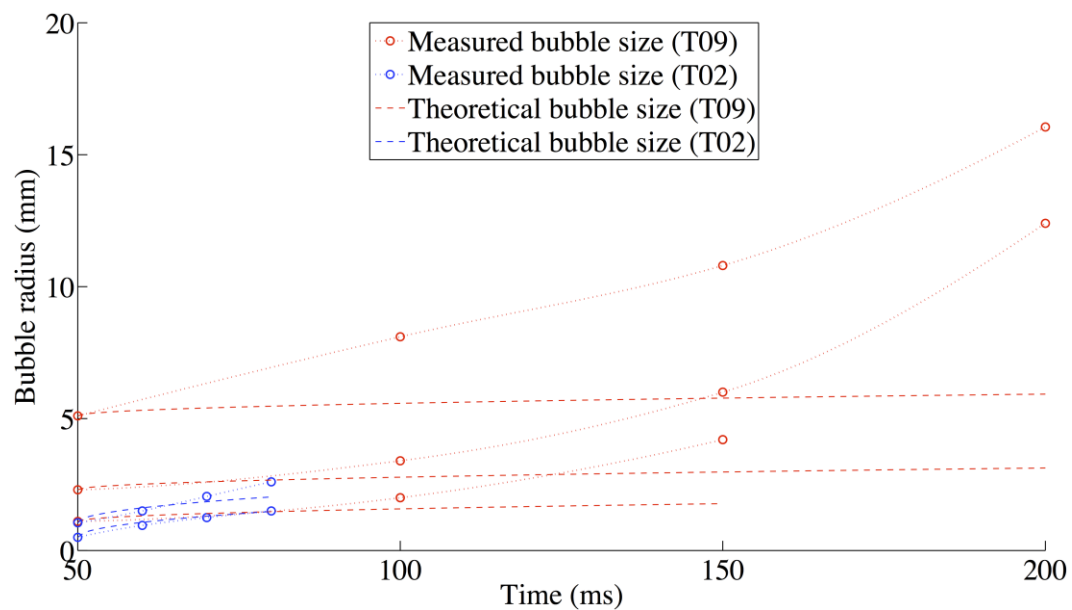
Figure 5-17. Comparison of measured bubble radii against theoretical growth rates (tests T02 & T09).

during blowdown in order to monitor the behaviour of the liquid-vapour interface. A sequence of high-speed images acquired from the lower window is presented in Fig. 5-18. In frames 0048 and 0064 ($t = 16 - 21.3$ms), the liquid appears to remain stationary. The expanding vapour phase slips through the liquid free surface towards the top of the pressure vessel.

The two-phase plumes that are formed by the dynamic phase transition apparently accelerate at a much faster rate than the liquid bulk during these initial stages of the vapour growth. This can be explained by the large difference in inertia between the two phases. The vapour density is about 45 times less than the liquid density. The flow pattern above the initial liquid surface in frames 0064 and 0080 ($t = 21.3 - 26.7$ms) seems to be a mixed vapour-droplet flow regime, which is well established by the end of the image sequence.

In frame 0048 ($t = 16$ms) there appears to be some two-phase flashing at the interface between the liquid and the vapour, which occurs in a narrow zone at the surface. It is possible that turbulence due to agitation, foreign particles such as
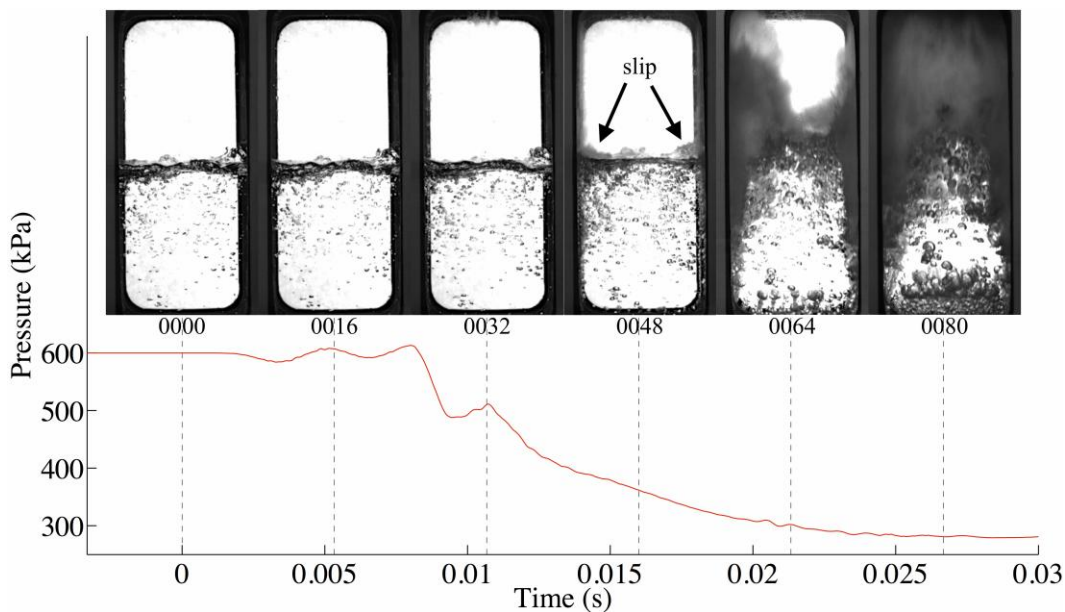
Figure 5-18. Flow visualisation of phase transition at the liquid surface (5.3ms time-step, test T06).

trapped dust suspended at the liquid surface, or local low pressures caused by complex rarefaction wave-interface interactions produce local conditions at the liquid surface that are conducive to the nucleation of vapour bubbles. Bubbles originating below the window in the steel pipe reservoir can be seen propagating upwards in frames 0064 to 0080 ($t = 21.3 - 26.7$ms).

The rate of vapour generation and growth observed was very rapid and is of the same order as that shown in Fig. 5-17. Once the rarefaction wave propagating from the rupture disc arrives at the bottom closed end of the pressure vessel, it is reflected and propagates back up through the flashing two-phase fluid mixture. Since the compressibility of the R-134a increases rapidly with the formation of vapour, the rarefaction wave reflection is rapidly attenuated. This would effectively dampen any 'water-hammer' type of pressure oscillations, which explains why there were no strong pressure fluctuations visible in the pressure measurement at the bottom of the pressure vessel.

The general phase transition features observed in the high-speed flow visualisations can be summarised as follows. Vapour formation begins around the time at which the measured pressure rapidly decreases to a minimum value. The primary bubble activation and growth mechanism appears to be heterogeneous nucleation at the vessel steel wall boundaries. The generation of vapour bubbles also occurs at any pre-existing liquid-vapour interfaces in the fluid. Independent bubbles growing in the liquid bulk were occasionally observed. These may have originated at microscopic foreign particles or non-condensable gas bubbles suspended in the liquid, although this cannot be visually confirmed due to resolution limitations. No vapour nucleation occurred on the glass windows through which the high-speed images were filmed.

The bubble growth proceeds from the outside walls towards the fluid in the centre of the pressure vessel. The velocity of the flashing vapour phase initially seems to have a vertical component towards the rupture disc at the top, as

well as a radial component towards the undisturbed superheated liquid at the centre of the cross-sectional flow area. The growth of the vapour phase takes place very rapidly, with bubble coalescence producing continuous two-phase plumes that accelerate towards the vacuum reservoir. About $30 - 40$ms after disc rupture, the images show a dense two-phase concentration suggestive of a high void fraction, which develops early in the transient blowdowns.

5.6. TWO-PHASE FLOW ACCELERATION

It was demonstrated in Fig. 5-12 that single-phase vapour choking occurred in test T07 following the opening of the rupture disc and the discharge transitioned to subsonic at about 12ms. The experiment was carried out with 10% of the pressure vessel filled with liquid and all of the tubes removed from the test section. The initial liquid and vapour pressures and temperatures were 604.7kPa and 17.3°C, and 600.7kPa and 19.7°C respectively. The pressures measured during the flow of the flashing two-phase mixture towards the vacuum reservoir are presented in Fig. 5-19. Following vapour choking, the pressures fall at location 2 until about 35ms and at location 3 until about 40ms, after which both pressures begin to climb at a similar rate.

The increase in pressure is due to the arrival of the accelerating two-phase fluid mixture front that had originated at the liquid level surface. The acceleration of the flashing two-phase mixture is shown in a high-speed image sequence in Fig. 5-20. The top images show the two-phase front propagation at the lower window ($14 - 21$ms after rupture) and the bottom images show the front propagation at the upper window ($29 - 32$ms after rupture). The position of the flashing front with respect to time determined from the high-speed images and the pressure transducer measurements is included on the right of Fig. 5-19. The estimated average velocities at each successive segment are also shown.
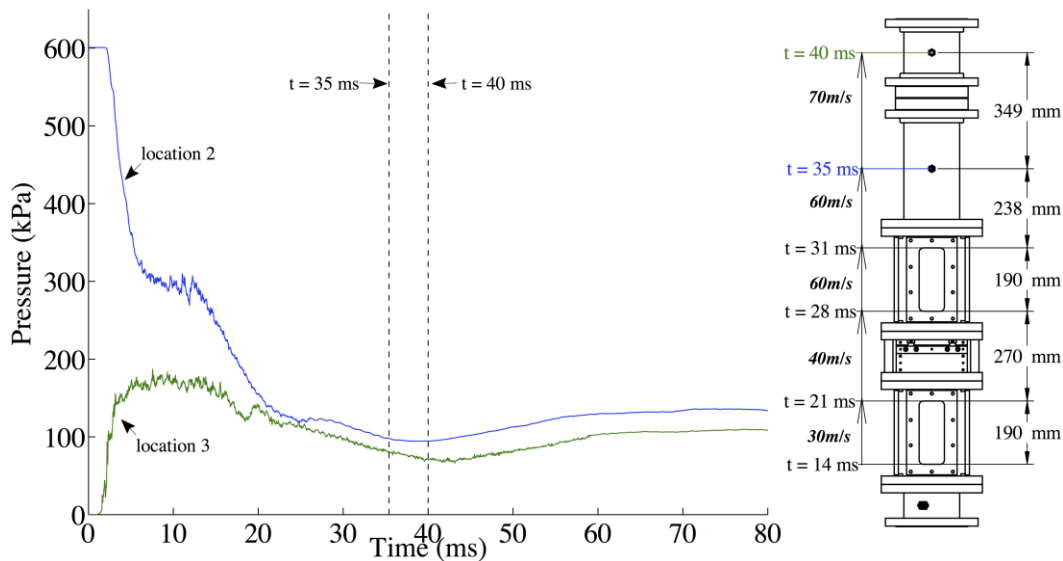
Figure 5-19. Pressure measurements at locations 2 & 3 and two-phase front velocity estimates from transducer signals and high-speed images (test T07).

The top image sequence in Fig. 5-20(a) shows the two-phase front propagating upwards at the lower window. The initial liquid surface is just below the window frame. In Fig. 5-20(b), the first frame shows two separate two-phase mixture concentrations. The top half of the frame is occupied by a flashing liquid-vapour mixture that had originated at the test section between the windows. This was due to prior steady-state condensation on the steel walls. At the bottom of the frame, the two-phase front that had originated at the liquid surface is seen entering the viewing area. The velocity of the two-phase mixture increases as it accelerates towards the vacuum reservoir. The average velocity is about 30m/s at the lower window, about 60m/s at the upper window, and about 70m/s discharging into the downstream vacuum reservoir.

Choked flow in single-phase compressible fluids has been widely investigated and is well understood. The introduction of a second phase however, substantially increases the phenomenon's complexity. There is no theoretical model available that completely describes all aspects of two-phase critical flow. While a basic understanding of the main flow mechanisms exists, complex liquid-

(a) Lower window: $t = 13.7 – 22$ms (1.67ms time-step).

(b) Upper window: $t = 27.7 – 31$ms (0.67ms time-step).
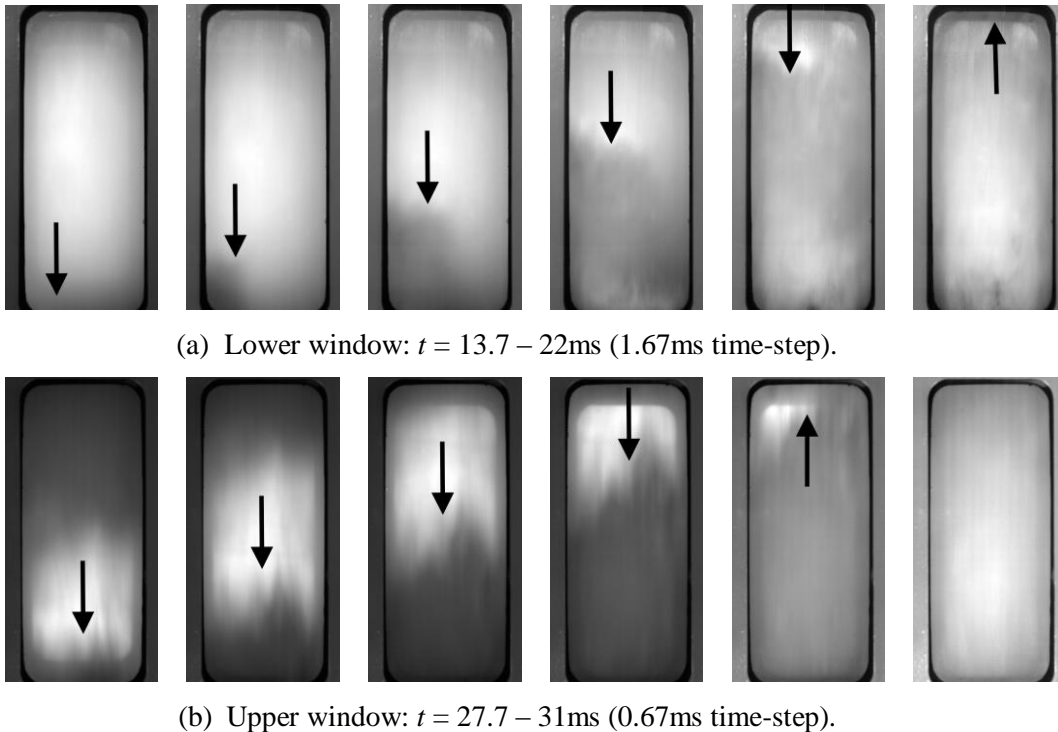
Figure 5-20. High-speed images of the two-phase front (test T07), (a) lower window, (b) upper window.

vapour interfacial phenomena make the accurate prediction of two-phase critical flow a difficult task (Levy, 1999).

When a flowing two-phase mixture flashes, the vapour generated reduces the average density of the fluid, thereby reducing the overall mass flow rate. The local speed of sound is also influenced substantially. While the choked and sonic velocities are equal in compressible single-phase flows, the presence of critical flow conditions in a two-phase mixture does not necessarily indicate that the maximum choked mass flow rate of the mixture has been attained. The presence of significant interfacial heat and mass transfer processes can produce maximum mass discharge at subsonic flow conditions (Städtke, 2006).

Perhaps the simplest available model for predicting two-phase critical flow is the Homogeneous Equilibrium Model (HEM), which assumes that the two phases are always in mechanical (no-slip) and thermal (no temperature difference)

equilibrium. The HEM produces reasonable choked flow rate predictions in long pipes with small discharge areas, in which the assumptions of mechanical and thermal equilibrium are justified (Wallis, 1980). For subcooled liquids and low quality saturated mixtures, the assumption of thermal equilibrium can result in an under-prediction of the void fraction since liquid superheat is not accounted for (Pinhasi *et al.*, 2005). For choked two-phase flow in short pipes, the liquid and vapour phase velocities do not have sufficient time to equalise and the slip effects result in an under-prediction of the choked flow velocity. When the discharge area is large, the thermal equilibrium assumption over-predicts the two-phase mixture density at the discharge plane. The net effect for sufficiently large discharge areas is an over-prediction of the choked flow rate (Fthenakis *et al.*, 2003).

Pressure measurements and high-seed images of the accelerating two-phase mixture in test T08 are shown in Fig. 5-21. The initial liquid surface is inside the tube bundle, in which six tube rows were mounted. Similar to Fig. 5-12, the initial pressures of 170kPa and 300kPa indicate that single-phase choked flow conditions exist at discharge. The transition to subsonic discharge occurs at about 7ms. The high-speed image sequence shows the two-phase front propagation at the upper window. The fluid enters the bottom of the frame at $t = 10$ms and reaches the top at $t = 13.7$ms. The arrival times of the two-phase front at locations 2 and 3, determined from the pressure signals, are also included in Fig. 5-21.

The average velocity of the two-phase mixture increases from about 52m/s at the window to about 58m/s at discharge. The initial discharge velocity of the two-phase mixture in test T08 is lower than that of test T07 by about 10m/s. The homogeneous equilibrium sonic velocity was computed for a range of void fractions from Eq. (5-4) based on the pressures measured at location 2 in tests T07 and T08. The results are plotted in Fig. 5-22. The discharge velocity of 70m/s corresponds to an equilibrium void fraction of 0.985 in test T07 (thermodynamic quality $x = 0.19$). For test T08, the void fraction corresponding to the discharge velocity of 60m/s is 0.975 ($x = 0.16$). It is logical that the void fraction is lower in
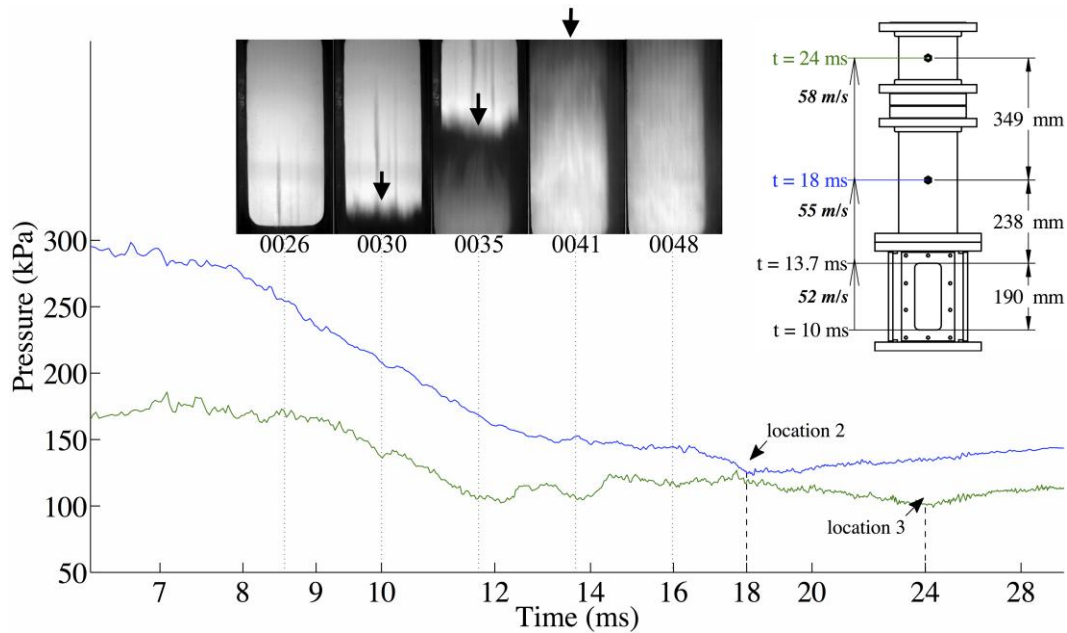
Figure 5-21. Accelerating two-phase mixture front propagation (test T08).

test T08, since the liquid surface was located closer to the transducer point and less time was therefore available for the liquid to flash to vapour. This also explains the higher velocities observed in test T07. The velocity approaches the single-phase vapour speed of sound at higher void fractions.

5.7. QUASI-STEADY BLOWDOWN

The transient pressure amplitude during a two-phase blowdown is determined by the net effect of the rate of vapour generation, which produces an increase in pressure, and the rate of fluid discharge, which results in a decrease in pressure. The initial liquid volume and the test section geometry were found to have a pronounced effect on the transient pressure amplitudes in the present experiments. Following the initial unsteady stages described in the previous sections, the pressure was observed to achieve a 'quasi-steady' condition in which the amplitude remained relatively constant over a significant portion of the two-phase blowdown discharge process. The duration of the quasi-steady blowdown
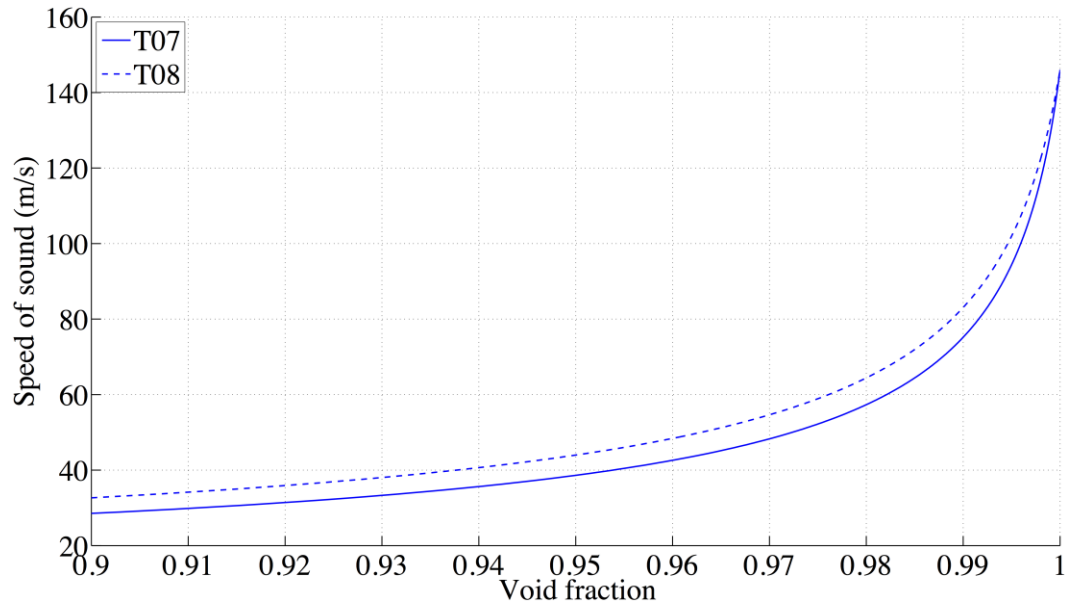
Figure 5-22. Homogeneous speed of sound calculation for tests T07 ($p = 95$kPa) & T08 ($p = 125$kPa).

period and the pressure amplitude during this stage were significantly influenced by the initial experimental conditions.

A comparison of the transient pressure measured at the bottom measurement station of the pressure vessel (location 1) for test T06 with 6 rows of tubes and test T03 with no tubes mounted in the test section is given in Fig. 5-23. The two tests were performed with similar initial liquid levels, 21% and 23% of the pressure vessel filled with liquid R-134a respectively. The rate of the depressurisation during the initial stage of the transient ($t = 0 - 20$ms) is very rapid. The restriction to the discharging flow imposed by the tube bundle in test T06 results in the upstream pressure being a little higher than the case with no tubes.

At about 35ms, the generation of vapour and acceleration of the two-phase flow produces an increase in the pressure upstream of the tube bundle (test T06) until about 75ms, whereupon the upstream pressure remains constant for the next few hundred milliseconds. High-speed flow images filmed in test T06 indicated
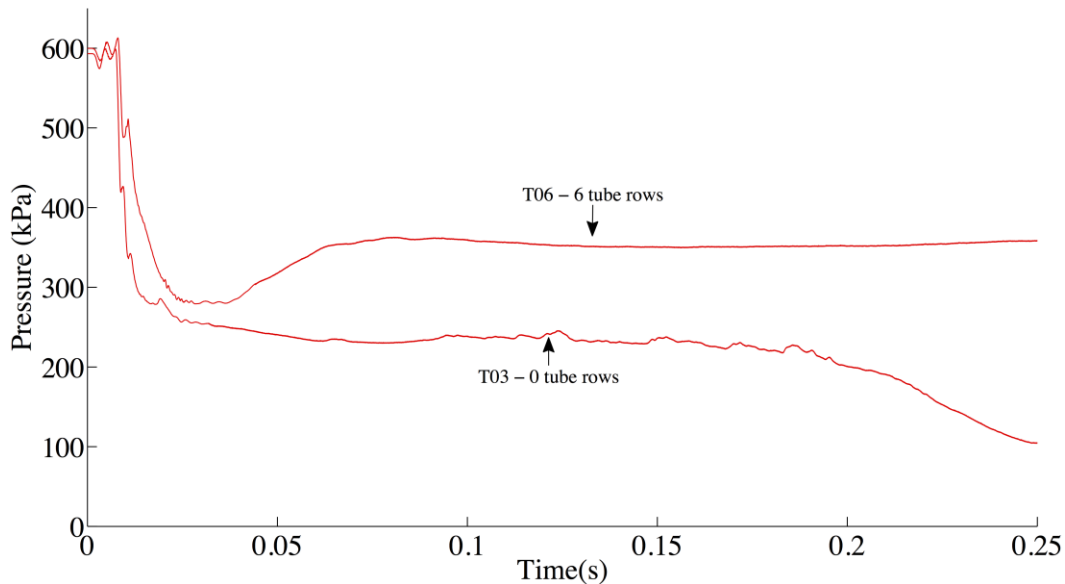
Figure 5-23. Comparison of pressure measurements at location 1 (tests T03 & T06).

that after the initial rapid depressurisation, a significant amount of vapour was produced at about 20 − 30ms (refer to Fig. 5-18). The swarm of bubbles grows rapidly and occupies most of the space formerly filled with liquid. The heat-transfer driven phase transition occurs at the growing liquid-vapour interfaces and the explosive generation of vapour brings the pressure to a maximum about 65 − 75ms after the initiation of the blowdown.

The initial rate of fluid discharge is significantly higher when there are no tubes mounted in the test section (test T03) because of the much lower downstream resistance to the flow. As a result, the flashing two-phase mixture is rapidly discharged towards the vacuum reservoir and the initial rate of vapour generation cannot be sustained. The pressure therefore does not recover to a maximum as was observed in test T06. The liquid inventory is depleted more rapidly, the transient pressure decreases monotonically, and the overall duration of the blowdown is much shorter in test T03.

In both tests T03 and T06, the pressure was observed to achieve a quasi-steady condition approximately 75ms into the blowdown. This stable quasi-steady

pressure suggests that the flow is choked. The maximum possible flow rate is reached and the upstream pressure is no longer controlled by the downstream pressure. The tube bundle introduces a flow restriction that increases the mass 'hold-up' in the pressure vessel upstream and prolongs the blowdown discharge process.

When the tube bundle restriction is removed (test T03), more vapour is able to escape through the discharge flow area (high slip ratio) resulting in a lower quasi-steady pressure amplitude. The tube bundle traps more of the vapour that is being generated in the vessel so that the pressure increases to a higher amplitude. The theoretical limiting maximum pressure occurs when both phases are discharged with equal velocities and equal temperatures so that the two-phase mixture does not flash any further (equilibrium quality). This is essentially the homogeneous equilibrium assumption, for which the maximum pressure amplitude would recover to the initial saturation pressure of the liquid.

5.8. INVENTORY DEPLETION

High-speed flow visualisation images filmed during the final stages of transient blowdown test T07 are presented along with the pressures measured at locations 1 and 3 (bottom and top of pressure vessel) in Fig. 5-24. The experiment was performed with 10% of the pressure vessel filled with liquid and no tubes mounted in the test section. The two-phase flow towards the end of the blowdown at $t = 0.12 - 0.14$s appears to be homogeneous. During this stage, the rate of vapour generation in the vessel cannot sustain the quasi-steady pressure that existed with the initially established choked flow discharge. A depressurisation towards equilibrium conditions is observed in both pressure measurements.

At $t = 0.16$s, entrained liquid droplets are visible in the flow. At this point in the transient, the liquid phase has lost most of its sensible heat. The temperature of the liquid drops sufficiently to limit the occurrence of further flashing and
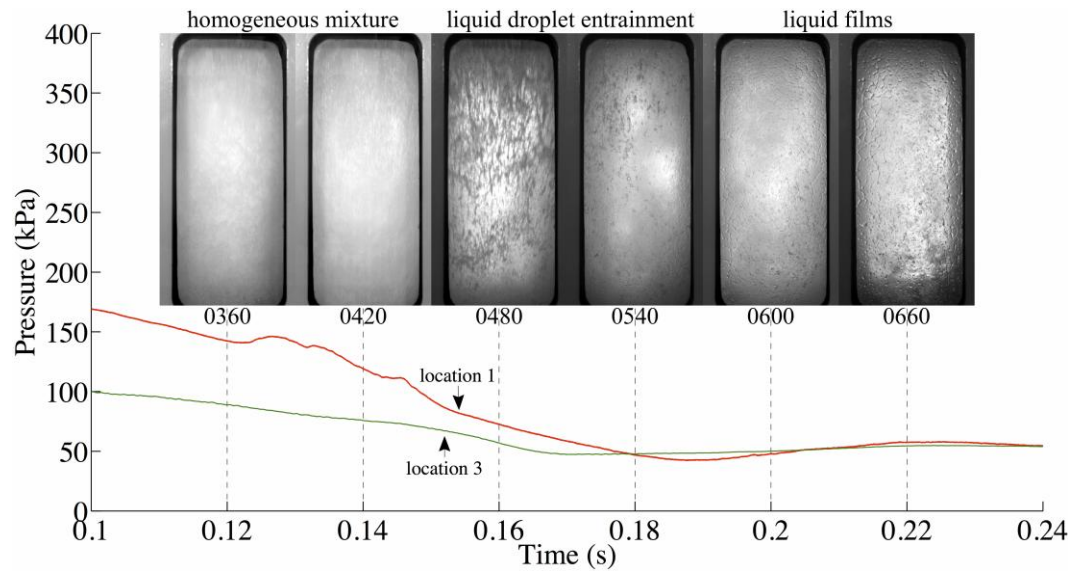
Figure 5-24. High-speed images of end of blowdown transient (20ms time-step, test T07).

phase transition. The droplet concentration is reduced by $t = 0.18$s and the liquid inventory depletion is nearly complete by this time. As the blowdown transient proceeds towards completion, equilibrium conditions are established in the reservoir at about $t = 0.18$s. Relatively slowly evaporating liquid films and droplets are visible on the glass window at $t = 0.2 - 0.22$s.

The pressure oscillations that begin at about 0.18s are caused by acoustic wave phenomena. The damped periodic oscillation behaviour is characteristic of the propagation of acoustic waves through a compressible medium in a long tube. The oscillations were stronger at the closed end of the pressure vessel. The period is about 60ms, which gives a cycle frequency of about 17Hz. The natural frequency, f_n, can be estimated from Eq. (4-18) as

$$f_n = \frac{c}{4(L+0.4d)} = \frac{144}{4(1.767)} = 20 \text{ Hz} ,$$

which is similar to the experimentally observed oscillation frequency.

CHAPTER 6. PARAMETRIC STUDY OF BLOWDOWN THERMAL HYDRAULICS

The general thermal-hydraulic phenomena presented in Chapter 5 can be summarised as follows. The initial rapid transient stages directly following the opening of the rupture discs are dominated by unsteady acoustic phenomena. The specific details of the wave propagation behaviour depend on the initial liquid levels in the pressure vessel. Significant liquid flashing to vapour develops a few milliseconds later and the mass flow rate of the discharging fluid increases rapidly. Subsequently, the upstream pressure stabilises and remains steady for a few hundred milliseconds, which suggests that the two-phase flow is choked during this time.

The duration of this quasi-steady discharge phase of the blowdown depends strongly on the initial liquid level in the reservoir and the restriction to the flow imposed by the tube bundle in the test section. The blowdown tapers off when the liquid inventory is reduced sufficiently that the pressure level cannot be maintained by vapour generation in the pressure vessel. This chapter provides a parametric study of the influence of the initial conditions on the transient thermal-hydraulic phenomena encountered in these experiments. The two-phase fluid dynamics are explained through the pressure and temperature measurements.

6.1. COMPARABILITY OF RESULTS FROM DIFFERENT EXPERIMENTS

The initial liquid level, temperature, and pressure at rupture are all impossible to control precisely. This section explains the differences that were observed in the experiments due to the variability in the initial conditions. The final

outcomes, especially the phenomena of most importance related to fluid loading of the tube bundle, were essentially unaffected. Measurements obtained at locations 1 and 3 (refer to Fig. 3-1) in tests C03, C04, and T06, which were all performed with 6 rows of tubes in the test section, are shown in Fig. 6-1. The graphs on the left show the initial 100ms of the transient and the full transient duration is shown on the right. The similarity of the measurements over the full transient duration is reasonably good. The rates of the change in pressure were comparable and the deviations in the pressure amplitudes were relatively small.

The variations between the measurements may be partly attributed to the differences in the initial conditions. The initial liquid pressures in the tests varied from 568kPa to 600kPa, the liquid temperatures varied from 17.5°C to 18.8°C, and the liquid surface heights from the bottom of the pressure vessel ranged from 266mm to 297mm. Although the timings of the transient pressure signals in all three tests were consistent, the amplitude discrepancies were greater during the
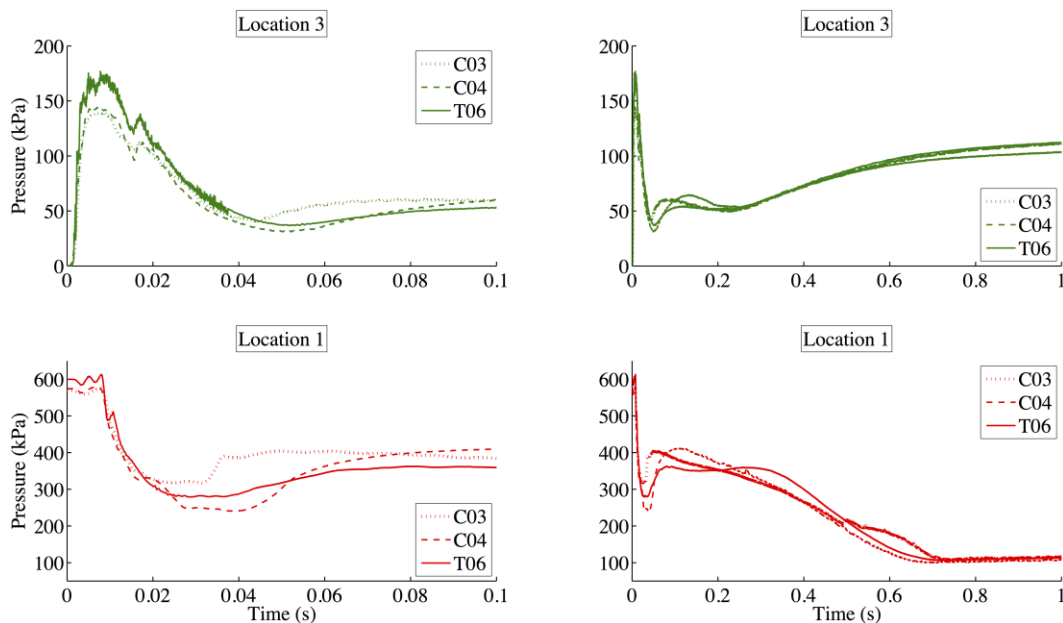
Figure 6-1. Pressure measurement comparison (tests C03, C04, & T06), location 1 (bottom), location 3 (top), $t = 0 - 0.1$s (left), $t = 0 - 1$s (right).

initial stages of the transient and were more pronounced at location 1 than at location 3.

The minimum pressure amplitude in liquid (location 1) following the initial rapid depressurisation, the rate of pressure recovery during liquid flashing, and the amplitude of the pressure 'plateau' during quasi-steady blowdown all varied between the three tests. Potentially influential factors such as nucleation site density and precise blowdown initiation pressure were difficult to control experimentally. For instance, the rupture disc burst pressure tolerance of ±5% ranges from 555kPa to 613kPa. The vapour generation and growth mechanisms were filmed in tests C03 and T06 and are compared in Fig. 6-2.

The phase transition appears to be more intense in test C03 compared to test T06. In the 15ms time-span shown, the bubbles grow to the full viewing area by about 12ms following the observed flashing initiation in test C03. In test T06
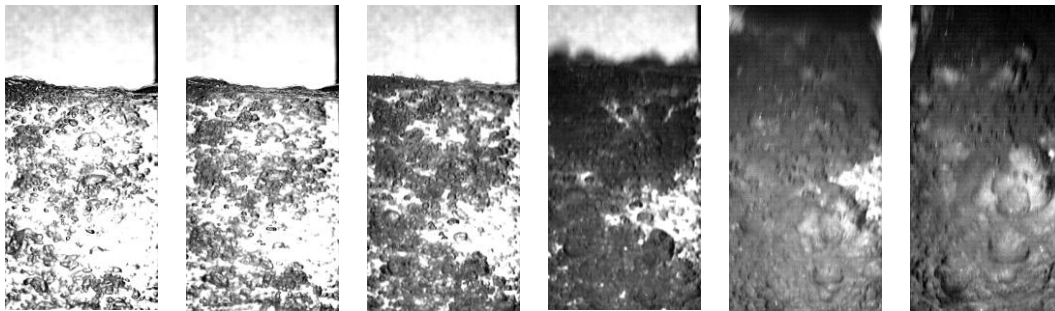
(a) Test C03: Rapid growth of pre-existing gas bubbles
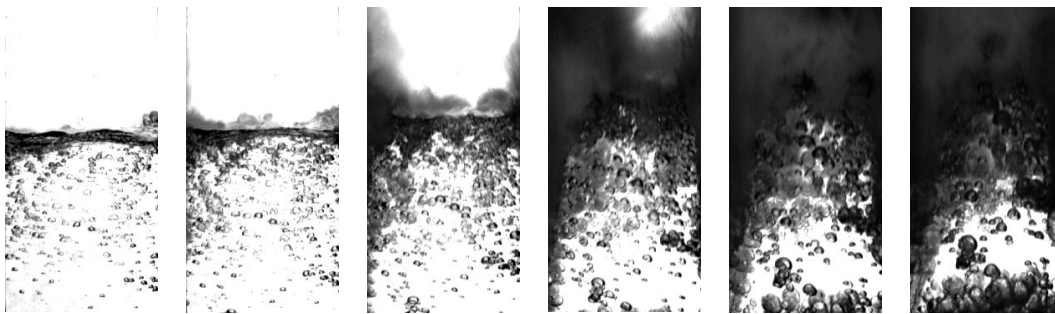
(b) Test T06: Limited vapour generation inside bulk liquid

Figure 6-2. Comparison of initial rate of vapour generation (3ms time-steps), (a) test C03, (b) test T06.

however, a considerable portion of the liquid remains unperturbed even in the last frame at the end of the 15ms segment. This can be explained by the higher initial concentration of bubbles distributed in the liquid in test C03, which results in a faster rate of superheat relief and vapour growth. This would produce a faster rise in pressure and a higher pressure amplitude, which matches the pressure behaviour observed in test C03 at location 1. In addition, the pressure measurements are sensitive to local three-dimensional transient effects especially in the initial stages of the blowdowns, before average conditions are established across the cross-sectional flow area.

In order to better investigate the transient pressure quantitatively during the blowdowns, it is more instructive to plot the pressure drop, $\Delta p_{1\text{-}3}$, measured across the bottom and top of the pressure vessel, normalised by the upstream pressure (location 1), p_u, according to Eq. (6-1),

$$\frac{\Delta p_{1-3}}{p_u} = \frac{p_u - p_d}{p_u} = 1 - \frac{p_d}{p_u}, \tag{6-1}$$

where p_d is the downstream pressure (location 3). The transient normalised pressure ratio obtained from Eq. (6-1) is plotted for tests C03, C04, and T06 in Fig. 6-3. The pressure downstream of the rupture disc is initially 0kPa (vacuum) and the initial pressure ratio is therefore equal to one at $t = 0$. The pressure ratio converges to zero when the upstream and downstream pressures approach other towards the end of the blowdown.

Despite the individual pressure traces at locations 1 and 3 being not exactly the same, the non-dimensional pressure ratio parameter collapses the three experimental curves quite well. This is especially true for the most important time segment during which the pressure ratio remained nearly constant and the pressure drop across the tube bundle was maximum (0.1s to 0.25s). The pressure ratio is directly related to the mass flow rate in the pressure vessel, which remains constant
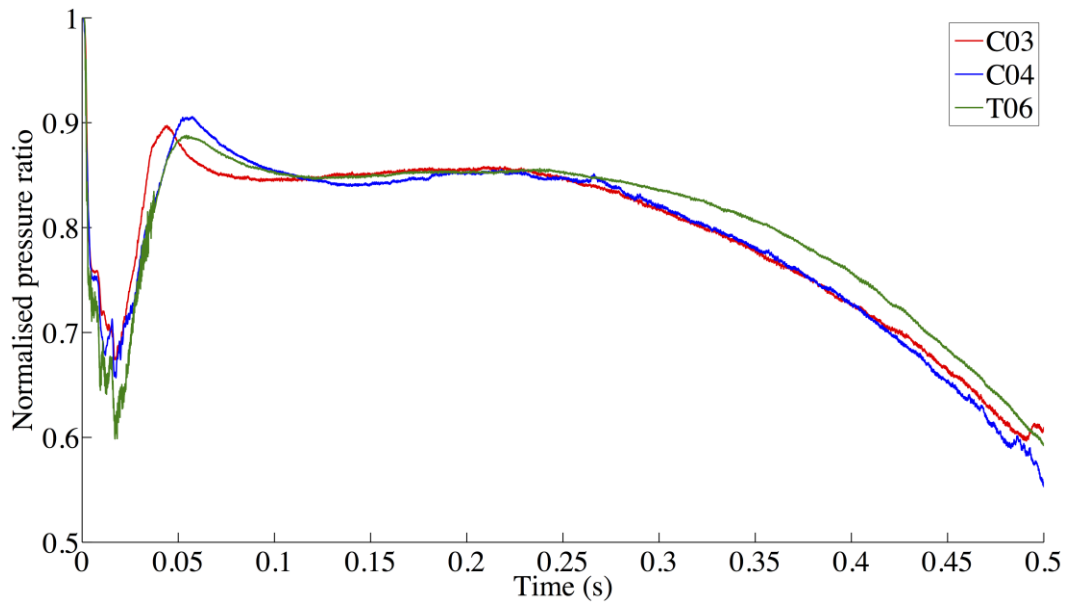
Figure 6-3. Normalised pressure ratio (tests C03, C04, & T06).

when the flow is choked and the fluid properties and discharge flow area are the same.

The pressure ratio remains higher for slightly longer in test T06 than the other tests. This can be explained by the lower quasi-steady amplitude to which the pressure recovered (due to a slower rate of bubble growth) prolonging the duration of the discharge process. Hence, the difficulty in precisely controlling all the initial conditions and the additional random boiling effects did not influence the quasi-steady pressure ratio when the flow rate was maximum. Generally, the variations in the details of the pressures in the initial stages had little discernible influence on the average transient measurements over the full blowdown duration.

6.2. EFFECT OF THE INITIAL PRESSURE

The initial fluid pressure was determined by the pressure difference at which the rupture disc opened and was different for each experiment. The transient thermal hydraulic phenomena were not influenced by the rupture pressure. The

transient pressures acquired at location 1 in tests C05 and T05 are compared in Fig. 6-4. The initial test conditions were almost identical for both tests save for the initial pressures, which were 573kPa and 616kPa in tests C05 and T05 respectively. In particular, the initial liquid temperatures (and therefore saturation pressures) were practically the same at 17.5°C and 17.7°C respectively.

The transient pressure trends, including the rate of pressure reduction and the amplitude at the end of the transient blowdown, were virtually the same in both tests. The main difference between the two was that the minimum pressure following the initial rapid depressurisation in liquid was higher in test T05. The amplitude of the subsequent quasi-steady pressure was also higher in test T05 by about the same amount. Apart from the difference in the quasi-steady pressure between both tests (about 40kPa in the first 250ms) the measurements were practically identical. The deviations in the pressure trends in the first 50ms and between 650 – 850ms can be readily attributed to the limitations in precisely controlling the initial conditions.
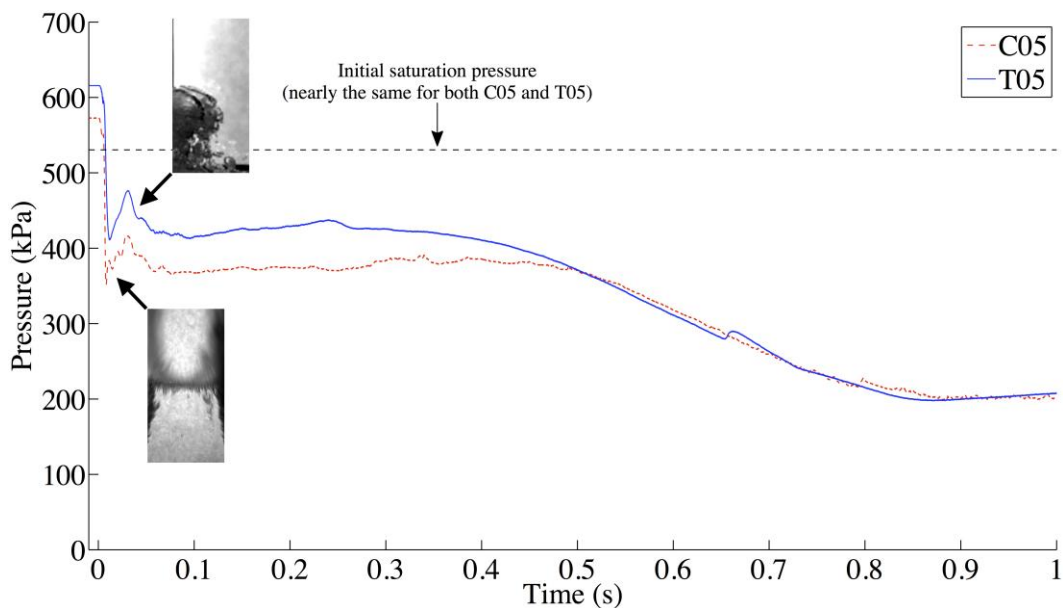
Figure 6-4. Comparison of pressure at location 1 (tests C05 & T05).

If the effect of the initial pressure on the transient amplitude were indeed important, then the transient amplitude in test T06 in Fig. 6-1 (initial pressure of 600kPa) would be higher than in tests C03 and C04 (initial pressures of 568kPa and 574kPa respectively). In fact, the opposite was observed, which was explained by the difference in the rate of vapour growth shown in Fig. 6-2. It was also shown in Fig. 6-1 that the discrepancies in the pressure amplitudes could be even greater than the 40kPa difference observed in Fig. 6-4.

The vapour generation mechanisms also appear to have played an important role in establishing the transient pressure amplitudes in tests C05 and T05. A high-speed flow visualisation snapshot of the vapour growth mechanism during the early stages of phase transition is provided for each of the two tests in Fig. 6-4. Vapour bubbles existed in the liquid before blowdown in test T05. These promoted a more rapid rate of vapour growth than in test C05, in which the vapour generation was largely restricted to the pressure vessel walls.

From the transient pressure measurements, it may be inferred that the quiescent liquid, which did not contain any bubbles prior to blowdown initiation (test C05), permitted a deeper penetration into the superheated regime before phase transition occurred. When gas bubbles were previously dispersed in the liquid (test T05), the transient vapour growth process was facilitated and occurred earlier in comparison. Hence, the point at which the pressure began to recover was higher. It is therefore entirely plausible that the higher initial interfacial area concentration, which led to increased vapour generation and growth activity, was responsible for the difference observed in the subsequent quasi-steady pressure amplitudes. It may be concluded then that the initial liquid pressure (subcooling) has no discernible effect on the transient pressures compared to the physical driver (heat transfer) of vapour generation and growth. The transient phase change phenomena had little effect on fluid loading of the tube bundles.

6.3. EFFECT OF THE INITIAL TEMPERATURE

The initial liquid saturation pressure, which depends on temperature, determines the subsequent fluid pressure during phase change to some extent. The impact of these effects on the pressure drop and fluid loading across the tubes was found to be negligible in these experiments. A comparison of the transient pressures measured at location 1 in tests C05 and T04 is presented in Fig. 6-5. The initial liquid temperatures were 17.5°C and 21.1°C respectively. Unlike the comparison in Fig. 6-4 in which the initial saturation pressures were nearly the same, the 3.6°C temperature difference results in initial liquid saturation pressures of 529kPa and 591kPa respectively.

The transient pressure amplitude in test T04 was consistently higher than in test C05 throughout the entire duration of the blowdown transient. The overall trends in both tests were very similar and the minor deviations in the local measurement details can be attributed to random effects and parameters that cannot
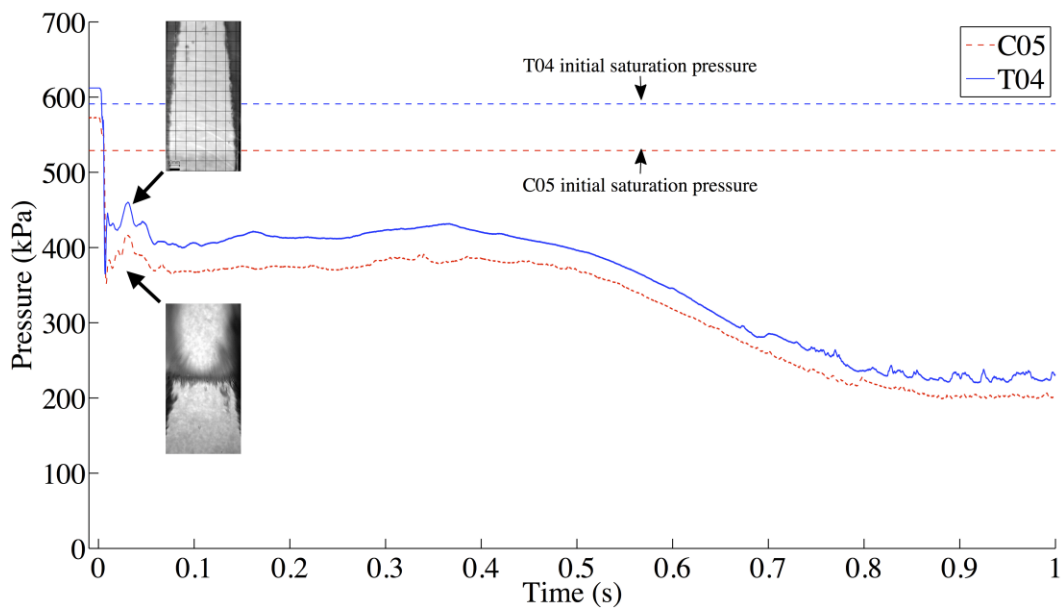
Figure 6-5. Comparison of pressure at location 1 (tests C05 & T04).

be precisely controlled. The vapour growth mechanisms observed in the high-speed images were also very similar for both tests. The liquid in both cases was initially quiescent and the bubble generation was largely restricted to the vessel walls.

The results indicate that, the vapour formation mechanisms being similar, a 3.6°C increase in initial liquid temperature, which corresponds to a 62kPa increase in the initial saturation pressure, may have an influence on the transient pressure amplitude during the blowdown. This influence of the initial temperature is not surprising given that it has also been encountered in similar blowdown experiments published in the literature (Pinhasi *et al.*, 2005).

The liquid flashing process begins when a sudden depressurisation brings a liquid from an initially subcooled state into a superheated state. The liquid depressurises to a level lower than the normal boiling pressure corresponding to its initial temperature (saturation) before explosive flashing to vapour is triggered. This phenomenon has been extensively studied in blowdown experiments performed using high-temperature high-pressure liquids and is commonly referred to as the 'pressure undershoot' (Edwards & O'Brien, 1970; Lienhard *et al.*, 1978).

The pressure undershoot is the difference between the saturation pressure of the liquid and the pressure level at which a reversal occurs due to the rapid phase transition from liquid to vapour, defined as the point of 'flashing inception'. The formation of the vapour phase and the subsequent bubble growth is related to the state of superheat in the ambient liquid. These transient phenomena depend significantly on the extent of the pressure undershoot.

Typically, vapour generation following a rapid depressurisation is modelled using homogeneous nucleation principles by attempting to reproduce experimentally measured pressure undershoots and pressure recovery amplitudes. Empirical 'heterogeneous factors' are employed, which correct for the level of superheat at which the pressure is minimum and allow better agreement with experimental results. Various pressure undershoot and heterogeneous factor

correlations can be found in the published literature (Alamgir & Lienhard, 1981; Barták, 1990; Deligiannis & Cleaver, 1992; Elias & Chambré, 1993).

For similar depressurisation rates and vessel geometries, the pressure undershoot was determined to be affected mainly by the initial saturation pressure, which is a function of the initial temperature only. The initial pressure was found to have no significant influence on the pressure undershoot level. The initial temperature was also determined to have the most important influence on the subsequent maximum amplitude of pressure recovery.

The initial saturation pressure determines to some extent how much liquid superheat is permissible during rapid depressurisation before liquid to vapour transition begins. In Fig. 6-5, the initial saturation pressure was higher in test T04 than test C05. The minimum pressure at the end of the initial depressurisation was also higher, by about 15kPa. The initial liquid temperature also plays an important role in establishing the rate of vapour generation and growth, which is controlled by heat and mass transfer between the liquid and vapour phases. The quasi-steady pressure in Test T04 was consistently about 40kPa higher than in Test C05, which is in agreement with the initial temperature conditions.

Similar phenomena have also been reported in experimental investigations of BLEVEs (Boiling Liquid Expanding Vapour Explosions). BLEVEs are explosions encountered in the process industries that involve the sudden failure of vessels containing pressurised liquids above their boiling points. An even more powerful blast is produced by BLCBEs (Boiling Liquid Compressed Bubble Explosions), which are similar to BLEVEs with the added effect of compressed gas bubbles in the liquid prior to depressurisation (Venart *et al.*, 1993). When a liquid is suddenly depressurised, its initial flow rate is limited by its inertia. Therefore, any creation of vapour while very little liquid has been expelled would substantially increase the pressure since the liquid is virtually incompressible. The distribution of compressed bubbles in the liquid amplifies this phenomenon and

results in higher pressure amplitudes. The pre-existence of compressed gas bubbles produces more violent phenomena, which may explain the higher pressure recovery amplitudes observed in Fig. 6-4.

The transient pressures at location 1 in tests C01 and T03 are compared in Fig. 6-6. Both tests were initiated with similar liquid inventories ($22 - 23\%$). The main difference was that the liquid in test C01 was initially saturated while the liquid in test T03 was initially 89kPa subcooled. The pressure transients were practically the same save for the duration of the blowdown process, which lasted about 180ms in test C01 and 200ms in test T03. Since the tube bundle was removed in both tests, the initial rate of fluid discharge through the full pipe cross-sectional flow area in both tests was very rapid. The initial liquid inventory was therefore unable to sustain the rate of vapour generation required to produce a recovery in pressure following the initial rapid depressurisation.

The fluid pressure decreased monotonically throughout the duration of the blowdown for both tests C01 and T03. Starting at about 80ms, the rates of vapour
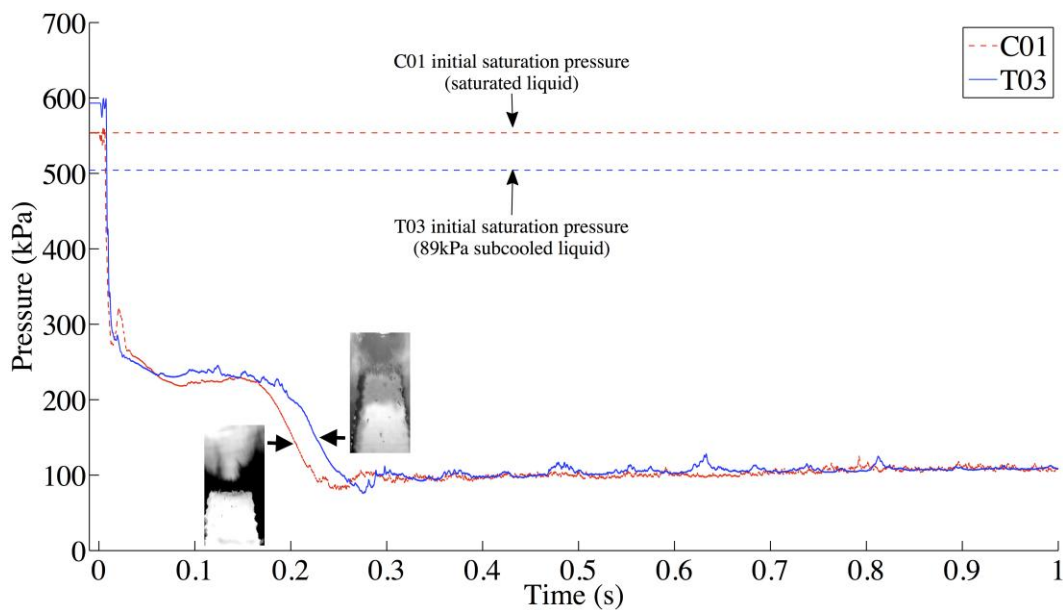
Figure 6-6. Comparison of pressure at location 1 (tests C01 & T03).

generation and fluid discharge cancelled each other out and the net effect was a nearly constant pressure amplitude for the next 100ms or so. The majority of the liquid inventory had been depleted by the end of this quasi-steady stage and the pressures dropped towards equilibrium conditions. If the effect of the initial liquid pressure were significant, then test T03, which was subcooled with an initial pressure of 593kPa, would have produced a higher rate of liquid flashing and a shorter blowdown duration. The opposite was observed in Fig. 6-6.

The duration of the transient was shorter for test C01, in which the liquid temperature was initially higher. Higher temperatures promote faster phase transitions, which produce a more rapid depletion of the superheated liquid. The liquid inventory in test C01 was slightly lower than in test T03, which would also shorten the duration of the blowdown. The vapour formation mechanisms observed in both tests were remarkably similar. The liquid was initially quiescent and the phase transition took place mainly at the pressure vessel walls. The darker shades represent two-phase plumes.

The effect of the initial conditions on the transient pressure amplitudes can be summarised as follows. The main factors that influence the rate of phase transition and the amplitude of pressure recovery in these experiments were related to the rate and mechanism of vapour generation. Pre-existing liquid-vapour interfaces in the liquid prior to blowdown initiation promoted faster phase transitions and higher pressure recovery amplitudes. This was due to the larger initial interfacial surface area available for phase transition, which resulted in greater heat and mass transfer between the liquid and vapour phases. When the vapour nucleation mechanisms were similar, the rate of liquid to vapour phase transition increased with temperature due to the higher amount of thermal energy available for heat transfer.

In these experiments, there was inevitably variability in the initial liquid pressures from one test to the next. This was due to factors such as the rupture disc

burst pressure tolerance, the liquid hydrostatic head variation, and the compressed gas pressure boost. Due to the insufficiency of experimental data and a lack of precise control over these independent parameters, the direct individual contribution of each was difficult to establish with absolute certainty.

The vapour generation mechanisms in the initial stages of the blowdown experiments played a significant role in determining the subsequent transient pressure amplitudes. When compressed gas pockets were introduced into the pressure vessel from the pressurisation lines, the increased interfacial surface area promoted a more vigorous phase transition and higher pressure amplitudes. The initial temperature of the liquid also affected the phase transition phenomena. However, the range of initial liquid temperatures (~7°C) was not enough to produce any substantial effects. The degree of initial liquid subcooling (pressure) had no discernible influence on the transient blowdown pressures. Overall, the variation in the initial conditions produced differences in the measurements that had no significant impact on the main phenomena of interest in this study.

6.4. EFFECT OF THE INITIAL LIQUID FILL

A comparison of the pressures measured in the pressure vessel below the rupture disc in tests T02, T03, and T07 is provided in Fig. 6-7. The top graph shows the measurements obtained at location 2, initially in vapour, and the bottom graph shows the measurements at location 1, initially in liquid. The three tests were performed with similar initial thermodynamic conditions, identical pressure vessel dimensions, and all of the tubes removed from the test section. The liquid surface heights from the bottom of the reservoir were 499mm, 290mm, and 129mm in tests T02, T03, and T07 respectively. These heights correspond to pressure vessel liquid volume fills of 39%, 23%, and 10% respectively. The initial liquid level for each test is illustrated on the right of Fig. 6-7.

By performing the tests with different initial liquid levels, the influence of the initial liquid volume on the transient blowdown pressures can be studied. A main difference observed between the pressures at both locations is that the rapid depressurisation begins at the same time in the vapour region, whereas the delay time for depressurisation in the liquid region increases with decreasing liquid volume. This is due to the wave propagation velocity, which is about 4 times faster in liquid than in vapour. A higher liquid surface results in faster wave propagation towards location 1. The depressurisation therefore begins earlier when the liquid surface in the pressurised reservoir is higher.

The rates and amplitudes of the depressurisations at location 2 are practically identical across all three tests, which is an indication of the excellent reproducibility and uniformity of the disc opening behaviour. The drop in pressure from about 600kPa to 300kPa is complete in approximately 4ms, which is about the duration for the full opening of the discs. The initial mass flow rate of the single-phase vapour discharge can be determined from Eq. (5-5). The mass flow
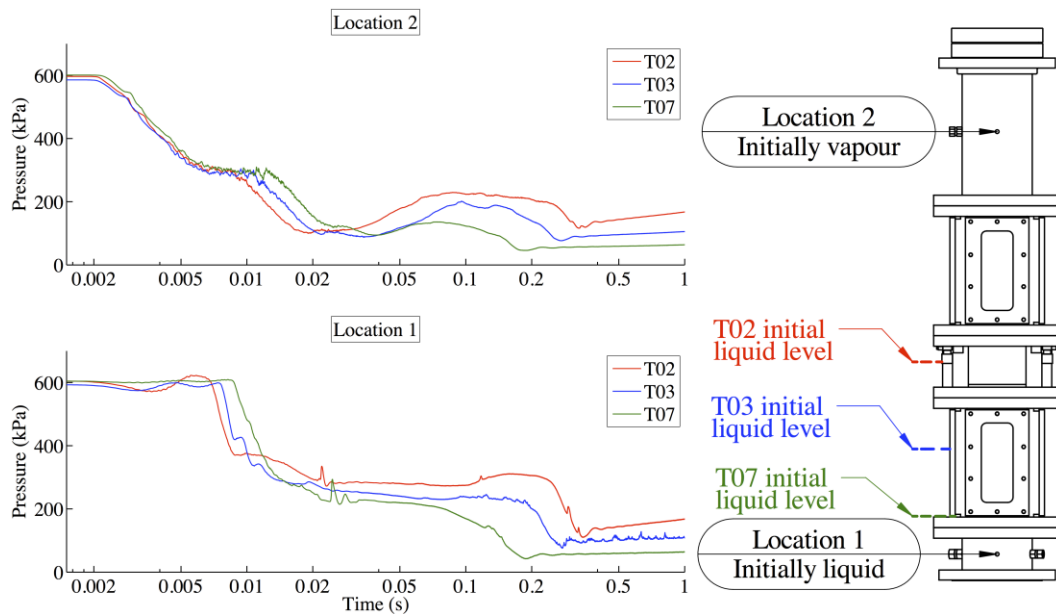
Figure 6-7. Transient pressure comparison (tests T02, T03, & T07), location 2 (top), location 1 (bottom).

rate changes as the vapour R-134a is discharged through the rupture disc and the pressure decreases to a temporary steady value of about 300kPa. The steady choked discharge can be determined from Eq. (4-7). The pressure decreases again when the discharge flow becomes subsonic, until the upstream accelerating flashing two-phase mixture arrives causing an increase in the pressure.

The time for flow transition from choked to subsonic is linearly proportional to the initial mass of vapour as shown in Eq. (4-14), if the initial conditions and choked flow rate are similar. An average choked flow rate, w_{av}, can be assumed as defined by Eq. (6-2),

$$w_{av} = \frac{dm_g}{dt_{trans}} \, , \qquad\qquad (6\text{-}2)$$

where dm_g represents the mass of vapour discharged in the time dt_{trans} between the opening of the rupture disc and the transition to subsonic flow. The initial mass of vapour R-134a was 0.41kg, 0.52kg, and 0.62kg in each of tests T02, T03, and T07 respectively. The transition times observed in Fig. 6-7 were about 8.9ms, 10.7ms, and 12.2ms respectively. This yields average discharge rates of 46.1kg/s, 48.6kg/s, and 50.8kg/s respectively, which are relatively similar. This indicates that the vapour discharge conditions were comparable in all three tests.

The volume of liquid in the pressure vessel determines to a certain extent the transient pressure amplitudes and the duration of the blowdown discharge. When the initial liquid inventory is smaller, less vapour is generated, and the overall pressure amplitudes are therefore lower. Similarly, smaller liquid inventories produce shorter blowdowns. Since the discharge flow area in all of the experiments is the same when the tube bundle is removed from the test section, the discharge rates are similar.

The quasi-steady pressure 'plateau' was less flat when the initial volume was lower since the rate of vapour generation could not be sustained to match the

rate of fluid discharge. Small pressure spikes were recorded at location 1 in test T02 at 22ms and test T07 at 24.5ms. These were presumably caused by vapour generation at the pressure transducer surface. This demonstrates the capability of the transducers to capture such rapid pressure time-scales associated with bubble nucleation phenomena.

By averaging the experimental results and obtaining representative quantities of the various fluid properties, the details of the effects of the fluid inventory on the discharge phenomena can be compared. The effect of the initial liquid volume on the blowdown pressure can be quantitatively investigated by averaging the transient pressure amplitudes with respect to the blowdown durations. An average pressure was computed by numerically integrating the area under the transient pressure curve and dividing by the time required for the pressure at both ends of the pressure vessel to equalise. The three pressure measurements at location 1 from tests T02, T03, and T07 are shown in Fig. 6-8 along with the calculated average pressure values (dashed lines). Unsurprisingly, the average pressure increases with increasing initial liquid volume. The average pressures calculated for tests T02, T03, and T07 were 271kPa, 219kPa, and 185kPa respectively. The average pressure computed in this manner was sensitive to the accumulation of R-134a discharged from the pressure vessel into the vacuum reservoir. The final equilibrium pressure was higher when the initial liquid volume was larger.

The transient pressure drop between locations 1 and 3 (the bottom of the vessel and above the rupture disc) is plotted in Fig. 6-9 for tests T02, T03, and T07. The corresponding calculated average pressure drops are also shown by the dashed lines. The transient pressure drop was obtained simply by subtracting the instantaneous pressure measured at location 3 from the simultaneous upstream pressure measured at location 1. Since the pressure downstream of the rupture disc was initially nearly 0kPa, the initial pressure drop at $t = 0$ is the same as the initial
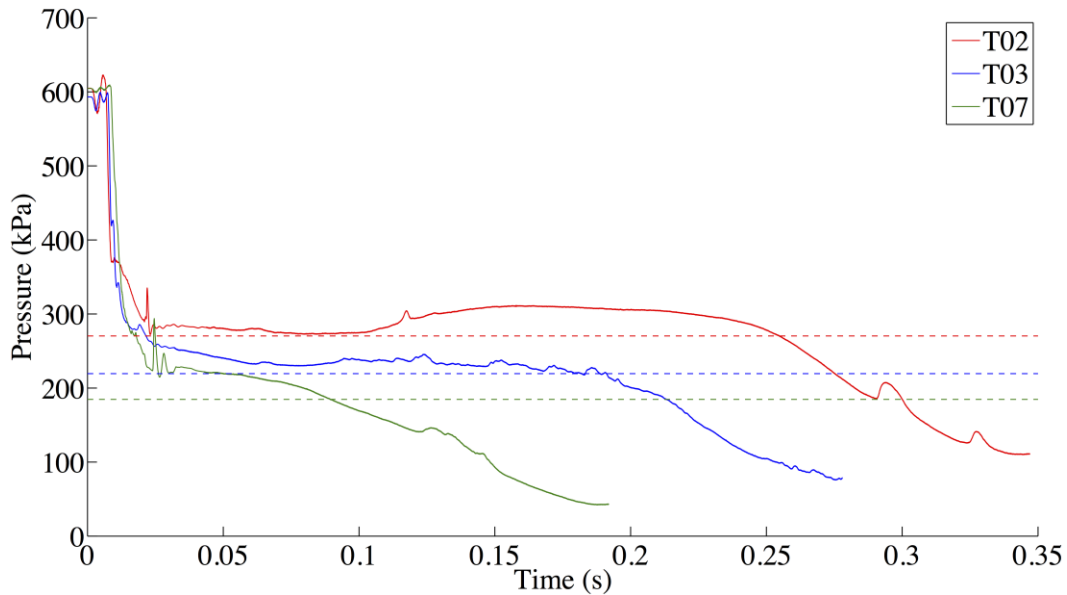
Figure 6-8. Measured transient pressure at location 1 (tests T02, T03, & T07) and calculated average

pressure (dashed line).

pressure in the pressure vessel. The pressure drop at the end of the transient, once the pressures at the two locations have equalised, converges to 0kPa.

The calculated average pressure drops were 121kPa, 107kPa, and 96kPa for tests T02, T03, and T07 respectively. Since the pressure vessel geometry and initial fluid conditions were practically the same for the three tests, the pressure drop depends mainly on the fluid mass flow rate during discharge. The calculated average pressure drop was normalised with respect to the duration of the discharge, which means that the average pressure drop will be nearly proportional to the initial R-134a liquid inventory if the average flow velocity does not significantly change. Accordingly, the relationship between the initial liquid inventory (39%, 23%, and 10%) and the average pressure drop (121kPa, 107kPa, and 96kPa) was found to be approximately linear.

The average pressure drop and the average mass flow rate can be related by the Bernoulli equation (neglecting losses) according to Eq. (6-3),
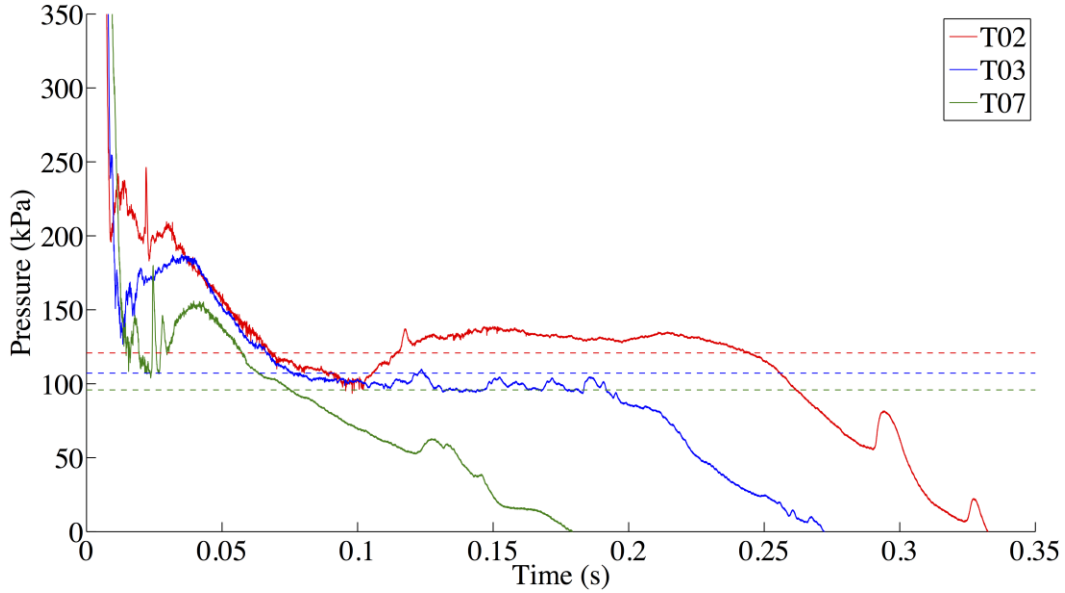
Figure 6-9. Measured transient pressure drop between locations 1 & 3 (tests T02, T03, & T07) and calculated average pressure drop (dashed line).

$$p_1 = p_3 + \frac{1}{2}\rho_{av}u_3^2 + \rho_{av}g\Delta H , \qquad (6\text{-}3)$$

where p_1 and p_3 are the pressures measured at locations 1 and 3 respectively, ρ_{av} is the average fluid density, u_3 is the flow velocity at location 3, g is the gravitational acceleration constant, and ΔH is the vertical distance between locations 1 and 3. Equation (6-3) can be rearranged as shown in Eq. (6-4),

$$w_{av} = A_{cs}\sqrt{2\left(\rho_{av}\Delta p_{1-3} - \rho_{av}^2 g\Delta H\right)} , \qquad (6\text{-}4)$$

where w_{av} is the average mass flow rate, A_{cs} is the cross-sectional flow area, and $\Delta p_{1\text{-}3}$ is the pressure drop between locations 1 and 3.

The average pressure drop can be determined as shown in Fig. 6-9, and an average mass flow rate can be computed by dividing the initial mass of R-134a in the pressure vessel over the time duration of the blowdown transient. Thus, an average density can be computed from Eq. (6-4) based on measured experimental

parameters. From the average pressure and average density, an equilibrium void fraction, ε, can be obtained according to Eq. (6-5),

$$\rho_{av} = \rho_l\left(1-\varepsilon\right) + \rho_g\varepsilon \,, \tag{6-5}$$

where ρ_l and ρ_g are the saturated liquid and vapour densities respectively. A homogeneous equilibrium speed of sound, c_H, can be computed from Eq. (5-4), from which a pseudo-single-phase homogeneous mass flow rate, w_H, can be computed as given by Eq. (6-6),

$$w_H = \rho_{av}c_H A_{cs} \,. \tag{6-6}$$

From the initial R-134a masses of 11.9kg, 7.2kg, and 3.6kg and blowdown durations of 347ms, 278ms, and 192ms in tests T02, T03, and T07, the average mass flow rates were estimated to be 34.2kg/s, 25.9kg/s, and 18.6kg/s respectively. The average densities computed for tests T02, T03, and T07 were 14.6kg/m^3, 9.4kg/m^3, and 5.4kg/m^3. The flow-averaged properties gave corresponding mass flow rate values of 28.2kg/s, 19.7kg/s, and 13.3kg/s. The homogeneous equilibrium treatment of the flow results in a 72% − 82% under-prediction of the estimated average mass flow rate. The homogeneous thermodynamic flow quality does not account for liquid superheat, which may under-predict the actual void fraction. Since the flow velocity increases with void fraction, the homogeneous flow calculation predicts lower flow velocities.

The transient normalised pressure ratio between locations 1 and 3 was computed from Eq. (6-1) and is plotted in Fig. 6-10 for tests T02, T03, and T07. The downstream pressure was initially about 0kPa and the pressure ratio is therefore equal to one at $t = 0$. The pressure ratio converges to zero as the upstream and downstream pressures equalise towards the end of the blowdown. The computed average pressure ratio is also shown for each of the three tests by a dashed line. The average ratio was similar for the three tests at about 0.417. This gives a downstream to upstream pressure ratio of 1 − 0.417 = 0.583.
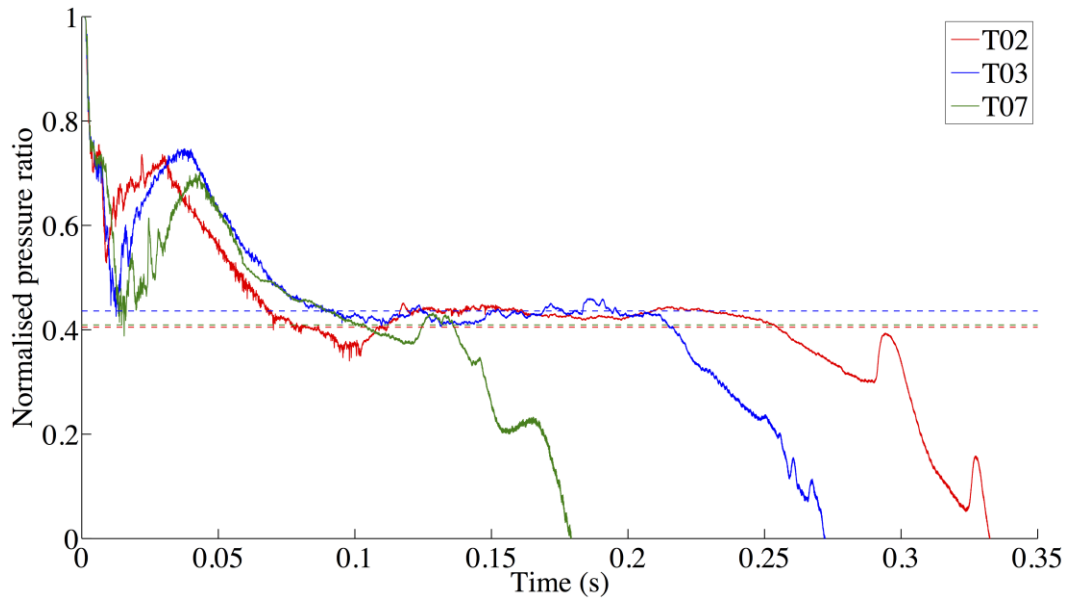
Figure 6-10. Measured transient normalised pressure ratio between locations 1 & 3 (tests T02, T03, & T07) and calculated average normalised pressure ratio (dashed line).

The critical pressure ratio, η, can be determined from Eq. (4-6) based on the computed average flow properties, where the specific heat ratio, γ, is defined according to Eq. (6-7),

$$\gamma = \frac{c_H^2 \rho_{av}}{p_{3,av}}.$$ (6-7)

The computed critical pressure ratios were 0.585, 0.583, and 0.583 for tests T02, T03, and T07 respectively. These values are within 1% of the average downstream to upstream pressure ratio measured in the three experiments. The pressure ratio was observed to remain constant at the average value between $90 - 250$ms in test T02, $90 - 200$ms in test T03, and $70 - 120$ms, in test T07. The agreement between the measured pressure ratios and the theoretical critical pressure ratios suggests that the R-134a discharge was choked during the quasi-steady discharge portion of these blowdown experiments. The computed average flow properties are

summarised in Table 6-1 and the corresponding pseudo-single-phase homogeneous flow properties are summarised in Table 6-2.

6.5. DISCUSSION OF TWO-PHASE FLUID DYNAMICS

In the present blowdown experiments, the blowdown discharge always occurs through the same uniform diameter of the opened rupture discs. The size of the discharge area has been identified in several previous experimental two-phase blowdown investigations to have a significant effect on the extent of thermal non-equilibrium between the two phases during the blowdown process (Winters & Merte, 1979). For slow depressurisation rates in vessels with relatively small discharge areas, the two-phase fluid expansion may be accurately represented by a homogeneous equilibrium model that assumes equal phase temperatures. The transient pressure in this case would be equal to the thermodynamic equilibrium saturation pressure corresponding to the two-phase fluid temperature. For small characteristic lengths however (small vessel volume to discharge break area ratio), the two-phase expansion rate may be high enough that thermal equilibrium cannot be maintained by heat and mass transfer between the liquid and vapour phases.

When a rapid transient blowdown occurs under thermal non-equilibrium conditions, the temperature of the liquid before it transitions to vapour remains higher than the saturation temperature corresponding to the local pressure conditions. The temporarily superheated liquid is defined to be in a 'meta-stable'

Table 6-1. Calculated average blowdown properties based on transient measurements.

Test	Initial liquid fill (%)	$m_{R\text{-}134a}$ (kg)	$\Delta t_{discharge}$ (ms)	$p_{1,av}$ (kPa)	$\Delta p_{1\text{-}3,av}$ (kPa)	$p_{3,av}$ (kPa)	w_{av} (kg/s)	Average pressure ratio (3:1)
T02	39	11.88	347	271	121	150	34.2	0.595
T03	23	7.21	278	219	107	112	25.9	0.564
T07	10	3.58	192	185	96	89	18.6	0.591

Table 6-2. Calculated properties based on flow-averaged homogeneous pseudo-single-phase treatment.

Test	ρ_{av} (kg/m^3)	ε (%)	x_{eq}	c_H (m/s)	w_H (kg/s)	γ	η
T02	14.6	99.48	0.52	106	28.2	1.097	0.585
T03	9.4	99.74	0.62	115	19.7	1.108	0.583
T07	5.4	99.95	0.87	135	13.3	1.107	0.583

state (Carey, 2008) and a thermodynamic phase equilibrium assumption would lead to an inaccurate description of the blowdown process. Pronounced thermal non-equilibrium phenomena have been noted in many published accounts of blowdown experiments available in the literature (Edwards & O'Brien, 1970; Lienhard *et al.*, 1978; Winters & Merte, 1979; Barták, 1990; Deligiannis & Cleaver, 1996; Hahne & Barthau, 2000; Reinke & Yadigaroglu, 2001).

Larger blowdown discharge areas produce greater departures from thermodynamic phase equilibrium. The reason is that the rate of depressurisation is controlled by the size of the vessel discharge area. Small discharge areas allow more time for the two phases to maintain thermal equilibrium during transient discharge, whereas large discharge areas result in faster depressurisations and discharge rates, promoting higher levels of non-equilibrium. Similarly, blowdowns initiated from pipes with identical diameters and discharge areas were found to exhibit greater departures from thermal phase equilibrium when shorter pipes were used (Winters & Merte, 1979). Smaller volumes result in higher rates of depressurisation, producing greater departures from thermal equilibrium. Non-equilibrium thermodynamic phenomena were also observed in the present experiments. The transient two-phase blowdown fluid dynamics are analysed in this section.

The analysis of transient thermal phenomena in the current experiments was made possible by temperature measurements obtained from rapid response thermocouples. Sample temperature measurements obtained for two different tests

(T02 and T03) at locations 1 and 2, the regions initially filled with liquid and vapour respectively, are presented in Fig. 6-11. The measurements indicate different transient temperatures of the liquid and vapour phases during the blowdown at the different points in the pressure vessel. The thermocouple signal fluctuations at location 1 at $50 - 280$ms in test T02 and $30 - 160$ms in test T03 represent temperature discrepancies between the boiling liquid and expanding vapour at the local measurement point.

The extent of thermal non-equilibrium during the blowdown can be determined by comparing the equilibrium saturation temperatures computed from local pressure measurements to the measured transient temperatures. When a two-phase fluid is in thermodynamic equilibrium, its temperature matches the saturation temperature corresponding to its pressure. The temperature of a superheated fluid is higher than the saturation temperature that corresponds to the fluid's pressure under thermodynamic equilibrium. Computed saturation temperatures are compared to the measured transient temperatures in tests T02 and T03 in Fig. 6-12.
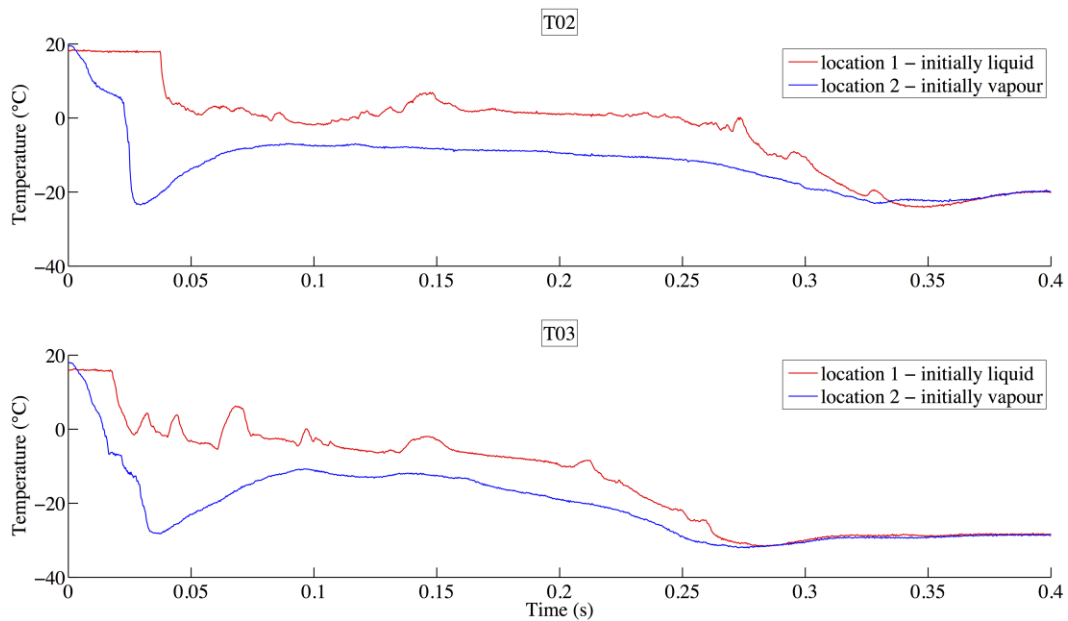
Figure 6-11. Measured transient temperatures at locations 1 & 2 (top: test T02, bottom: test T03).

Measurements from location 2, initially in vapour, are plotted in the top graph, and from location 1, initially submerged in liquid, are plotted in the bottom graph.

The comparisons demonstrate that in both locations, the fluid temperature approaches and then follows the saturation temperature corresponding to the local pressure. The temperature measured in the vapour region (location 2) drops rapidly immediately following the opening of the rupture disc as the single-phase superheated vapour depressurises. The vapour expansion results in a significant reduction in its temperature. The temperature stabilises briefly once the single-phase expansion is complete. The temperature then drops rapidly at 28ms in test T02 and 34ms in test T03 towards saturation conditions. These points coincide with the timing of the arrival of the two-phase flashing mixture front accelerating from the bottom of the pressure vessel. The agreement between the local temperatures and computed saturation temperatures indicate that the two-phase fluid is in a
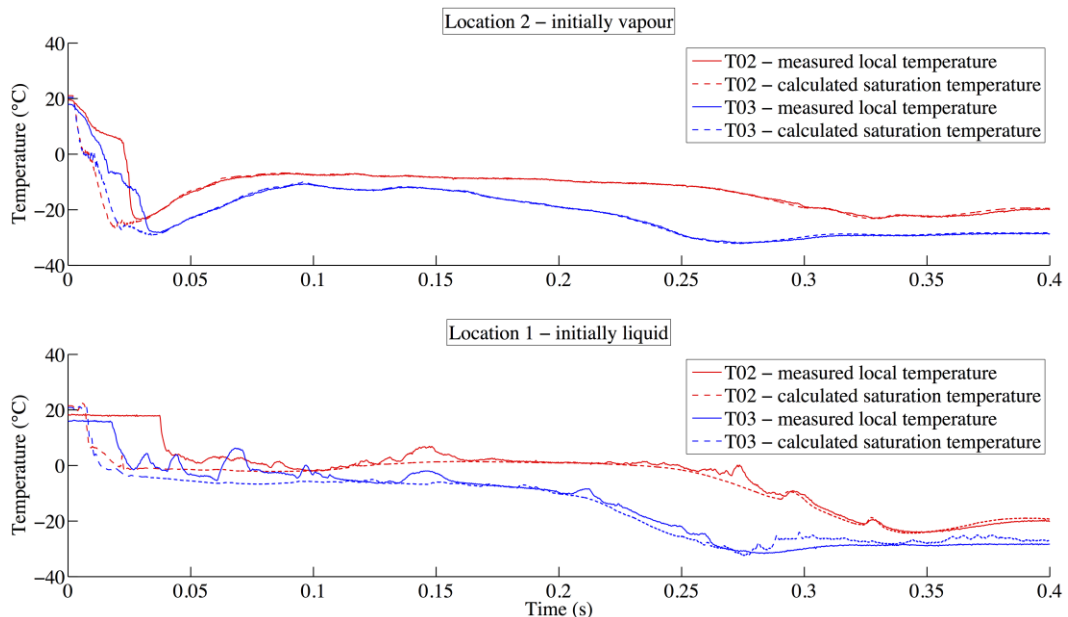
Figure 6-12. Comparison of measured temperature and calculated saturation temperature (tests T02 & T03): location 2 (top), location 1 (bottom).

saturated thermodynamic state. This condition is maintained for the remaining duration of the blowdown transient.

The liquid retains its temperature during the initial rapid transient phase of the depressurisation. After a brief time (17ms in test T03 and 37ms in test T02), the temperature measurement drops rapidly and approaches the saturation temperature corresponding to the local pressure. This rapid drop in temperature occurs some time following the initiation of liquid to vapour phase transition, during the vigorous vapour generation and growth stage. These observations can be explained by interpreting the physical measurement at the thermocouple point of contact with the fluid. The hot junction is surrounded by superheated liquid, which is in a non-equilibrium 'meta-stable' state, during the initial rapid transient depressurisation. Once the liquid in the thermocouple vicinity boils off, the temperature rapidly drops towards that of the vapour generated by liquid flashing, which is at the saturation temperature corresponding to the local pressure.

The response of the thermocouples was observed to be rapid. The measured temperature during the transient never dropped below the calculated saturation temperature. This is in agreement with the expected behaviour, since liquid subcooling is not possible during flashing. The vapour temperature was in perfect agreement with the saturated thermodynamic temperature corresponding to the local pressure conditions for the majority of the transient.

The rapid liquid depressurisation process can be idealised as an incompressible saturated liquid undergoing an isentropic expansion. For test T02, the change in the specific enthalpy of the liquid R-134a, dh_l/dt, can be determined from the energy equation according to Eq. (6-8),

$$\frac{dh_l}{dt} = T_l \frac{ds}{dt} + \frac{1}{\rho_l} \frac{dp}{dt} , \qquad (6\text{-}8)$$

where T_l is the liquid temperature, ds/dt is the change in entropy (0 for an isentropic expansion), ρ_l is the liquid density (1233kg/m³ at $T_l = 18.2°C$), and dp/dt is the depressurisation rate, which was determined from the experimental measurements to be 115.8MPa/s. From Eq. (6-8), dh_l/dt was determined to be 93.9kJ/kg·s. The change in the liquid temperature is given by Eq. (6-9),

$$c_P = \frac{dh_l}{dT_l} \, , \qquad\qquad (6\text{-}9)$$

where c_P is the specific isobaric heat capacity of the liquid R-134a (1.4kJ/kg·K). The liquid temperature change associated with the isentropic expansion was therefore estimated as 0.14°C.

The negligible temperature change calculated for a rapid isentropic depressurisation of an incompressible liquid corroborates the interpretation of the measurements in the first 37ms of Fig. 6-12 for test T02, where the rapid depressurisation in the liquid region was initially isothermal and the liquid remained superheated. This also indicates that the substantial rapid temperature drop at 37ms cannot be due to a change in the temperature of the liquid, and must be caused by the rapid liquid phase transition to vapour. Similar patterns have also been recorded in blowdown temperature comparisons with high-speed images (Deligiannis & Cleaver, 1996). The temperatures dropped when bubble nucleation was observed at the thermocouple tips, continued to decrease as the bubbles grew, and increased when the bubbles detached and departed. In some cases, no nucleation occurred at the thermocouples and the temperature remained constant until a two-phase front arrived at the thermocouple point.

The deviations from the saturation temperature in the present blowdown experiments were all in the superheated regime. This suggests that the thermocouple hot junction during these times was in contact with superheated liquid flowing towards the downstream vacuum reservoir. Due to the thermocouple response time characteristics and the transient nature of the phenomena, it cannot

be confirmed whether the temperatures recorded during these fluctuations were the actual liquid temperatures or somewhere in between the vapour and liquid phase temperatures.

The degree of transient superheat observed in the current experiments was as large as 20°C – 30°C. Experimental results available in the published literature indicate transient blowdown superheats of similar magnitudes. The rapid depressurisation of water initially at 290°C was observed to produce a pressure undershoot of 62°C superheat and a quasi-steady superheat of 37°C (Barták, 1990). Experiments using R-12 initially at 35°C produced transient superheats of 46°C and quasi-steady superheats of 20°C (Deligiannis & Cleaver, 1996). Vapour nucleation at the vessel walls did not affect the liquid superheat at the vessel centre-line. Thermal equilibrium models do not predict pressure undershoots below saturation and quasi-steady transient superheats (Winters & Merte, 1979). In order to represent rapid non-equilibrium two-phase fluid expansions physically, the local rates of heat and mass transfer associated with the transient phase transition must be properly accounted for.

6.6. EFFECT OF THE TUBE BUNDLE ON THE TRANSIENT BLOWDOWN PHENOMENA

The introduction of the tube bundle to the test section imposes a significant restriction to the flow during the transient blowdown. The effect of this restriction in the pressure vessel on the transient fluid dynamics is shown in Fig. 6-13. The graph presents a comparison of measured pressures and calculated saturation pressures in tests T02 (without tubes) and T05 (with six rows of tubes). Aside from the presence of the tube bundle, all of the experimental parameters and initial conditions were similar between tests T02 and T05. The initial pressures were 605kPa and 615.7kPa and the initial temperatures were 18.2°C and 17.7°C in tests T02 and T05 respectively.
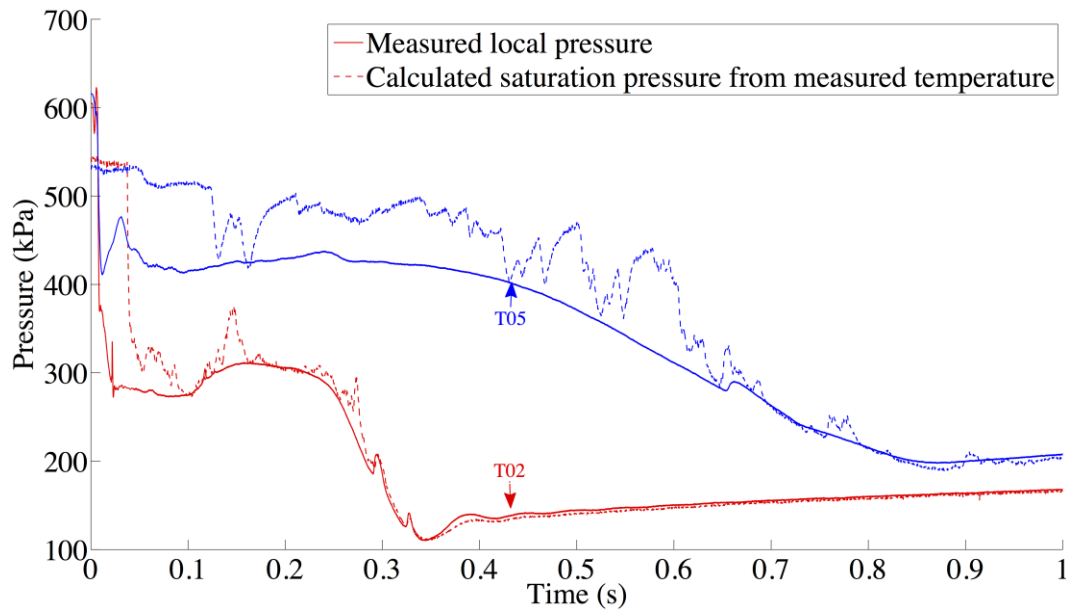
Figure 6-13. Comparison of measured pressures and calculated saturation pressures at location 1: test T02 without tube bundle, test T05 with tube bundle.

The main influence of the tube bundle was the significant reduction in the discharge rate of the R-134a below the tubes. The result was increased mass hold-up, a higher pressure amplitude during fluid discharge, a longer transient blowdown duration, and an extended quasi-steady pressure 'plateau' during discharge. The rate of depressurisation towards final equilibrium conditions was also slower. During the quasi-steady stage of the blowdown, which lasted until about 350ms into the blowdown, the rate of pressure increase due to vapour generation matched the rate of fluid discharge through the tube bundle. When the tube bundle was removed from the test section, the quasi-steady discharge condition existed for only about 200ms, after which the rate of vapour generation could not be sustained to match the higher rate of fluid discharge.

Similar observations are documented in the literature, for rapid two-phase expansions from pipes with varying volume to discharge area ratios (Winters & Merte, 1979). Smaller ratios (larger discharge areas) resulted in lower pressure plateaus during transient discharge. This was attributed to greater departures from

thermodynamic equilibrium between the liquid and vapour phases. Under significant thermal non-equilibrium conditions, the rate of vaporisation would be slower relative to the rate of discharge, which results in pressures much lower than the saturation pressures corresponding to the initial temperatures. In contrast, when the rate of discharge is sufficiently reduced, vapour generation and mixing between the two phases allows the pressure to recover to higher amplitudes up to the saturation pressure for thermal equilibrium conditions.

The reduced rate of fluid discharge through the tube bundle in test T05 was responsible for the observed increase in the blowdown duration. Since the tube bundle controls the depressurisation rate, the rate of vapour formation was also slower when the tube bundle was inserted (T05) compared to the unobstructed pipe blowdown case (T02). Because of the reduced intensity of the phase transition activity, the thermocouple in test T05 seemed to remain in contact with superheated liquid for longer periods throughout the transient. Thermocouple output dips recorded in test T05 at 162ms, 430ms, 525ms, and 647ms matched the computed saturation pressure. This indicates that the vapour generated below the tubes during the transient was in a saturated thermodynamic state.

Occasionally, the observed amplitude of the sudden thermocouple measurement dips was not large enough to reach the saturation pressure. This occurred at 131ms, 467ms, and 548ms. The most plausible explanation is that the dips in thermocouple output represent vapour bubbles flowing past the thermocouple junction. When the bubbles flow past fast enough that the transient output signal has not yet fully responded, the signal recovers towards the superheated liquid temperature before reaching the saturation point.

A better agreement between the measured and calculated pressures was observed in test T02. This is likely due to the higher degree of superheat at the point of vapour formation and the subsequent higher rate of vapour formation, which would result in a greater activation of nucleation sites. This increases the

likelihood of the thermocouple junction itself serving as a nucleation site. The thermocouple output was observed to remain at saturation for longer periods during the transient, with occasional upward spikes. The saturated temperature would indicate vapour growth, and the superheated temperature would represent bubble departure and thermocouple contact with liquid. The temperature never dropped below saturation since it was impossible for either of the two phases to become subcooled during the rapid depressurisation.

During the bubble growth process, heat transfer from the liquid causes vaporisation at the bubble interface. The rate of growth of the bubble is controlled by inertia when the liquid superheat is sufficiently high. In this case, heat is transferred across the bubble wall faster than the bubble can expand and the process is controlled by the pressure of the vapour pushing the surrounding liquid away. Under constant ambient pressure conditions, inertia is only important in the first few microseconds of bubble growth. For rapidly decreasing pressures however, inertia can continue to be an important limiting factor well into the bubble growth process (Winters & Merte, 1979).

In Fig. 6-13, test T02 measurements indicate that the vapour temperature becomes saturated with respect to the ambient pressure about 0.1s after the initiation of the blowdown. Prior to this time, the thermocouple measurement appears to indicate that the pressure of the saturated vapour is higher than the surrounding liquid pressure. Such a pressure difference would exist during inertia-controlled bubble growth when a higher bubble pressure is required to accelerate the surrounding liquid. For inertia-controlled bubble growth, the pressure of a vapour bubble, p_b, can be evaluated according to the linearised form of the Clapeyron equation given by Eq. (6-10) (Carey, 2008),

$$p_b = p_a + \frac{\rho_g h_{lg} \left[T_g - T_{sat}(p_a) \right]}{T_{sat}(p_a)}, \qquad (6\text{-}10)$$

where p_a is the ambient pressure (280kPa), ρ_g is the vapour density, h_{lg} is the latent heat of vaporisation, T_g is the vapour temperature (275K), and $T_{sat}(p_a)$ is the saturation temperature corresponding to the ambient pressure (272K). The pressure was determined from Eq. (6-10) as 310kPa, which is in good agreement with the saturation pressure indicated by the thermocouple measurement. Hence, the discrepancy between the pressures in the first 0.1s of bubble growth in test T02 is due to inertial effects.

The surface area of the dynamic pressure transducer is large relative to the growing bubbles. This means that it is probably at least partially wetted during the vigorous phase transition stage. The dynamic pressure measurement is therefore more likely to be a representation of the continuous liquid phase pressure. At about 0.025s, a brief pressure spike was observed that was possibly caused by bubble nucleation phenomena. Once the pressure difference between the vapour bubbles and the surrounding liquid diminishes, the bubble growth process becomes controlled by heat diffusion through the bubble wall. The saturation pressure of the vapour during this stage matches the ambient pressure and the extent of thermal non-equilibrium between the liquid and the vapour determines the bubble rate of growth.

The 'degree of non-equilibrium' may be quantified by the Jakob number, which is essentially the ratio of the sensible heat absorbed during vaporisation to the latent heat energy. The Jakob number, Ja, is defined during a rapid depressurisation according to Eq. (6-11) (Pinhasi *et al.*, 2005),

$$\text{Ja} = \frac{\rho_l c_{pl} \left(T_{sat,l} - T_{sat,g} \right)}{\rho_g h_{lg}}, \tag{6-11}$$

where ρ_l is the liquid density, c_{pl} is the liquid specific heat capacity, $T_{sat,l}$ is the initial liquid saturation temperature (295K in T02 and 296K in T05), $T_{sat,g}$ is the saturation temperature of the vapour phase (273K in T02 and 283 in T05), ρ_g is the

vapour density, and h_{lg} is the latent heat of vaporisation. The Jakob number was estimated to be 15.2 for test T02 and 6.2 for T05, which further supports the interpretation of a greater degree of non-equilibrium and a higher rate of vapour growth in test T02.

Vapour nucleation is an inherently random phenomenon. In some cases, the temperature in the liquid region did not converge towards the saturation temperature until near the end of the transient blowdown. An example obtained in test T09 is shown in Fig. 6-14. The liquid remained at the initial superheated temperature for virtually the entire blowdown duration. The level of superheat during the transient blowdown was between 8°C – 13°C. The signal indicates that no nucleation took place at the thermocouple junction and that the thermocouple was in contact with superheated liquid for the entirety of the blowdown.

The two-phase flow composition observed in the high-speed images was markedly different below and above the tubes (refer to Figs. 5-2 and 5-3). A two-
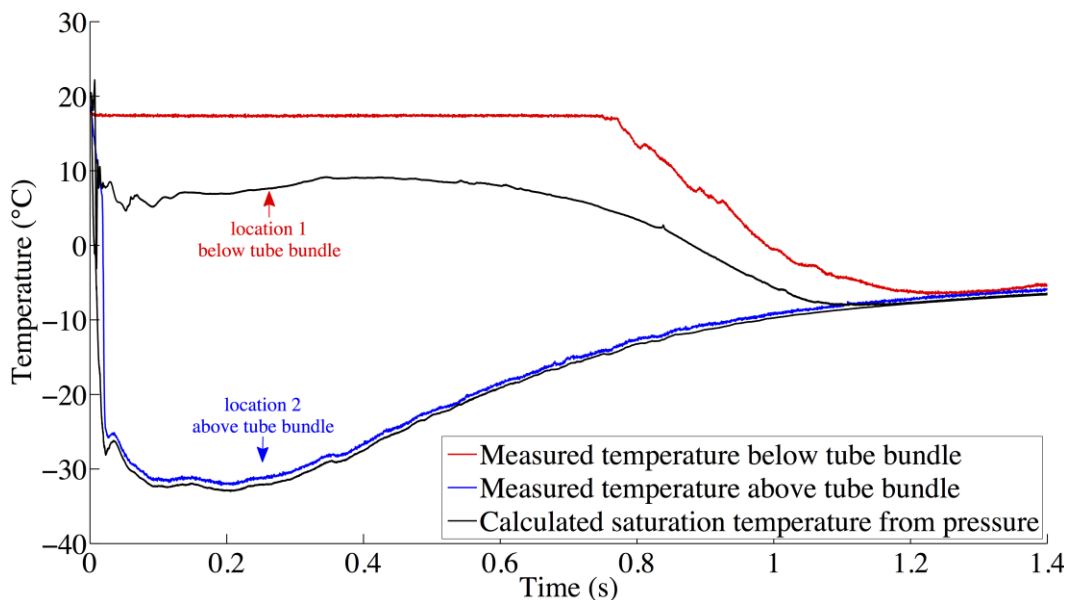
Figure 6-14. Comparison of measured temperature and calculated saturation temperature at locations 1 & 2 (test T09).

phase mixture, which was in a saturated thermodynamic state, was rapidly established downstream of the tube bundle. This is demonstrated by the agreement between the measured and calculated temperatures at location 2. Below the tubes, the liquid remained superheated throughout the transient. This indicates that even with the reduction of the discharge rate due to the restriction imposed by the tube bundle, the extent of departure from thermal equilibrium was significant in these experiments. The physical modelling of such non-equilibrium transient two-phase phenomena is very difficult and beyond currently available numerical capabilities.

A high-speed image sequence of the blowdown discharge flow filmed above the tubes in test C05 is presented in Fig. 6-15. The images provide insight into the two-phase mixture composition at the exit of the tube bundle towards the final stages of the transient. The pressure measurement downstream of the tube bundle is also shown in Fig. 6-15. The first image at t = 0.35s appears to show a homogeneous fluid mixture with dispersed liquid droplets.
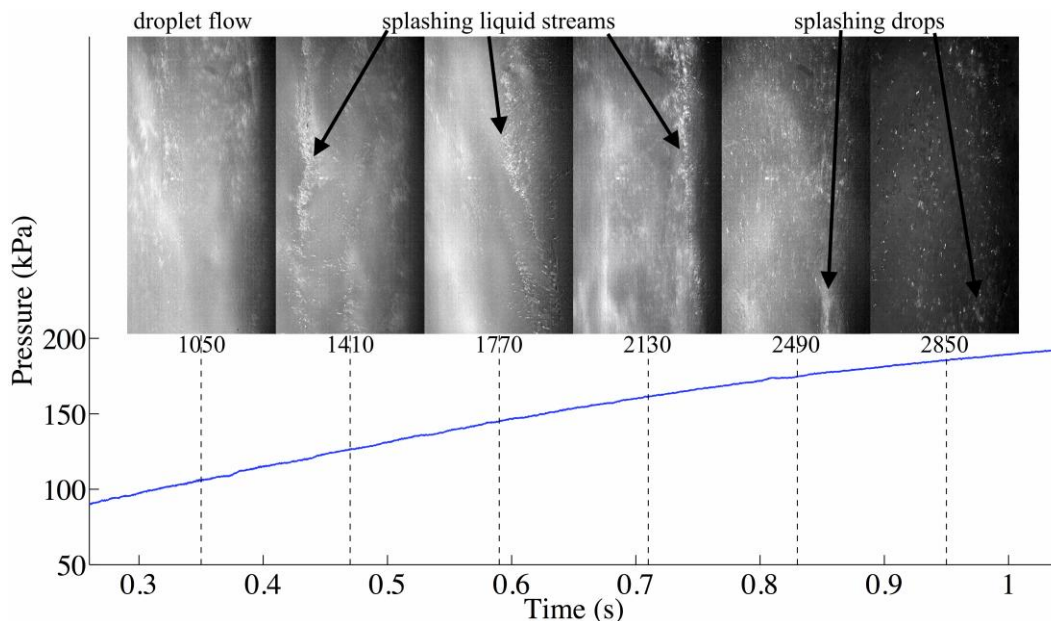
Figure 6-15. High-speed image sequence of transient two-phase mixture downstream of the tube bundle and pressure measurement at location 3 (test C05).

The images from $t = 0.47$s to $t = 0.71$s show entrained liquid streams in the discharging two-phase mixture, which splash against the glass windows as the fluid flows upwards towards the downstream vacuum reservoir. This behaviour suggests that the two-phase fluid is choked at the tube bundle. The fluid mixture maintains a distinct liquid-vapour composition, which passes through the tube bundle and emerges with the flow pattern observed. It seems that the reduction from the initial rate of vapour generation upstream of the tube bundle results in more liquid entrainment in the final stages of the blowdown.

The void fraction seemingly increases around $t = 0.83$s. Towards the end of the transient, at $t = 0.95$s, the two-phase mixture appears to consist mainly of high-quality vapour flow, with dispersed liquid droplets visible mostly towards the outside perimeter of the cross-sectional flow area. The continuous medium throughout the transient is observed to be the vapour phase, which explains the saturated thermodynamic measurements downstream of the tube bundle.

A comparison of the rates of vapour formation and growth observed in the high-speed flow visualisations in tests T03 (without the tube bundle) and T06 (with six rows of tubes) is shown in Fig. 6-16. The images are presented in 6ms time-steps, starting with the point of phase transition initiation. In both tests, the liquid surface was initially visible through the lower window below the tube bundle. The images demonstrate the influence of the tube bundle on the rate of vapour growth. Two-phase plumes develop rapidly in test T03, covering the entire viewing area by the fifth frame. The rate of vapour growth is faster than in test T06. Even with pre-existing vapour bubbles distributed in the liquid in the first and second frames (which provide increased interfacial surface area for phase transition), the rate of vapour growth over the 30ms segment shown in test T06 does not keep up with that observed in test T03. This confirms that the tube bundle controls the rate of discharge and vapour formation in the region upstream of the tubes.

(a) Test T03: lower window, 0 rows of tubes above

(b) Test T06: lower window, 6 rows of tubes above
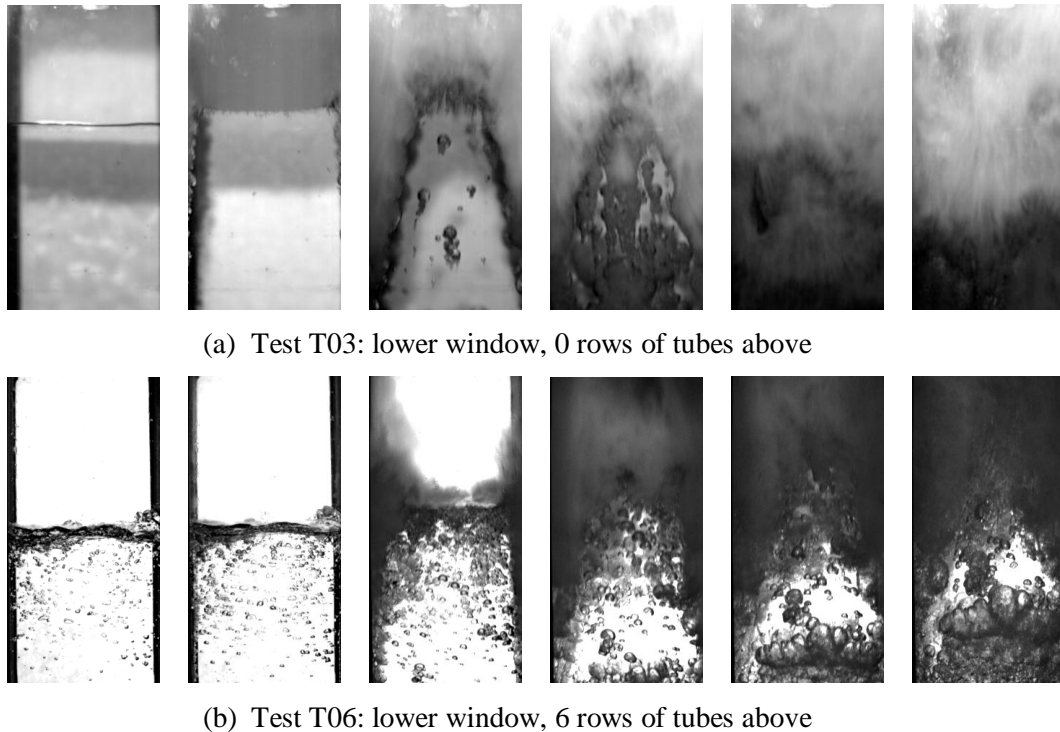
Figure 6-16. High-speed image sequence of vapour growth rate (6ms time-steps): (a) T03, (b) T06.

High-speed image sequences observed through the upper window in tests C05 and T05 are presented in Fig. 6-17. This enables a comparison of the rates of vapour generation when the initial liquid free surface was above the tube bundle. The images are presented in 6ms time-steps beginning with the initiation of phase transition. Six rows of tubes were mounted in the test section in both of the experiments. Since the liquid R-134a in this region was directly exposed to the full break area of the rupture discs without any obstruction in between, the vapour generation rates were virtually identical.

An accelerating two-phase mixture appears at the bottom of the third frame in both tests, which had originated at the surface of the tubes in the tube bundle below. The rate of vapour growth in this region is not influenced by the presence of the bundle. This further validates that the tube bundle only affects the pressure drop across the tubes and the vapour generation rate upstream.
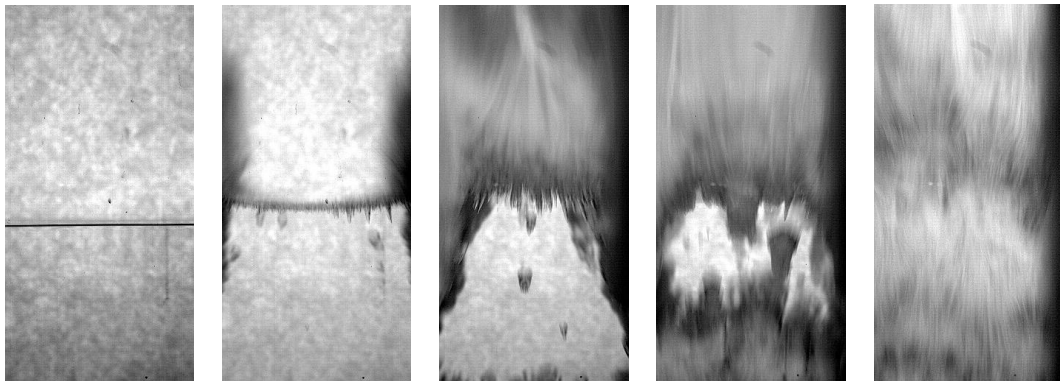
(a) Test C05: upper window, tube bundle below
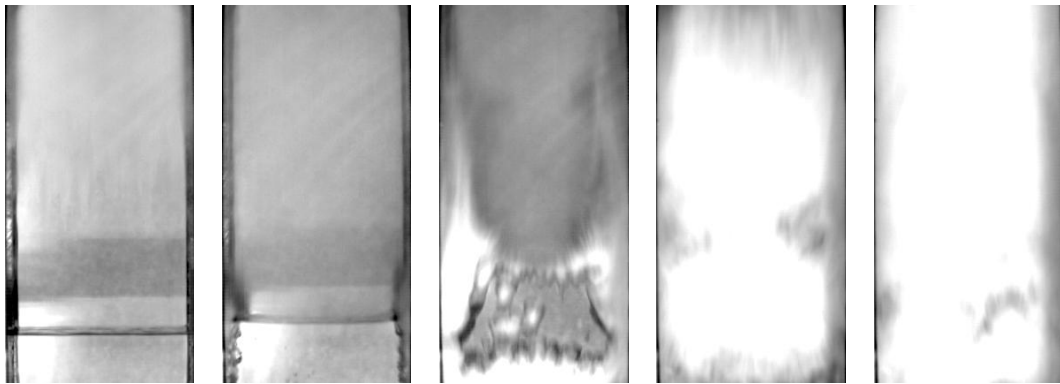
(b) Test T05: upper window, tube bundle below

Figure 6-17. High-speed image sequence of vapour growth rate (6ms time-steps): (a) C05, (b) T05.

A comparison of the measurements obtained at location 1 in tests T03 and T06 is presented in Fig. 6-18. When the tube bundle was removed (T03), the transient blowdown duration was shorter and the rate of vapour generation was higher. The temperature measurements indicate increased phase transition and vapour nucleation activity at the thermocouple junction in test T03. In contrast, the thermocouple trace in test T06 appears to remain in contact with superheated liquid for longer.

The phase transition activity was observed to be less pronounced in test T06 when the rate of depressurisation and phase transition was controlled by the flow restriction of the downstream tube bundle. The pressure upstream of the tubes started to increase at about 35ms. This corresponds to the time when the vapour
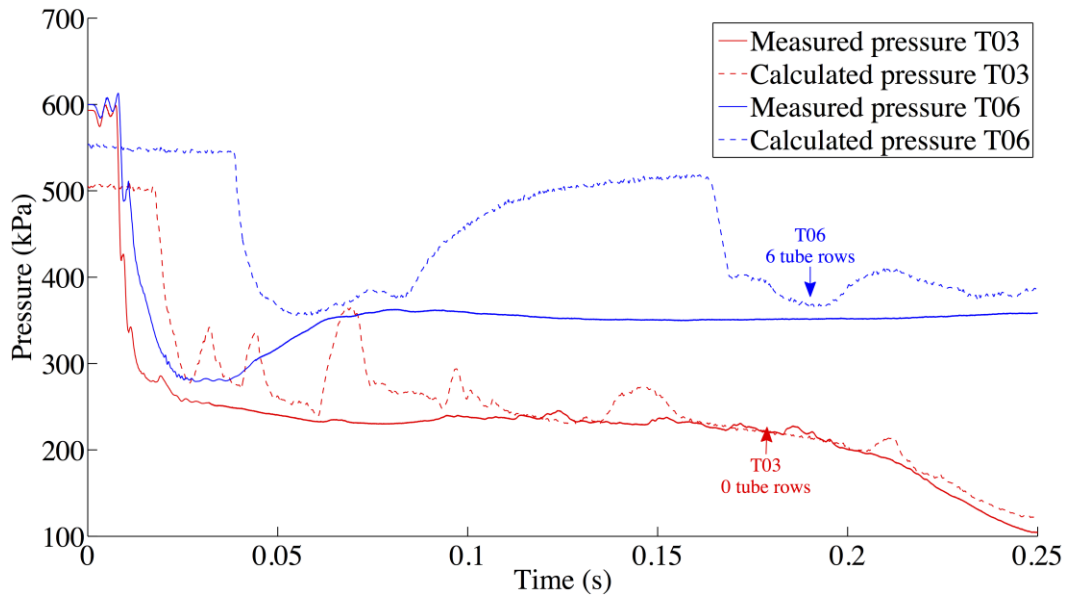
Figure 6-18. Comparison of measured pressures and calculated saturation pressures at location 1 (tests T03 & T06).

expansion rate exceeds the fluid discharge rate. At this point, the two-phase fluid mixture accelerates through the tube bundle. The pressure drop across the tubes is then controlled by the tube bundle for the remainder of the transient blowdown. These measurements corroborate the interpretations of the high-speed image observations in Fig. 6-16.

6.7. DISCUSSION OF THE PRESSURE DROP ACROSS THE TUBE BUNDLE

The total pressure drop of a two-phase fluid flowing in cross-flow over a tube bundle is composed of the total changes in the potential energy, the kinetic energy, and the skin friction or form drag losses. At high Reynolds numbers, the skin friction is negligible compared to the form drag. The steady pressure drop can be analytically formulated using the homogeneous model, which assumes that the liquid and vapour phases are in thermal and mechanical equilibrium such that the

velocity and density can be averaged across the cross-sectional flow area. The total two-phase pressure drop, Δp_{total}, is the sum of the gravitational component (hydrostatic elevation head), Δp_{static}, the accelerational component (momentum flux), Δp_{mom}, and the form drag component, Δp_{drag}, as given by Eq. (6-12) (Collier & Thome, 1994),

$$\Delta p_{total} = \Delta p_{static} + \Delta p_{mom} + \Delta p_{drag} \,. \tag{6-12}$$

For a homogeneous two-phase fluid, the static pressure drop, Δp_{static}, is given by Eq. (6-13),

$$\Delta p_{static} = \rho_H gH \sin\theta \,, \tag{6-13}$$

where ρ_H is the homogeneous density, g is the gravitational acceleration, H is the total height of the flow channel, and θ is the angle of elevation. The homogeneous density can be determined from Eq. (6-5). The two-phase mixture void fraction, ε, is given by Eq. (6-14),

$$\varepsilon = \frac{1}{1 + \left(\dfrac{u_g}{u_l} \dfrac{(1-x)}{x} \dfrac{\rho_g}{\rho_l} \right)}, \tag{6-14}$$

where u_g and u_l are the vapour and liquid phase velocities respectively, and x is the thermodynamic quality. At very low void fractions, the static pressure drop for non-zero angles approaches the liquid hydrostatic head, and at high void fractions and flow rates, the static pressure drop is usually negligible due to the relatively low vapour densities.

The accelerational pressure drop reflects the change in the kinetic energy of the flow due to the dynamic change in the vapour quality. The homogeneous pressure drop between the flow inlet and outlet planes due to the change in the momentum flux, Δp_{mom}, is given by Eq. (6-15),

$$\Delta p_{mom} = G_{total}^2 \left\{ \left[\frac{(1-x)^2}{\rho_l(1-\varepsilon)} + \frac{x^2}{\rho_g \varepsilon} \right]_{outlet} - \left[\frac{(1-x)^2}{\rho_l(1-\varepsilon)} + \frac{x^2}{\rho_g \varepsilon} \right]_{inlet} \right\}, \qquad (6\text{-}15)$$

where G_{total} is the overall two-phase mixture mass flux. This pressure drop term is caused by the change in the two-phase flow quality and would not arise in a pure liquid or gas phase where the velocity (and hence momentum flux) is constant. If there is no change in two-phase flow quality along the length of the conduit and through the tube bundle, and no resultant change in the homogeneous density, then the contribution of the momentum pressure drop to the overall pressure drop reduces to zero.

The form drag pressure drop of an external two-phase flow past a bluff body such as a bank of tubes is related to the flow dynamic head and is given by Eq. (6-16),

$$\Delta p_{drag} = \frac{C_{drag} A_p}{2} \rho_H u_H^2, \qquad (6\text{-}16)$$

where C_{drag} is the flow drag coefficient and A_p is the projected area. The drag coefficient is empirically determined and is a function of the Reynolds Number, Re, which is given by Eq. (6-17),

$$\text{Re} = \frac{G_{total} d}{\mu_H}, \qquad (6\text{-}17)$$

where μ_H is the homogeneous two-phase viscosity defined by Eq. (6-18),

$$\mu_H = x\mu_g + (1-x)\mu_l, \qquad (6\text{-}18)$$

where μ_g and μ_l are the single-phase vapour and liquid viscosities respectively. A number of alternative two-phase viscosity definitions are provided in the literature, which produce better agreement with experimental results for specific flow

conditions. The dependence of the pressure drop on the choice of viscosity definition is generally small (Collier & Thome, 1994).

The transient pressure drop measured between locations 1 and 2 (across the test section) and locations 2 and 3 (across the rupture disc) in test T04 is shown in Fig. 6-19. The initial liquid level was above the tube bundle in this experiment. The initial steady-state pressure drop of 14kPa across the test section consists of the elevation head of the R-134a (10kPa) and the pressure boost supplied by the compressed gas accumulator just before disc rupture (4kPa). The static pressure drop decreases with the initiation of the blowdown as the pressure is relieved through the rupture disc and the fluid density is reduced by rapid phase transition from liquid to vapour.

The initial pressure drop across the rupture disc was equivalent to the absolute vessel pressure of 598kPa since the region downstream of the rupture disc was initially in a vacuum with a pressure of nearly 0kPa. The opening of the rupture disc results in a rapid discharge of the saturated vapour directly upstream. The downward propagation of the rarefaction wave decreases the pressure drop
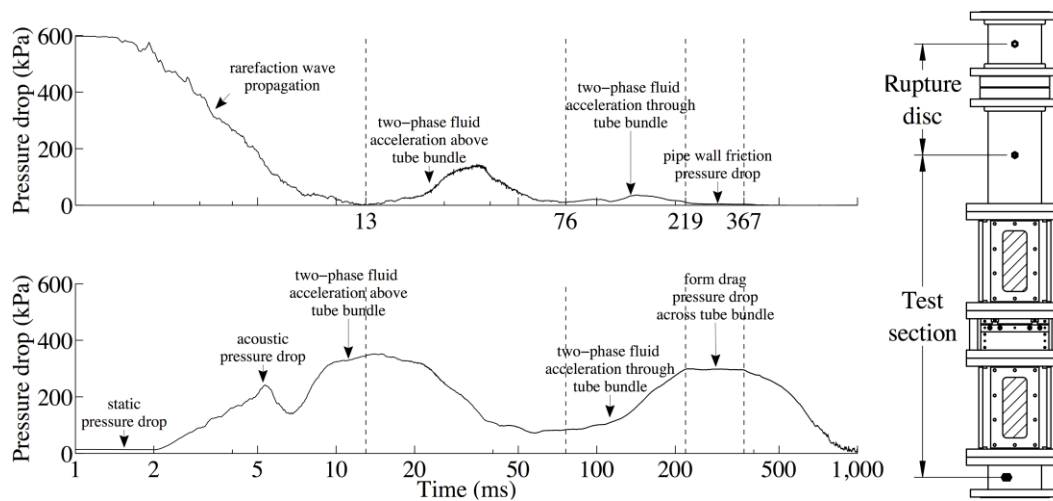
Figure 6-19. Transient pressure drop measured along the pressure vessel with the tube bundle installed (test T04), across the rupture disc (top), across the test section (bottom).

across the rupture disc to a minimum at about 13ms, at which point most of the single-phase saturated vapour has been discharged through the rupture disc.

The upstream propagation of the rarefaction wave produces an unsteady pressure drop across the test section, which is labelled as the 'acoustic' pressure drop. The transient pressure drop begins to rise at about 2ms, when the rarefaction wave passes location 2 (above test section), and peaks at about 5ms, when the wave arrives at location 1 (below test section). The pressure drop then begins to decrease due to liquid depressurisation. Following the arrival of the rarefaction wave, the liquid R-134a flashes to vapour and accelerates upwards, resulting in a rise in the two-phase pressure drop caused by the change in the fluid momentum flux.

The increase in the accelerational pressure drop begins at about 7ms across the test section and about 13ms across the rupture disc. The peak in the accelerational pressure drop across the test section also occurs at about 13ms. The increase in the pressure drop was caused by the upward acceleration of the flashing two-phase fluid front that had originated at the liquid surface above the tubes. The measurements indicate that this accelerating two-phase front passes the pressure transducer at location 2 at about 13ms.

The flow restriction imposed by the tube bundle limits the rate of the depressurisation and discharge below the tubes. The acceleration of the liquid below the tubes is limited by its inertia. When the average mass flux downstream of the tube bundle begins to equalise and the accelerational pressure drop component begins to drop (at about 21ms and 37ms across the test section and rupture disc respectively), the blowdown discharge through the tube bundle begins in earnest and the two-phase fluid below the tubes accelerates upwards.

Viscous effects in the test section become dominant beginning at about 76ms until the end of the transient. During this time, the pressure drop across the rupture disc was comparatively negligible since friction at the pipe wall is small relative to the hydraulic drag at the tube bundle. The drag pressure drop across the

tube bundle equalises at about 219ms. A quasi-steady flow discharge condition is then established with a maximum velocity and pressure drop across the tube bundle, which is greater than 300kPa. The pipe wall friction downstream of the tube bundle diminishes when the discharge flow reaches this quasi-steady state.

When the tube bundle is removed from the test section, the viscous fluid resistance (friction) along the pressure vessel wall becomes uniquely responsible for the pressure drop during quasi-steady discharge. An example from test T02 is shown in Fig. 6-20. The initial liquid free surface was at the test section level in this experiment. The tubes were all removed and the pressure vessel was essentially a uniform cross-sectional area pipe. The trends in the pressure drop across the test section and rupture disc regions were similar to those observed in Fig. 6-19, the difference being that the form drag losses in the tube bundle did not appear in the measurements.

The pressure difference across the rupture disc remained constant at about 130kPa from about 9ms to about 12ms. This is associated with single-phase vapour discharge choking. The peak in the 'acoustic' pressure drop occurred at about 7ms,
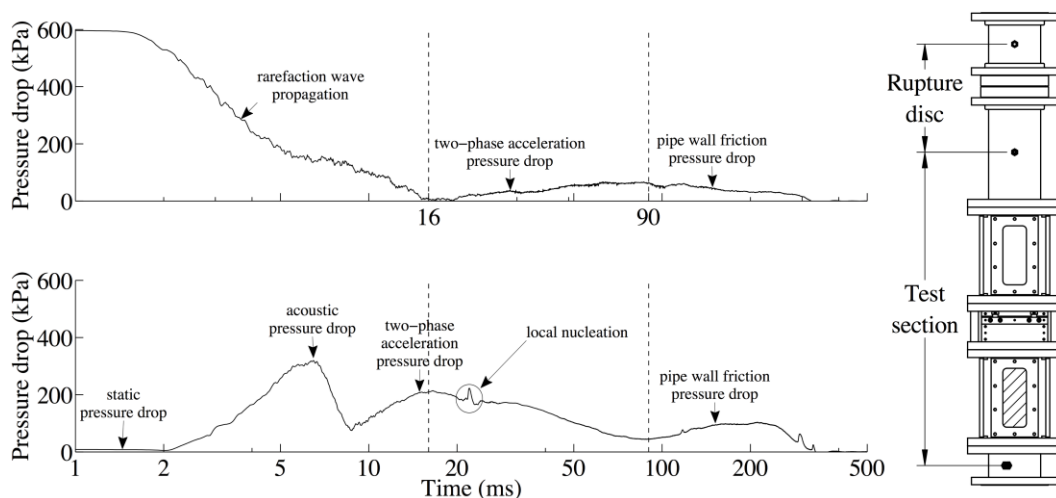
Figure 6-20. Transient pressure drop measured along the pressure vessel with the tube bundle removed (test T02), across the rupture disc (top), across the test section (bottom).

the instant at which the rarefaction wave passed location 1. The accelerational pressure drop across the test section increased shortly afterwards, starting at about 9ms and peaking at about 16ms. Once again, this coincides with the timing of the increase of the accelerational pressure drop across the rupture disc. As was previously observed in Fig. 6-19, this indicates that the accelerating two-phase front passed location 2 at 16ms. The 3ms delay in test T02 compared to test T04 was due to the lower initial level of liquid in the pressure vessel, resulting a greater propagation distance towards location 2.

The accelerational pressure drop was greater in magnitude in test T04 (350kPa at $t = 13$ms) compared to test T02 (200kPa at $t = 16$ms). This is because the rate of change of the momentum flux, which is related to the fluid inertia, was greater in test T04 than in test T02. Test T04 was performed with 15.4L of liquid R-134a, while test T02 was performed with only 9.3L. A greater pressure drop was therefore required to accelerate the fluid towards the vacuum reservoir. The small pressure spike observed at 22ms in test T02 was presumably caused by local nucleation effects on the pressure transducer surface.

The rapid flashing and acceleration of the two-phase fluid continued to contribute to the pressure drop until about 90ms. The average mass flow rate then equalised and a pressure gradient was established along the pipe for the remainder of the blowdown transient, due to friction at the pipe walls. The quasi-steady flow condition suggests that the flow in the pipe was choked during this time. The frictional pressure drop during this stage was considerably smaller in amplitude than the quasi-steady form drag pressure drop observed in test T04.

A direct comparison of the pressure drop measured across the test section (locations 1 and 2), with and without the tube bundle installed (tests T06 and T03 respectively), is shown in Fig. 6-21. The initial liquid volumes in these two tests were similar (21% and 23% respectively). The initial unsteady acoustic pressure drop was observed to be very similar for both tests and did not appear to be

influenced by the presence of the tube bundle. The wave propagation timings depend on the initial liquid level. The peak acoustic pressure drop was slightly delayed in test T06 due to the slightly lower initial liquid free surface (265mm in test T06 and 290mm in test T03).

Following the initial unsteady pressure wave propagation effects, the pressure drop across the test section increased due to the acceleration of the two-phase fluid. The peak in the momentum pressure drop observed at 11ms in test T06 was produced by a small amount of flashing liquid, which had collected on the steel surfaces in the tube bundle before the transient began, due to steady-state condensation. The liquid discharge was controlled by the tube bundle and the liquid below the tubes therefore only began to accelerate through the tubes at about 23ms. The rate of discharge was higher in test T03 and the fluid acceleration began earlier at about 14ms. These physical interpretations are supported by the high-speed flow visualisations that were presented in Fig. 6-16.
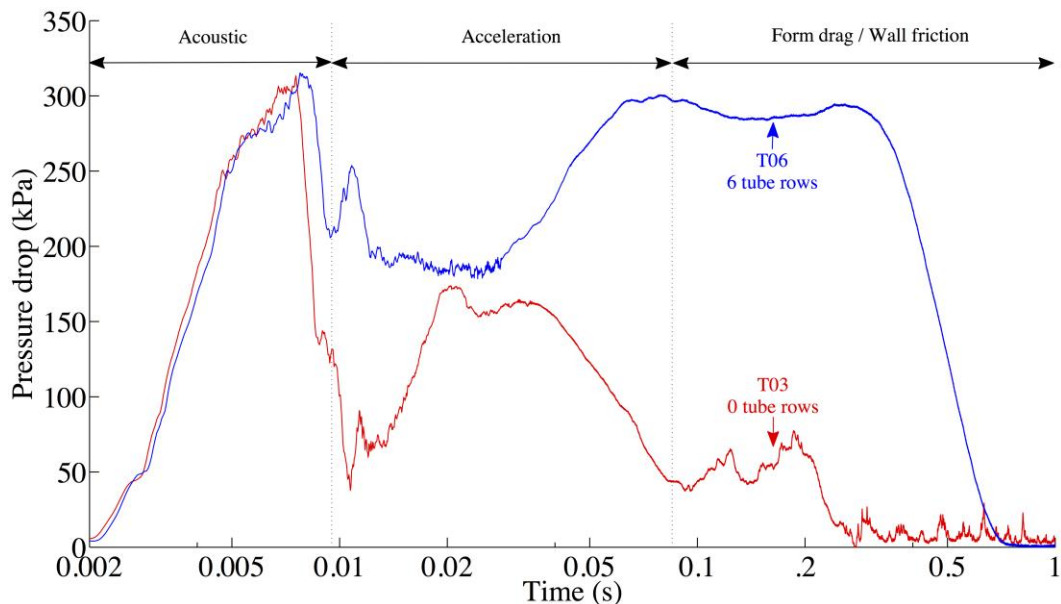
Figure 6-21. Transient pressure drop measured across the test section with and without the tube bundle installed (tests T06 & T03).

High-speed flow visualisations of the initial stages of flashing and fluid acceleration in test T06 are shown in Fig. 6-22. A two-phase fluid mixture can be observed accelerating upwards in the upper window at $t = 10$ms while the liquid in the lower window had not yet began flashing to vapour. This two-phase mixture cannot have originated anywhere other than between the two windows where the tube bundle was located. By $t = 20$ms, the accelerating two-phase mixture had disappeared, and the liquid below the tubes had already began rapidly transitioning to vapour.

↑ above tube bundle ↑

↓ below tube bundle ↓

| $t = 0$ms | $t = 10$ms | $t = 20$ms | $t = 30$ms | $t = 40$ms |
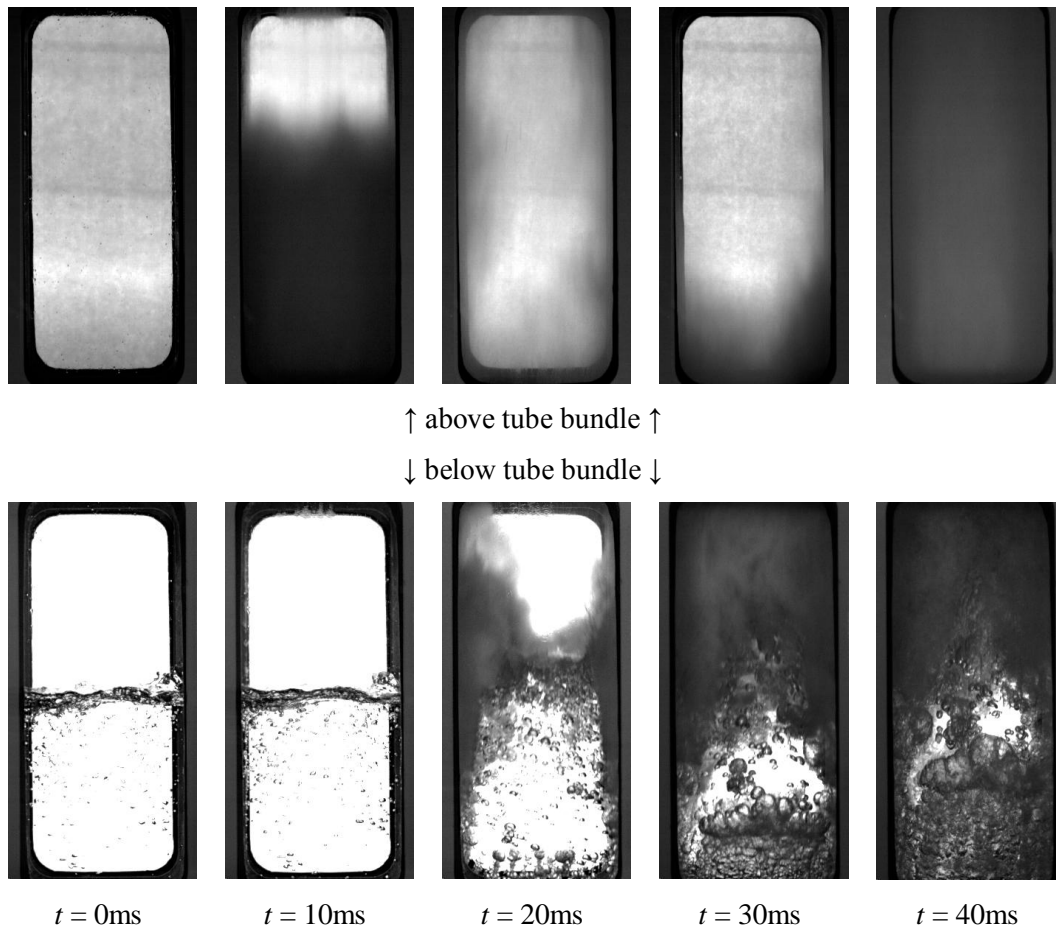
Figure 6-22. High-speed flow visualisation of accelerating two-phase fluid front through the tube bundle (test T06), upper window (top), lower window (bottom).

The two-phase mixture that originated at the liquid level surface can be seen entering at the bottom of the frame in the upper window at $t = 30$ms, after which a continuous two-phase flashing mixture persists for the entire duration of the blowdown transient. The timing of the acceleration of this two-phase fluid front ($t = 30 – 40$ms) coincides with the increase in the accelerational pressure drop through the tube bundle in test T06. Therefore, the peak at $t = 11$ms must have been caused by a flashing two-phase mixture, which had originated on the surface of the tubes in the tube bundle.

A peak in the pressure drop was also observed in test T03 at 11ms, similarly caused by previous steady-state condensation at the steel side-walls of the test section. Since the tubes were removed in this experiment, the surface area available for condensation was smaller and a lower amplitude was recorded for the peak pressure drop. The pressure drop increased to about 170kPa at 21ms and then decreased briefly. At about 25ms, rapid vapour generation in the pressure vessel produced a temporary recovery in the pressure. The pressure drop then decreased to about 50kPa and remained steady for the remainder of the transient until the liquid inventory was depleted.

The individual transient pressures measured at the three transducer locations along the pressure vessel are shown for tests T03 and T06 in Fig. 6-23. It was shown in Fig. 6-21 that the form drag losses in the tube bundle produced the maximum transient pressure drop amplitude across the tubes. Looking at the pressure gradients in Fig. 6-23, it can be observed that the pressure drop across the tube bundle in test T06 significantly contributed to the overall pressure drop, whereas in test T03 a smaller pressure gradient was established. The pressure increases during a two-phase blowdown in an unobstructed pipe with increased mass hold-up. This can occur due to choking at the exit of the pressure vessel or viscous losses at the pipe walls reducing the downstream pressure, which would result in the vaporisation of superheated liquid entrained in the discharging two-phase flow.
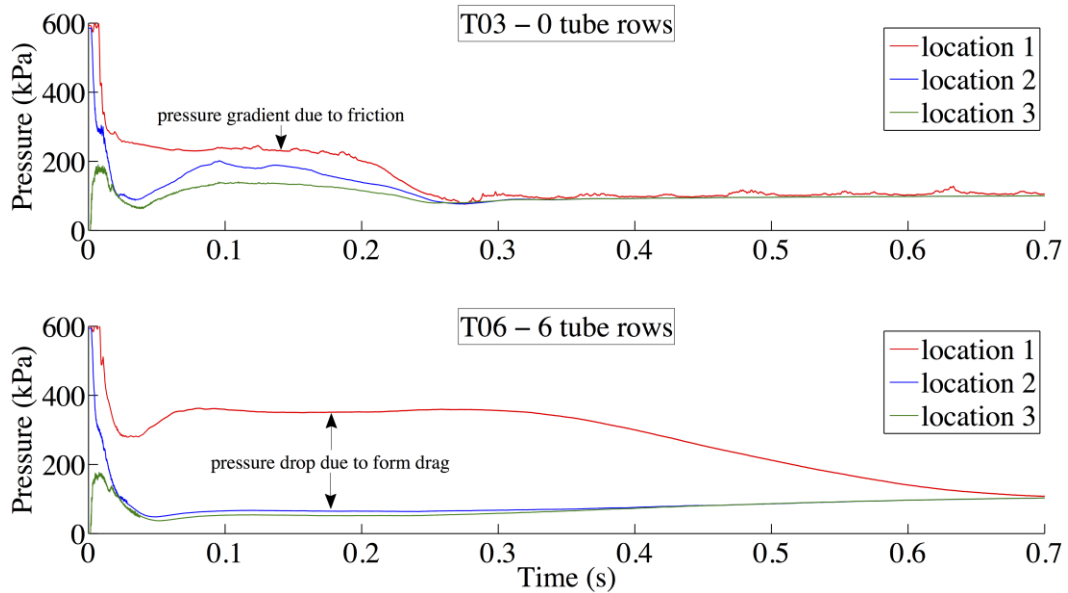
Figure 6-23. Individual transient pressure measurements in the pressure vessel (tests T03 & T06), without the tube bundle (top), with the tube bundle (bottom).

The transient pressure drop measurement across the tube bundle depends largely on the fluid mass flux during the blowdown. The upstream pressure in test T06 increased at about 30ms due to the acceleration of the flashing two-phase fluid. At about 75ms, the pressure drop across the tube bundle reached its maximum amplitude and remained constant until about 300ms. This quasi-steady condition suggests that the two-phase flow through the tube bundle was choked during this time. The upstream pressure remained constant while the two-phase mixture was being discharged through the tube bundle at maximum velocity. This continued until the liquid inventory was reduced to the point that the maximum rate of vapour generation could no longer be maintained. In terms of fluid drag on the tubes, the maximum drag was established when the fluid mass flow rate through the tube bundle was maximum, which occurred when the two-phase flow was choked in the early stages of the transient.

A schematic diagram illustrating the instantaneous pressure profile along the pressure vessel at $t = 0.25$s in test T06 is shown in Fig. 6-24. Prior to the

blowdown, the pressure drop across the tube bundle consists of the fluid hydrostatic head and the pressure drop across the rupture disc is equal to the upstream pressure. When the rupture disc opens, unsteady acoustic and momentum flux effects are recorded in the dynamic pressure signals. The pressure wave propagation occurs at acoustic velocities in the first 10ms or so, and the dynamic change in the rate of momentum along the pressure vessel occurs in about the first 100ms of the transient blowdown. The flow across the tube bundle was then observed to achieve a quasi-steady condition corresponding to choked flow from 0.1s to 0.3s, during which the pressure drop was maximum.

When the flow through the tube bundle is choked, the discharge of the two-phase fluid below the tubes is controlled by the restriction imposed by the tubes. Friction effects are negligible during this time. This is confirmed by pressure drop measurements obtained across the rupture disc, which essentially diminish to zero when the two-phase flow inside the tube bundle is choked. During this quasi-steady
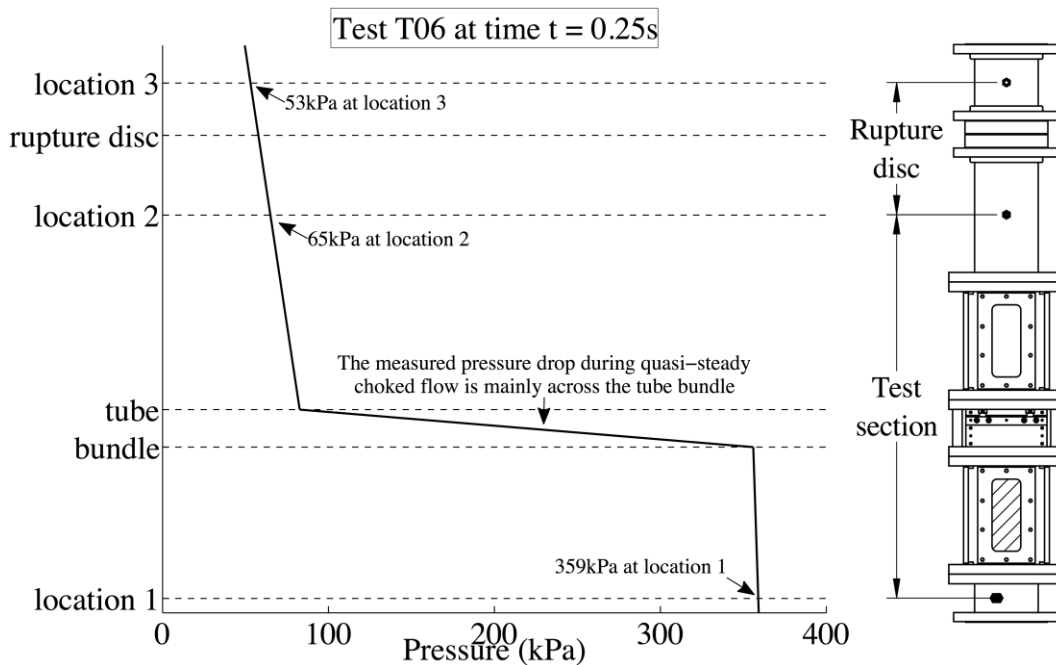
Figure 6-24. Illustration of instantaneous pressure measurements in test T06 at $t = 0.25$s.

discharge period, the pressure drop measured across the test section is dominated by the sharp pressure gradient at the tube bundle due to form drag losses and flow choking. The static pressure drop component between the bottom pressure transducer and the tube bundle is also included in the measurement. The amplitude of the initial static head was never greater than 3% of the overall pressure drop across the tube bundle.

CHAPTER 7. DYNAMIC TUBE LOADING RESULTS AND ANALYSIS

The dynamic pressure drop that is established across the tube bundle during the blowdown transient produces a significant hydraulic drag loading on the tubes. The dynamic loads on the tube bundle were measured and can be interpreted in terms of the two-phase fluid mechanics described in the previous chapters. The maximum pressure drop across the tube bundle was established early during the blowdown experiments after the initial unsteady effects were complete. These were associated with the propagation of pressure waves and the subsequent rate of change of momentum of the flashing two-phase fluid.

About 0.1s into the transients, the rate of vapour generation below (upstream of) the tubes was stabilised by the rate of fluid discharge through the tube bundle, producing a quasi-steady pressure condition. During this stage of the blowdown, the flow through the tube bundle was choked and the pressure drop was maximum. This persisted until the liquid inventory upstream of the tube bundle was depleted to the point that the maximum rate of vapour generation could not be sustained. The two-phase flow through the bundle then displayed increasing liquid entrainment, which was accompanied by a reduction in the upstream pressure. The result was a deceleration of the flow and a decrease of the pressure drop across the tube bundle, which eventually diminished to zero at the end of the transient blowdown discharge.

The overall objective of the dynamic tube loading analysis in this chapter is to develop a physical understanding of the relationship between the observed transient hydraulic drag loads and the two-phase flow development in the experiments. This can then be used to predict expected dynamic loads under operating steam generator conditions. From a design perspective, it is of primary

interest to predict the maximum loads in order to ensure tube integrity. Therefore, while an understanding of the transient load development during the blowdown process provides useful information pertaining to the two-phase flow physics, the emphasis here is on the maximum amplitude of the tube loading.

7.1. DESCRIPTION OF DYNAMIC LOAD MEASUREMENT

A sample transient load measurement obtained during test T05, which was performed with a tube bundle containing 6 rows of tubes, is presented in Fig. 7-1. The initial volume of liquid in the pressure vessel was 12.1L, which corresponds to a liquid column height of 670mm. The liquid free surface level was visible at the upper window in the pressure vessel, above the tube bundle. The physical mechanisms of fluid transient tube loading during the blowdown were determined based on the thermal hydraulic phenomena described in Chapters 5 and 6 as well as the synchronised high-speed flow visualisations observed through the sight windows located below and above the tube bundle.

The oscillations in the first 0.1s of the load signal, which persisted throughout the remainder of the transient at reduced amplitudes, were caused by vibrations of the pressure vessel at its natural axial frequency. The same vibration frequencies were measured by an accelerometer mounted at the test section. The vessel vibrations were also identifiable in the high-speed flow visualisations. The mean tube loading trends in the signal are representative of the general load behaviour observed in all of the tests performed with multiple tube rows mounted in the test section.

The initial stage of the transient was characterised by a significant rate of change in the fluid's momentum. The load signal increased rapidly as the vapour downstream of the tube bundle accelerated away from the tubes and the two-phase fluid below the tubes accelerated through the tube bundle. At about 150ms, the tube loading began to level off at about 7.9kN as the flow rate through the
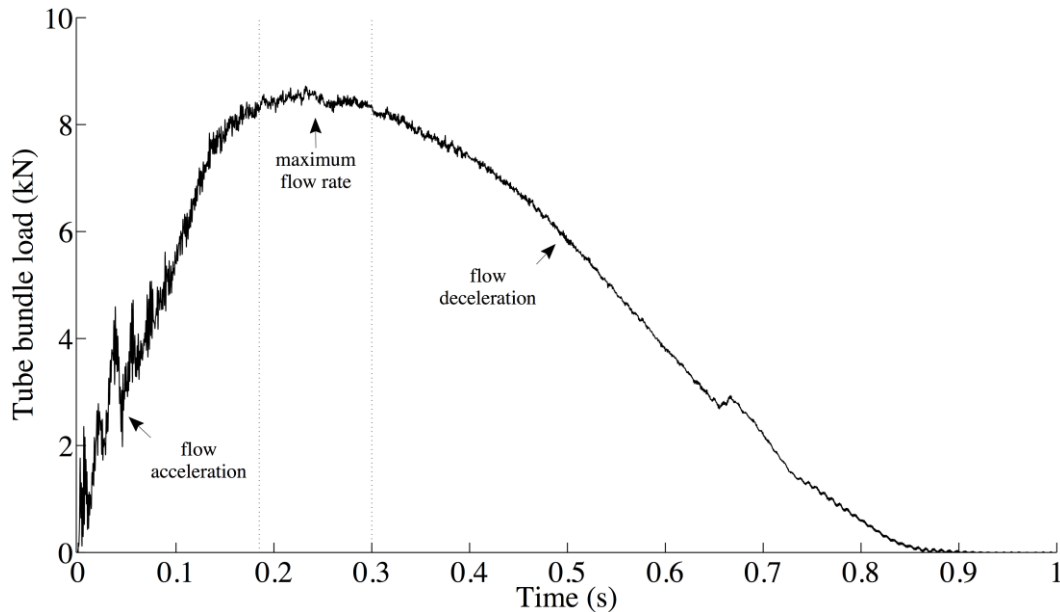
Figure 7-1. Sample tube load transient (test T05).

tube bundle became established. The tube bundle loading then attained a maximum value of about 8.5kN. This continued at a nearly constant amplitude for about 100ms. The two-phase mixture flow rate then began to decrease once enough of the liquid inventory below the tubes had been depleted and the initial rapid rate of vapour generation could not be sustained. As the two-phase flow through the bundle continued to decelerate, the load signal tapered off and converged towards 0kN.

The maximum tube loading occurred when the two-phase fluid flow rate (and pressure drop) through the tube bundle was maximum. This 'quasi-steady' discharge was associated with two-phase flow choking through the tube bundle relatively early in the transient. Critical (choked) pressure values were estimated for the upstream pressure of about 430kPa during quasi-steady discharge in test T05. The calculations were performed using the assumptions of the homogeneous equilibrium (HEM) and homogeneous frozen (HFM) critical flow models. The results are shown by the dashed lines in Fig. 7-2.
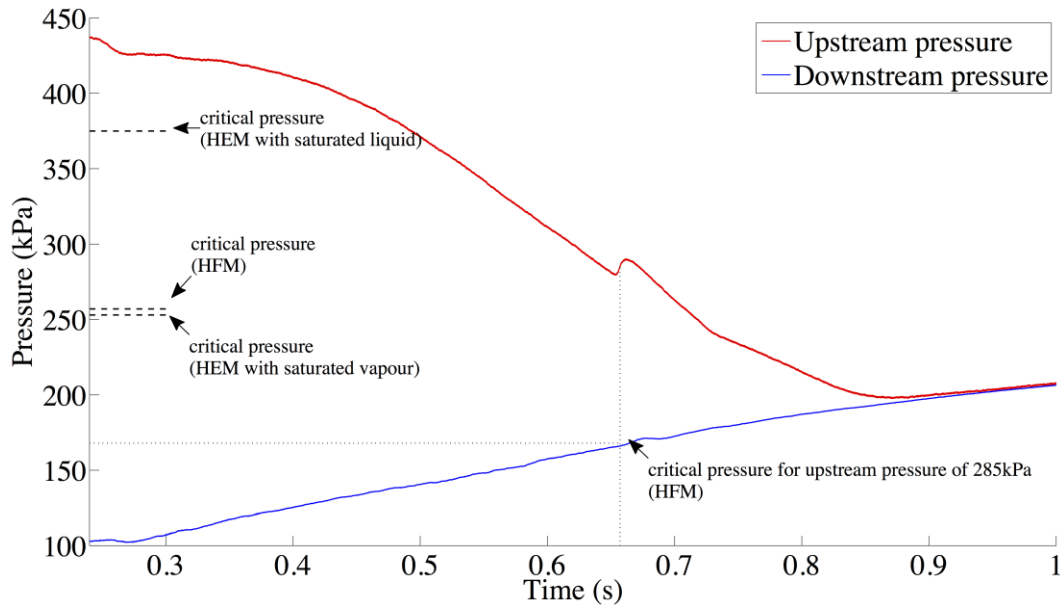
Figure 7-2. Critical HEM and HFM pressure estimates for test T05 (calculations based on p_u = 430kPa at t = 0.25s and p_u = 285kPa at t = 0.66s).

The HEM calculation was performed assuming initially saturated liquid as well as initially saturated vapour conditions below the tubes. In both cases, the flow at the critical plane was assumed to be in thermal and mechanical equilibrium. The critical pressure was obtained by solving iteratively for the maximum critical mass flux, G_c, according to Eq. (7-1),

$$G_c = \frac{1}{v_c}\sqrt{2\left(h_0 - h_c\right)},\qquad(7\text{-}1)$$

where h_0 is the stagnation enthalpy, h_c is the enthalpy at the critical plane, and v_c is the specific volume at the critical plane. On the other hand, the HFM assumes that the liquid is incompressible and that the quality remains constant (no vaporisation). The critical pressure ratio is given by Eq. (4-6). In real two-phase flows, the quality changes so that it is not completely frozen, but not as much as predicted by the equilibrium model. The critical pressure ratio is typically

between the two limiting cases, usually closer to the HEM prediction. The HFM generally provides better predictions for the critical mass flux (Whalley, 1987).

The critical pressure ratios computed for the quasi-steady conditions of test T05 using both models were similar when the flow quality was high. At high flow qualities, the models tend to predict similar critical flow properties. In all cases, the pressure measured downstream of the tube bundle was far lower than the predicted critical pressure. Hence, the flow through the tube bundle was choked and independent of the downstream conditions. A small 'hump' was observed in the upstream pressure at about 660ms. For the corresponding measured upstream pressure of 285kPa, the computed critical pressure ratio was 0.593. This gives a critical pressure of 169kPa, which was very close to the 168kPa pressure measured downstream of the tube bundle at 660ms.

It would appear based on these observations that the two-phase flow through the tube bundle remained choked well into the transient blowdown after the quasi-steady stage. The 'hump' may represent a transition from choked flow to subsonic flow through the tube bundle. High-speed flow visualisations obtained above the tube bundle also indicated a change in the flow pattern at around the same pressures and stages during the transient (refer to Fig. 6-15 for an example). The 'hump' was also measured in the load signal shown in Fig. 7-1. The following sections describe the physical mechanisms responsible for maximum tube loading and present a study of the influential experimental parameters and predictive methodologies for design.

7.2. EFFECT OF THE INITIAL LIQUID LEVEL ON TUBE LOADING

A number of experiments were carried out with the identical pressure vessel and tube bundle geometry while varying the initial amount of liquid R-134a in the pressurised reservoir. This enabled the investigation of the influence of the liquid level in the pressure vessel, or more specifically, the initial location

of the liquid free surface with respect to the tube bundle, on the transient loading of the tubes. Industrial steam generators are typically designed such that the tube bundle is submerged in water at all times during operation but the tubes may become uncovered if the water level falls sufficiently. The quality of the saturated steam-water mixture also varies at different locations in the steam generator and with different amounts of heat transferred from the tubes. A comparison of the pressure drop measured across the tube bundle is presented in Fig. 7-3 for tests T04 and T06.

The liquid free surface was initially above and below the tube bundle in tests T04 and T06 respectively. The transient pressure drop measurements in the first 45ms contained rapid changes that were associated with unsteady wave propagation and the acceleration of the fluid downstream of the tubes. These phenomena did not produce any significant effect on the tube bundle drag loading. The subsequent steady increase in the measured pressure drop, which began at about 25ms in T06 and 55ms in T04, was produced by fluid acceleration from the

Figure 7-3. Comparison of the pressure drop across the tube bundle with different initial liquid levels (tests T04 & T06).

bottom of the pressure vessel towards the vacuum reservoir. The amplitude of the maximum pressure drop during the quasi-steady discharge stage of the blowdown in both tests was the same at about 285 – 295kPa.

A comparison of the transient tube loads measured in tests T04 and T06, for which the transient pressure drops were shown in Fig. 7-3, is given in Fig. 7-4. As was observed in the pressure drop measurements, the tube loading comparison demonstrates that the initial liquid level did not significantly affect the maximum load amplitude established during quasi-steady discharge. A maximum tube bundle loading of about 7.8kN was established during the blowdown between 0.22 – 0.35s in test T04 and between 0.11 – 0.27ms in test T06. The pressure drop and tube load measurements showed very similar trends. This suggests that a correlation exists between the transient two-phase tube loading and the transient pressure drop across the tube bundle if the tube bundle geometry and fluid properties are similar.
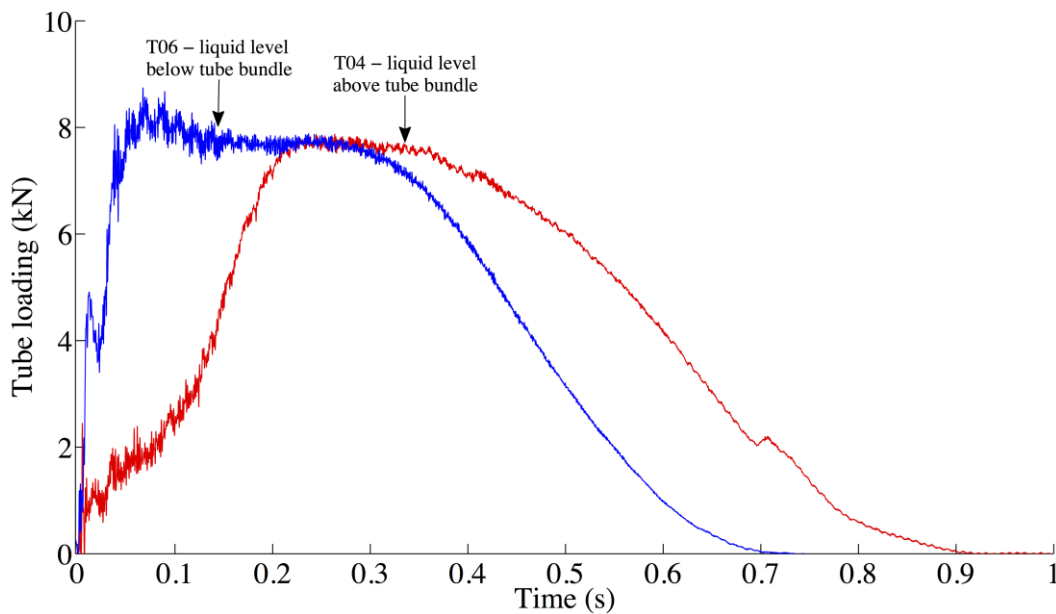
Figure 7-4. Comparison of the effect of the initial liquid level on tube bundle loading (tests T04 & T06).

When the region inside and downstream of the tube bundle was initially occupied by vapour (liquid initially below the tubes, test T06), the maximum load plateau across the tubes was established more rapidly. Since the liquid inventory was lower (4.9L of liquid R-134a in T06 compared to 15.4L in T04), the blowdown time was also shorter. When the liquid was initially above the tube bundle, the fluid acceleration through the tube bundle was limited by the inertia of the liquid. This resulted in a relatively slower increase in the pressure drop and tube loading amplitudes. A delay of about 0.2s was observed before maximum flow rate and tube loading was established. The rates of vapour generation and fluid discharge below the tubes are controlled primarily by the resistance to the flow of the tube bundle. The maximum fluid load on the tube bundle during quasi-steady discharge therefore depends mainly on the upstream thermodynamic conditions and the tube bundle geometry, and is not influenced by the initial liquid level.

In order to better illustrate the differences in the initial transient loading behaviour in tests T04 and T06, the measured loads in the first 0.25s are presented on a logarithmic time-scale in Fig. 7-5. Signal fluctuations with an amplitude of about 0.5kN occurred in the first few milliseconds of the blowdowns, before the arrival of the rarefaction wave at the test section. These minor oscillations were probably caused by the significant vibrations and stress waves that are induced by the opening of the rupture disc. The rarefaction wave arrived at the top row of the tube bundle 3.7ms and 5.4ms after the rupture disc burst in tests T04 and T06 respectively. The velocity and timing of the wave propagation changes with the amount of liquid initially above the tube bundle as expected, because of the differences in wave propagation velocity. The wave passes through the test section very rapidly and does not produce any discernible load measurement.

It has been shown that for shallow staggered tube arrays with a depth to height ratio of less than one (the present tube bundle depth to height ratio is 0.63), the speed of sound is negligibly affected by the tube bundle presence (Ziada *et al.*,
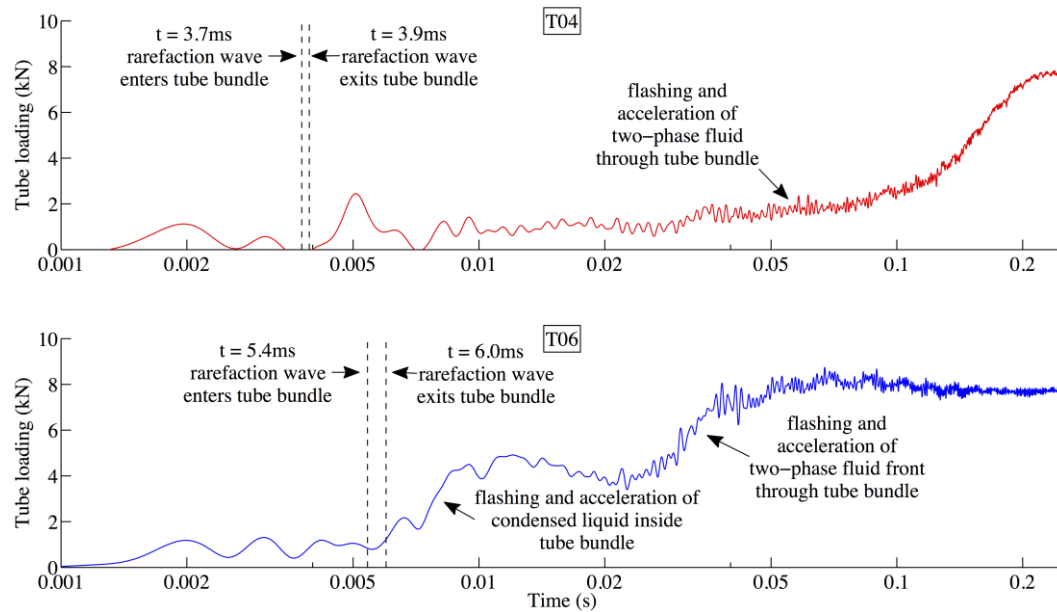
Figure 7-5. Dynamic loads measured in the first 0.25s (tests T04 & T06).

1989). The rarefaction wave was computed to propagate through the tube bundle in about 0.6ms in vapour and 0.2ms in liquid. In order to measure the amplitude of a rapid transient input accurately, the instrument response time must be at least 5 times longer than the rise time of the input signal. The response time constant of the piezoelectric load cells is about 0.04ms, which gives an accurate rise time of about 0.2ms (details are provided in Appendix C.4.3).

The rarefaction wave front in the experiments was not perfectly one-dimensional due to the hemi-spherical (or conical) opening pattern of the rupture discs. The wave front would therefore be expected to be distributed over the 3ms opening time of the rupture discs, and any resultant loading would be captured by the dynamic load cells. In test T04, a peak dynamic load of about 3kN was measured at about 5ms, and in test T06, a dynamic load of about 2.5kN was observed in the signal at 6.5ms. The load signals in these acoustically dominated stages of the transient were difficult to distinguish from the initial vibration artefacts and no satisfactory explanation was found for these observed peaks. Importantly, the load amplitude in these early stages of the transient is

insignificant compared to the maximum load signals measured later in the transient due to the fluid drag loading of the tube bundle.

The load rises as the fluid below the tubes accelerates through the bundle. A dynamic load with a peak of nearly 5kN was observed in test T06 at about 12ms. This load measurement was produced by the acceleration of a flashing two-phase mixture inside the tube bundle, due to liquid condensation on the surface of the tubes before the blowdown began. This phenomenon was demonstrated in Figs. 6-22 and 6-23 where it was shown that an isolated flashing front had developed between 9 – 13ms. The corresponding rise in the load signal matches the timing of the acceleration of this fluid mixture. This gives an indication of the rapidity of the flashing phenomenon, which took place immediately after the passage of the rarefaction wave. The measurements also demonstrate the response time adequacy of the load instrumentation system for measuring flow-induced hydraulic loads on the tube bundle. The dynamic load amplitude decreased briefly at about 14ms and increased again beginning at about 21ms. This was also shown in Fig. 6-23 to be related to the acceleration of the flashing two-phase fluid front initially below the tubes.

The acceleration of the high void fraction fluid through the tube bundle is very rapid. This produced a peak in the pressure drop measurement at about 65ms. Looking at the first 250ms in Fig. 7-5, it can be observed that the dynamic load was also higher initially when the two-phase front accelerated through the bundle, resulting in a brief loading of about 8.1kN between 60ms and 90ms in test T06 for the case of initial liquid below the bundle. This load was slightly higher than the 7.8kN quasi-steady load established in the later stages of the blowdown (by about 4%). Typically, in an operating steam generator, the tubes are submerged in liquid and the initial dynamic load produced by the accelerating two-phase front would not be expected to be as pronounced. The slower increase in the dynamic load observed for the case with the liquid above the tubes (test T04) is more representative of the behaviour expected for operating steam generator conditions.

The relative volume of liquid R-134a below the tubes before blowdown, or the ratio of liquid to vapour in the pressure vessel, was also studied in these experiments. Test T01 was carried out with a small initial liquid inventory of 0.8L whereas test T08 was performed with the same pressure vessel dimensions and test section geometry but with 14.3L of liquid R-134a. The respective liquid volume fills in tests T01 and T08 were 3% and 52%. Unfortunately, there is no direct measurement of tube loading available for test T01. The pressure drop measured across the tube bundle is relied on instead for a quantitative comparison of the relative load magnitudes. The relationship between the tube loading and pressure drop was demonstrated to be a reliable indicator of the relative load magnitudes in Figs. 7-3 and 7-4.

A comparison of the pressure drop measured across the tube bundle in tests T01 and T08 is presented in Fig. 7-6. The pressure drop in test T08 reached a maximum pressure that was greater than 300kPa. On the other hand, the pressure drop in test T01 only increased briefly as the two-phase mixture accelerated through the tubes, reaching a peak pressure drop of about 200kPa at 95ms. The pressure drop then decreased for the remainder of the transient. Although the liquid level was previously observed not to influence the amplitude of tube loading, the comparison between tests T01 and T08 shows that the maximum load amplitude might not be attained if there is an insufficient initial liquid inventory below the tubes. This indicates that in order to establish maximum upstream quasi-steady conditions (maximum flow rate and pressure drop), a minimum amount of liquid is required to sustain the associated maximum vapour generation rate below the tubes.

The increase in the pressure below the tubes is caused by the generation of vapour when the rate of volumetric expansion exceeds the rate of volumetric discharge. The experimental results demonstrate that under similar initial thermodynamic conditions, pressure vessel dimensions, and tube bundle geometries, the pressure drop across the tube bundle will have the same maximum
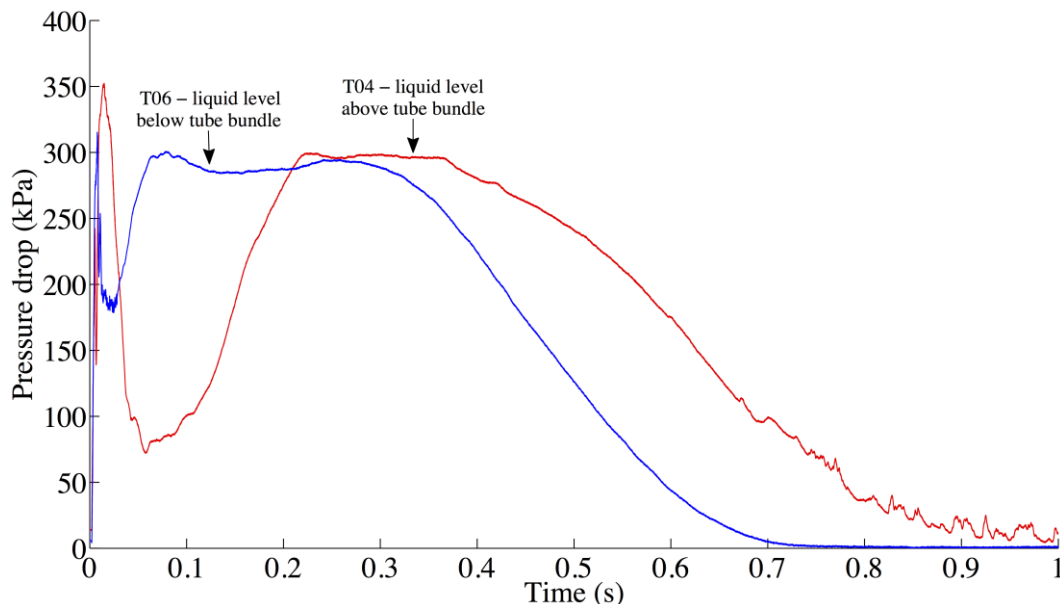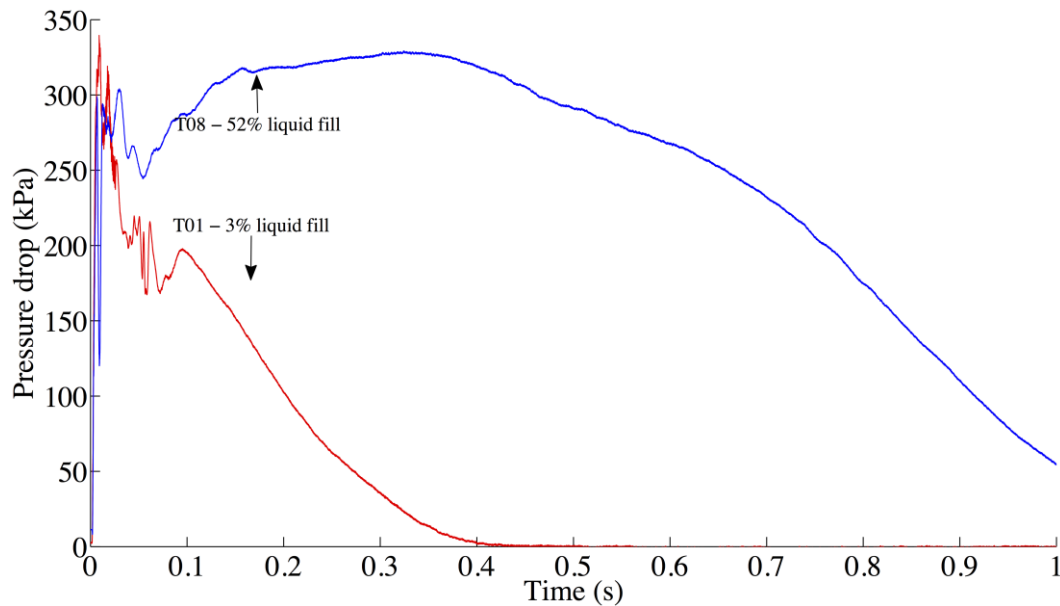
Figure 7-6. Comparison of the pressure drop across the tube bundle with different initial liquid inventories (tests T01 & T08).

amplitude regardless of the initial volume of liquid. This is if a maximum rate of vapour generation can be sustained during the transient blowdown discharge by making a sufficient superheated liquid inventory available. The maximum pressure drop across the tube bundle occurs when the fluid flow through the tube bundle is at its maximum because it is choked. As long as there is a sufficient liquid inventory below the tubes to sustain the maximum vapour generation rate, changing the liquid level location with respect to the tube bundle affects the time of onset of maximum loading but does not affect the maximum amplitude significantly.

7.3. EFFECT OF THE PRESSURE VESSEL VOLUME ON TUBE LOADING

A comparison of the pressure drop and tube load measurements obtained using different pressure vessel volumes is shown in Fig. 7-7. Test T04 was carried

out using a 23.6L pressure vessel and test T08 was performed with a longer pipe section at the bottom of the vessel giving a total pressure vessel volume of 27.8L. The percentage of the vessel volume filled with liquid was 67% in test T04 and 52% in test T08. This corresponds to a liquid column height of 848mm in test T04 and 788mm in test T08. The initial liquid level was above the tube bundle in test T04 whereas in test T08 the liquid free surface was at about the top (downstream) row in the tube bundle.

Since the region above the tubes was initially occupied by vapour in test T08, the pressure drop across the tube bundle increased rapidly. This produced a rapid rise in the transient tube loading in the first 50ms of the blowdown. Additionally, given that the liquid R-134a inventory below the tubes was greater in test T08 compared to test T04, the time duration of the blowdown and the quasi-steady discharge stage were longer. The larger initial liquid inventory below the tubes sustained a longer period of maximum vapour generation and maximum two-phase flow through the tube bundle.
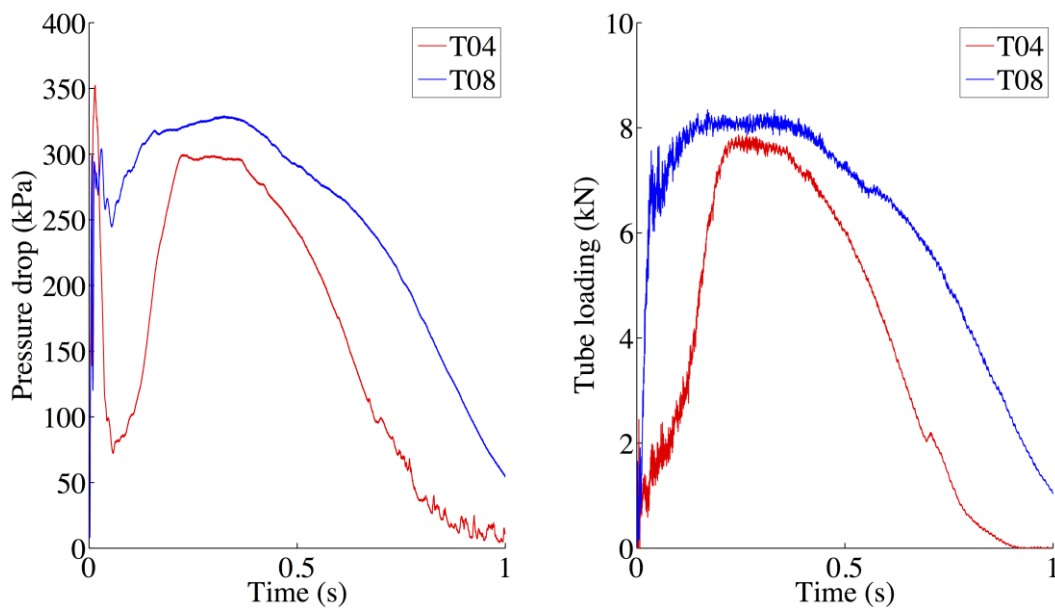
Figure 7-7. Comparison of pressure drop and tube load with different vessel volumes (tests T04 & T08).

The amplitude of the maximum pressure drop was slightly higher in test T08, for which the pressure vessel was larger (325kPa compared to 300kPa). Similar observations are documented in the literature. For blowdowns performed with similar discharge areas and downstream pressures (atmospheric), the pressure difference between the vessel and the downstream ambient conditions was higher when the pressure vessel was larger (Winters & Merte, 1979). The lower pressures for smaller vessels were attributed to a greater departure from thermodynamic equilibrium. When the vessel volume is increased relative to the discharge area, greater overall mixing allows the pressures to recover to higher amplitudes during rapid phase transition relative to the downstream pressure. This phenomenon was discussed at length in Section 6.6.

The tube loading was also higher for the larger vessel volume (8.3kN compared to 7.7kN). Quantitatively, the relationship between the amplitude of the maximum pressure drop and tube loading was not affected by the vessel volume, if the number of rows of tubes in the bundle remained the same. The tube load signal was observed to be slightly 'flatter' than the pressure drop measured across the tubes in the quasi-steady stage of the blowdown. This may have been caused by the dynamic instrumentation discharge properties due to the AC-coupled signal conditioning of the piezoelectric load cells (details are provided in Appendix C.4.1).

The effect occurs over a maximum of 3% of the total signal output, which is within the uncertainty bounds of the load measurements. When averaged over the quasi-steady signal duration, the quantitative influence of this behaviour was found to be negligible. Hence, a larger vessel volume upstream of the tube bundle results in a longer blowdown and a slightly higher tube bundle load for similar thermodynamic conditions.

7.4. EFFECT OF THE NUMBER OF TUBE ROWS ON TUBE LOADING

In order to extract practical information from the results, it was important to study the quantitative relationship between the measured pressure drop and tube bundle loading. Given that the relationship was constant for the same number of rows of tubes in the bundle, a parametric study of the effect of the number of rows of tubes was thought to be useful. Varying the number of rows of tubes reveals additional information about the underlying physics, which is valuable for developing a predictive methodology for tube loading during a blowdown.

It has been demonstrated that under similar initial thermodynamic conditions, pressure vessel sizes, and tube bundle geometries, the tube bundle was subjected to the same maximum load amplitudes (refer to Fig. 7-4). The maximum loads occurred during the quasi-steady two-phase discharge stage and remained the same regardless of whether the initial liquid level was below or above the tube bundle. It has also been demonstrated that a sufficient liquid inventory is required below the tubes in order to sustain the maximum rate of vapour generation (refer to Fig. 7-6). By having the region downstream of the tube bundle initially occupied by vapour, the maximum pressure drop across the tubes was established faster. This allowed for a longer duration of maximum quasi-steady drag loading.

A relatively long duration of the maximum two-phase flow rate through the tube bundle was desirable for the reliable quantitative analysis of the pressure drop and tube loading. This was achieved by charging the liquid in the pressure vessel up to the test section level, which corresponds to a liquid fill of about 50% for the 27.8L vessel. The test section was designed so that the number of rows of tubes could be readily modified between each test run. The effect of the number of tube rows on the dynamic tube bundle was investigated in a series of experiments that were performed with different numbers of rows of tubes. These

were tests T08, T09, T10, T11, and T12, carried out with 6, 5, 4, 3, and 2 rows of tubes respectively. The initial liquid fill ranged between $50\% - 54\%$ and the range of initial liquid temperatures was 14.1°C to 18.3°C.

A comparison of the transient tube loads obtained in tests T08 and T11, with six and three tube rows respectively, is presented in Figure 7-8. The initial liquid fill was 52% and 53% in tests T08 and T11 respectively. The initial liquid level was inside the tube bundle for both tests. The trends of the transient tube load measurements were observed to be very similar. In particular, the rates of the change in the transient drag loading and the timing of the flow transition from the initial acceleration to the quasi-steady flow through the tubes were almost the same in both tests. The main difference between the two measurements was the amplitude of the maximum load. The maximum amplitude was about 8.1kN for six tube rows and about 6.6kN for three tube rows.

The duration of the transient loading was also different in both tests, with the deeper tube bundle producing a longer blowdown. The restriction imposed on
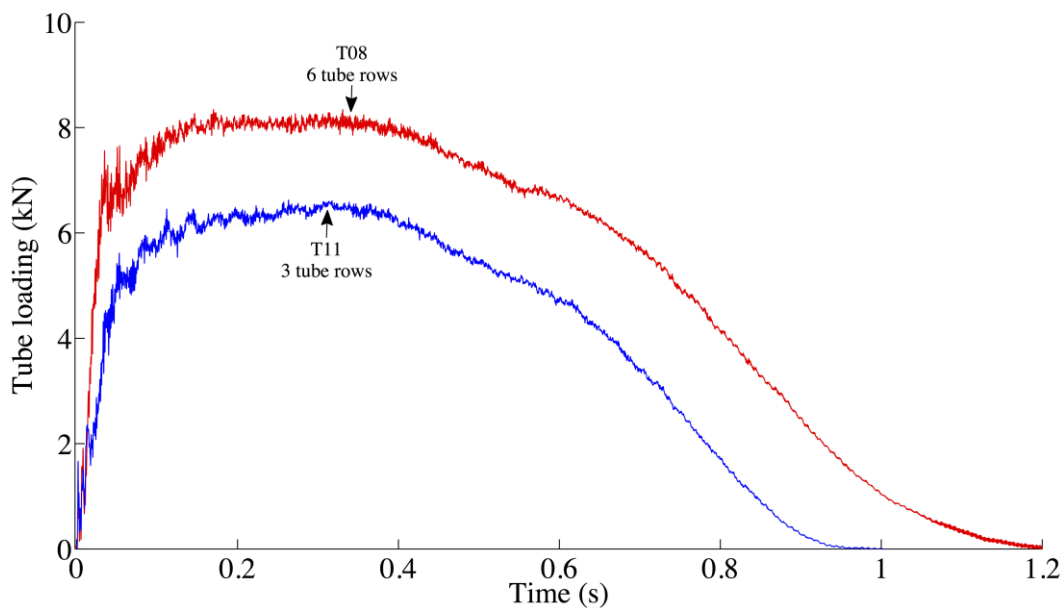
Figure 7-8. Comparison of tube bundle load with different numbers of tube rows (tests T08 & T11).

the discharging two-phase flow was greater when the tube bundle contained a larger number of rows. The flow through the bundle during the quasi-steady stage is controlled by two-phase flow choking inside the tube bundle. Calculations indicated that even for the case with only 2 rows of tubes, the downstream pressure (115kPa) was lower than the critical pressure (210kPa) corresponding to the upstream pressure (355kPa) and the flow was still choked. The mass hold-up increases with additional rows of tubes as more flow losses are encountered and more liquid vaporisation takes place inside the tube bundle. The flashing retards the flow discharge and results in an increased build-up of pressure upstream.

It may be noted here that the maximum pressure drop measured in the various blowdown experiments did not necessarily decrease monotonically with the decreasing number of rows of tubes. This would only be true if the mass flow rate through the tube bundle was the same in each test. In order to explain the differences that arose between different tests better, a comparison of the pressure drops and tube loads measured for tests T04 and T05 is presented in Fig. 7-9. The tests were both performed with six rows of tubes and similar initial conditions. However, the pressure drop and tube bundle load peaked earlier in test T05, and the associated amplitudes were greater.

It was demonstrated in Fig. 6-4 that compressed gas bubbles in the liquid before the blowdown began in test T05 resulted in a more violent pressure recovery. Hence, maximum vapour generation was established earlier at a higher pressure amplitude. The comparison of the maximum pressure drop and tube load signals reveals that the quantitative relationship between the two during quasi-steady flow was practically unaffected. This is unsurprising given that the tube bundle geometry was the same and the flow was choked in both experiments.

The transient trends observed in test T10, performed with four rows of tubes, were similar to those observed in test T05 (shown in Fig. 7-9). A comparison of the measurements of tests T09, T10, and T11, with five, four, and
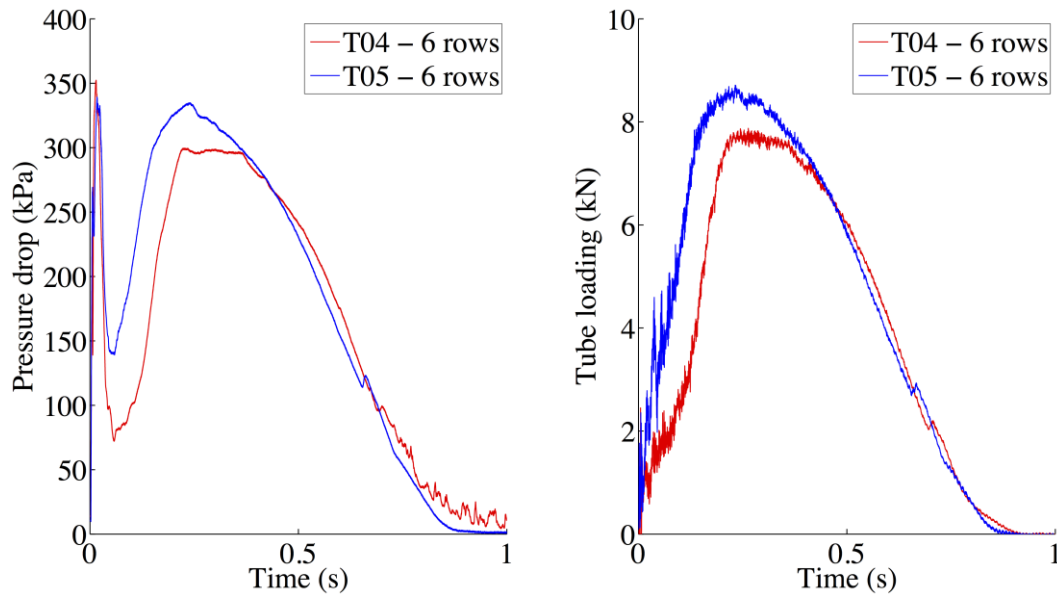
Figure 7-9. Comparison of pressure drop and tube load in tests T04 & T05.

three rows of tubes respectively, is presented in Fig. 7-10. Similar to the peculiar behaviour of test T05, the pressure drop and transient load peaked earlier in test T10 compared to the other two tests. The result was a higher peak in the pressure drop measurement than would be expected if the pressure drop were to follow a monotonically decreasing trend. Based on the physical phenomena observed in test T05, the trends in test T10 were probably caused by increased vaporisation activity because of compressed gas bubbles distributed in the liquid bulk before blowdown. Unfortunately, no high-speed video corroboration is available for this experiment.

Although the pressure drop in test T10 (four rows) was greater than the pressure drop in test T09 (five rows), the tube loading was not. This further confirms that the quantitative relationship between the pressure drop and tube loading only depends on the number of rows and is independent of the amplitude of the loading or pressure drop. When the number of rows of tubes increases, the same pressure drop will produce a higher amplitude of tube loading. The pressure
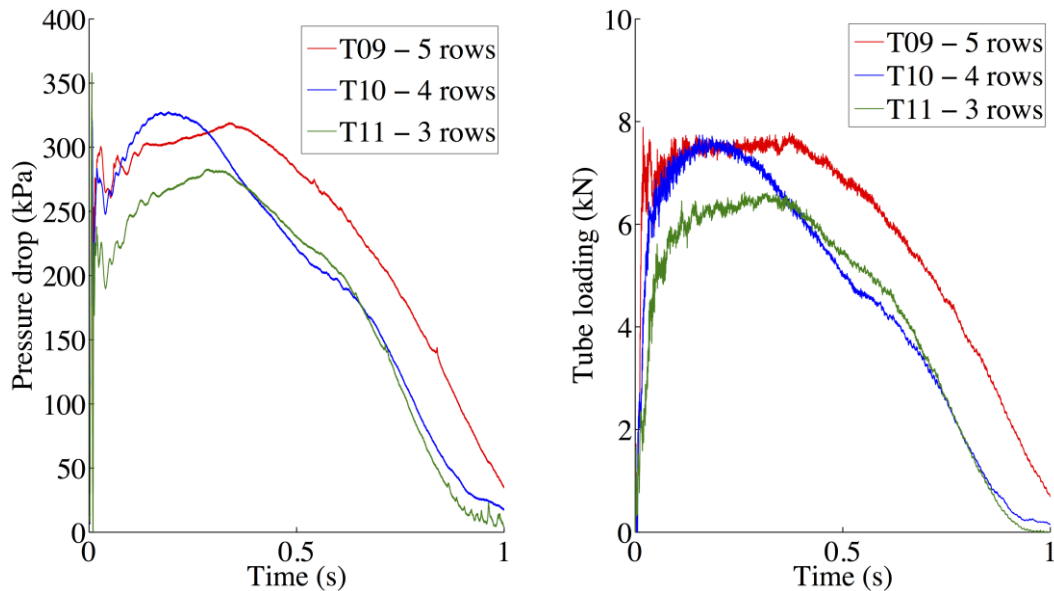
Figure 7-10. Comparison of pressure drop and tube load with different numbers of tube rows (tests T09, T10 & T11).

drop for the same number of rows will be the same if the flow properties are the same.

Since the independent parameters (density, velocity, and mass flow rate) could not be precisely controlled in these experiments, there was variability in the amplitude of the maximum pressure drop. The pressure drop did not decrease monotonically with the number of rows. However, the relationship between the maximum pressure drop and tube loading, which is most important in terms of modelling, was observed to be consistent irrespective of the maximum pressure drop amplitude across the tube bundle. For the same pressure drop, the maximum load increased monotonically with the number of rows of tubes in the bundle.

7.5. TUBE BUNDLE DRAG LOAD COEFFICIENT

The dynamic tube bundle drag load measured in test T04, which was performed with six rows of tubes and 67% of the vessel initially filled with liquid,

is compared to the pressure drop measured across the tube bundle in Fig. 7-11. The dynamic pressure drop across the tube bundle was computed simply by subtracting the pressure above the tubes (location 2) from the pressure below the tubes (location 1). After the first 55ms of the transient, in which the acoustic and inertial effects downstream of the tube bundle were significant, the trends in the pressure drop measurement followed the load signal very closely for the entire remaining duration of the transient.

Under steady-state conditions, the drag force exerted on the tube bundle, F_{drag}, is directly proportional to the form drag pressure drop established across the full array of tubes, Δp_{drag}. The proportionality constant is a product of the cross-sectional flow area, A, and a drag coefficient, C_{drag}, as given by Eq. (7-2),

$$F_{drag} = C_{drag} \cdot A \cdot \Delta p_{drag} \,. \tag{7-2}$$

In the present experiments, the cross-sectional area was constant, the drag load on the tube bundle was measured directly, and the pressure drop was measured between locations 1 and 2 (refer to Fig. 3-1). It was shown in Section 6.7 that the
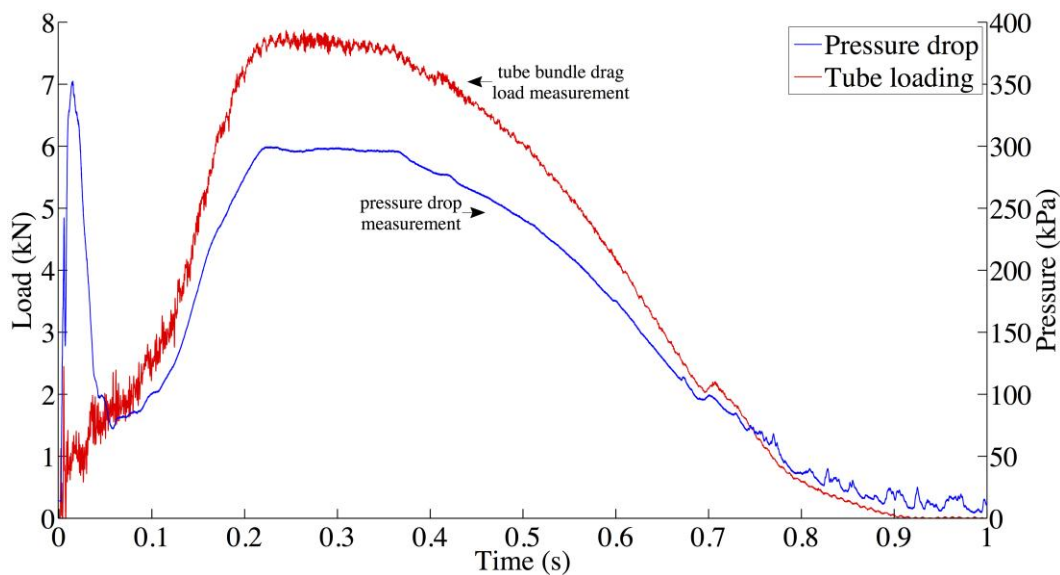
Figure 7-11. Comparison of measured tube load and pressure drop across the tube bundle (test T04).

pressure drop measured during the quasi-steady stage of the transient, $\Delta p_{measured}$, basically consisted of the steep pressure gradient across the tube bundle, Δp_{drag}, and the static head of the flow between the bottom pressure sensor and the tube bundle, Δp_{static}, as shown by Eq. (7-3),

$$\Delta p_{measured} = \Delta p_{drag} + \Delta p_{static} . \qquad (7\text{-}3)$$

Hence, the drag coefficient was related to the transient measurements as given by Eq. (7-4),

$$C_{drag} = \frac{F_{drag}}{A\left(\Delta p_{measured} - \Delta p_{static}\right)} . \qquad (7\text{-}4)$$

It is difficult to determine what the actual magnitude of the static pressure drop was accurately during the transient blowdown. For calculations purposes, the static pressure drop component was assumed to remain constant and equal to the initial static pressure of the subcooled liquid below the tubes. This was computed based on the initial density and height of the liquid, up to a maximum height of the distance between the tube bundle and the measurement location. Given that the liquid column observed in the high-speed flow visualisations remained relatively unperturbed well into the quasi-steady stage of the transient, the constant static head assumption was deemed reasonable.

This method over-predicts the actual static head since the generation of vapour would reduce the average fluid density below the tubes. The computed constant static head was typically very small and was never greater than about 3% of the maximum pressure drop measured. This means that if the static pressure drop were closer to zero in reality than the computed estimate, the drag load coefficient would be over-predicted by a maximum factor of 3%. Hence, the method is conservative in terms of determining the total contribution of the drag pressure drop across the tubes towards the hydraulic drag loading.

The tube loading drag coefficient was numerically determined by matching the area under the tube load and pressure drop curves for the quasi-steady segment of the transient. During this time, the flow through the bundle was choked and the vapour generation rate below the tubes was maximum, producing maximum amplitudes in both the load and pressure drop measurements. Essentially, this procedure gives mean values of the results over the measurement period. The static head computed for test T04 from Eq. (6-13) based on the initial density of 1,222kg/m^3 and height of 524mm was 6.3kPa. The mean drag load coefficient is shown at the bottom of Fig. 7-12. The standard deviation was also numerically computed and is shown by the dashed lines. The top and central graphs show the tube load and pressure drop measurements respectively.

The drag load coefficient for the 6-row tube bundle in test T04 was numerically determined to be 1.405 ± 0.011. This procedure effectively eliminates subjective bias in determining the drag coefficient and provides a value for which the transient pressure drop and tube load signals agree very well with each other
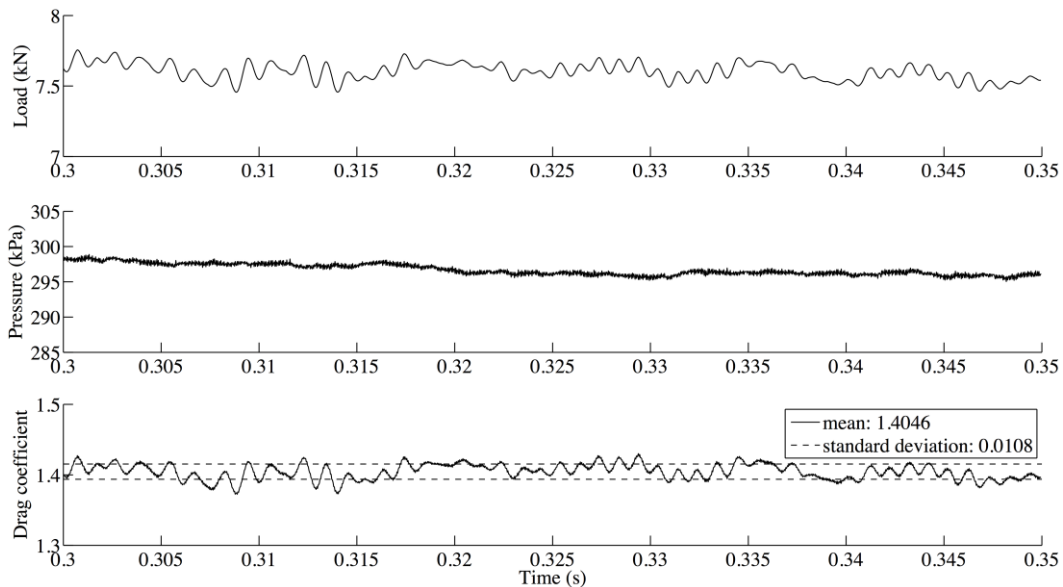
Figure 7-12. Graphical representation of drag load coefficient (test T04): tube loading (top), pressure drop (centre), numerically determined drag coefficient (bottom).

for the majority of the blowdown transient as shown in Fig. 7-13. Hence, the dynamic load measured on the 6-row tube bundle during the blowdown can be quantitatively related to the transient pressure drop across the tube bundle by simply multiplying the measured pressure drop, the pressure vessel cross-sectional flow area, and the drag load coefficient according to Eq. (7-2).

The fluid drag loading on the tube bundle depends on the two-phase mass flow rate, the tube bundle geometry, and the number of rows of tubes. By determining the drag load coefficient for different numbers of rows of tubes, the measured dynamic load can be related to the measured transient pressure drop across the tube bundle for any experiment, through a drag coefficient per tube row relationship. The computed drag coefficient for the experiments performed with various numbers of rows of tubes is shown in Table 7-1 and the overall relationship is plotted in Fig. 7-14. The procedure for establishing the drag coefficient was identical to that presented above and the complete set of graphical results is provided in Appendix F.
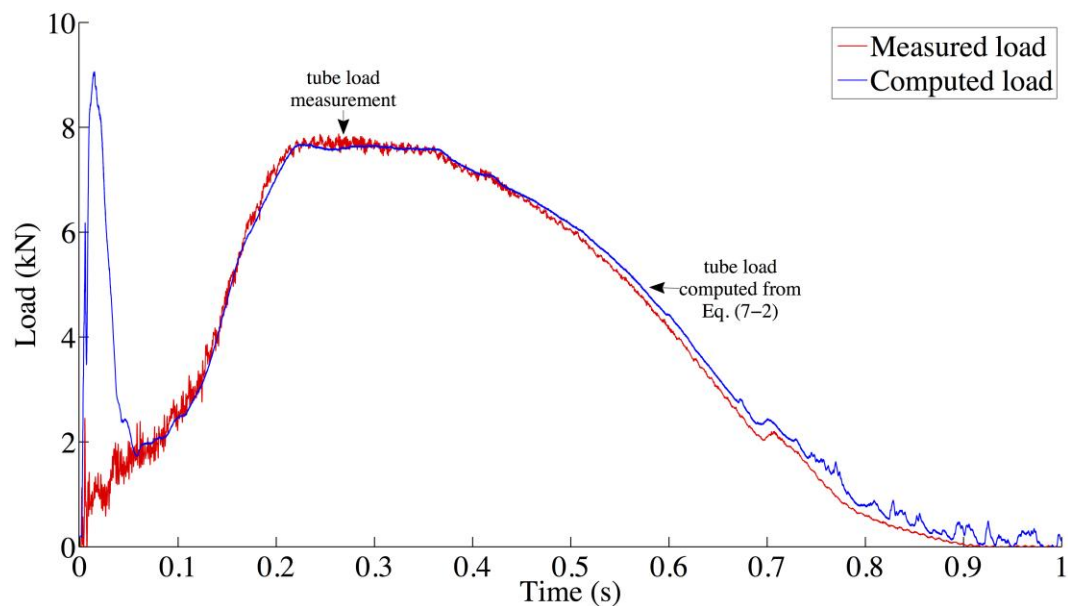
Figure 7-13. Comparison of measured tube loading and computed pressure loading (test T04).

Table 7-1. Computed tube bundle drag load coefficient values from two-phase blowdown experiments.

Test	T12	T11	T10	T09	T08	T06	T05	T04
Number of tube rows	2	3	4	5	6	6	6	6
Drag load coefficient	1.230	1.285	1.328	1.370	1.405	1.410	1.408	1.405

The overall hydraulic drag on the tube bundle is proportional to the number of rows of tubes in the bundle. The mean pressure drop for a single transverse row can be determined by dividing the total pressure drop across the entire tube bundle by the number of rows of tubes. If the number of rows of tubes in a staggered tube array is less than 10, the pressure drop per tube row may increase as the number of transverse rows is reduced (Zukauskas, 1987). This is because the flow losses and downstream wake effects in the first row become significant when the number of tube rows is 3 or less. Hence, the pressure drop per tube row in the first few rows can be significantly different from the rest of the tube bundle.

In steady-state incompressible flow calculations for tube bundles in cross-flow, correction factors are typically employed to determine the drag coefficient for the leading rows of tubes. For high velocity flows (Re $> 10^5$) in a staggered bank of tubes the correction factor is about 50% for the 1st row, 17% for the 2nd row, and 2% for the 3rd row. The pressure drop across the tube bundle varies in the first three rows, and becomes fully developed by about the fourth row. The pressure drop per tube row is then expected to increase proportionally with the number of transverse tube rows.

The relationship between the computed drag load coefficients from the current two-phase blowdown results and the number of tube rows is shown by the dashed line in Fig. 7-14. As expected, the drag coefficient for two rows does not fall on the line since the flow is not typical of that in deeper tube bundles. This
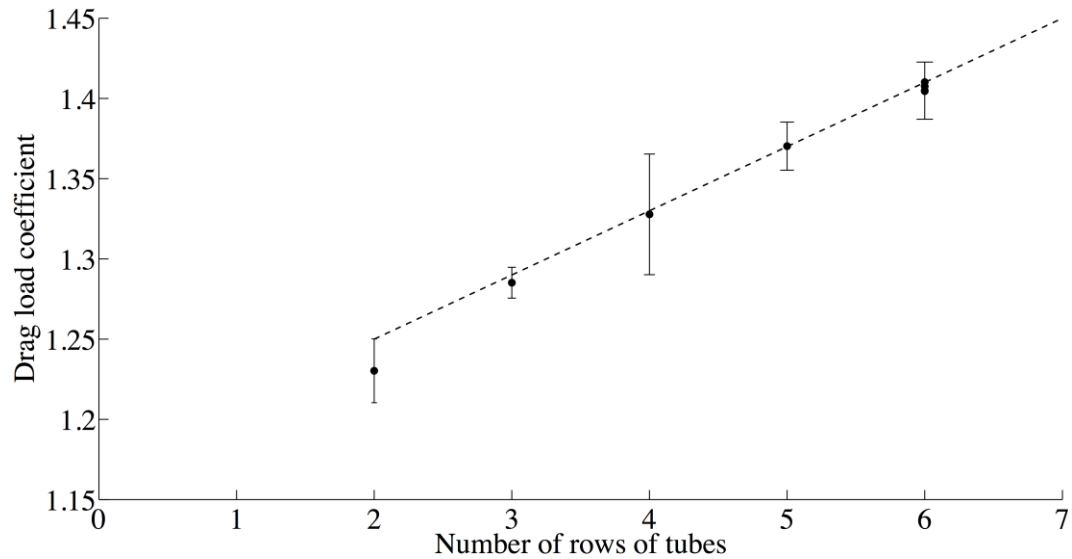
Figure 7-14. Tube bundle drag load coefficient.

trend is also seen for the case of three rows of tubes although the departure from the linear fit is smaller. The relationship between the drag load coefficient and the number of tube rows is given by Eq. (7-5),

$$C_{drag} = 1.17 + 0.04z, \tag{7-5}$$

where z is the total number of tube rows in the bundle. The 'error bars' are the standard deviation of the mean computed coefficients and provide an indication of the associated uncertainties for each point. The uncertainty observed for the 4-row experiment (test T10) was relatively greater than the other experiments. This was because the maximum load peaked earlier in test T10 (refer to Fig. 7-10) where the signals contained significant fluctuations caused by the vessel vibrations in the early stages of the transient. The actual precision in the mean signal was better than what the computed standard deviation suggests.

The drag loads computed from Eqs. (7-2) and (7-5) based on the measured pressure drops are compared to the measured dynamic loads for experiments carried out with different numbers of tube rows in Fig. 7-15. The experiments

were all performed using the same pressure vessel volume, similar initial conditions, and an initial liquid fill of about 50%. The results show that the drag load coefficient computed from Eq. (7-5) scales the pressure loading measured for all of the tests quite well. Despite having been developed using only the brief quasi-steady stage of the transient, the computed pressure loads matched the measured tube loading trends very well for the majority of the blowdown durations.

7.6. STEADY STATE FLOW COMPARISONS

As the objective of the present study is to develop a fundamental understanding of the rapid transient two-phase flow through a tube bundle during a blowdown, it was desired to verify whether any of the existing steady-state models for the pressure drop across a tube bundle could provide useful estimates of the transient pressure drop measured in this study. There has been much work in the fields of heat transfer, fluid dynamics, and flow-induced vibrations of tube
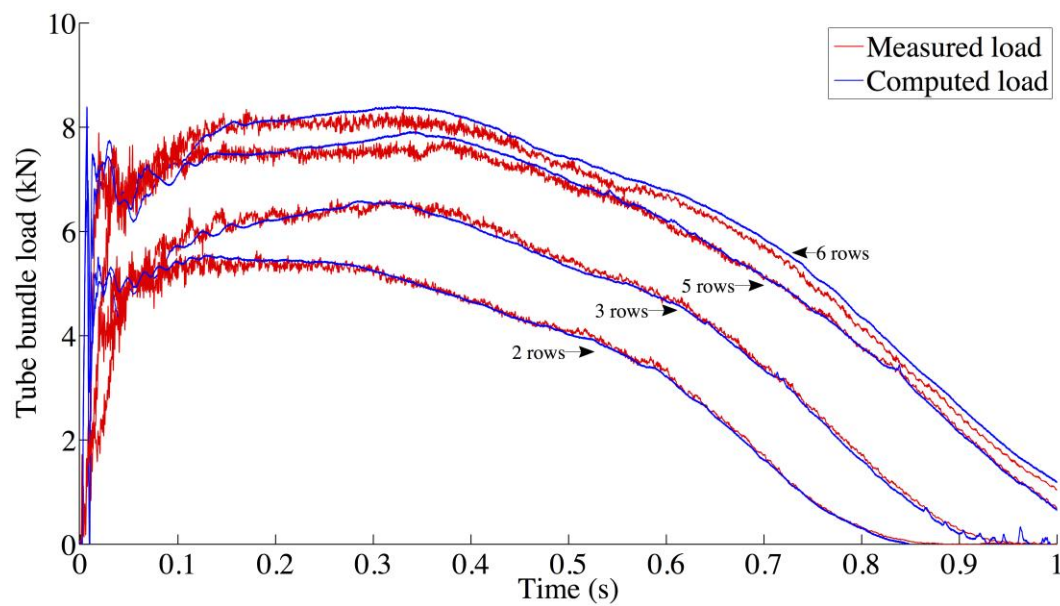
Figure 7-15. Comparison of computed pressure loads and measured loads (tests T08, T09, T11, & T12).

bundles investigating the drag of a tube within a bundle in cross-flow. The hydraulic drag is generally formulated as a function of pressure drop and empirical drag coefficients. These depend on the spacing between the tubes, the number of transverse rows, and the fluid properties.

Two-phase drag coefficients for tube bundles are empirically determined from experimental investigations. One of the most widely adopted correlations (Ishihara *et al.*, 1980) uses two-phase friction multipliers for the liquid and vapour phases. The pressure drop based on the two-phase friction multipliers does not approach the natural limits for single-phase liquid and vapour flows, and contains an unrealistic step discontinuity at the transition Reynolds number of 2000 (Consolini *et al.*, 2006). Furthermore, the two-phase friction multipliers only depend on an empirical two-phase turbulence correction parameter, which does not account for void fraction or mass flow rate. Generally, the accuracy of two-phase pressure drop correlations for tube bundles presented in the literature is limited by the range of the experimental mass flow, fluid properties, and tube bundle geometries for which the models were developed. The predictive capabilities of currently available models are not yet fully resolved and the prediction of two-phase pressure drop across tube bundles continues to be the focus of much research (Ribatski & Thome, 2007).

Under steady incompressible flow conditions, the accelerational component of the pressure drop can be estimated by determining the rate of change of momentum. When compressibility and phase change effects are included due to boiling and depressurisation, the associated changes in state can produce rapid increases in the velocity with a reduction in the fluid density. Therefore, the rate of change of momentum may not be constant through the various rows of the tube bundle. It follows then that even the relatively simple case of steady evaporating two-phase flow through a tube bundle with heat and mass transfer presents considerable modelling difficulties. For analytical modelling purposes, the transient two-phase pressure drop in the current

blowdown experiments must be approximated using simplifying assumptions due to the complex nature of the dynamic flow development through the tube bundle.

A 'single-phase' treatment of the flow using average fluid properties offers a starting point for analysing the transient pressure drop across the tube bundle during the blowdown. The flow through the tube bundle can be idealised as saturated vapour with a uniform average density and velocity. The assumption is conservative in that the choked velocity of a single-phase gas is higher than that of a two-phase mixture. This assumption is also supported by the present experimental observations, which suggest that the maximum discharge occurs during the early quasi-steady stages of rapid vapour generation.

During the initial stages of the transient blowdowns, the vapour was observed to slip past the relatively static liquid and the flow downstream of the tube bundle appeared to be homogeneous with a high void fraction. This persisted throughout the quasi-steady stage. When the pressure drop across the tube bundle began to decrease, the flow downstream of the tube bundle showed entrained liquid streams that were not present during the preceding maximum discharge stage. Hence, the pressure drop across the tube bundle was highest in the early stages when the two-phase discharge void fraction was high. The highest tube load amplitudes and flow velocities were also observed during this time.

There are several predictive tools published in the literature dealing with the steady-state pressure drop through a tube bundle for an incompressible flow. An attempt is made here to relate the measured blowdown two-phase flow through the tube bundle to steady-state pressure drop models available in the literature. In particular, the three models that were investigated and compared to the present blowdown results were the Zukauskas, Idel'chik, and Martin pressure drop models (Zukauskas, 1987; Idel'chik, 1996; Martin, 2002).

An average Reynolds number was computed from the transient 'quasi-steady' blowdown results based on estimates of the average blowdown mass flux

and inter-tube velocity. From this, a steady-state pressure drop coefficient was estimated assuming sonic single-phase saturated vapour flow conditions according to Eq. (7-6) (Zukauskas, 1987),

$$\Delta p = \frac{1}{2}\rho u^2 \xi z \, , \qquad\qquad (7\text{-}6)$$

where Δp is the pressure drop across the tube bundle, ρ is the average vapour density, u is the mean vapour velocity at the minimum cross-section in the tube bundle, ξ is an empirical steady-state pressure drop coefficient based on the tube bundle geometry and the Reynolds number, and z is the number of rows of tubes in the bundle. The vapour velocity was assumed equal to the speed of sound. For high Reynolds numbers, the skin friction coefficient of the pressure drop is negligible since the form drag is mainly responsible for the losses. Shear effects due to thermal variations are also negligible. Details of the pressure drop calculations are provided in Appendix G.

A comparison of the three steady-state pressure drop models against the transient pressure drop measured in test T08 is presented in Fig. 7-16. Test T08 was performed with a tube bundle containing six rows of tubes. The variations in the pressure drop in the first 50ms of the blowdown were associated with unsteady acoustic wave propagation and acceleration effects of the fluid downstream of the tube bundle, which did not significantly affect the loading on the tubes. The subsequent acceleration of the fluid upstream of the tubes through the tube bundle produced an increase in the pressure drop, which was observed in the measurement to begin at about 54ms. The trend of the tube loading measurement also followed the pressure drop starting at this point of the transient (refer to Fig. 7-15).

The results demonstrate that for this particular experiment, the Zukauskas model provided a good prediction of the quasi-steady two-phase pressure drop that was associated with the maximum amplitude of tube loading. The Martin
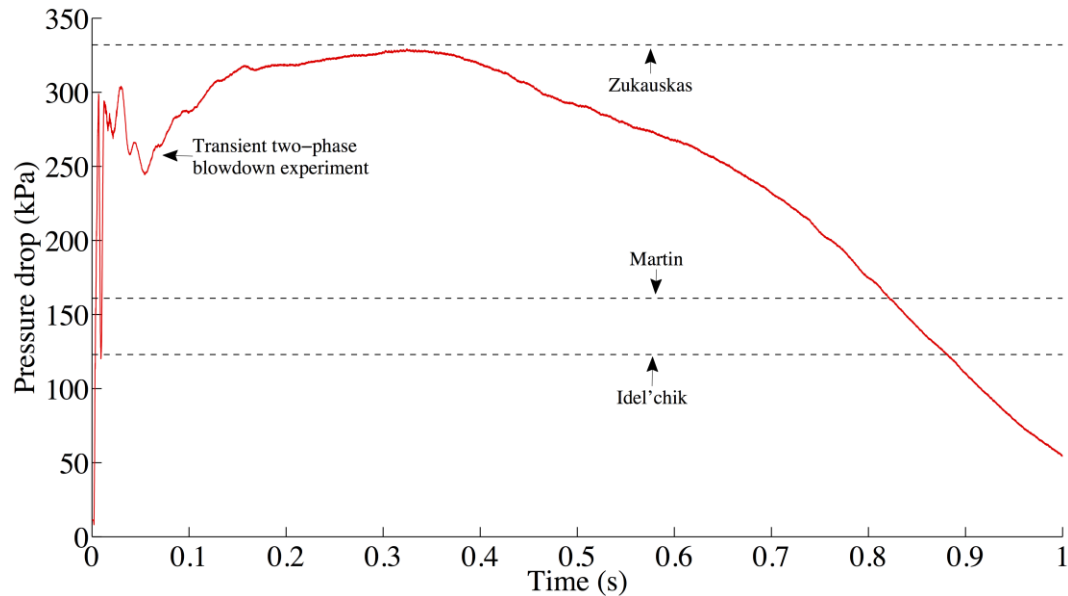
Figure 7-16. Comparison of two-phase blowdown pressure drop against computed steady-state choked vapour flow pressure drops (test T08, 6 tube rows).

model under-predicted the measured maximum pressure drop and was therefore not conservative. The Martin prediction was based on the assumption of sonic saturated vapour flow and the thermodynamic properties were obtained from the experimental quasi-steady conditions downstream of the tube bundle (125kPa). The Martin model predictions were generally found to be unsatisfactory for other cases as well.

The Zukauskas and Idel'chik predictions were also based on the assumption of sonic vapour flow but the upstream thermodynamic conditions were used in the calculations (425kPa). The Idel'chik model significantly under-predicted the pressure drop for test T08, and was found to give similarly poor pressure drop predictions for all of the experiments in this study. On the other hand, the Zukauskas model predictions were generally conservative for the experiments performed with six rows of tubes. For five rows, the Zukauskas prediction did not provide a conservative estimate, and the predictions continued to deteriorate as the number of tube rows decreased.

The Martin and Idel'chik models did not provide satisfactory results based on the attempted simplified single-phase treatment of the flow. The range of applicability for the Idel'chik and Martin models is Re $< 10^5$ and Re $< 3 \cdot 10^5$ respectively and the computed single-phase Reynolds numbers for the present experiments were between $6.7 \cdot 10^5$ and $3.51 \cdot 10^6$. This may explain the poor predictions of these two models, since the pressure drop coefficient at very high Reynolds numbers tends to level off at a nearly constant value rather than continue to decrease.

The Zukauskas model provided acceptable predictions for the experiments performed with six rows of tubes, but was not satisfactory for smaller numbers of rows. The Zukauskas model under-predictions for the shallow tube bundles may be related to the general tube row correction provided in the model, which does not consider details such as the pitch ratio. These comparisons suggest that the Zukauskas model may perhaps be adequate to use as a starting point for the conservative prediction of the maximum pressure drop across a tube bundle during transient two-phase blowdown cross-flow for bundles of sufficient depth. However, the validation from the present experiments was only obtained for tests performed with six rows of tubes and further verification of the model's adequacy for deeper tube bundles is recommended.

CHAPTER 8. SUMMARY AND CONCLUSIONS

There is very little in the published literature pertaining to the experimental study of tube bundles subjected to a rapid two-phase cross-flow during a transient blowdown. The drag load on the tubes during such events has therefore remained difficult to predict with confidence. This experimental laboratory research was undertaken to study the transient drag loading effects of a simulated blowdown on a bank of steam generator tubes in a Main Steam Line Break accident scenario. The goal of the research was to develop a better understanding of the transient two-phase tube loading and its prediction such that structural tube failures can be avoided in industrial steam generators.

A purpose built experimental facility was used containing a normal triangular tube array with a pitch ratio of 1.36. The working fluid was refrigerant R-134a, which boils at near standard pressure and temperature. Dynamic measurements of pressure, temperature, and tube loading, as well as simultaneous high-speed flow visualisations, were taken at conditions simulating a full-scale operating steam generator. The thermal-hydraulic data was obtained to study the details of the fluid transients and their effects on the tube loading. The load measurements provided a direct indication of the transient hydraulic loads on the tube bundle. No similar experimental investigations are available in the published literature and the dynamic load measurements represent a novel and original contribution of the research.

Commissioning tests showed that the shock produced by the initiation of the blowdown and the associated sudden drop in fluid temperature degraded the output signals from the sensors. The load signals could not be explained physically and initially had to be discarded as unreliable. It was considered important in this experimental investigation to correct these measurement issues

and eliminate the spurious signal sources. Thus, a program of instrumentation development was initiated to generate reliable measurement capabilities for the research.

Remedial measures were developed, which proved to be effective in eliminating the spurious effects in the output data. The noise and ringing in the pressure transducer measurements were reduced through custom designed and built shock and vibration isolation devices. These devices along with a thin surface coating of thermal insulation proved effective in eliminating the undesired effects on the signals for the duration of the blowdown transient. The high-amplitude noise and datum shift of the load measurements were also resolved using shock-absorption methodologies. Following the effort to anticipate and minimise the mechanical shock effects, the signal distortions were successfully addressed and the mean dynamic loads measured could be related to the desired fluid drag loading phenomena.

Compressed single-phase nitrogen gas blowdown tests were carried out to validate the instrumentation system using easily tractable and reasonably accurate theoretical models. The results showed that the measurements taken from the shock and thermally isolated transducers compared well with theoretical predictions. The developed experimental techniques are useful for any research applications dealing with sensors and measurements that are severely affected by violent structural dynamics produced by rapid transient phenomena. The improved flow measurement techniques could potentially lead to a better understanding of underlying physical phenomena in the fields of turbulence, hydrodynamics, multi-phase flow, and fluid-structure interaction. The shock isolation techniques are generally applicable to any related problems involving rapid pressure transients of an explosive nature.

Having established confidence in the instrument credibility, a two-phase experimental program was developed. The two-phase blowdown phenomenon is

important in many industrial applications. The results of these blowdown experiments provide a physical understanding that is useful for a wide range of problems including the design of boilers, refrigeration systems, desalination equipment, cryogenic systems, autoclave leaching processes, the transfer and storage of liquefied gases, and boiling and pressurised water nuclear reactors.

The initial stages of the blowdowns were characterised by acoustic effects related to the propagation of rarefaction waves from the breakage point. The tube bundle was not found to influence the propagation of the rarefaction waves. The sudden depressurisation in the liquid region triggered an explosive phase transition. The two-phase transient experiments indicated a significant amount of thermal non-equilibrium between the liquid and vapour phases during the blowdown. The liquid was observed to remain in a superheated state whereas the vapour temperatures rapidly dropped towards saturated thermodynamic conditions. Following the sudden depressurisation, the rapid phase transition from liquid to vapour and the associated volumetric expansion resulted in a recovery in the pressure amplitudes. The two-phase mixture accelerated towards the discharge plane and the velocity of the accelerating front was traced using high-speed imaging as well as pressure signals measured at the sensor points.

Eventually, the rates of vapour generation and fluid expulsion equalised producing a 'quasi-steady' flow condition, the duration of which depends on the test section geometry and initial liquid volume. The flow was choked during this period. When the liquid inventory was no longer capable of sustaining a vapour generation rate to match the rate of discharge, the pressure decreased and converged towards the equilibrium conditions of the containment system. The blowdowns typically lasted for about one second. The thermal-hydraulic results and high-speed flow images provide a unique large-pipe blowdown database with specific application potential in numerical code validation and verification.

A parametric study of the variation in the initial conditions and their influence on the thermal-hydraulic phenomena was performed to develop a physical understanding of the transient two-phase tube loading aspects. The experiments were conducted with varying initial liquid levels and numbers of rows of tubes in the tube bundle. The mechanisms of vapour generation and growth determined to some extent the details of the transient pressure amplitudes but had no discernible effect on the tube loading phenomena. A mass flow rate averaging procedure of the transient flashing two-phase flow gave values that were close to theoretical choked flow properties.

The pressure drop across the tube bundle controlled the rate of the system depressurisation and the maximum flow rate of the two-phase fluid, which exits the tube bundle at the critical flow rate. The two-phase flow through the bundle appeared to become choked very rapidly and the maximum amplitude of tube loading was observed to occur during this 'quasi-steady' flow discharge stage of the blowdown. After the initial unsteady effects were over, the pressure drop measured across the tube bundle was mostly due to the flow dynamic head. This pressure drop correlates very well with the tube loading measurements.

The initial liquid level with respect to the tube bundle was found to influence the timing of onset of maximum loading but did not significantly affect the maximum load amplitude. The volume of the pressure vessel upstream of the tube bundle influenced the duration of the maximum load 'plateau' but also had no significant effect on the maximum load amplitude. The maximum load was achieved early in the transients when the vapour generation rate was maximum and the flow through the bundle was choked. The maximum load value decreased monotonically with the number of rows of tubes.

The tube load measurements were generalised and can be estimated according to an empirically derived drag load coefficient for all tube bundle geometries tested in this study once the pressure drop is known. The physics of

how this loading develops during a transient two-phase blowdown are now well understood. Ultimately, the knowledge gained from this research will enable the development of a theoretical framework to estimate the dynamic load on tube bundles in nuclear steam generators during a blowdown. To use this empirical model to predict the tube loading during a blowdown, the pressure drop through the tube bundle is required as input. Normally, this must be done using a suitable transient thermal-hydraulics numerical code. Such computations are very complex and some calculations using simple steady state flow models from the literature suggest that the model proposed by Zukauskas might be useful for this purpose. However, more research is required to establish the efficacy of such an approach.

8.1. RECOMMENDATIONS FOR FUTURE WORK

Further investigation of the practical aspects of the research such as the tube array geometry and pitch ratio would be useful. While the general physical behaviour is not expected to change, such results would permit application to commercial designs with pitch ratios and patterns different from those used in the present experiments. In addition, the development of advanced transient two-phase instrumentation would uncover valuable details on the two-phase fluid dynamics that establish the transient loading on the tubes. This includes non-intrusive measurement techniques for the instantaneous void fractions, densities, and mass flow rates. The transient two-phase data acquired using such instrumentation could potentially be used to assist in the development of improved theoretical modelling of two-phase flow transients.

LIST OF REFERENCES

1.   Alamgir, M., & Lienhard, J. (1981). Correlation of pressure undershoot during hot-water depressurization. *Journal of Heat Transfer, 103*(1), 52-55.

2.   Allemann, R., Gustafson, J., Neuls, A., Townsend, W., Wilburn, N., & Witherspoon, M. (1971). *Coolant blowdown studies of a reactor simulator vessel containing a simulated reactor core*. Richland, WA: U.S. Atomic Energy Commission, Pacific Northwest Laboratory.

3.   Barták, J. (1990). A study of the rapid depressurization of hot water and the dynamics of vapour bubble generation in superheated water. *International Journal of Multiphase Flow, 16*(5), 789-798.

4.   Beaton, R., & Fletcher, C. (2003). *TRAC-M simulations of MB-2 Steam Line Breaks*. Rockville, MD: U.S. Nuclear Regulatory Commission, Information Systems Laboratories.

5.   Bhasin, V., Kushwaha, H., Mahajan, S., & Kakodkar, A. (1993). *Structural analysis of steam generator internals following Feed Water/Main Steam Line Break: DLF approach*. Bombay, India: Government of India Atomic Energy Commission, Bhabha Atomic Research Centre.

6.   Blevins, R. (1979). *Formulas for natural frequency and mode shape*. New York, NY: Van Nostrand Reinhold Company.

7.   Carey, V. (2008). *Liquid-vapor phase-change phenomena* (2nd ed.). New York, NY: Taylor and Francis.

8.   Chao, T., & Shepherd, J. (2004). Comparison of fracture response of preflawed tubes under internal static and detonation loading. *Journal of Pressure Vessel Technology, 126*(3), 345-353.

9.   Chappidi, P., Kannapel, M., Vaidya, N., & Singhal, A. (1993). *Steam Line Break and primary tube leak analysis of a Model-F generator with ATHOS-MOD1*. Huntsville, AL: Electric Power Research institute, CFD Research Corporation.

10. Collier, J., & Thome, J. (1994). *Convective boiling and condensation* (3rd ed.). Oxford, UK: Clarendon Press.

11. Consolini, L., Robinson, D., & Thome, J. (2006). Void fraction and two-phase pressure drops for evaporating flow over horizontal tube bundles. *Heat Transfer Engineering, 27*(3), 5-21.

12. Deligiannis, P., & Cleaver, J. (1992). Determination of the heterogeneous nucleation factor during a transient liquid expansion. *International Journal of Multiphase Flow, 18*(2), 273-278.

13. Deligiannis, P., & Cleaver, J. (1996). Blowdown from a vented partially full vessel. *International Journal of Multiphase Flow, 22*(1), 55-68.

14. Edwards, A., & O'Brien, T. (1970). Studies of phenomena connected with the depressurization of water reactors. *Journal of the British Nuclear Energy Society, 9*, 125-135.

15. Elias, E., & Chambré, P. (1993). Flashing inception in water during rapid decompression. *Journal of Heat Transfer, 115*(1), 231-238.

16. Forrest, C. (1995). *Flaw tolerance of steam generator tubes under accident conditions*. Ottawa, ON: Atomic Energy Control Board, Regulatory Research and Support Program.

17. Fthenakis, V. (1993). *Prevention and control of accidental releases of hazardous gases*. New York, NY: Van Nostrand Reinhold.

18. Fthenakis, V., Rohatgi, U., & Chung, B. (2003). A simple model for predicting the release of a liquid-vapor mixture from a large break in a pressurized container. *Journal of Loss Prevention in the Process Industries, 16*(1), 61-72.

19. Hahne, E., & Barthau, G. (2000). Evaporation waves in flashing processes. *International Journal of Multiphase Flow, 26*(4), 531-547.

20. Hamouda, O. (2011). *An experimental rig and investigation of steam generator tube loading during Main Steam Line Break* (M.A.Sc. Thesis). McMaster University, Hamilton, ON.

21. Huber, M., & Ely, J. (1994). A predictive extended corresponding states model for pure and mixed refrigerants including an equation of state for R134a. *International Journal of Refrigeration, 17*(1), 18-31.

22. Idel'chik, I. (1996). *Handbook of hydraulic resistance* (3rd ed.). New York, NY: Begell House.

23. Ishihara, K., Palen, J., & Taborek, J. (1980). Critical review of correlations for predicting two-phase flow pressure drop across tube banks. *Heat Transfer Engineering, 1*(3), 23-32.

24. Ishii, M., & Zuber, N. (1979). Drag coefficient and relative velocity in bubbly, droplet or particulate flows. *AIChE Journal, 25*(5), 843-855.

25. Jo, J., & Moody, F. (2015). Transient thermal-hydraulic responses of the nuclear steam generator secondary side to a Main Steam Line Break. *Journal of Pressure Vessel Technology, 137*(4). Advance Online Publication. doi:10.1115/1.4028774.

26. Kalra, S., & Adams, G. (1980). Thermal hydraulics of steam line break transients in thermal reactors - simulation experiments. *Transactions of the American Nuclear Society, 35*, 297-298.

27. Kang, K., Park, H., Cho, S., Choi, N., Bae, S., Lee, S., Kim, Y., Choi, K., Baek, W., & Kim, M. (2011). Experimental study on the blowdown load during the steam generator feedwater line break accident in the evolutionary pressurized water reactor. *Annals of Nuclear Energy, 38*(5), 953-963.

28. Krotiuk, W. (2004). *Pressurized Water Reactor steam generator internal loading following a Main Steam or Feedwater Line Break*. Washington, DC: U.S. Nuclear Regulatory Commission, Office of Nuclear Regulatory Research.

29. Lee, S., Bae, C., Prucka, R., Fernandes, G., Filipi, Z., & Assanis D. (2005). Quantification of thermal shock in a piezoelectric pressure transducer. *Society of Automotive Engineers Transactions, 114*(3), 1370-1381.

30. Levy, S. (1999). *Two-phase flow in complex systems*. New York, NY: John Wiley.

31. Lienhard, J., Alamgir, M., & Trela, M. (1978). Early response of hot water to sudden release from high pressure. *Journal of Heat Transfer, 100*(3), 473-479.

32. Martin, H. (2002). The generalized Lévêque equation and its practical use for the prediction of heat and mass transfer rates from pressure drop. *Chemical Engineering Science, 57*(16), 3217-3223.

33. Mendler, O., Takeuchi, K., & Young, M. (1986). *Loss of Feed Flow, Steam Generator Tube Rupture and Steam Line Break thermohydraulic experiments*. Washington, DC: U.S. Nuclear Regulatory Commission, Westinghouse Electric Corporation.

34. Moody, F. (1990). *Introduction to unsteady thermofluid mechanics*. New York, NY: Wiley.

35. Pinhasi, G., Ullmann, A., & Dayan, A. (2005). Modeling of flashing two-phase flow. *Reviews in Chemical Engineering, 21*(3-4), 133-264.

36. Reichelt, E. (2009). *Resolution of Generic Safety Issue 188: steam generator tube leaks or ruptures concurrent with containment bypass from Main Steam Line or Feedwater Line breaches (NUREG-1919)*. Washington, DC: U.S. Nuclear Regulatory Commission, Office of Nuclear Regulatory Research.

37. Reinke, P., & Yadigaroglu, G. (2001). Explosive vaporization of superheated liquids by boiling fronts. *International Journal of Multiphase Flow, 27*(9), 1487-1516.

38. Ribatski, G., & Thome, J. (2007). Two-phase flow and heat transfer across horizontal tube bundles ‐ A review. *Heat Transfer Engineering, 28*(6), 508-524.

39. Saha, P., Ghosh, A., Das, T., & Ray, S. (1993). Numerical simulation of pressure wave time history inside a steam generator in the event of Main Steam Line Break and Feedwater Line Break transients. *Transient Phenomena in Nuclear Reactor Systems (Proceedings of the ASME Heat Transfer Division), 245*, 131-140.

40. Sauvé, R., Tabatai, M., Savoia, D., & Kozluk, M. (1996). *Bruce 'B' steam generators flow induced vibration analysis blowdown conditions transient fatigue evaluation*. Toronto, ON: Ontario Hydro Technologies.

41. Shah, R., & Sekulić, D. (2003). *Fundamentals of heat exchanger design*. Hoboken, NJ: John Wiley & Sons.

42. Sireta, X. (1979). Experimental and theoretical study of the blowdown of the secondary side of a steam generator. *Transactions of the American Nuclear Society, 31*, 392-394.

43. Smith, B. (2010). Assessment of CFD codes used in nuclear reactor safety simulations. *Nuclear Engineering and Technology, 42*(4), 339-364.

44. Städtke, H. (2006). *Gasdynamic aspects of two-phase flow*. Weinheim, Germany: Wiley-VCH.

45. Tijsseling, A. (1996). Fluid-structure interaction in liquid-filled pipe systems: a review. *Journal of Fluids and Structures, 10*(2), 109-146.

46. Tinoco, H. (2002). Three-dimensional modeling of a Steam-Line Break in a Boiling Water Reactor. *Nuclear Science and Engineering, 140*(2), 152-164.

47. Venart, J., Rutledge, G., Sumathipala, K., & Sollows, K. (1993). To BLEVE or not to BLEVE: Anatomy of a Boiling Liquid Expanding Vapor Explosion. *Process Safety Progress, 12*(2), 67-70.

48. Wallis, G. (1969). *One-dimensional two-phase flow*. New York, NY: McGraw-Hill.

49. Wallis, G. (1980). Critical two-phase flow. *International Journal of Multiphase Flow, 6*(1-2), 97-112.

50. Whalley, P. (1987). *Boiling, condensation and gas-liquid flow*. Oxford, UK: Clarendon Press.

51. Winters Jr, W., & Merte Jr, H. (1979). Experiments and nonequilibrium analysis of pipe blowdown. *Nuclear Science and Engineering, 69*, 411-429.

52. Wolf, L. (1982). Experimental results of coupled fluid-structure interactions during blowdown of the HDR-vessel and comparisons with pre- and post-test predictions. *Nuclear Engineering and Design, 70*(3), 269-308.

53. Yu, S., & Jo, J. (2007). Analysis on transient piping pressure and force caused by high pressure steam flow disturbances. *Nuclear Engineering and Design, 237*(3), 260-267.

54. Ziada, S., Oengören, A., & Bühlmann, E. T. (1989). On acoustical resonance in tube arrays part I: Experiments. *Journal of Fluids and Structures, 3*(3), 293-314.

55. Zukauskas, A. (1987). Heat transfer from tubes in cross-flow. *Advances in Heat Transfer, 18*, 87-159.

56. Zukauskas, A., & Ulinskas, R. (1988). *Heat transfer in tube banks in cross-flow*. New York, NY: Hemisphere Publishing Corporation.

APPENDIX A. DESIGN DETAILS OF EXPERIMENTAL FACILITY

The basic concept of the design is to have a static fluid reservoir holding liquid at the appropriate temperature and pressure conditions, a test section model containing a sectional steam generator tube bundle, a pressure control device to suddenly release the pressure in the vessel, and a vacuum tank of sufficient volume that the blowdown transient is not controlled by rising downstream pressure. Calculations and practical considerations such as available space and cost led to a design based on 6" (15.24cm) standard Schedule 40 steel pipe and a 240gal (908.5L) vacuum tank. All of the components of the experimental facility were custom made at McMaster University except for standard off-the-shelf components and specially made custom parts by outside suppliers.

A.1. PRESSURE VESSEL

The pressurised liquid reservoir is made from standard 6" (15.24cm) Schedule 40 steel pipe with welded steel flanges. Drawings of the pressure vessel components are provided in Figs. A-1 and A-2. The total length of the bottom reservoir is 18" (45.72cm), with a welded standard 6" (15.24cm) blanking flange dividing the pipe into sections approximately 4" (10.16cm) and 14" (35.56cm) long. This way, the capacity of the liquid reservoir can be changed by about 4.6L by simply turning the reservoir over.

The transition sections containing the sight windows are identical. The inside cross-section is 5.437x5.437" (138mm square), which gives the same cross-sectional area as the 6" (15.24cm) standard pipe. Each side is fitted with a 1.25" (31.75mm) thick tempered quartz glass window specially ordered and produced by Specialty Glass Products of Willow Grove, PA, with a sighting area of 3x7.5"
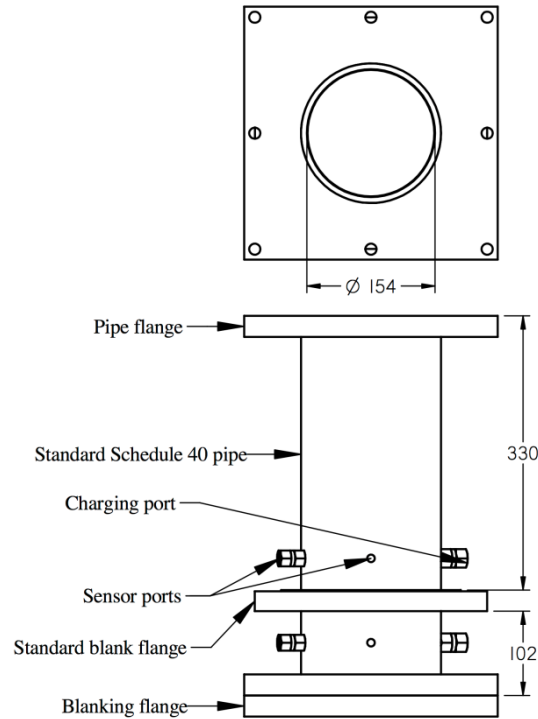
Figure A-1. Pressurised liquid reservoir (dimensions in mm).

(7.62x19.05cm). There are eight windows in total, each of which is sealed with neoprene gaskets between the glass window and its frame, and between the glass window and the clamping plate.

A.2. Tube Bundle Test Section

The test section contains a model tube bundle consisting of 0.5" (12.7mm) diameter tubes in a normal triangular geometry with a pitch ratio of 1.36. The tube bundle design is shown in Fig. A-3. The test section accommodates anywhere from 0 to 6 rows of tubes. When there are no tubes mounted in the test section, the drilled side walls are replaced by smooth blank walls. The tube array geometry, pitch ratio and tube diameter are similar to those used in CANDU steam generators. The frame holding the tube bundle is supported by four piezoelectric load cells that measure the dynamic load on tube bundle during the blowdown.
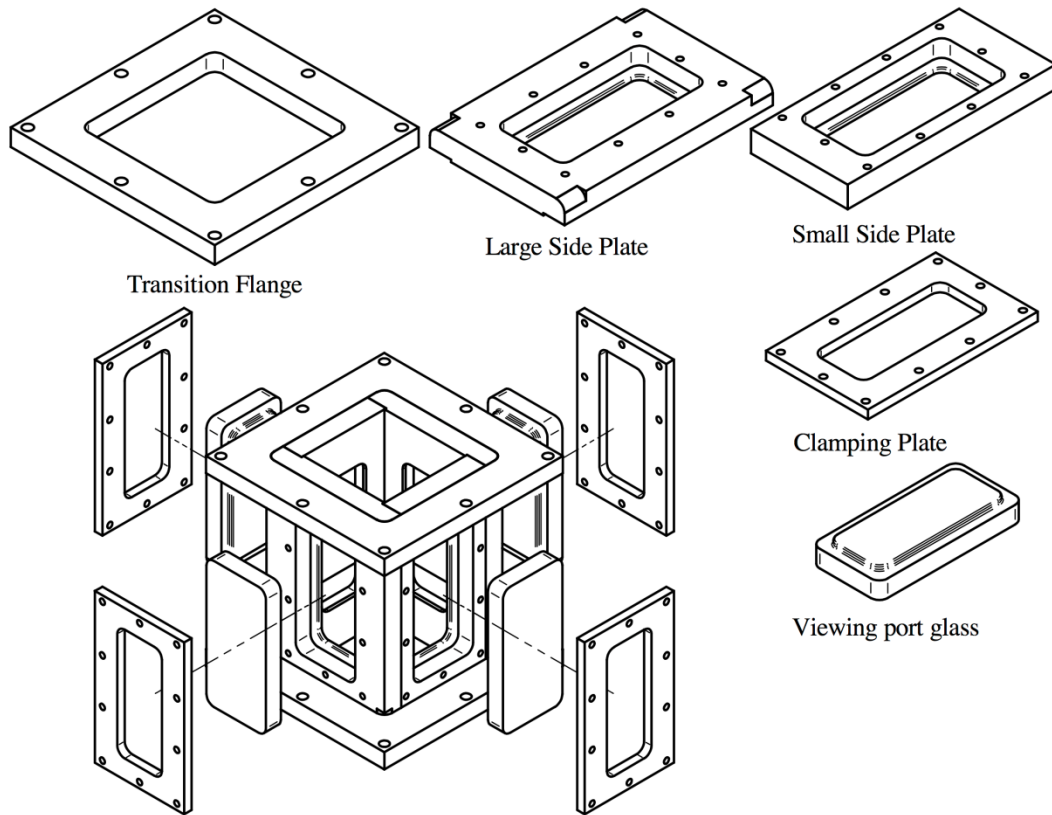
Figure A-2. Transition section assembly containing viewing windows.

The test section casing was designed so that the load cells were sealed from the R-134a using O-rings. The transient fluid blowdown load is transferred from the tube bundle to the load cells, while sealing the latter from contact with the working fluid. It was necessary to ensure that the load cells were sealed since their performance and durability cannot be guaranteed when submerged in or exposed to any liquid. This posed a significant challenge from a design perspective and the constructed test section was the product of several design iterations and intricate machining.
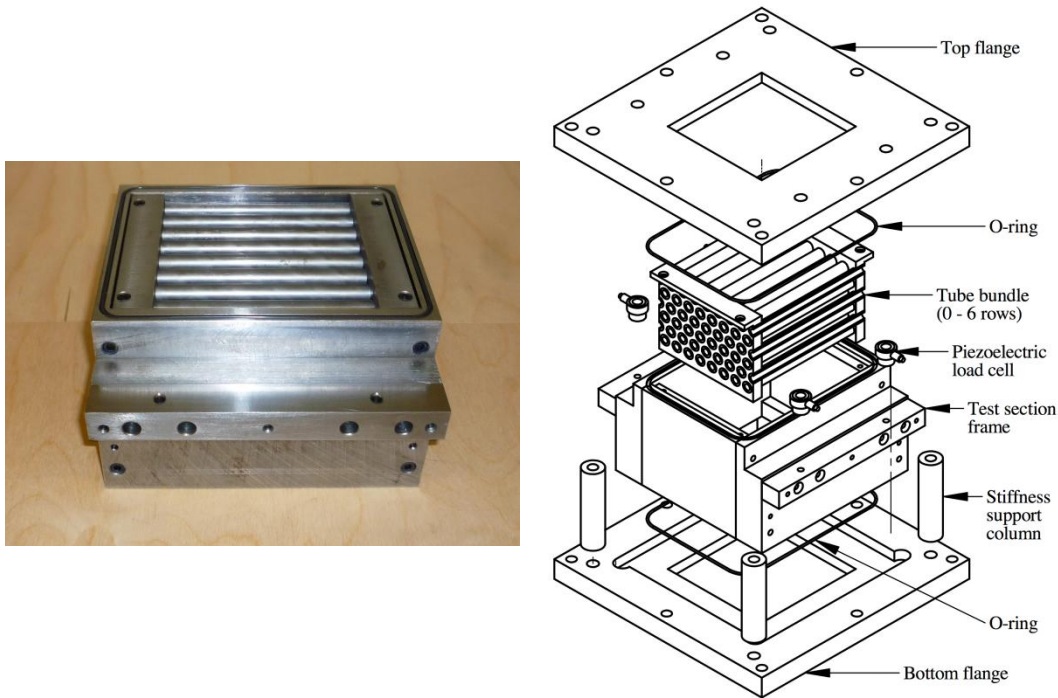
Figure A-3. Test section with tube bundle.

A.3. PRESSURE RELIEF SECTION

The device used to suddenly release the test section pressure and produce the blowdown is clearly a very important part of the design. The design criteria were that the flow area should be as close as possible to that of the pressure vessel serving the device, that the pressure difference across the device at which pressure release occurs should be controllable, and that the device should go from closed to fully open in as short a time as possible. It was decided that a rupture disc assembly was the best choice. The determining factor was the opening time of the order of milliseconds, more than ten times faster than quick-opening valves of the same size. An assembly drawing and photographs are shown in Fig. A-4.

Aluminum rupture discs (6" Poly-SD) supplied by Fike Canada were used in this study. The rupture discs are non-fragmenting and always open completely

208
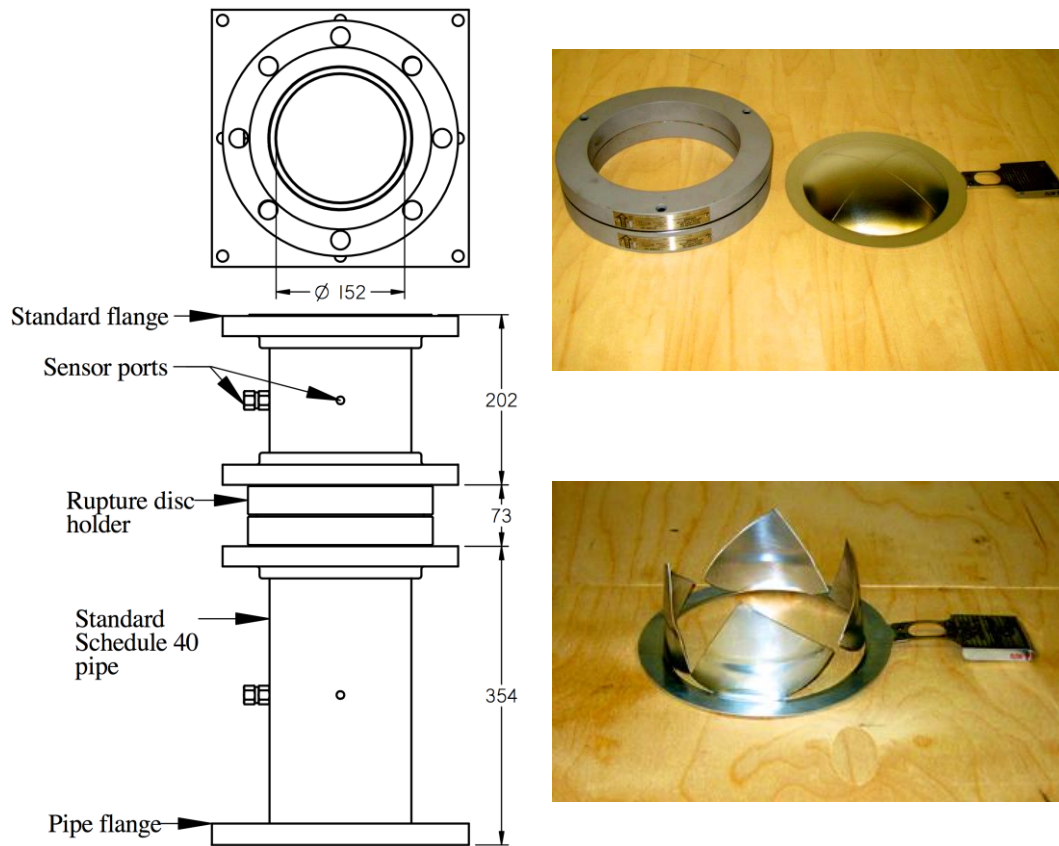
Figure A-4. Pressure relief section (left, dimensions in mm), new rupture disc (top right), open rupture disc (bottom right).

with a predictable opening pattern. The disc holder is fixed between standard 6" (15.24cm) flanges in the pipe between the transition section and the vacuum tank.

A.4. VACUUM RESERVOIR

The volume of liquid in the pressure vessel determines to some extent the length of the blowdown transient and the required volume of the vacuum tank receiver. Calculations indicated that the liquid-to-receiver volume ratio should be of the order of 60 for the maximum design pressure of 690kPa. The primary design criteria for the vacuum tank receiver were therefore that it should provide an expansion ratio of 60 or greater for the liquid R-134a in the pressure vessel,

and that it should withstand dynamic pressures at least equal to the maximum pressure in the reservoir of 690kPa. A design drawing of the vacuum tank is provided in Fig. A-5. The vacuum tank was built by Steel Fab in Oakville, ON, to ASME Code with a volume capacity of about 908L and design pressures from vacuum to 1.38MPa. The combined volume of the vacuum tank and the pipe section above the rupture disc gives a total vacuum reservoir volume of 0.913m^3.
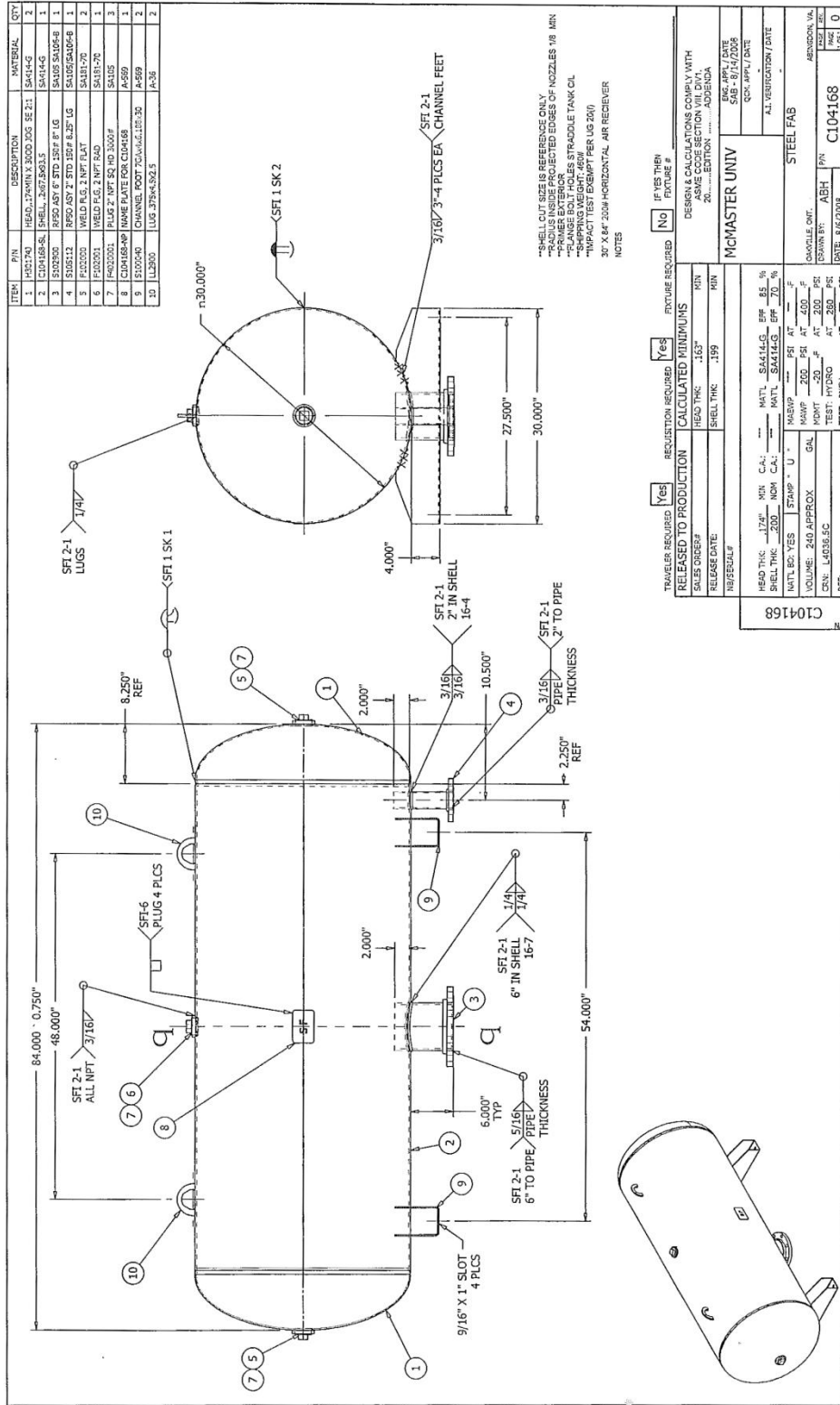
Figure A-5. Vacuum tank design.

APPENDIX B. INSTRUMENTATION DESIGN DETAILS

The following sections describe the design details associated with the selection of instruments used to acquire data in these experiments. The procedures employed for instrument calibration and the recorded output sensitivities are described in the sections corresponding to each particular measurement device. The manufacturer specifications for the entire instrumentation system are included at the end of each section.

B.1. PRESSURE SENSORS

The manufacturer specifications for the static and dynamic pressure transducers used in this experimental study are provided in Figs. B-5 to B-7. Custom designed vibration isolation devices were manufactured to eliminate vibration-induced artefacts in the dynamic pressure signals. An illustration of the assembly components of the vibration isolation device is shown in Fig. B-1. During operation, the pressure transducer is inserted into a brass ring, which significantly adds to the mass of the vibrating system. The pressure transducer and brass ring are supported by a soft elastomeric material, which reduces the transmission of mechanical vibration to the system. The design requirements were that the elastomer must not react chemically with R-134a, should provide acceptable mechanical isolation to the transducer in both the radial and transverse directions, and can withstand the maximum pressures in the rig.

The device is assembled by moulding the elastomeric material in a specially machined aluminum die with dowel pin locators. A thin layer of oil lubrication is initially applied to the aluminum surfaces to prevent adhesion during assembly. The brass ring (component 2 in Fig. B-1) is placed in the aluminum fixture (component 3) and prevented from rotating by the dowel pin
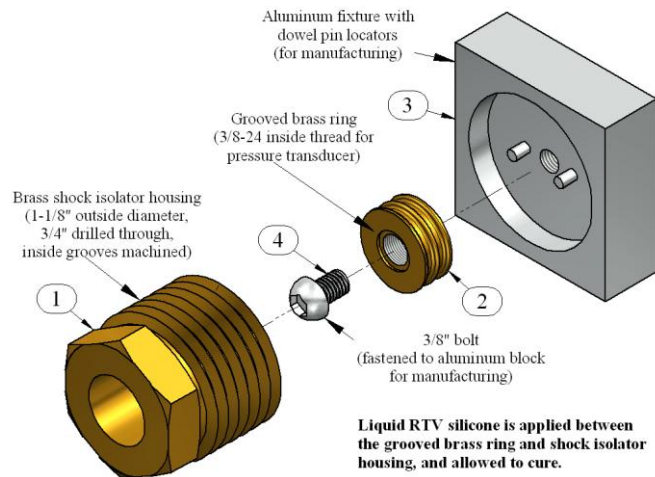
Figure B-1. Vibration isolation device manufacturing procedure.

locators. The ring is then bolted into place (component 4). Next, the isolator housing (component 1) is placed in the aluminum fixture, after which liquid RTV silicone is applied between this housing and the brass ring and allowed to cure. The bolt occupies the smooth flat machined surface in the brass ring and prevents RTV silicone encroachment. This is important to maintain pressure transducer sealing capability. The inside of the housing and the exterior of the brass ring are to provide maximal surface area for elastomer adhesion during curing.

B.1.1 PRESSURE CALIBRATION

The pressure sensors were calibrated with a pneumatic pressure-vacuum hand pump (Ralston Instruments model DPPV) using a precision pressure calibrator as the pressure reference. The test pump generates pressures from vacuum to 700kPa and allows for precise pressure adjustment within ±7Pa. The dynamic pressure transducers were difficult to calibrate because of their short discharge time constants (1.8s). Their sensitivities needed to be determined using a dynamic pressure calibration technique. A calibration device was built to provide controlled repeatable static and dynamic pressures. The device consists of a small plenum chamber that can be opened and shut using a quick-acting

solenoid valve controlled by an electrical switch. A photograph of the pressure calibration system with all of the sensors installed is shown in Fig. B-2.

The plenum configuration permits the determination of the sensor output voltages to known static as well as dynamic pressure inputs. A sample pressure measurement from each of a static and dynamic pressure sensor for a 138kPa dynamic drop in pressure in the plenum chamber is shown in Fig. B-3. Both sensors are observed to respond accurately to the transient pressure input of 80ms duration, indicating that the dynamic response of the static sensors is acceptable for such timescales. Using this device, all of the pressure sensors were calibrated against known static and dynamic pressures.

The average of three independent measurements was used to establish each dynamic pressure data point and the sensitivity was determined from seven data points ranging from 34 – 240kPa. This meant 21 measurements in total for each sensor. The sensors all showed repeatable linear dynamic response. A sample calibration chart is shown in Fig. B-4. The calibrated sensitivity of 7.52mV/kPa is within 7% of the factory provided reference sensitivity of the individual pressure transducer (7.05mV/kPa) and within 4% of the nominal specified sensitivity of the dynamic pressure transducers (7.25mV/kPa).

Figure B-2. Plenum chamber for pressure sensor calibration and response characterisation.
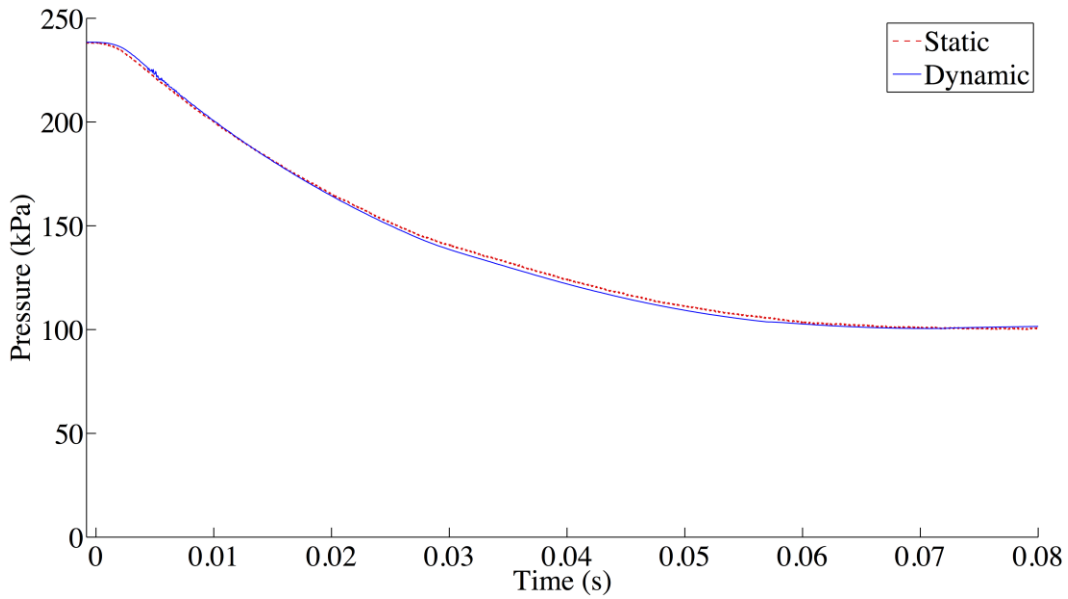
Figure B-3. Calibrated static and dynamic pressure sensor outputs for a 138kPa drop in pressure.
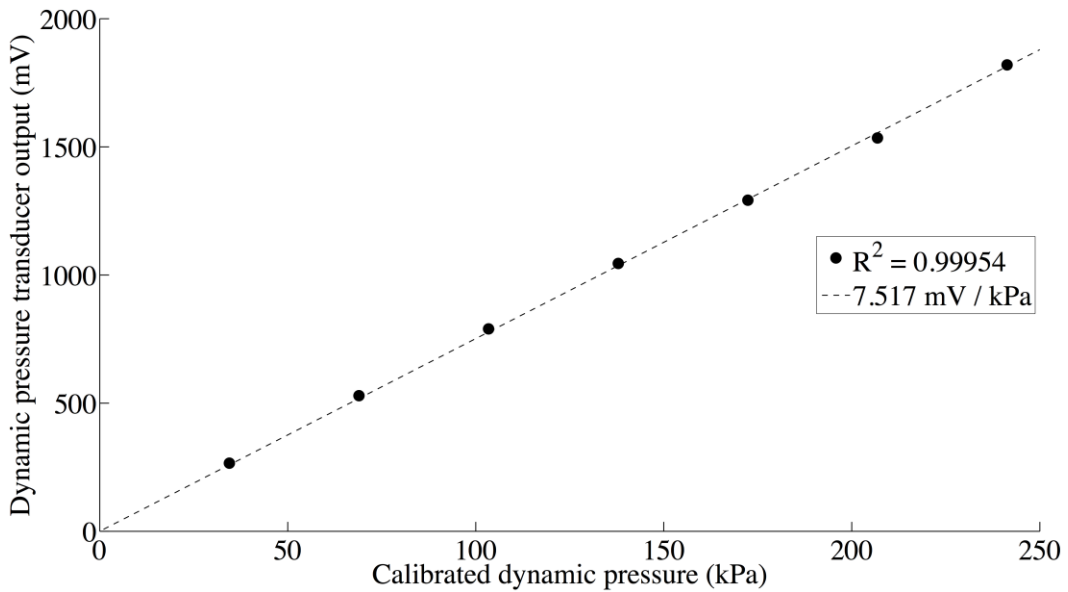
Figure B-4. Sample dynamic pressure calibration chart, $34 - 240$kPa range (nominal sensitivity 7.25mV/kPa).

PERFORMANCE SPECIFICATIONS

Ambient Temperature: 25°C (unless otherwise specified)

PARAMETERS	MIN	TYP	MAX	UNITS	NOTES
Accuracy	-0.5		0.5	%F.S. BFSL	001psiG @ 25°C
(combined non linearity, hysteresis, and repeatability)	-0.25		0.25	%F.S. BFSL	005psi @ 25°C
	-0.1		0.1	%F.S. BFSL	>005psi, <01Kpsi @ 25°C
	-0.25		0.25	%F.S. BFSL	≥01Kpsi, ≤05Kpsi @ 25°C
Isolation, Body to any Lead	1			MΩ	@ 25Vdc
Pressure Cycles	1.00E+6			FS Cycles	
Proof Pressure			3X	Rated	
Burst Pressure			4X	Rated	
Long Term Stability (1 year)	-0.25		0.25	%F.S.	001psiG
	-0.1		0.1	%F.S.	≥005psi, ≤05Kpsi
Total Error Band (over compensated range)	-1.25		1.25	%F.S.	001psiG
	-1		1	%F.S.	005psi
	-0.75		0.75	%F.S.	>005psi, ≤05Kpsi
Compensated Temperature	0		50	°C	001psiG
	0		70	°C	005psi
	-20		+85	°C	≥005psi, ≤05Kpsi
Operating Temperature	-40		+125	°C	001psi
	-40		+125	°C	≥005psi, ≤05Kpsi, Cable 105°C
Storage Temperature	-40		+125	°C	Cable 105°C
Load Resistance (R_L)	R_L > 100k			Ω	Voltage Output
Bandwidth	DC to 1KHz (Typical)				
Shock (11ms)	50g, 11msec Half Sine Shock per MIL-STD-202G, Method 213B, Condition A				
Vibration (20 to 200kHz)	±20g, MIL-STD-810C, Procedure 514.2, Fig 514.2-2, Curve L				

Figure B-5. Static pressure sensor MS U5100 specifications.

SPECIFICATION	VALUE	UNITS
PHYSICAL		
WEIGHT	6.0	GRAMS
SIZE (HEX X HEIGHT) MODEL 2200V1	.438 X 1.31	INCHES
MODEL 2201V1	.438 X 1.20	
MOUNTING PROVISION [1]	3/8-24 UNF-2A MALE THREAD	
CONNECTOR, AXIALLY MOUNTED AT TOP	10-32 UNF-2A	
BODY/CONNECTOR MATERIAL	STAINLESS STEEL, HARDENED	17-4 PH
DIAPHRAGM MATERIAL	STAINLESS STEEL	316L
PERFORMANCE		
SENSITIVITY, +20%/-10%	50	mV/Psi
RANGE F.S. FOR +5 VOLTS OUT	+100	Psi
MAXIMUM PRESSURE	1000	Psi
MOUNTED RESONANT FREQUENCY, NOM.	300	kHz
MINIMUM RISE TIME OF INPUT PRESSURE PULSE	2	µSEC
EQUIVALENT ELECTRICAL NOISE FLOOR (RESOLUTION)	.0014	Psi
NON-LINEARITY (ZERO BASED BEST FIT ST.LINE METHOD) [2]	±1	%F.S.
ACCELERATION SENSITIVITY, AXIAL DIRECTION	.001	Psi/G
DISCHARGE TIME CONSTANT	2.0	SEC
LOWER -3db FREQUENCY	.08	Hz
ENVIRONMENTAL		
MAXIMUM VIBRATION	5000	G's RMS
MAXIMUM SHOCK	10,000	G,' s PEAK
TEMPERATURE RANGE	-100 TO +250	°F
MAXIMUM FLASH TEMPERATURE AT DIAPHRAGM	+3000	°F
THERMAL COEFFICIENT OF SENSITIVITY	0.01	%/°F
ENVIRONMENTAL SEAL	HERMETIC	WELDED/GLASS TO METAL
ELECTRICAL		
EXCITATION (COMPLIANCE) VOLTAGE RANGE	+18 TO +30	VDC
EXCITATION CURRENT RANGE [3]	2 TO 20	mA
OUTPUT IMPEDANCE, NOM.	100	Ohms
OUTPUT BIAS VOLTAGE, NOM	+10	VDC
OUTPUT SIGNAL POLARITY FOR INCREASING PRESSURE	POSITIVE GOING	

Figure B-6. Dynamic pressure transducer Dytran 2200V1 specifications.

COMMON SPECIFICATIONS | **VALUE** | **UNITS**

COMMON SPECIFICATIONS	VALUE	UNITS
RESONANT FREQUENCY, NOM.	500	kHz
SENSITIVITY RANGE	0.33 to 20	mV/PSI
ACCELERATION SENSITIVITY	.001	PSI/G
LINEARITY	± 1	%
TEMPERATURE RANGE [1]	-100 to +250	^{O}F
COEFFICIENT OF THERMAL SENSITIVITY	.03	%/^{O}F
TIME CONSTANT RANGE	2.0 to 100.0	Seconds
OUTPUT IMPEDANCE, NOM	150	OHMS
BIAS VOLTAGE OF INTEGRAL AMPLIFIER	+7.5 to +9.5	VOLTS
BIAS REQUIREMENTS	+7.5 to +9.5	VOLTS
MAXIMUM SHOCK	10,000	G's
MAXIMUM VIBRATION	± 5000	G's
MAXIMUM PRESSURE (DIAPHRAGM BURST)	18,000	PSI
SUPPLY CURRENT RANGE	2 to 20	mA
COMPLIANCE (SUPPLY) VOLTAGE RANGE [2]	+18 to +30	VDC
MATERIAL, HOUSING/DIAPHRAGM	17-4ph /316L	ST. STEEL
MOUNTING 2300V SERIES	EXTERNAL 5-16/24 THREADS	
CONNECTOR	10-32	COAXIAL
ENVIRONMENTAL SEAL	WELDED, GLASS TO METAL	HERMETIC
WEIGHT	6	GRAMS

SPECIFICATIONS FOR SPECIFIC MODELS

MODEL	RANGE (PSI)	SENSITIVITY (mV/PSI)	MAX. PRESS (PSI) [3]	ELECT NOISE (Psi)	DISCHARGE TIME CONSTANT (SECONDS)	-3db LOW FREQ. (Hz)
2300V1	250	20 (± 15%)	5000	0.004	2.0	0.08

Figure B-7. Dynamic pressure transducer Dytran 2300V1 specifications.

B.2. THERMOCOUPLES

The manufacturer specifications for the fine-wire thermocouples used in this study are provided in Fig. B-9. An illustration of a thermocouple mounted in the pipe wall of the experimental facility is shown in Fig. B-8. In order to achieve a satisfactory seal, 0.125" (3.175mm) stainless steel tube fittings were inserted into the walls and the threads were sealed normally using regular pipe joint sealant. Blank Teflon ferrules for 0.125" (3.175mm) compression fittings were used instead of standard stainless steel bored ferrules. The blank ferrules were bored using a 0.27mm drill, which provides minimal clearance so that the thermocouple sheaths can be inserted carefully all the way through. The tube fittings were then mounted with the thermocouples in place, causing the Teflon ferrules to compress evenly onto the sheaths. This creates a soft non-destructive press fit that prevents leakage flow.

B.2.1 TEMPERATURE CALIBRATION

The thermocouples were calibrated against a thermistor embedded in the data acquisition connector block with a specified accuracy of $\pm 0.3°C$. During the blowdown experiments, the thermocouples measure rapid transient temperatures
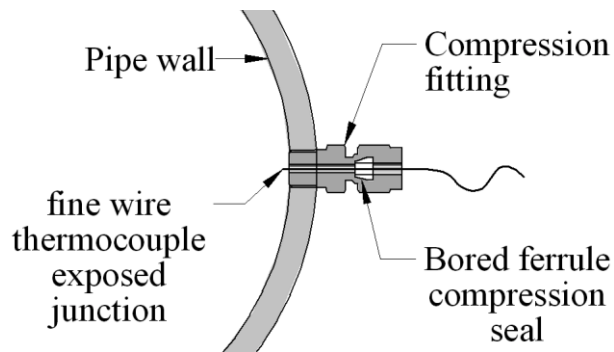
Figure B-8. Fine wire thermocouple assembly.

in the accelerating two-phase R-134a mixture. The complete phase transition from subcooled liquid to vapour occurs in about one second. During this time, the local measurements at the thermocouple junction locations represent instantaneous fluid temperatures.

The random nature of the non-equilibrium flashing phenomenon is manifested through irregular high-frequency variations in the temperature signal. The measured temperature values depend on the response time properties of the thermocouple. The response is a function of the fluid flow rate past the thermocouple junction and the heat transfer properties, which differ for each of the liquid and vapour phases. Given the extremely rapid nature of the experiments and the wide range of flow regimes encountered during the short transient time scales, the above-mentioned method of temperature calibration was regarded to be sufficient and the thermocouple measurements were deemed satisfactory.

MAXIMUM TEMPERATURE RANGE

Thermocouple Grade
− 328 to 1652°F
− 200 to 900°C

Extension Grade
32 to 392°F
0 to 200°C

LIMITS OF ERROR
(whichever is greater)
Standard: 1.7°C or 0.5% Above 0°C
1.7°C or 1.0% Below 0°C
Special: 1.0°C or 0.4%

COMMENTS, BARE WIRE ENVIRONMENT:
Oxidizing or Inert; Limited Use in Vacuum or Reducing; Highest EMF Change per Degree

TEMPERATURE IN DEGREES °C
REFERENCE JUNCTION AT 0°C
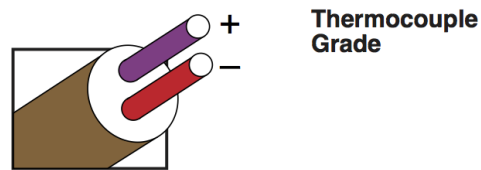
Thermocouple Grade

Nickel-Chromium
vs.
Copper-Nickel

Extension Grade

Figure B-9. Thermocouple OMEGA EMQSS-010E specifications.

B.3. LOAD CELLS

The transient fluid load on the tube bundle was measured using four load cells placed at the corners of the square test section. Manufacturer specifications for the load cells are provided in Fig. B-14. The tube bundle is mechanically isolated from the structural frame of the test section by O-rings placed between the tube bundle and the horizontal flanges above and below. The O-rings also provide sealing. They were designed to carry no load such that the load on the tube bundle is transferred entirely through the load cells.

If the clearance between the tube bundle and the flanges is compromised in any way, then the metal surfaces may come into contact. Although this would maintain a satisfactory seal and no obvious change in system behaviour would be observed, an alternate structural load path would be created, which could interfere with the desired load path for tube loading measurement. Even though the behaviour may be repeatable under similar loading conditions, it would be extremely sensitive to shock loading and external loading applied beyond the tubes, and cannot be accurately calibrated. It is therefore imperative that the designed O-ring clearance is maintained at all times for the reliable measurement of dynamic tube loading.

Several factors may influence the designed clearance. These include machining tolerances, dimensional mismatch, abrupt shock load accelerations, excessive O-ring compression due to load cell preloading, additional load exerted by the test section gravity weight, and steel flange deformation during mechanical fastening and loading. The load cell heights were examined and it was discovered that the dimensions varied by as much as 0.1mm. Since the test section had originally been precision machined to accommodate the load cell design dimensions, this dimensional mismatch resulted in an uneven distribution of the load on the tube bundle.

Upon close examination of the original test section design, the load cells were found to respond sensitively and undesirably to external loads applied beyond the tube bundle location. This indicated problems with load cell cross-sensitivity, load path transfer, and test section design. The sum of the four individual load cell signals gave the correct load in static tests, but the individual load readings were not the same and were very sensitive to any eccentricity in the loading.

In the original design, the gravity weight of the tube bundle pre-loaded the load cells in compression, and the drag loading on the tubes from the blowdown flow produced an opposite tensile force on the load cells. Upon further consideration, it was thought that the load cells might be better suited for measuring compressive forces instead. The test section was inverted so that the load cells were pre-loaded in compression between the flange and the test section frame. During the blowdown transient, the upward fluid drag loading produces further compressive loading on the load cells. The four load cells were pre-loaded by custom-built cylindrical spacers designed to account for any dimensional discrepancies and mounted between two flat polished parallel surfaces. The bolts fastening the tube bundle to the load cells were replaced by a sliding contact surface so that cross loading of the load cells would be minimised.

The O-rings employed in the original test section design were 0.127mm in diameter (model 2-173). It was postulated that alternate load paths might exist due to the small design clearances that are stipulated for standard industrial static O-ring seals of this size. A modified design was developed that implemented shallower O-ring grooves and larger O-rings (model 2-371) with a nominal thickness of 4.76mm intended to provide larger clearances of about 2mm. This was about 16 times the clearance of the original depth. The original and modified test section O-ring design clearances are shown in Fig. B-10. The objective of the change was to prevent the metal surfaces from coming into contact at any given instant during experimental rig operation. The modified design was found to

provide an impermeable seal with sufficient softness, which enabled the accurate measurement of dynamic loads on the tube bundle during the blowdown experiments.

B.3.1 DYNAMIC LOAD CALIBRATION

The average load on the tube bundle was calibrated in a manner that allowed the signals from the load cells to be correlated with the physical load on the tubes. Since the load cells are designed to measure rapidly changing forces, it was desirable to calibrate them dynamically. The calibration tests were performed by placing a known load statically on the tube bundle, allowing the dynamic signal to discharge completely, and then removing the load and recording the resultant output signal. A diagram of the process is shown in Fig B-11. The procedure begins with the suspension of known loads of up to 40kg from the tube bundle on braided high-strength wires. When the wires are suddenly cut, the weights fall to the ground and the load on the tube bundle is immediately released, producing a sharp and clean dynamic load signal.

In the transient blowdown experiments, the test section is dynamically loaded upwards towards the vacuum reservoir by fluid cross-flow through the tube bundle. Since the tube bundle perceives the load removal during calibration
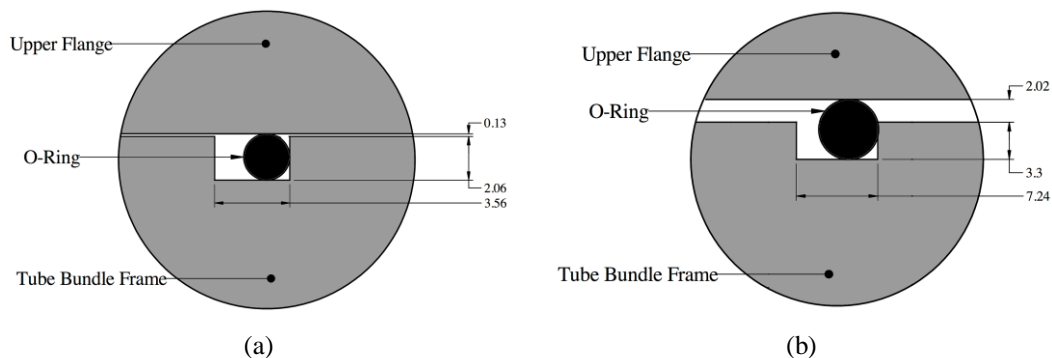
Figure B-10. Test section O-ring design clearance details: (a) original, (b) modified (dimensions in mm).
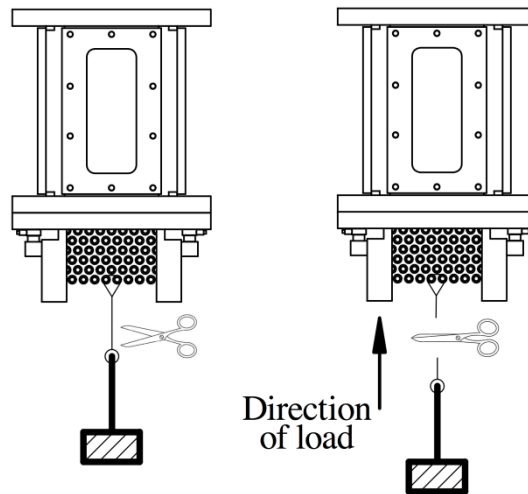
Figure B-11. Tube bundle dynamic load calibration method.

as a sudden load oriented vertically upwards, the signal polarity is the same. The procedure can be performed accurately in a controlled and repeatable fashion. For illustration purposes, a sample calibration trace of the total summed signal of the four load cells for a 31.8kg dynamic load is shown in Fig. B-12. The oscillations in the signals represent axial modes of vibration. The amplitude of the dynamic load cell response to the step input is recorded for calibration.

Figure B-13 shows the calibration chart constructed for the load cells installed in the test section assembly. The results include repeatability tests that were performed at 13.6kg, 22.7kg, and 31.8kg. The calibrated sensitivity of the load signal (0.1104mV/N) agrees within 2% of the factory specification of the load cells (0.1124mV/N). This yields an additional measure of confidence that the entirety of the load is measured through the load cells only, without any alternate load path. The calibration results of the dynamic load measurements were found to be highly repeatable and the linearity of the calibration curve demonstrates a high degree of precision in the tube loading measurements.
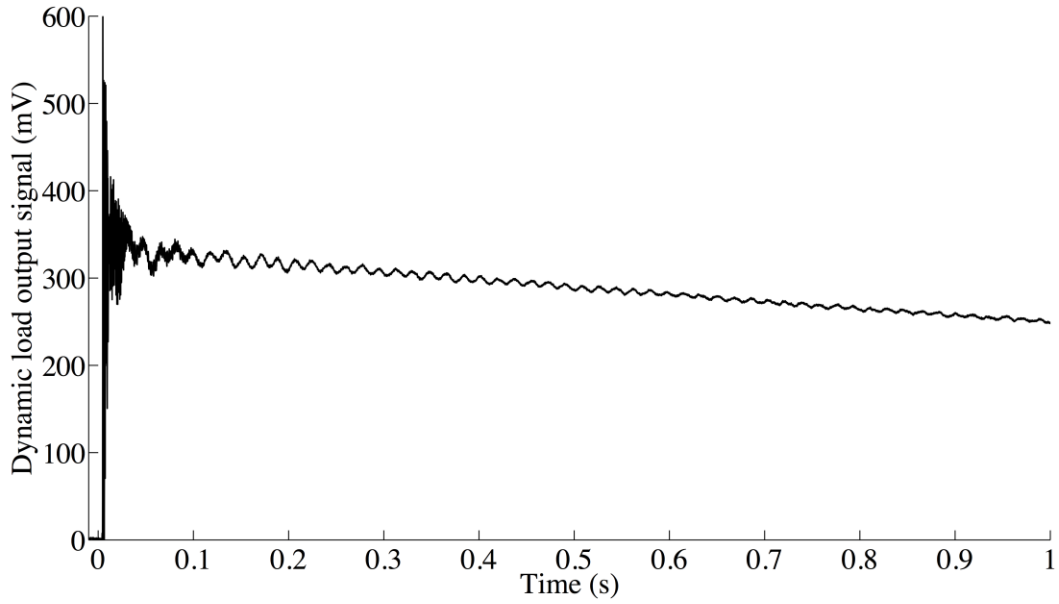
Figure B-12. Sample calibration test with 31.8kg unloading of the tube bundle.
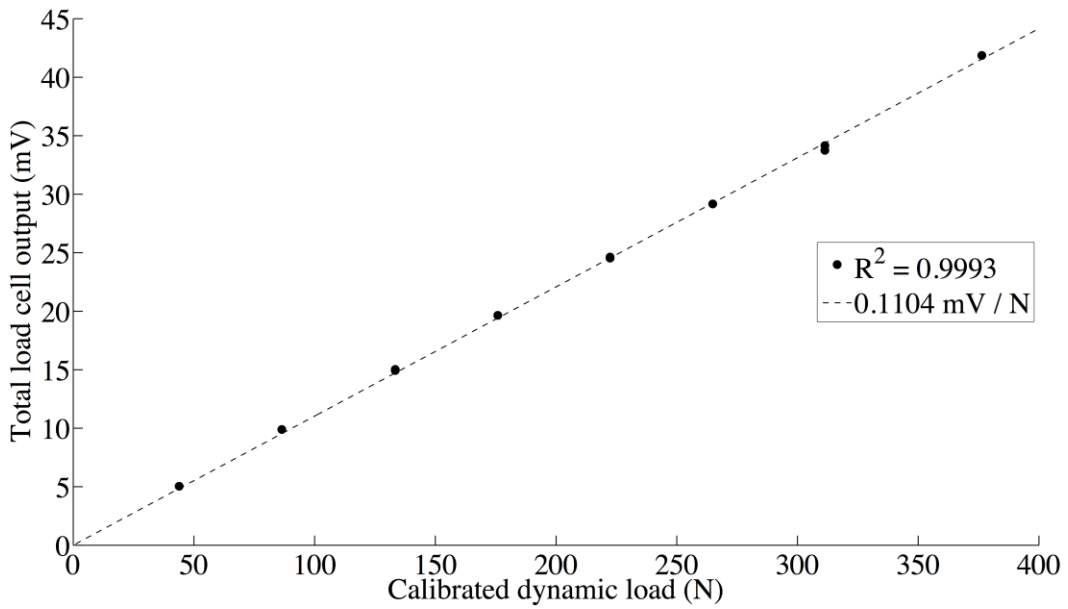
Figure B-13. Test section tube bundle dynamic load calibration curve.

SPECIFICATIONS
VOLTAGE OUTPUT
FORCE TRANSDUCER

MODEL NO		202A
RANGE (COMPRESSION)	lb	10000
USEFUL OVERRANGE	lb	15000
MAX FORCE	lb	15000
RESOLUTION	lb	.20
F.S. OUTPUT VOLTAGE	+volt	5
SENSITIVITY	mV/lb	0.50
RESONANT FREQUENCY	kHz	65
RISE TIME	μSec	10
DISCHARGE TIME CONST ⚠2	Sec	≥2000
LOW FREQ RESPONSE -5%	Hz	.0003
LINEARITY ⚠1	% FS	1
POLARITY		POSITIVE
OUTPUT IMPEDANCE	ohm	<100
OUTPUT BIAS	+volt	8 to 14
OVERLOAD RECOVERY	μSec	10
TEMP COEFFICIENT	%/°F	≤.03
TEMPERATURE RANGE	°F	-100 to +250
VIBRATION/SHOCK	G's peak	2000/5000
STIFFNESS	lb/μin	29
SEALING	welded	HERMETIC
CASE MATERIAL		ST STL
WEIGHT	gm (oz)	20 (.7)
CONNECTOR	coaxial	10-32
EXCITATION	+ VDC/mA	24-27/2-20

Figure B-14. Dynamic load cell PCB 202A specifications.

B.4. HIGH-SPEED CAMERAS

Visualisations of the transient flow through the sight glasses located below and above the test section were recorded using two high-speed cameras (Photron FastCam models SA4 and SA5) at a frame rate of 3000fps. The digital camera specifications are provided in Figs. B-16 and B-17. Time-synchronised high-speed imaging was established so that the transient fluid phenomena could be physically substantiated against the measurements. This permitted a fundamental interpretation of the blowdown physics, which is particularly important when it comes to determining the fluid drag loading behaviour. Valuable physical insights were gained by observing the acceleration of the liquid surface and fluid bulk and monitoring the velocity of the discharging fluid during blowdown. A photograph of the experimental facility showing the high-speed camera system set-up is provided in Fig. B-15.

Figure B-15. Photograph of experimental facility showing instrumentation and high-speed cameras.

Specifications: Partial Frame Rate / Recording Duration Table

FRAME RATE (fps)	RESOLUTION Horizontal	Vertical	MAXIMUM SHUTTER SPEED	RECORD DURATION (12-BIT) TIME (Sec.) 8GB	16GB	32GB	64GB	FRAMES 8GB	16GB	32GB	64GB
1,000	1,024	1,024		5.45	10.91	21.84	43.68	5,457	10,918	21,841	43,686
2,000	1,024	1,024		2.72	5.45	10.92	21.84	5,457	10,918	21,841	43,686
3,000	1,024	1,024		1.81	3.63	7.28	14.56	5,457	10,918	21,841	43,686
3,600	1,024	1,024		1.51	3.03	6.06	12.13	5,457	10,918	21,841	43,686
5,000	1,024	768		1.45	2.91	5.82	11.64	7,276	14,558	29,121	58,248
6,750	1,024	576	1 µs	1.43	2.87	5.75	11.5	9,701	19,410	38,829	77,665
6,750	768	768		1.43	2.87	5.75	11.5	9,701	19,410	38,829	77,665
7,500	1,024	512	1/1,000,000 sec	1.45	2.91	5.82	11.64	10,914	21,837	43,682	87,372
10,000	768	512		1.45	2.91	5.82	11.64	14,552	29,116	58,243	116,497
12,500	640	480		1.49	2.98	5.96	11.92	18,627	37,269	74,551	149,114
13,500	512	512		1.61	3.23	6.47	12.94	21,829	43,674	87,365	174,746
27,000	512	256		1.61	3.23	6.47	12.94	43,658	87,349	174,730	349,485
36,000	384	240		1.72	3.45	6.90	13.8	62,092	124,230	248,505	497,045
45,000	256	256		1.94	3.88	7.76	15.53	87,317	174,698	349,461	698,970
50,000	320	192		1.86	3.72	7.45	14.91	93,138	186,345	372,758	745,585
86,400	256	128		2.02	4.04	8.08	16.18	174,634	349,397	698,922	1,397,973
125,000	128	128		2.79	5.59	11.18	22.36	349,269	698,794	1,397,845	2,795,878
225,000	128	64		3.10	6.21	12.42	24.85	698,538	1,397,589	2,795,690	5,591,893
360,000	128	32		3.88	7.76	15.53	31.06	1,397,077	2,795,178	5,591,381	11,183,786
500,000	128	16		5.58	11.18	22.36	44.73	2,794,154	5,590,357	11,182,762	22,367,573

Sensor — 12-bit ADC (Bayer system color, single sensor) with 20 µm pixel

Shutter — Global electronic shutter from 16.7ms to 1 µs independent of frame rate

Lens Mount — Interchangeable F-mount and C-mount using supplied adapters

Extended Dynamic Range — Selectable in twenty steps (0 to 95% in 5% increments) to prevent pixel over-exposure

Memory — 8GB (standard: 5,457 frames @ maximum resolution)
16GB (option: 10,918 frames @ maximum resolution)
32GB (option: 21,841 frames @ maximum resolution)
64GB (option: 43,686 frames @ maximum resolution)

Video Output 1 — NTSC/PAL composite VBS (BNC). Ability to zoom, pan and tilt within image via keypad. Live video during recording

Video Output 2 — HD-SDI: HD-SDI 2 channel (BNC) digital output

Camera Control — Through optional keypad with integrated viewfinder and Gigabit Ethernet or RS-422

User Preset Switches — Four user selectable camera function controls mounted on the camera's rear panel

Low Light Mode — Low light mode drops the frame rate and shutter time to their maximum values, while maintaining other set parameters, to enable users to position and focus the camera

Triggering — Selectable positive or negative TTL 5Vp-p or switch closure

Trigger Delay — Programmable delay on selected input and output triggers, 100ns resolution

Timing — Internal clock or external source

Phase Lock — Enables cameras to be synchronized precisely together to a master camera or external source, such as IRIG/GPS time codes

Event Markers — Ten user entered event markers mark specific events within the image sequence in real time. Immediately accessible through software

Dual Speed Recording — Enables the recording speed to be changed up or down by a factor of 2, 4 or 8 during a recording

Trigger Modes — Start, End, Center, Manual, Random, Random Reset, Random Center, Random Manual and Duals Speed Recording

Saved Image Formats — JPEG, AVI, TIFF, BMP, RAW, PNG, MOV and FTIF. Images can be saved with or without image or comment data

Data Display — Frame Rate, Shutter Speed, Trigger Mode, Date or Time, Status (Playback/Record), Real Time, Frame Count and Resolution

Partitioning — Up to 64 memory segments for multiple recording in memory

Data Acquisition — Supports Photron MCDL and DAQ

Cooling — Actively cooled

Operating Temperature — 0 - 40 degrees C (32 - 104 degree F)
Range Version increases upper limit to 45 deg. C (113 deg. F)

Mounting — 1 x 1/4 - 20 UNC, 1 x 3/8 - 16 UNC, 6 x M6

Dimensions — 160mm (6.30")H×153mm (6.02")W×242.5mm (9.55")D *excluding protrusions

Weight — 5.9 kg (13 lbs)

Power Requirements — 100V-240V AC ~ 1.5A, 50-60Hz
DC operation 20-36 V DC, 100VA

Figure B-16. High-speed camera Photron SA4 specifications.

Specifications: Partial Frame Rate / Recording Duration Table

FRAME RATE	MAXIMUM RESOLUTION		MAXIMUM SHUTTER SPEED	RECORD DURATION (12-BIT)							
(fps)	Horizontal	Vertical		TIME (Sec.)				FRAMES			
				8GB	16GB	32GB	64GB	8GB	16GB	32GB	64GB
1,000	1,024	1,024		5.46	10.92	21.84	43.68	5,457	10,918	21,841	43,686
2,000	1,024	1,024		2.73	5.46	10.92	21.84	5,457	10,918	21,841	43,686
4,000	1,024	1,024		1.36	2.73	5.46	10.92	5,457	10,918	21,841	43,686
5,000	1,024	1,024		1.09	2.18	4.37	8.73	5,457	10,918	21,841	43,686
7,000	1,024	1,024		0.78	1.56	3.12	6.24	5,457	10,918	21,841	43,686
7,500	1,024	1,000		0.75	1.49	2.98	5.96	5,588	11,180	22,365	44,735
9,300	1,024	800		0.75	1.50	3.01	6.01	6,985	13,975	27,956	55,918
10,000	1,024	744	1 μs	0.75	1.50	3.01	6.01	7,511	15,027	30,061	60,127
15,000	960	528		0.75	1.51	3.01	6.02	11,289	22,587	45,182	90,374
20,000	832	448	1/1,000,000 sec	0.77	1.54	3.07	6.14	15,352	30,716	61,443	122,898
30,000	768	320		0.78	1.55	3.11	6.21	23,284	46,586	93,189	186,396
50,000	512	272		0.82	1.64	3.29	6.57	41,090	82,211	164,452	328,934
75,000	320	264		0.90	1.81	3.61	7.22	67,737	135,523	271,097	542,244
100,000	320	192		0.93	1.86	3.73	7.45	93,138	186,345	372,758	745,585
150,000	256	144		1.03	2.07	4.14	8.28	155,230	310,575	621,264	1,242,642
300,000	256	64		1.16	2.33	4.66	9.31	349,269	698,794	1,397,845	2,795,946
420,000	128	64		1.66	3.33	6.66	13.31	698,538	1,397,589	2,795,690	5,591,893
525,000	128	48		1.77	3.55	7.10	14.20	931,384	1,863,452	3,727,587	7,455,857
775,000	128	24		2.40	4.81	9.62	19.24	1,862,769	3,726,904	7,455,175	14,911,715
930,000	128	16	369 ns	3.00	6.01	12.02	24.05	2,794,154	5,590,357	11,182,762	22,367,573
1,000,000	64	16	1/2,712,000 sec	5.59	11.18	22.37	44.73	5,588,309	11,180,714	22,365,525	44,735,146

OPTION SUBJECT TO EXPORT LICENSE CONTROL RESTRICTIONS WHERE APPLICABLE

Sensor	12-bit ADC (Bayer system color, single sensor) with 20 μm pixel
Shutter	Global electronic shutter from 16.7ms to 1 μs independent of frame rate
Lens Mount	Interchangeable F-mount and C-mount using supplied adapters
Extended Dynamic Range	Selectable in twenty steps (0 to 95% in 5% increments) to prevent pixel over-exposure
Memory	8GB (standard: 5,457 frames @ maximum resolution) 16GB (option: 10,913 frames @ maximum resolution) 32GB (option: 21,841 frames @ maximum resolution) 64GB (option: 43,686 frames @ maximum resolution)
Video Output 1	NTSC/PAL composite VBS (BNC). Ability to zoom, pan and tilt within image via keypad. Live video during recording
Video Output 2	HD-SDI: HD-SDI 2 channel (BNC) digital output
Camera Control	Through optional keypad with integrated viewfinder and Gigabit Ethernet or RS-422
User Preset Switches	Four user selectable camera function controls mounted on the camera's rear panel
Low Light Mode	Low light mode drops the frame rate and shutter time to their maximum values, while maintaining other set parameters, to enable users to position and focus the camera
Triggering	Selectable positive or negative TTL 5Vp-p or switch closure
Trigger Delay	Programmable delay on selected input and output triggers, 100ns resolution
Timing	Internal clock or external source
Phase Lock	Enables cameras to be synchronized precisely together to a master camera or external source, such as IRIG/GPS time codes

Event Markers	Ten user entered event markers mark specific events within the image sequence in real time. Immediately accessible through software
Dual Speed Recording	Enables the recording speed to be changed up or down by a factor of 2, 4 or 8 during a recording
Trigger Modes	Start, End, Center, Manual, Random, Random Reset, Random Center, Random Manual and Duals Speed Recording
Saved Image Formats	JPEG, AVI, TIFF, BMP, RAW, PNG, MOV and FTIF. Images can be saved with or without image or comment data
Data Display	Frame Rate, Shutter Speed, Trigger Mode, Date or Time, Status (Playback/Record), Real Time, Frame Count and Resolution
Partitioning	Up to 64 memory segments for multiple recording in memory
Data Acquisition	Supports Photron MCDL and DAQ
Cooling	Actively cooled
Operating Temperature	0 - 40 degrees C (32 - 104 degree F)
Mounting	1 x 1/4 - 20 UNC, 1 x 3/8 - 16 UNC, 6 x M6
Dimensions	165mm (6.50")H×153mm (6.02")W×242.5mm (9.55")D *excluding protrusions
Weight	6.2 kg (13.67 lbs)
Power Requirements	100V-240V AC ~ 1.5A, 50-60Hz DC operation 18-36 V DC, 100VA

Figure B-17. High-speed camera Photron SA5 specifications.

B.5. ACCELEROMETER

An accelerometer supplied by PCB (model 352A24) was mounted on the blowdown rig in each test to quantify the rig vibrations and validate the inertial measurements of the load cells due to these vibrations. The accelerometer has a measurement range of $\pm490\text{m/s}^2$ and a nominal sensitivity of $10\text{mV/(m/s}^2)$. The manufacturer specifications are provided in Fig. B-18. By comparing the frequency content of the accelerometer and load cell signals, the vibration component of the signal can be determined and removed from the load measurements resulting in an improved mean measurement of the transient fluid drag loading on the tube bundle.

Performance	ENGLISH	SI	
Sensitivity(± 10 %)	100 mV/g	10.2 mV/(m/s²)	
Measurement Range	± 50 g pk	± 490 m/s² pk	
Frequency Range(± 5 %)	1.0 to 8000 Hz	1.0 to 8000 Hz	
Frequency Range(± 10 %)	0.8 to 10,000 Hz	0.8 to 10,000 Hz	
Frequency Range(± 3 dB)	0.4 to 12,000 Hz	0.4 to 12,000 Hz	
Resonant Frequency	≥ 30 kHz	≥ 30 kHz	
Broadband Resolution(1 to 10,000 Hz)	0.0002 g rms	0.002 m/s² rms	[1]
Non-Linearity	≤ 1 %	≤ 1 %	[2]
Transverse Sensitivity	≤ 5 %	≤ 5 %	

Environmental

Overload Limit(Shock)	± 5000 g pk	± 49,050 m/s² pk	
Temperature Range(Operating)	-65 to +250 °F	-54 to +121 °C	
Temperature Response	See Graph	See Graph	

Electrical

Excitation Voltage	18 to 30 VDC	18 to 30 VDC	
Constant Current Excitation	2 to 20 mA	2 to 20 mA	
Output Impedance	≤ 300 ohm	≤ 300 ohm	
Output Bias Voltage	8 to 12 VDC	8 to 12 VDC	
Discharge Time Constant	0.4 to 1.5 sec	0.4 to 1.5 sec	
Settling Time(within 10% of bias)	<8 sec	<8 sec	
Spectral Noise(1 Hz)	80 µg/√Hz	785 (µm/s²)/√Hz	
Spectral Noise(10 Hz)	15 µg/√Hz	147 (µm/s²)/√Hz	[1]
Spectral Noise(100 Hz)	4 µg/√Hz	39 (µm/s²)/√Hz	[1]
Spectral Noise(1 kHz)	1 µg/√Hz	9.8 (µm/s²)/√Hz	[1]
Electrical Isolation(Base)	≥ 10^8 ohm	≥ 10^8 ohm	

Physical

Sensing Element	Ceramic	Ceramic	
Sensing Geometry	Shear	Shear	
Housing Material	Anodized Aluminum	Anodized Aluminum	
Sealing	Epoxy	Epoxy	
Size (Height x Length x Width)	0.19 in x 0.48 in x 0.28 in	4.8 mm x 12.2 mm x 7.1 mm	
Weight	0.03 oz	0.8 gm	[1]
Electrical Connector	3-56 Coaxial Jack	3-56 Coaxial Jack	
Electrical Connection Position	Side	Side	
Mounting	Adhesive	Adhesive	

CE [3]
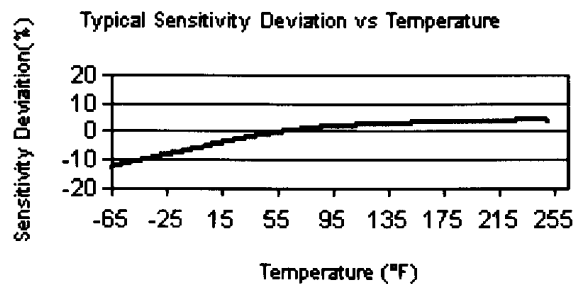
Figure B-18. Accelerometer PCB 352A24 specifications.

B.6. DATA ACQUISITION SYSTEM

Two separate cards were used for data acquisition. The dynamic pressure and load signals were obtained using an 8-channel dynamic signal acquisition card supplied by National Instruments (model PCI-4472), which has a 24-bit resolution and a 102.4kHz maximum simultaneous sampling rate for 8 analogue channels. Since the quasi-steady behaviour of the transient was of interest in this study, the data acquisition card was DC-coupled, bypassing its cut-off frequency. Two couplers (Kistler model 5134) were used to provide excitation power and signal conditioning for the piezoelectric sensors. With a -3dB cut-off frequency of 0.036Hz and a discharge time constant of 4.42s, it was possible using these power supplies to capture relatively slower events.

For the temperature and static pressure measurements, a 16-channel analogue input data acquisition card (model PCI-6221) and a connector block (model SCC-68) supplied by National Instruments were used. This provided a 16-bit resolution and a 250kHz sampling rate over the seven channels used for the thermocouples and static pressure sensors. The connector block has an embedded temperature sensor with an accuracy of ±0.3°C for cold-junction compensation of the thermocouple measurements. Signal processing for all of the measurements was performed using LabVIEW software and data reduction and processing was performed using MATLAB software. Manufacturer specifications for the DAQ systems are provided in Figs. B-19 to B-21.

In order to avoid artificial instrument phase distortion, the measurements were all accurately synchronised to a hardware-timed clock that was shared simultaneously between all of the measurement channels. The data collection system acquired simultaneous data from each instrument connected to the central data acquisition board at a rate of 30kHz. This provided a smooth signal for data analysis, which allowed proper investigation of high-frequency phenomena. An

elaborate dynamic sensor-activated triggering system was also incorporated, which initiated data recording upon the detection of a pressure rise immediately downstream of the rupture disc. This way, complete data collection was ensured for each test.

Specifications

Typical for 25 °C unless otherwise noted.

Analog Input

Channel Characteristics

Number of channels
  NI 4472 Series .... 8, simultaneously sampled
  NI 4474 Series .... 4, simultaneously sampled
Input configuration .... Unbalanced differential
Resolution .... 24 bits, nominal
Type of ADC .... Delta-sigma
Oversampling, for sample rate (f_s):
  1.0 kS/s $\leq f_s \leq$ 51.2 kS/s .... 128 f_s
  51.2 kS/s $< f_s \leq$ 102.4 kS/s .... 64 f_s
Sample rates (f_s) .... 1.0 to 102.4 kS/s in 190.7 µS/s
                                                    increments for $f_s >$ 51.2 kS/s
                                                    or 95.36 µS/s increments
                                                    for $f_s \leq$ 51.2 kS/s
Frequency accuracy .... ±25 ppm
Input signal range .... ±10 V peak
FIFO buffer size .... 1,024 samples
Data transfers .... DMA

Transfer Characteristics

Offset (residual DC) .... ±3 mV, max
Gain (amplitude accuracy) .... ±0.1 dB, max, f_{in} = 1 kHz

Amplifier Characteristics

Input impedance (ground referenced)
Positive input .... 1 MΩ in parallel with 60 pF
Negative input (shield) .... 50 Ω in parallel with 0.02 µF
Flatness (relative to 1 kHz) .... ±0.1 dB, DC to 0.4535 f_s, max,
                                                    DC-coupled
-3 dB bandwidth .... 0.4863 f_s
Input coupling .... AC or DC, software-selectable
AC -3 dB cutoff frequency
  NI 4472, NI 4474 .... 3.4 Hz
  NI 4472B .... 0.5 Hz
Overvoltage protection
  Positive input .... ±42.4 V
  Positive inputs protected .... CH<0..7>
  Negative input (shield) .... Not protected, rated at ±2.5 V
Common-mode rejection ratio (CMRR)
  $f_{in} <$ 1 kHz .... >60 dB, minimum

Dynamic Characteristics

Alias-free bandwidth (passband) .... DC (0 Hz) to 0.4535 f_s
Stop band .... 0.5465 f_s
Alias rejection .... 110 dB
Spurious-free dynamic range .... 130 dB, 1.0 kS/s $\leq f_s \leq$ 51.2 kS/s

118 dB, 51.2 kS/s $< f_s \leq$ 102.4 kS/s THD, f_{in} = 1 kHz
  0 dBFS input .... <-90 dB
  20 dBFS input .... <-100 dB
  60 dBFS input .... <-60 dB
IMD .... <-100 dB (CCIF 14 kHz + 15 kHz)
Crosstalk[1] (channel separation), f_{in} = 0 to 51.2 kHz
  Between channels 0 and 1, 2 and 3, 4 and 5, or 6 and 7
    Shorted input .... <-90 dB
    1 kΩ load .... <-80 dB
  Other channel combinations
    Shorted input .... <-100 dB
    1 kΩ load .... <-90 dB
Phase linearity .... <±0.5 deg
Interchannel phase mismatch .... <f_{in} (in kHz) x 0.018 deg + 0.082 deg
Interchannel gain mismatch .... ±0.1 dB
Filter delay through ADC .... 38.8 sample periods

Onboard Calibration Reference

DC level .... 5.000 V ±2.5 mV
Temperature coefficient .... ±5 ppm/°C maximum
Long-term stability .... ±20 ppm/$\sqrt{1{,}000}$ h

Signal Conditioning

Constant current source (software-controlled)
Current .... 4 mA, ±5%
Compliance .... 24 V
Output impedance .... >250 kΩ at 1 kHz
Current noise .... <500 pA/$\sqrt{Hz}$

Triggers

Analog Trigger

Source .... CH<0..7>
Level .... -10 to +10 V, full scale,
                                                    programmable
Slope .... Positive or negative
                                                    (software-selectable)
Resolution .... 24 bits, nominal
Hysteresis .... Programmable

Digital Trigger

Compatibility .... 5 V TTL/CMOS
Response .... Rising or falling edge
Pulse width .... 10 ns, minimum
Bus Interface
Type .... Master, slave

Power Requirements

+3.3 VDC
  PXI .... 400 mA, maximum
+5 VDC
  PCI .... 2.6 A, maximum
  PXI .... 2.2 A, maximum
+12 VDC .... 120 mA, maximum
-12 VDC .... 120 mA, maximum

Figure B-19. Data acquisition card NI 4472 specifications.

Technical Data

Type	Units	5134
Sensor Supply Factory Set	mA	4
Optional	mA	2 … 18
Gain Setpoints (±0.5 %)		1, 2, 5, 10, 20, 50
(±1 %)		100
Frequency Range (bandwidth -3 dB)		
Gain = 1 (30 kHz filter)	Hz	0.036 … 30k
Gain = 100 (10 kHz filter)	Hz	0.036 … 8k
Lowpass Filters		
2-pole Butterworth 2nd order	dB/octave	-12
Cut-off frequencies (-3 dB)	Hz	100, 1k, 10k, 30k
Frequency accuracy	%	±7
Highpass Filters (2 pole passive)	dB/octave	-12
Cut off frequency (-3 dB)	Hz	0.036
Time constant	s	3.5
Frequency accuracy	%	±10
System Test Signal:	type	white noise
Amplitude	mVrms	10
Bandwidth	Hz	1 … 30k
Flatness	dB	±10
Output:		
Voltage	V	±10
Current	mA	± 5
Impedance	Ω	100
Zero offset [1]	mV	<25

Figure B-20. Signal conditioner Kistler 5134 specifications.

Number of channels
  NI 6220/6221 .... 8 differential or
                                             16 single ended
  NI 6224/6229 .... 16 differential or
                                             32 single ended
  NI 6225 .... 40 differential or
                                             80 single ended

ADC resolution .... 16 bits

DNL .... No missing codes
                                             guaranteed

INL .... Refer to the *AI Absolute*
                                             Accuracy Table

Sampling rate
  Maximum .... 250 kS/s single channel,
                                             250 kS/s multi-channel
                                             (aggregate)
  Minimum .... No minimum
  Timing accuracy .... 50 ppm of sample rate
  Timing resolution .... 50 ns

Input coupling .... DC

Input range .... ±10 V, ±5 V,
                                             ±1 V, ±0.2 V

Maximum working voltage for analog inputs
(signal + common mode) .... ±11 V of AI GND

CMRR (DC to 60 Hz) .... 92 dB

Input impedance
  Device on
    AI+ to AI GND .... >10 GΩ in parallel
                                           with 100 pF
    AI– to AI GND .... >10 GΩ in parallel
                                           with 100 pF
  Device off
    AI+ to AI GND .... 820 Ω
    AI– to AI GND .... 820 Ω

Input bias current .... ±100 pA

Crosstalk (at 100 kHz)
  Adjacent channels .... –75 dB
  Non-adjacent channels .... –90 dB[1]

Small signal bandwidth (–3 dB) ...... 700 kHz

Input FIFO size .... 4,095 samples

Scan list memory .... 4,095 entries

Data transfers
  PCI/PXI devices .... DMA (scatter-gather),
                                             interrupts,
                                             programmed I/O
  USB devices .... USB Signal Stream,
                                             programmed I/O

Figure B-21. Data acquisition card NI 6221 specifications.

APPENDIX C. UNCERTAINTY ANALYSIS

Physical measurement uncertainties can be estimated through an analysis of the individual contributing factors. The overall uncertainty of a specific measurement, Δ, is determined from Eq. (C-1) as

$$\Delta = \sqrt{\sum_{i=1}^{n}\left(\delta_i\right)^2}\,,\qquad\qquad\text{(C-1)}$$

where δ_i refers to the individual uncertainty for any particular measured parameter. The sensor uncertainties, usually specified by the manufacturer, as well as additional uncertainties introduced by calibration procedures and the data collection system, have all been considered and incorporated in the present analysis. Generally, it was found that independent measurements obtained from multiple tests suggested a level of accuracy that is higher than specified by the manufacturers.

C.1. PRESSURE MEASUREMENT UNCERTAINTY

The uncertainty associated with the pressure calibration was ±6.9Pa. The maximum static pressure sensor measurement uncertainties, caused by output signal inaccuracies due to signal non-linearity, hysteresis, and repeatability effects, are specified by the manufacturers as ±2.07kPa. In addition, the static pressure sensors have a specified long-term stability uncertainty of ±2.07kPa. The dynamic pressure transducers have a specified signal non-linearity of ±17.2kPa and an electrical noise resolution of ±27.6Pa. The total uncertainty in the pressure measurements calculated from Eq. (C-1) for the static pressure sensors and the dynamic pressure transducers was

$$\delta p_{static} = \sqrt{\left(6.9\times10^{-3}\right)^2 + \left(2.1\right)^2 + \left(2.1\right)^2} = \pm3.0 \text{ kPa},$$

$$\delta p_{dynamic} = \sqrt{\left(6.9\times10^{-3}\right)^2 + \left(17.2\right)^2 + \left(27.6\times10^{-3}\right)^2} = \pm17.2 \text{ kPa}.$$

Simultaneous independent measurements obtained from the dynamic and static sensors during calibration agreed very well with each other to within about ±2.5kPa, suggesting that the actual measurement uncertainties were lower than the above estimates. The average deviation observed in the dynamic pressure transducer signals over a set of 21 calibration tests was between 0.5 – 1.5%. A maximum deviation of 4.3% was obtained for the smallest dynamic pressure drop of 34.5kPa. The maximum uncertainty in the pressure amplitude during dynamic calibration was found to be ±1.9kPa (0.7mV).

C.2. TEMPERATURE MEASUREMENT UNCERTAINTY

Several factors can directly contribute towards errors in the thermocouple measurements. Sources of uncertainty include isothermal error between the cold-junction thermistor and the actual cold junction formed by the thermocouple at the screw terminals of the connector block, variations in ambient temperature, heat dissipation within the connector block module, and conduction along the thermocouple wires. The thermocouple signals, being in the millivolts range, were also susceptible to external sources of noise. Furthermore, additional errors were introduced by temperature gradients within the thermocouples and metal impurities across the wires.

The cold-junction compensation uncertainty was ±0.3°C. The overall uncertainty, which implicitly accounts for all of the above factors, is ±0.85°C. The temperature uncertainty was estimated from Eq. (C-1) as

$$\delta T_{thermocouple} = \sqrt{\left(0.3\right)^2 + \left(0.85\right)^2} = \pm0.9 \text{ °C}.$$

Saturation temperatures computed based on the pressures measured in the experiments showed consistently good agreement. Corresponding temperature amplitudes from independent measurements further confirm the small uncertainty margins and the quality of the data. The average difference between the temperature measurements and the computed saturation temperatures was generally observed to be about ±0.5°C.

C.3. TUBE BUNDLE LOAD MEASUREMENT UNCERTAINTY

The weights used to calibrate the tube bundle loading were verified using an electronic scale with an uncertainty of ±0.018kg, which translates to a weight uncertainty of ±0.18N. The individual signal resolution of the load cells is ±0.89N and the signal linearity is specified by the manufacturer as ±0.44kN. Since the overall tube bundle load was measured by summing the output signal of four force transducers in parallel, the maximum uncertainty is determined by combining the uncertainty of the four individual force sensors. The individual sensor uncertainty and the overall tube loading uncertainty were estimated from Eq. (C-1) as

$$\delta F_{sensor} = \sqrt{\left(0.18\times10^{-3}\right)^2 + \left(0.89\times10^{-3}\right)^2 + \left(0.44\right)^2} = \pm 0.4 \text{ kN},$$

$$\delta F_{tubes} = \sqrt{4\times\left(0.4\right)^2} = \pm 0.8 \text{ kN}.$$

The load signal outputs during dynamic calibration suggested actual measurement uncertainty levels that were smaller than the above estimates. The load cell non-linearity quoted by the manufacturers is for the full sensor measurement range of about 180kN. The maximum loads measured in this experimental study were less than 10kN, which is only about 5% of the full measurement span. The linearity of the sensors in this range is expected to be closer to that observed during calibration.

The average load deviation during calibration was observed to be about 1.5%. A maximum deviation of 4% occurred when calibrating using the smallest dynamic load of 43.9N. The maximum amplitude of the tube load uncertainty during calibration was found to be ±5.8N (0.6mV). The linearity during calibration was observed to be about ±3.5mV, which translates to a full-span load measurement uncertainty of ±0.03kN. This is an order of magnitude lower than the computed uncertainty estimates from Eq. (C-1).

C.4. DYNAMIC RESPONSE CHARACTERISTICS

The transient nature of the blowdown phenomena investigated in this study necessitates that the instrumentation system dynamic properties must satisfy the response time and accuracy requirements of the measurements. When an input that is to be measured varies rapidly with time, the sensor output signal will generally not follow the specified linear calibration with perfect accuracy. This is because the sensors cannot respond instantly to a changing stimulus. There will always be a finite phase lag inherently associated with dynamic measurements that approach an instantaneous step change. The dynamic characteristics of sensor response must therefore be verified in order to quantify the time-dependent uncertainty involved.

The valid frequency bandwidth for measurements of acceptable accuracy can be estimated by evaluating the high and low frequency response characteristics of the instrumentation system. The frequency response specifies how fast a sensor, modelled as a first-order system, can react to changes in input. A commonly used frequency limit is the -3dB cut-off frequency, the point at which the output signal drops to about 70.7%. The upper cut-off frequency characterises how fast a sensor can react and the lower frequency characterises the slowest changing input that a sensor can accurately measure.

C.4.1 LOW-FREQUENCY RESPONSE

Direct Current (DC) coupled sensors respond accurately to static steady-state inputs of 0Hz frequency. Dynamic piezoelectric transducers do not posses this type of true static response and cannot measure events that occur at a dynamic rate below a specified cut-off frequency. This behaviour is characterised by the Discharge Time Constant (DTC), τ, of the sensors. The DTC is the time taken for the sensor output voltage to discharge 63.2% of its initial amplitude immediately following the application of a long-term steady input change. The DAQ system electronics can introduce additional low-frequency limitations (DTCs) and the system behaviour will reflect the combined effect of the sensor as well as system low-frequency characteristics. For a transient input that lasts less than 10% of the smallest DTC, the total discharge time can be estimated from Eq. (C-2),

$$\tau_{total} = \frac{\tau_{sensor} \times \tau_{electronic}}{\tau_{sensor} + \tau_{electronic}} . \qquad \text{(C-2)}$$

As a general 'rule of thumb', the relationship between the DTC and the cut-off frequency, $f_{cut\text{-}off}$, can be estimated using Eq. (C-3) for the -3dB cut-off frequency (70.7%) and Eq. (C-4) for the -5% cut-off frequency (95%),

$$\tau = \frac{1}{2\pi f_{-3dB}} = \frac{0.16}{f_{-3dB}} , \qquad \text{(C-3)}$$

$$\tau = \frac{3}{2\pi f_{-5\%}} = \frac{0.5}{f_{-5\%}} . \qquad \text{(C-4)}$$

To achieve adequate low-frequency sensor performance with less than 10% output signal discharge at the end of an input square wave, the width of the input signal pulse must not be greater than 10% of the measurement system DTC.

C.4.2 HIGH-FREQUENCY RESPONSE

Assuming no electronic limitations, the high-frequency response of a piezoelectric sensor is governed by its lowest resonant frequency. As the natural frequency of the sensor is approached, the sensitivity begins to rise rapidly and non-linearly. The mechanical structure within the sensor therefore imposes a high-frequency limit below which the response is linear and sufficiently accurate. If a sensor is modelled as a single degree-of-freedom mass-spring system with no damping, general dynamic 'rules of thumb' can be applied for determining acceptable rise-time response.

The rise time of a sensor, t_r, is defined as the time required to go from 10% to 90% of the signal amplitude upon exposure to a sudden step change. The upper frequency limit at which the sensor sensitivity will begin to deviate by greater than 5% occurs at approximately 20% of the resonant frequency. At 33% of the resonant frequency, the non-linearity error can be as high as 10%. For less than 10% signal overshoot, the duration of the shortest input pulse must therefore be at least 5 times the sensor natural period and the rise time of the input signal must be greater than 2.5 times the sensor natural period.

In addition to sensor high-frequency limitations, electronic measurement systems also impose high-frequency limitations. Generally, signal aliasing occurs at frequencies higher than half the sampling frequency and anti-aliasing filters will have cut-off frequencies just below this frequency, also known as the Nyquist frequency. In order to avoid excessive signal deterioration, the rise time of the input signal must be at least 0.45 divided by the -3dB cut-off frequency of the low-pass signal conditioner. By combining the rise times of the measurement components as the sum of the square root, an overall assessment of the rise time capability of a given measurement system can be performed. For valid high-frequency response, the desired rise time response must be at least 5 times longer

than the overall rise time of the system, which is established by sensor and electronic limitations.

C.4.3 DYNAMIC MEASUREMENT UNCERTAINTY

The dynamic characteristics specified by the manufacturers for the data collection and instrumentation system employed in this study are summarised in Table C-1. The valid frequency limits of the desired physical measurements can be determined from these frequency characteristics. The estimated frequency bandwidths for 90% measurement accuracy are presented in Table C-2 in terms of the longest pulse that can be accurately measured (low-frequency response limitation) and the shortest valid signal rise time (high-frequency limitation). By identifying the frequency range in which each instrument can perform within its acceptable margins of uncertainty, the interpretation of the dynamic measurements can be made with confidence in the calibrated linear sensitivities.

The transient pressure measurements over the full blowdown durations were acquired by combining the signals of the static and dynamic sensors. This methodology offered the advantage of an extended measurement frequency range. The validity of the signal outputs was established between steady-state 0Hz inputs and rise times as fast as 0.2ms, as shown in Table C-2. The adequate frequency response of the pressure instrumentation system was also confirmed during dynamic calibration tests and further demonstrated in the experimental blowdown measurements in this study.

The dynamic response of the temperature measurements depends on the thermal gradient established at the thermocouple junction, which is a function of the heat transfer properties of the adjacent fluid (fluid flow rate and thermal inertia). The response time of a thermocouple immersed in a pool of liquid is different from that in a gas flow due to the different heat transfer properties. The manufacturer quotes the following response times for iron-constantan 25μm fine-

Table C-1. Summary of signal acquisition system dynamic characteristics.

Instrumentation system component	Low-frequency characteristics			High-frequency characteristics		
	f_{-3dB} (Hz)	$f_{-5\%}$ (Hz)	τ (s)	f_n (kHz)	$f_{cut\text{-}off}$ (kHz)	t_r (µs)
Dynamic pressure transducers	0.08	0.25	2.0	300	60	8
Static pressure sensors	0	0	∞	N/A	1	450
Thermocouples	0	0	∞	N/A	air: 0.053 water: 0.16	air: 8438 water: 2813
Load cells	0.00008	0.00025	2000	65	13	38
Accelerometer	0.32	1	0.5	30	8	56
Dynamic DAQ	0	0	∞	N/A	13.605	33
Signal conditioner	0.036	0.1125	4.44	N/A	30	15
Static DAQ	0	0	∞	N/A	700	0.6

wire thermocouples: 50ms for a temperature change of 427°C to 38°C in still air, 4ms for the same temperature drop in air flowing at 20m/s, and 2ms for a temperature drop from 93°C to 38°C in still water.

The only available manufacturer specifications provided for the Chromel-Constantan fine-wire thermocouples used in this study are for 20m/s air flow at standard temperature and pressure. Based on the quoted response time of 3ms, the shortest valid corresponding rise time that can be accurately measured was estimated to be about 42ms. Independent response time measurements are also documented in the literature (Winters & Merte, 1979) for thermocouples dipped from room temperature into an ice water mixture. The response time was found to be about 1ms. The dynamic signal characteristics in ice water can be estimated

Table C-2. Frequency limitations of sensor measurements (to within 90% accuracy).

Measured property	Longest pulse		Shortest rise time	
	(Hz)	(ms)	(Hz)	(ms)
Dynamic pressure	7	138	2632	0.19
Static pressure	0	∞	217	2.3
Temperature	0	∞	air: 12 water: 71	air: 42 water: 14
Dynamic load	2	443	1923	0.26
Vibration	22	45	1515	0.33

from this result. The shortest valid rise time that can be measured was determined to be about 14ms.

The thermocouple response times can also be estimated analytically by modelling the heat transfer at the thermocouple junction. Since the thermocouples have very small junction diameters (63μm), the response to a step change in ambient temperature can be estimated based on simple lumped system convective analysis between the junction and the ambient fluid. Predicted thermocouple dynamic response curves for sudden exposure to 0°C conditions from room temperature (20°C) are plotted in Fig. C-1 for still air, flowing air with a velocity of 20m/s, still water, and still R-134a. The corresponding response times (63.2% of the signal output) and rise times (10% to 90% output) are given in Table C-3. The theoretical predictions demonstrate that the thermocouple response in liquid R-134a is between that of water and air. This is logical since water is a superior thermal conductor compared to R-134a, whereas air has a lower thermal conductivity.

It is difficult to quantify the actual thermocouple dynamic response in the present transient two-phase blowdown experiments due to the complex nature of the physical phenomena involved. The curves shown in Fig. C-1 provide a limited
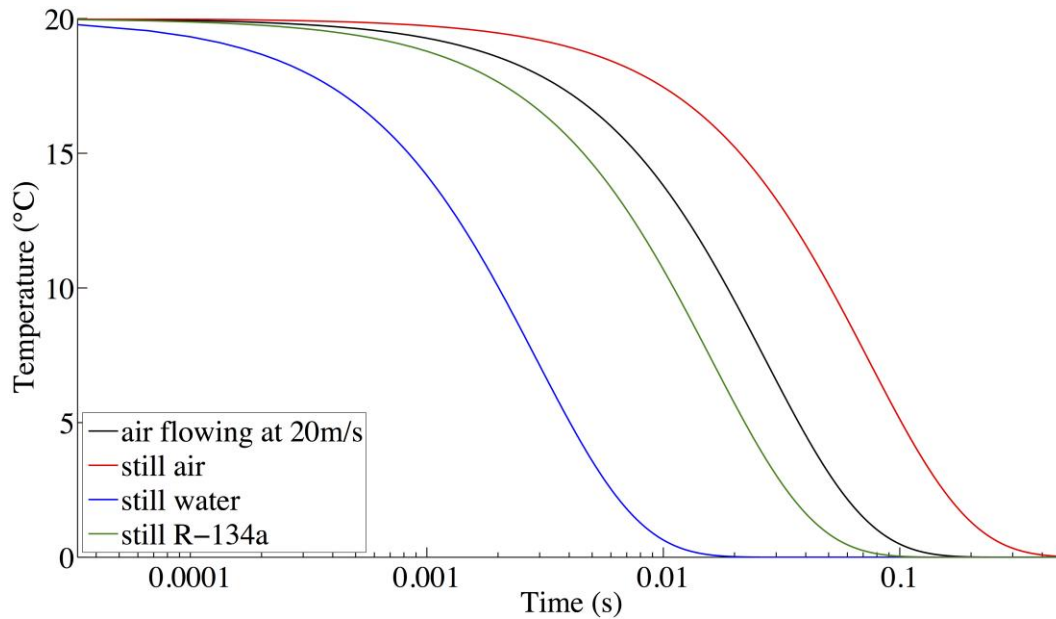
Figure C-1. Theoretical thermal response predictions for a 20°C drop in temperature.

qualitative overview for illustrative and comparative purposes only. The dynamic response estimates indicate that the thermocouple response in R-134a is expected to be faster than the quoted manufacturer response in air. Two-phase R-134a blowdown measurements performed in this study suggested a temperature response that was about the same as that of the pressure sensors. However, it is not possible to confirm whether the superheated liquid temperature measurements, which depart rapidly from the saturated vapour temperatures, represent the actual liquid temperatures or somewhere in between the vapour and liquid temperatures.

The dynamic load measurement validity range was established for load variations lasting for as long as 0.443s to as fast as about 0.3ms. Since the frequency characteristics are inherently related to the parent structure in which they are mounted (the test section), the actual dynamic response for the tube loading measurements may be different from the estimates in Table C-2. The calculations consider the load cells as independent units and do not account for

Table C-3. Predicted thermocouple output response.

Ambient fluid	Response time (ms)	Rise time (ms)
Flowing air	27	59
Still air	73	161
Still water	3	6
Still R-134a	15	35

any additional structural dynamics. Nevertheless, a broad range of acceptable dynamic performance was estimated, which was found to be satisfactory for the purposes of the tube load measurements in this study. The accelerometer validity range was estimated to be 22 – 1515Hz, which was suitable for accurately capturing the frequency content of the structural rig vibrations. These were typically observed to be in the range of about 30 – 200Hz.

APPENDIX D. EXPERIMENTAL CONDITIONS

Table D-1. List of initial test conditions arranged from smallest to largest pressure vessel liquid fill.

Experiment	R-134a Initial Conditions				V (L)		% Fill	H_l (mm)	Number of Tube Rows z
	Liquid		Vapour						
	p (kPa)	T (°C)	p (kPa)	T (°C)	Liquid	Vessel			
T01	600.3	13.9	597.8	19.1	0.8	27.5	3	45	6
T07	604.7	17.3	600.7	19.7	2.4	23.6	10	129	0
T06	599.8	18.8	594.0	19.8	5.0	23.2	21	266	6
C01	553.7	19.3	551.3	23.3	4.5	20.7	22	242	0
C04	574.3	17.9	571.4	21.2	5.2	23.2	22	277	6
T03	593.2	16.0	585.5	17.9	5.4	23.6	23	290	0
C03	568.4	17.5	565.3	20.0	5.5	23.2	24	297	6
T02	605.0	18.2	596.6	19.6	9.3	23.6	39	499	0
T09	586.4	17.7	575.5	18.4	13.7	27.5	50	751	5
T10	598.7	15.4	588.0	17.7	14.2	27.6	51	775	4
T05	615.7	17.7	605.0	19.5	12.1	23.2	52	670	6
T08	581.6	18.3	570.2	18.7	14.3	27.5	52	788	6
T11	595.6	15.9	583.8	18.1	14.6	27.7	53	794	3
T12	556.9	14.1	546.8	17.2	14.9	27.7	54	806	2
C02	578.8	16.3	571.7	21.7	11.5	20.7	56	618	0
C05	572.8	17.5	563.8	21.9	14.5	23.2	63	798	6
T04	612.1	21.1	598.1	20.1	15.4	23.2	67	848	6

APPENDIX E. EXPERIMENTAL DATA

The complete set of experimental data acquired for this research is provided here. Twelve experiments were carried out in total, which are presented in the chronological order in which they were performed. The results from five previously documented (Hamouda, 2011) preliminary commissioning tests are also included, denoted by the prefix C. These tests contain some reliable transient pressure and temperature data but, unfortunately, no reliable dynamic tube loads. Additional tests were also performed with compressed N_2 gas for instrumentation validation purposes. The results of the single-phase gas blowdowns will not be discussed here. Tables E-1 to E-17 provide the initial conditions for the respective experiments and Figs. E-1 to E-17 show measured pressures, computed saturation pressures from measured temperatures, and measured tube loads. Illustrations of the blowdown facility are also included showing the test section geometries and initial liquid surface levels for each experiment.

Table E-1. Test T01: 3% liquid, 6 tube rows.

l or g	p (kPa)	T (°C)	ρ (kg/m³)	V (L)	m (kg)	c (m/s)	H (mm)
Liquid	600.3	13.9	1248	0.8	1.05	559	45
Vapour	597.8	19.1	29.1	26.6	0.78	145	1449
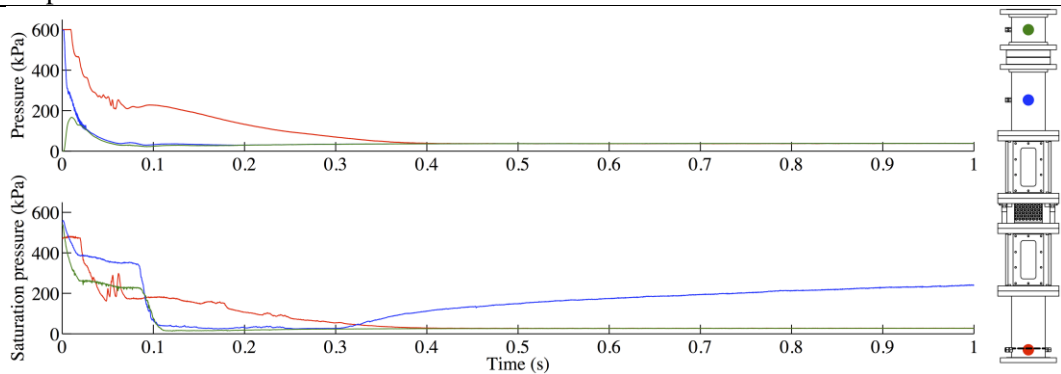
Figure E-1. Test T01: 3% liquid, 6 tube rows.

Table E-2. Test T02: 39% liquid, 0 tube rows.

l or g	*p* (kPa)	*T* (°C)	*ρ* (kg/m³)	*V* (L)	*m* (kg)	*c* (m/s)	*H* (mm)
Liquid	605	18.2	1233	9.3	11.47	539	499
Vapour	596.6	19.6	29	14.3	0.41	145	766
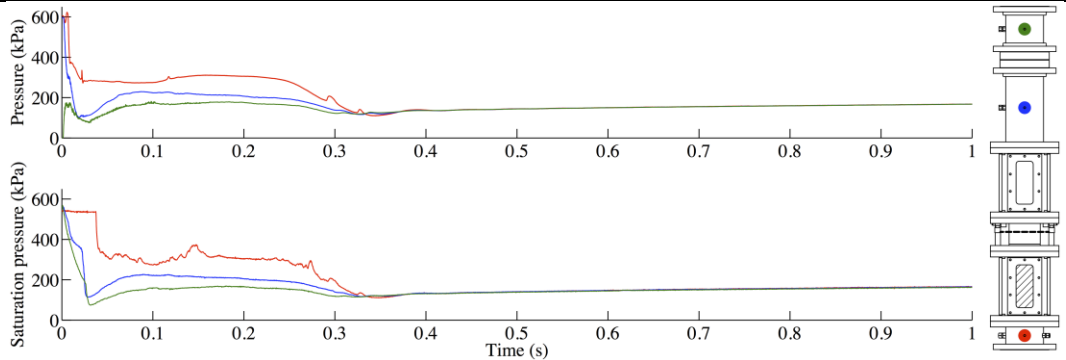
Figure E-2. Test T02: 39% liquid, 0 tube rows.

Table E-3. Test T03: 23% liquid, 0 tube rows.

l or g	*p* (kPa)	*T* (°C)	*ρ* (kg/m³)	*V* (L)	*m* (kg)	*c* (m/s)	*H* (mm)
Liquid	593.2	16	1240	5.4	6.69	549	290
Vapour	585.5	17.9	28.5	18.2	0.52	145	975
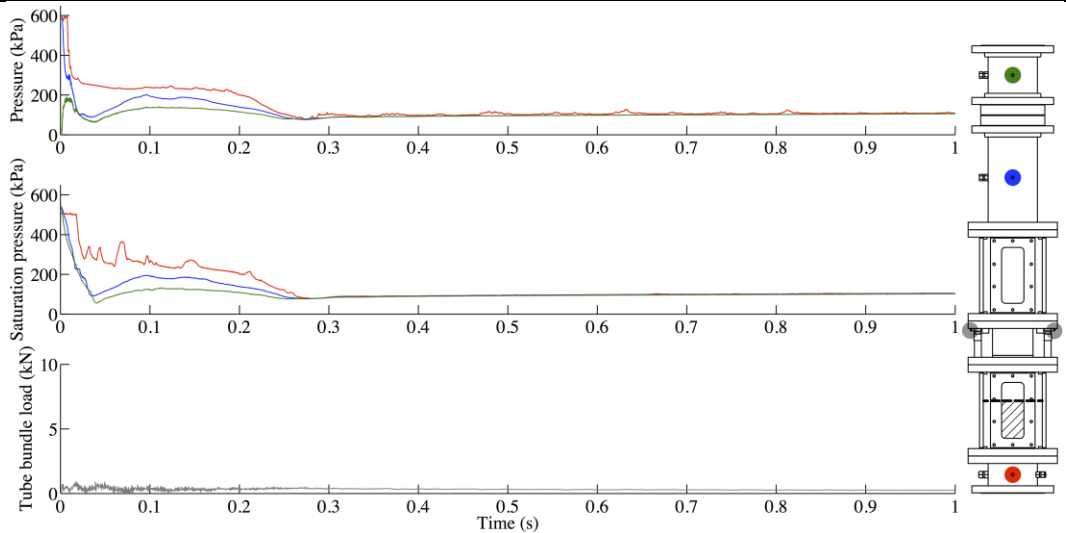
Figure E-3. Test T03: 23% liquid, 0 tube rows.

Table E-4. Test T04: 67% liquid, 6 tube rows.

l or g	p (kPa)	T (°C)	ρ (kg/m³)	V (L)	m (kg)	c (m/s)	H (mm)
Liquid	612.1	21.1	1222	15.4	18.87	525	848
Vapour	598.1	20.1	29.1	7.8	0.23	145	417
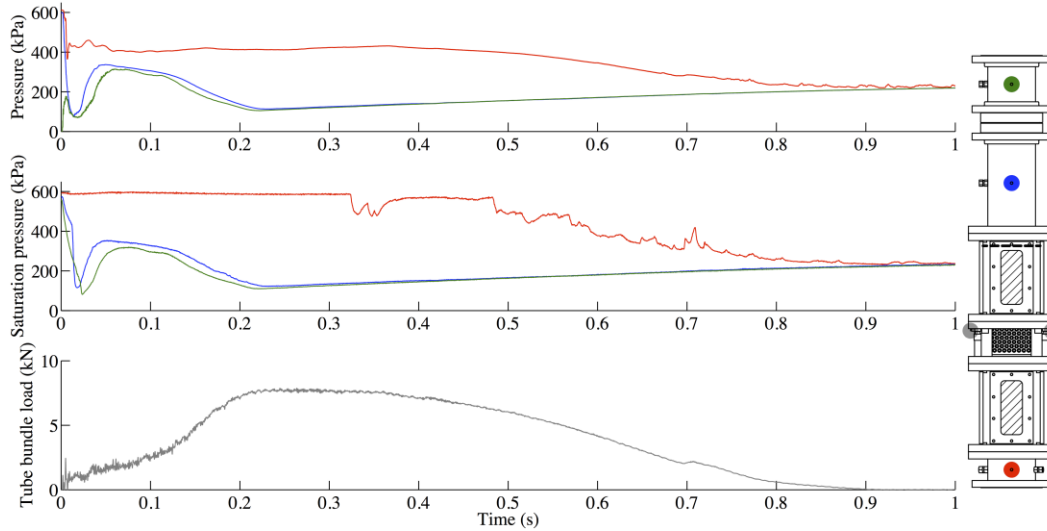
Figure E-4. Test T04: 67% liquid, 6 tube rows.

Table E-5. Test T05: 52% liquid, 6 tube rows.

l or g	p (kPa)	T (°C)	ρ (kg/m³)	V (L)	m (kg)	c (m/s)	H (mm)
Liquid	615.7	17.7	1234	12.1	14.96	541	670
Vapour	605	19.5	29.4	11.1	0.33	145	595
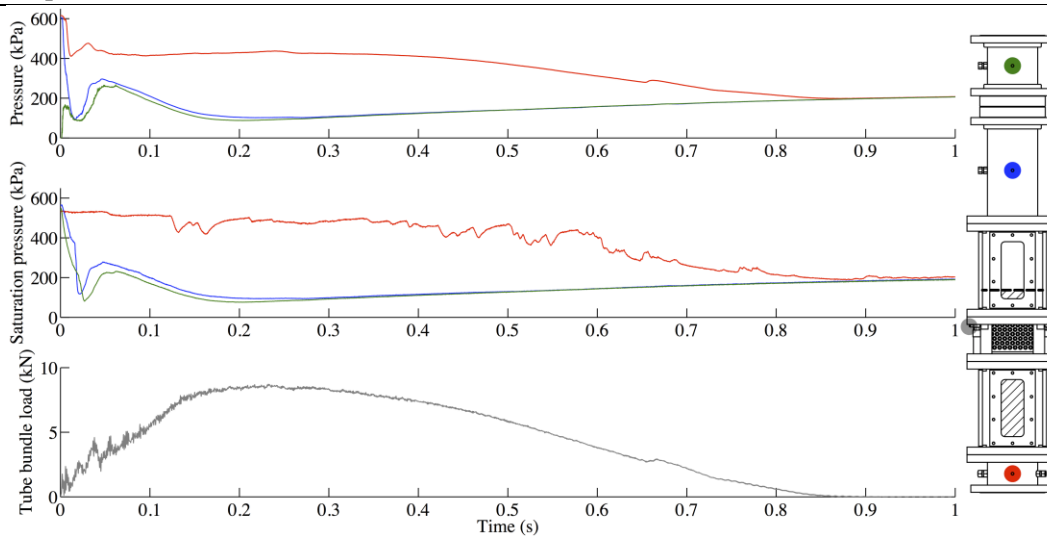
Figure E-5. Test T05: 52% liquid, 6 tube rows.

Table E-6. Test T06: 21% liquid, 6 tube rows.

l or g	p (kPa)	T (°C)	ρ (kg/m³)	V (L)	m (kg)	c (m/s)	H (mm)
Liquid	599.8	18.8	1230	5.0	6.09	536	266
Vapour	594	19.8	28.9	18.3	0.53	145	999
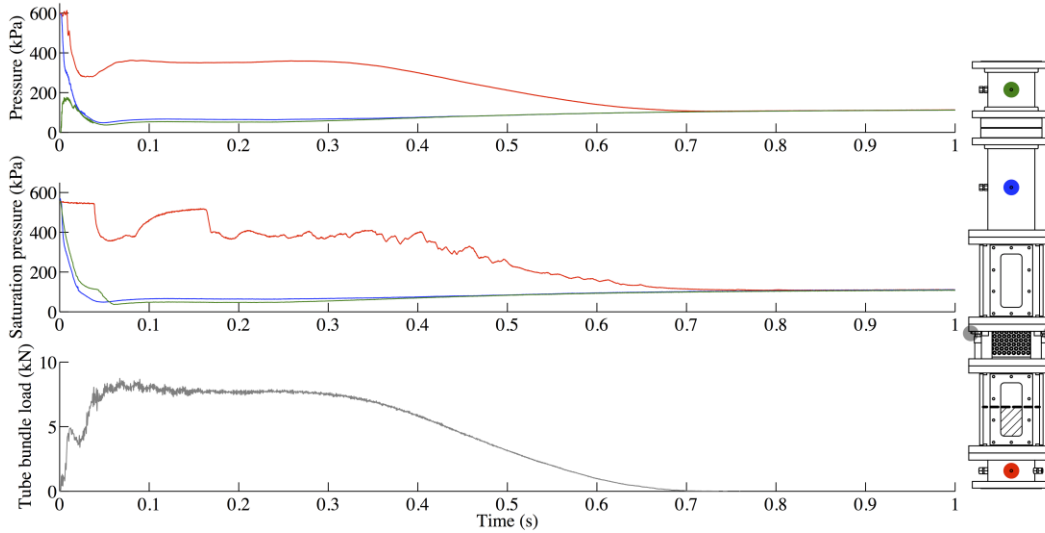
Figure E-6. Test T06: 21% liquid, 6 tube rows.

Table E-7. Test T07: 10% liquid, 0 tube rows.

l or g	p (kPa)	T (°C)	ρ (kg/m³)	V (L)	m (kg)	c (m/s)	H (mm)
Liquid	604.7	17.3	1236	2.4	2.96	543	129
Vapour	600.7	19.7	29.2	21.2	0.62	145	1136
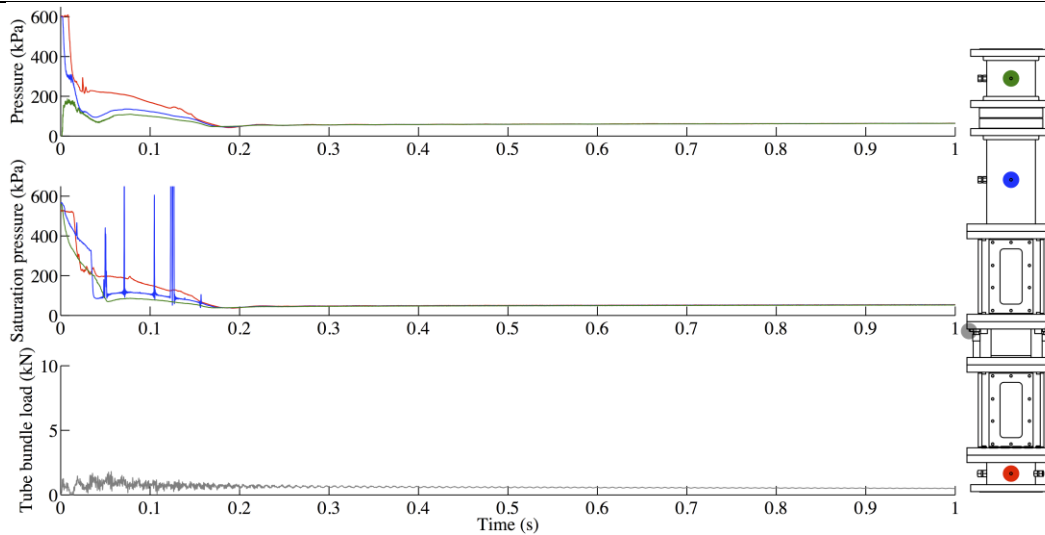
Figure E-7. Test T07: 10% liquid, 0 tube rows.

Table E-8. Test T08: 52% liquid, 6 tube rows.

l or g	p (kPa)	T (°C)	ρ (kg/m³)	V (L)	m (kg)	c (m/s)	H (mm)
Liquid	581.6	18.3	1232	14.3	17.65	538	788
Vapour	570.2	18.7	27.7	13.2	0.36	145	706
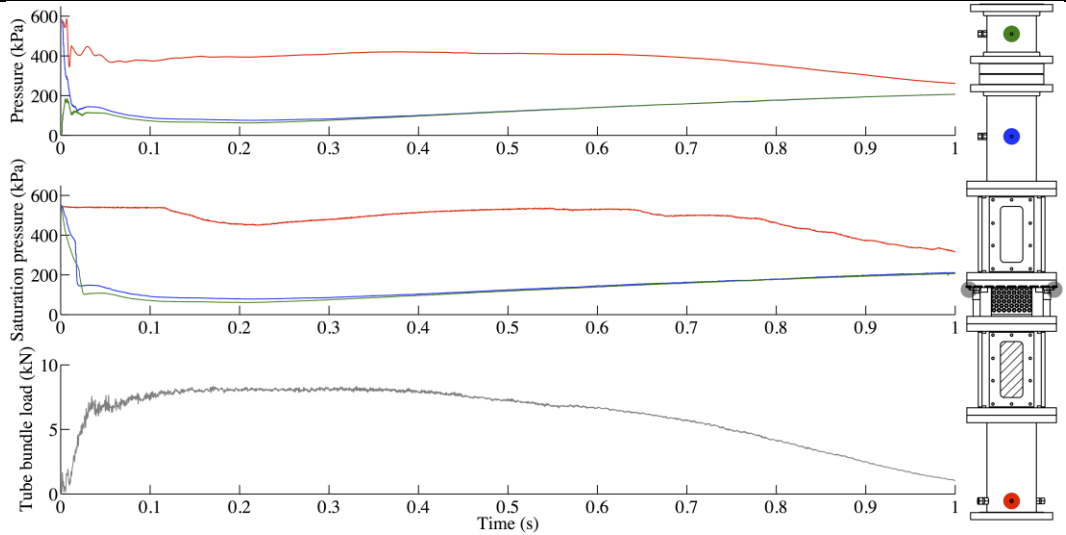
Figure E-8. Test T08: 52% liquid, 6 tube rows.

Table E-9. Test T09: 50% liquid, 5 tube rows.

l or g	p (kPa)	T (°C)	ρ (kg/m³)	V (L)	m (kg)	c (m/s)	H (mm)
Liquid	586.4	17.7	1234	13.7	16.89	541	751
Vapour	575.5	18.4	28	13.9	0.39	145	743
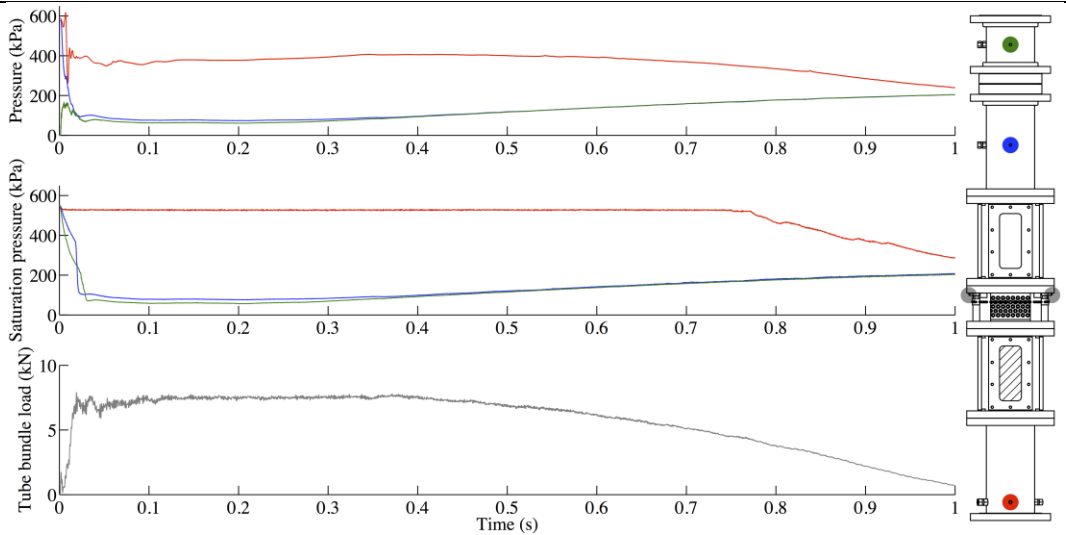
Figure E-9. Test T09: 50% liquid, 5 tube rows.

Table E-10. Test T10: 51% liquid, 4 tube rows.

l or g	p (kPa)	T (°C)	ρ (kg/m³)	V (L)	m (kg)	c (m/s)	H (mm)
Liquid	598.7	15.4	1242	14.2	17.63	552	775
Vapour	588	17.7	28.6	13.4	0.38	145	719
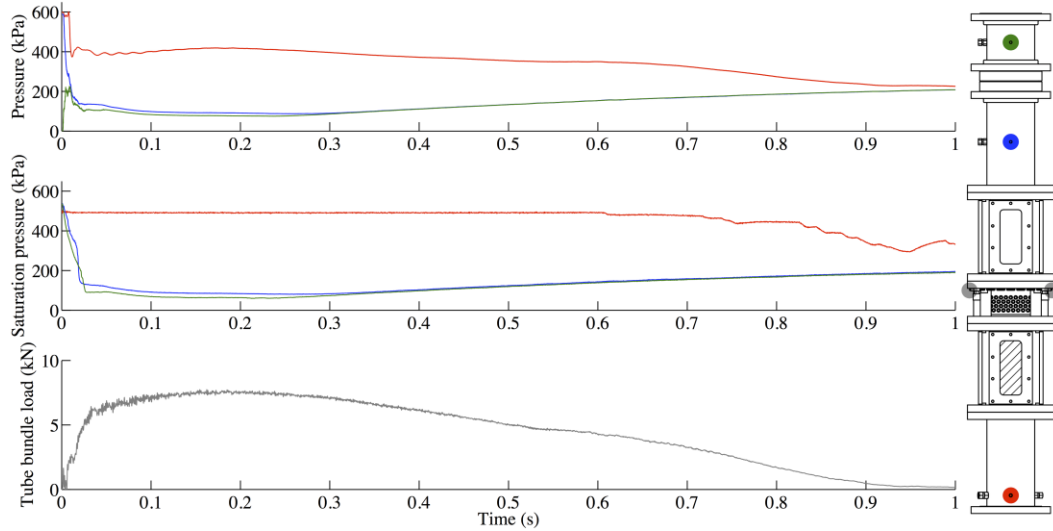
Figure E-10. Test T10: 51% liquid, 4 tube rows.

Table E-11. Test T11: 53% liquid, 3 tube rows.

l or g	p (kPa)	T (°C)	ρ (kg/m³)	V (L)	m (kg)	c (m/s)	H (mm)
Liquid	595.6	15.9	1241	14.6	18.14	549	794
Vapour	583.8	18.1	28.4	13.0	0.37	145	700
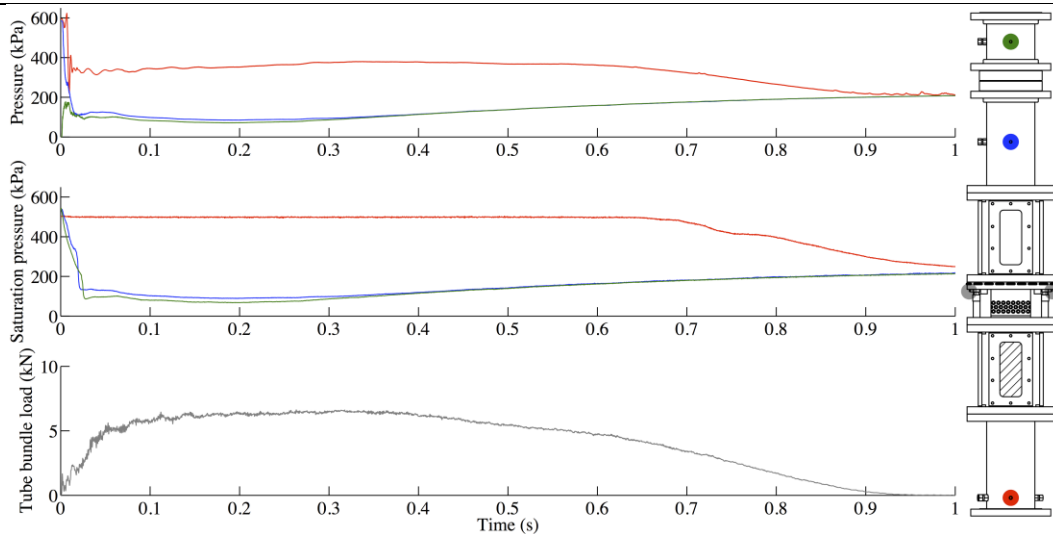
Figure E-11. Test T11: 53% liquid, 3 tube rows.

Table E-12. Test T12: 54% liquid, 2 tube rows.

l or g	p (kPa)	T (°C)	ρ (kg/m³)	V (L)	m (kg)	c (m/s)	H (mm)
Liquid	556.9	14.1	1247	14.9	18.57	558	806
Vapour	546.8	17.2	26.6	12.8	0.34	145	688
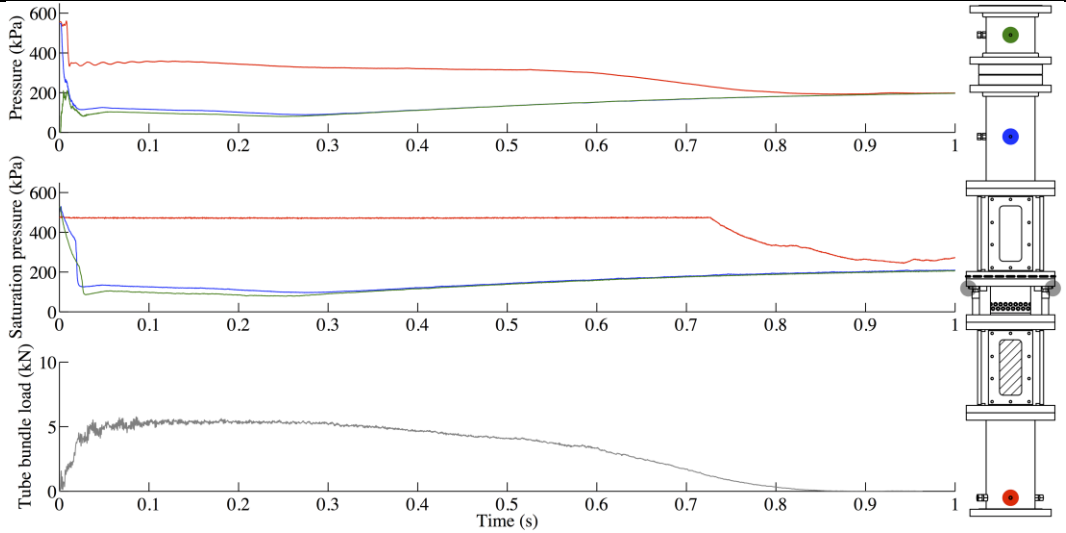
Figure E-12. Test T12: 54% liquid, 2 tube rows.

Table E-13. Test C01: 22% liquid, 0 tube rows.

l or g	p (kPa)	T (°C)	ρ (kg/m³)	V (L)	m (kg)	c (m/s)	H (mm)
Liquid	553.7	19.3	1229	4.5	5.5	534	242
Vapour	551.3	23.3	26.1	16.2	0.4	147	874
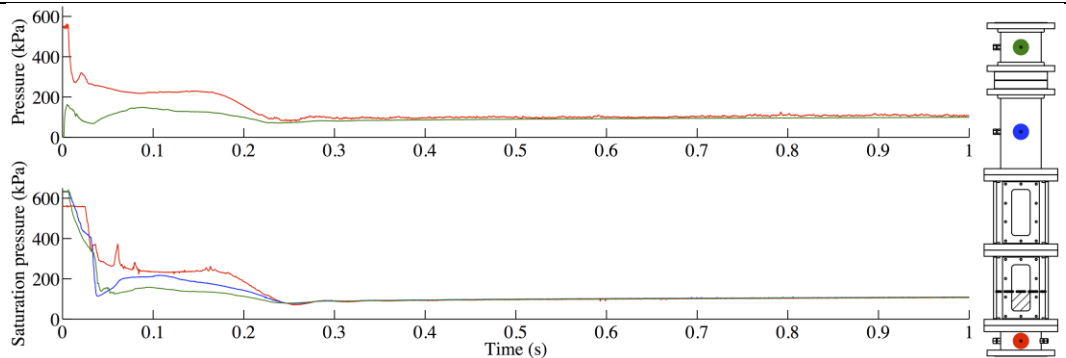
Figure E-13. Test C01: 22% liquid, 0 tube rows.

Table E-14. Test C02: 56% liquid, 0 tube rows.

l or g	p (kPa)	T (°C)	ρ (kg/m³)	V (L)	m (kg)	c (m/s)	H (mm)
Liquid	578.8	16.3	1239	11.5	14.3	547	618
Vapour	571.7	21.7	27.5	9.2	0.2	146	498
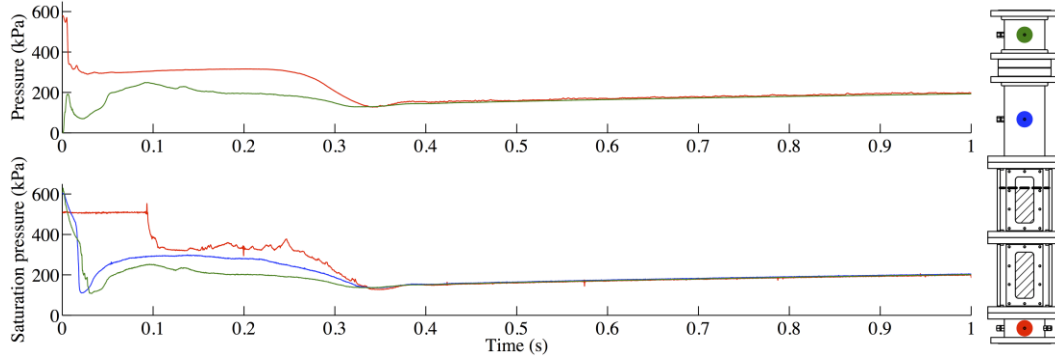
Figure E-14. Test C02: 56% liquid, 0 tube rows.

Table E-15. Test C03: 24% liquid, 6 tube rows.

l or g	p (kPa)	T (°C)	ρ (kg/m³)	V (L)	m (kg)	c (m/s)	H (mm)
Liquid	568.4	17.5	1235	5.5	6.8	542	297
Vapour	565.3	20	27.4	17.7	0.4	145	968
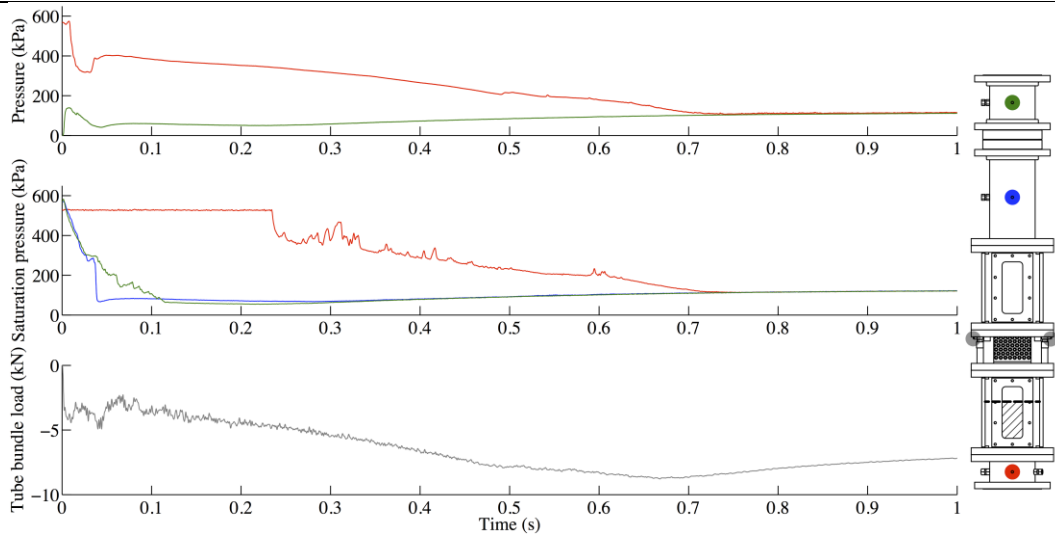
Figure E-15. Test C03: 24% liquid, 6 tube rows.

Table E-16. Test C04: 22% liquid, 6 tube rows.

l or g	p (kPa)	T (°C)	ρ (kg/m³)	V (L)	m (kg)	c (m/s)	H (mm)
Liquid	574.3	17.9	1233	5.2	6.4	540	277
Vapour	571.4	21.2	27.6	18	0.4	146	988
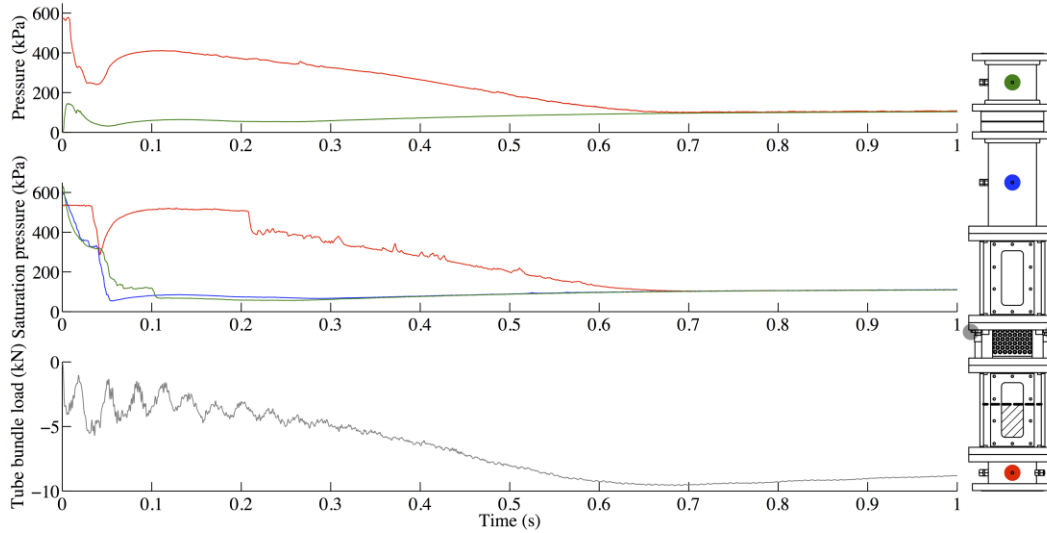
Figure E-16. Test C04: 22% liquid, 6 tube rows.

Table E-17. Test C05: 63% liquid, 6 tube rows.

l or g	p (kPa)	T (°C)	ρ (kg/m³)	V (L)	m (kg)	c (m/s)	H (mm)
Liquid	572.8	17.5	1235	14.5	17.9	542	798
Vapour	563.8	21.9	27	8.7	0.2	146	467
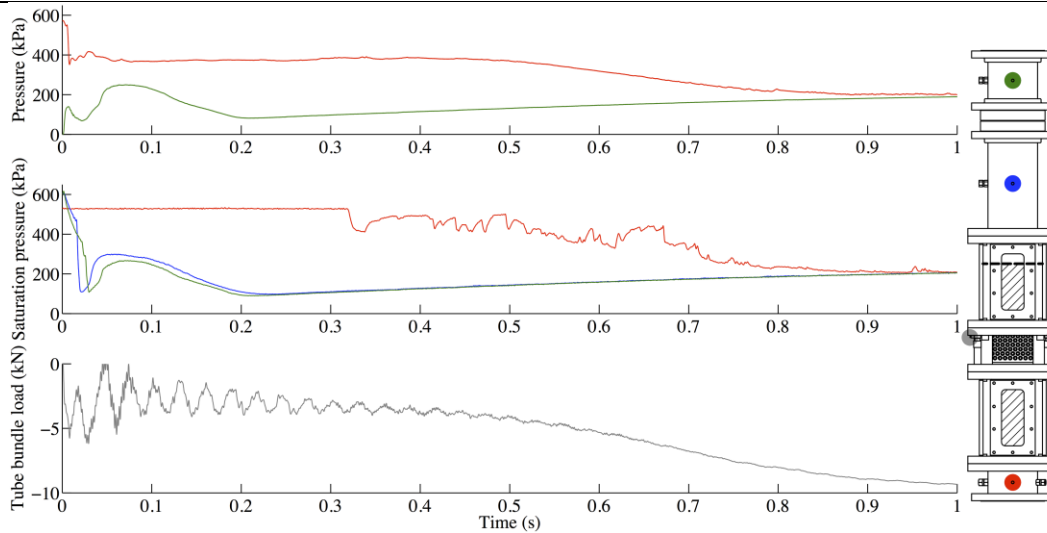
Figure E-17. Test C05: 63% liquid, 6 tube rows.

APPENDIX F. DRAG LOAD COEFFICIENT DATA
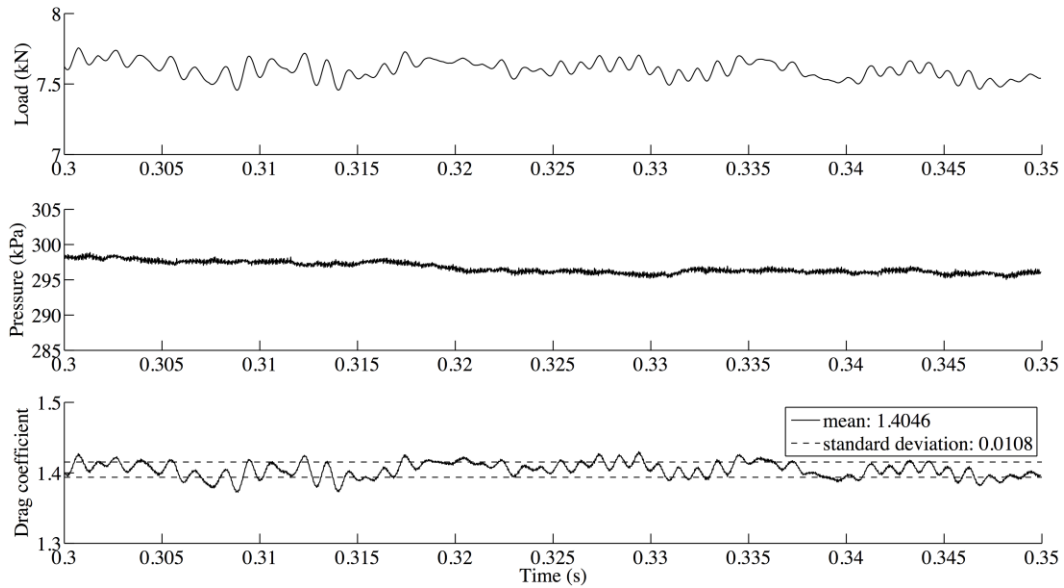
Figure F-1. Test T04 drag load coefficient.
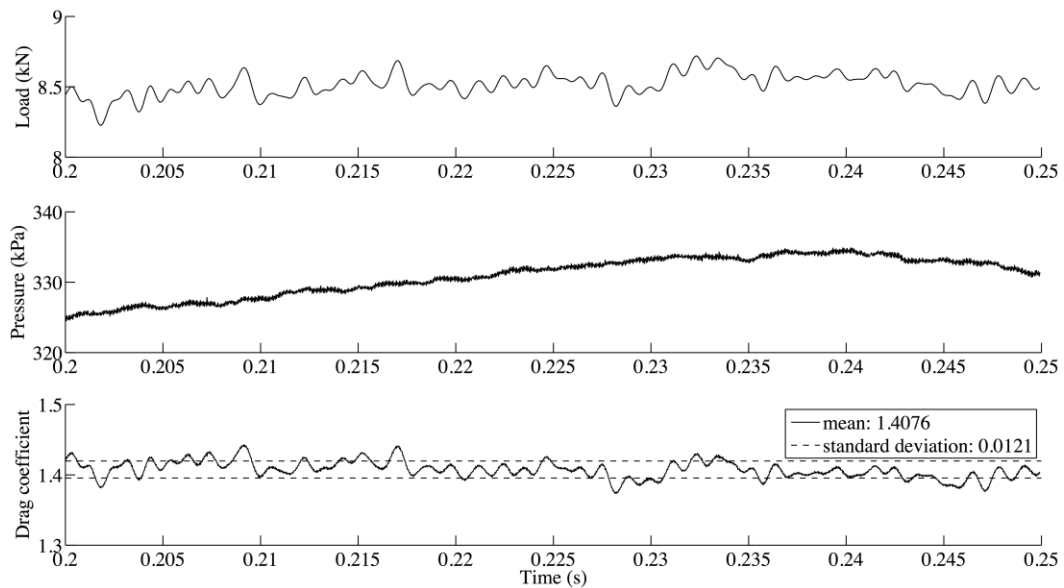
Figure F-2. Test T05 drag load coefficient.
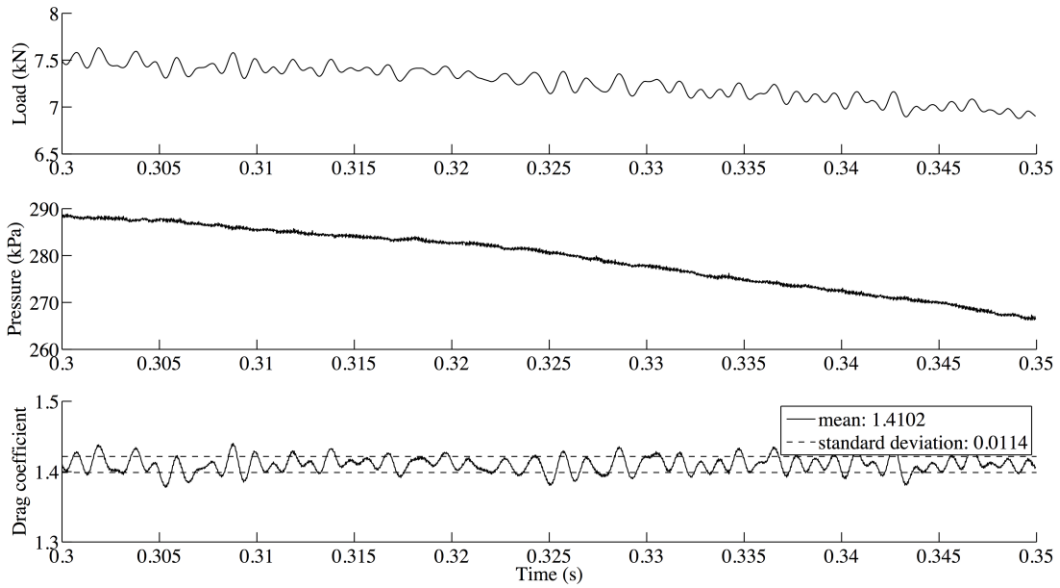
Figure F-3. Test T06 drag load coefficient.
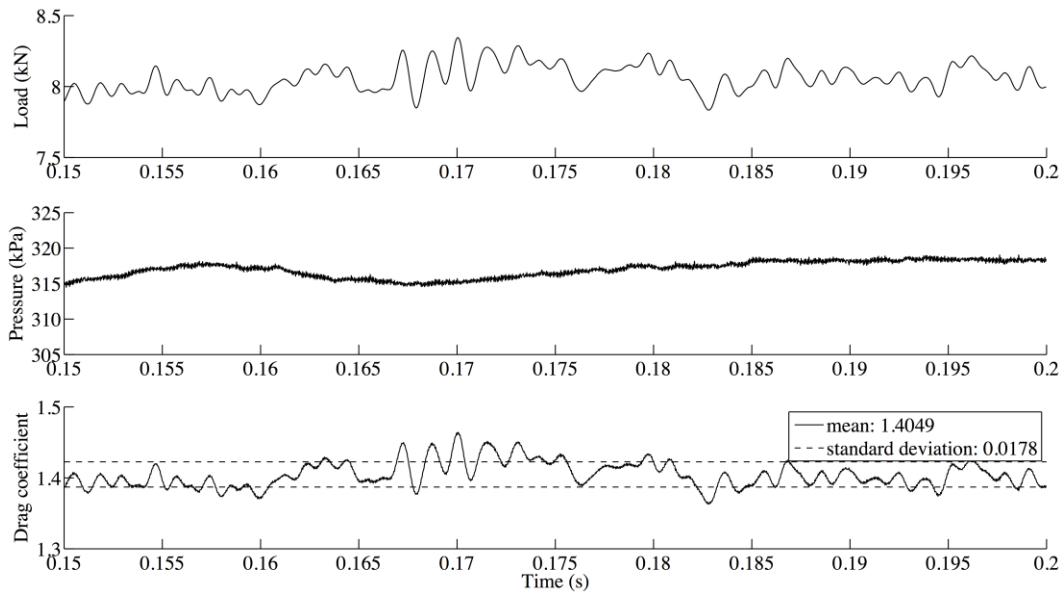
Figure F-4. Test T08 drag load coefficient.
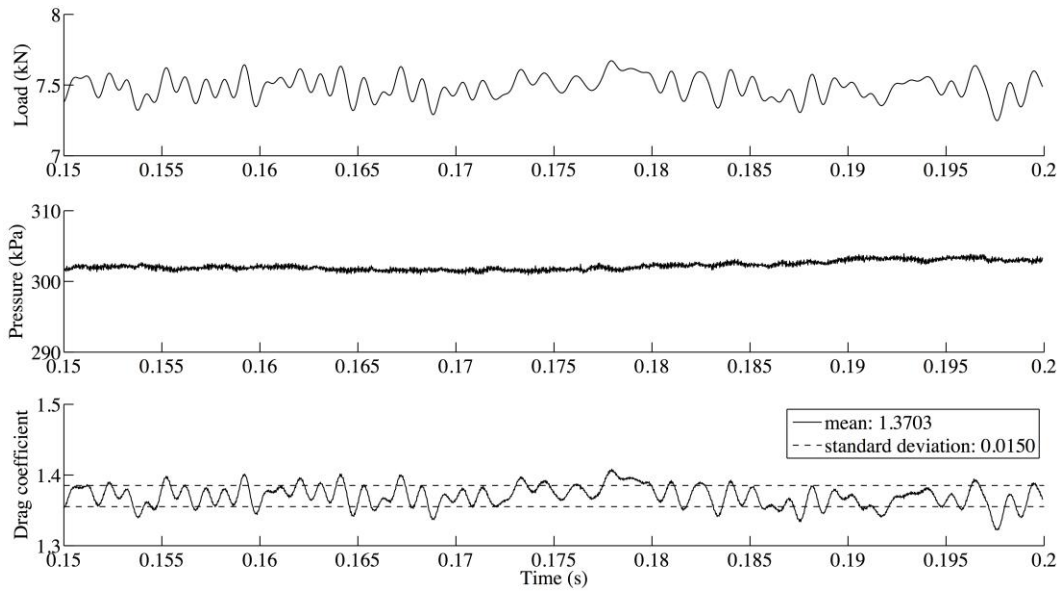
Figure F-5. Test T09 drag load coefficient.
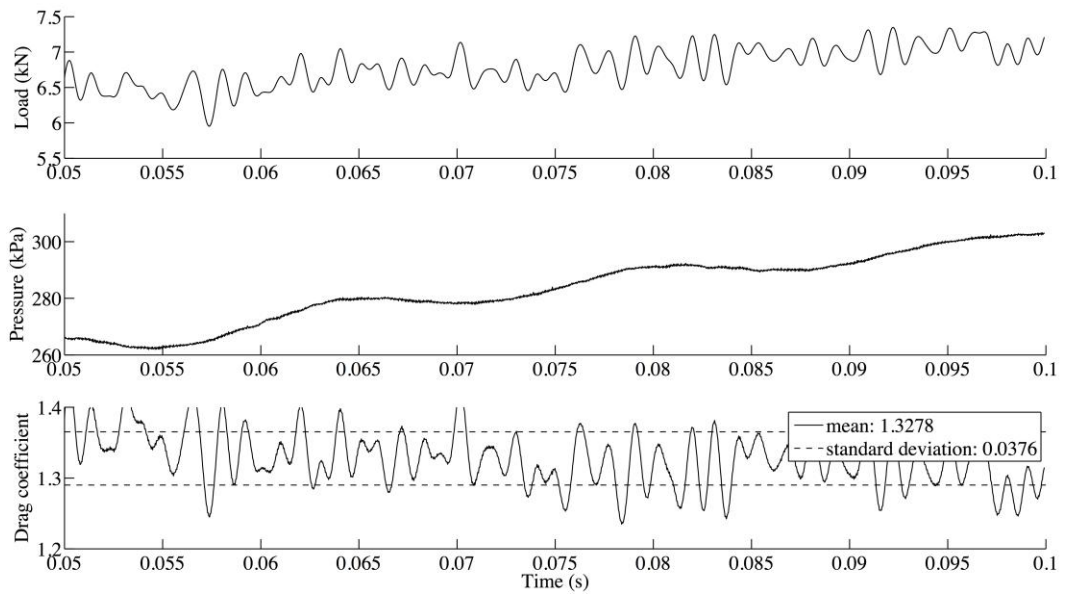
Figure F-6. Test T10 drag load coefficient.
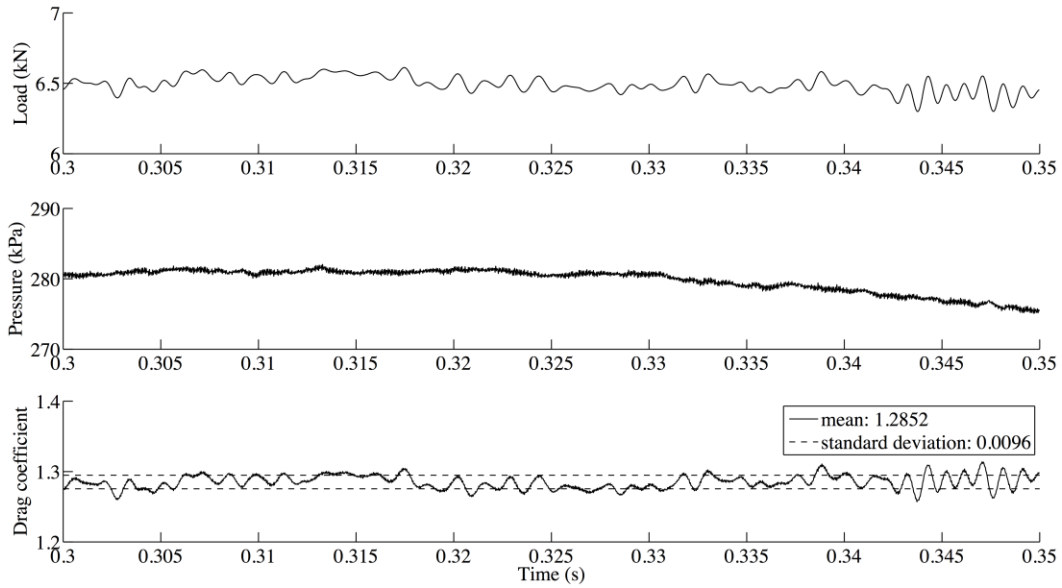
Figure F-7. Test T11 drag load coefficient.
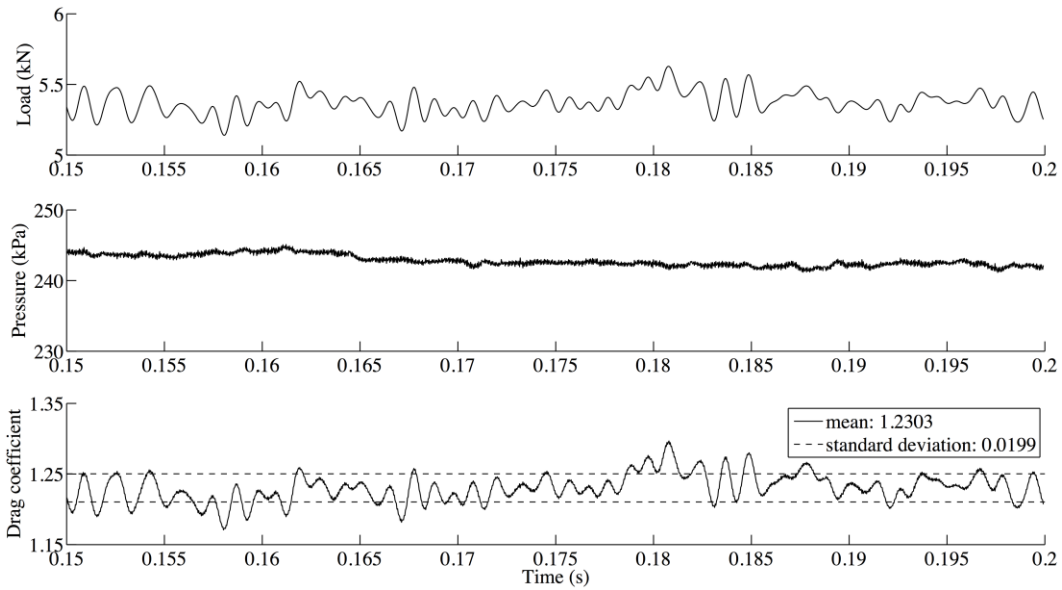
Figure F-8. Test T12 drag load coefficient.

APPENDIX G. PRESSURE DROP CALCULATIONS

The following sections provide sample pressure drop calculations for test T04 using steady state models published in the literature. Comparisons of the calculated and measured pressure drops for all of the tests that were performed are provided in Figs. G-1 to G-8. The steady-state pressure drops for all of the tests were computed using the procedures outlined below.

Tube bundle geometry parameters:

Tube diameter $d = 0.0127$ m,

Transverse pitch ratio $a = \dfrac{0.0173}{0.0127} = 1.36$,

Longitudinal pitch ratio $b = \dfrac{0.0150}{0.0127} = 1.18$,

Number of rows of tubes $z = 6$.

G.1. ZUKAUSKAS MODEL

Mean bulk fluid physical properties (425 kPa):

Density $\rho = 20.7$ kg/m^3,

Visosity $\mu = 11.1$ µPa·s,

Velocity $u = 146$ m/s.

Reynolds number calculation:

$$\mathrm{Re} = \frac{\rho u d}{\mu} = 3.46 \times 10^6.$$

Calculation of the resistance of an infinite bank of staggered tubes:

$$k = 2.016 - 1.675\left(\frac{a}{b}\right) + 0.948\left(\frac{a}{b}\right)^2 - 0.234\left(\frac{a}{b}\right)^3 + 0.021\left(\frac{a}{b}\right)^4 = 1.023.$$

For $a = 1.25$:

$$\frac{\text{Eu}}{k} = 0.245 + \frac{0.339 \times 10^4}{\text{Re}} - \frac{0.984 \times 10^7}{\text{Re}^2} + \frac{0.132 \times 10^{11}}{\text{Re}^3} - \frac{0.599 \times 10^{13}}{\text{Re}^4} = 0.246.$$

For $a = 1.5$:

$$\frac{\text{Eu}}{k} = 0.203 + \frac{0.248 \times 10^4}{\text{Re}} - \frac{0.758 \times 10^7}{\text{Re}^2} + \frac{0.104 \times 10^{11}}{\text{Re}^3} - \frac{0.482 \times 10^{13}}{\text{Re}^4} = 0.204.$$

Linearly interpolating for $a = 1.36$:

$$\frac{\text{Eu}}{k} = 0.227.$$

Euler number calculation for 6 rows of tubes:

$$\text{Eu}_6 = 1.115 \times \text{Eu} = 0.259.$$

Pressure drop calculation:

$$\Delta p = \text{Eu}_6 \frac{\rho u^2}{2} z = 343 \text{ kPa}.$$

G.2. IDEL'CHIK MODEL

Mean bulk fluid physical properties (425 kPa):

Density $\rho = 20.7 \text{ kg/m}^3$,

Visosity $\mu = 11.1 \text{ μPa} \cdot \text{s}$,

Velocity $u = 146 \text{ m/s}$.

Reynolds number calculation:

$$\text{Re} = \frac{\rho u d}{\mu} = 3.46 \times 10^6.$$

Calculation of resistance coefficient for staggered smooth-walled tube bundle:

Tube bundle geometric resistance $k = \dfrac{0.0173 - 0.0127}{0.0150 - 0.0127} = 2.02$,

$$\xi = (1.88 - a)(k + 1)^2 \text{ Re}^{-0.27} (z + 1) = 0.571.$$

Pressure drop calculation:

$$\Delta p = \xi \frac{\rho u^2}{2} = 126 \text{ kPa}.$$

G.3. Martin Model

Mean bulk fluid physical properties (125 kPa):

Density $\rho = 6.41 \text{ kg/m}^3$,

Visosity $\mu = 9.95 \text{ } \mu\text{Pa} \cdot \text{s}$,

Velocity $u = 146 \text{ m/s}$.

Reynolds number calculation:

$$\text{Re} = \frac{\rho u d}{\mu} = 1.19 \times 10^6.$$

Correction for small tube bundles:

$$k = \frac{1}{2a^2}\left(\frac{1}{z} - \frac{1}{10}\right) = 0.018.$$

Hagen number calculation for turbulent flow in staggered tube bundles:

$$\text{Hg}_{turb,s} = \left\{\left[1.25 + \frac{0.6}{(a-0.85)^{1.08}}\right] + 0.2\left(\frac{b}{a}-1\right)^3 - 0.005\left(\frac{a}{b}-1\right)^3\right\} \times \text{Re}^{1.75} + k\,\text{Re}^2$$

$$= 1.33 \times 10^{11}.$$

Hagen number calculation for Re > 250,000:

$$\text{Hg}_{turb,s,corr} = \text{Hg}_{turb,s}\left(1 + \frac{\text{Re} - 250,000}{325,000}\right) = 5.2 \times 10^{11}.$$

Hagen number calculation for laminar flow in tube bundles:

$$\text{Hg}_{lam} = 140\,\text{Re}\,\frac{(b^{0.5} - 0.6)^2}{a^{1.6}(4ab/\pi - 1)} = 1.35 \times 10^8.$$

Total Hagen number per tube row calculation for staggered tube bundles:

$$\text{Hg} = \text{Hg}_{lam} + \text{Hg}_{turb,s,corr}\left[1 - \exp\left(1 - \frac{\text{Re} + 200}{1000}\right)\right] = 5.21 \times 10^{11}.$$

Pressure drop calculation:

$$\Delta p = \frac{\mu^2}{\rho g}\frac{z}{d^2}\text{Hg} = 299 \text{ kPa}.$$
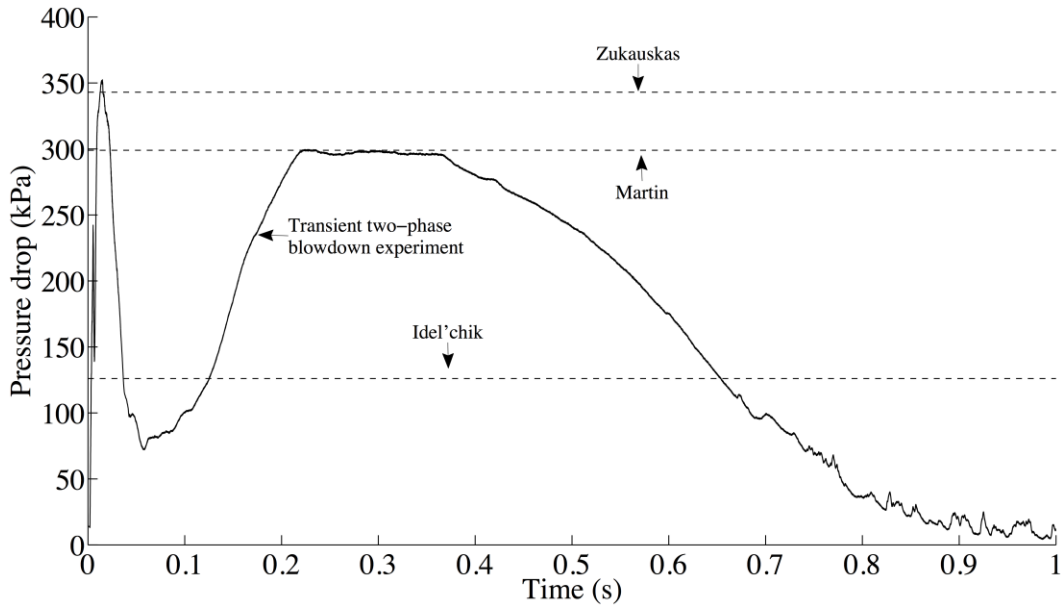
G.4. PRESSURE DROP COMPARISONS

Figure G-1. Test T04 pressure drop comparison (6 rows, small vessel, liquid above tubes).
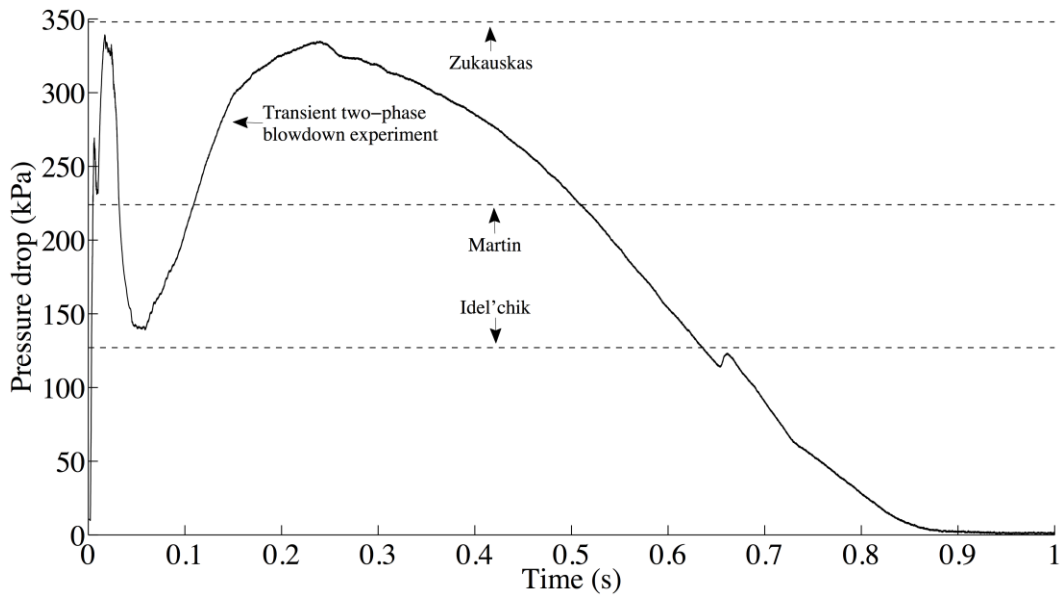

Figure G-2. Test T05 pressure drop comparison (6 rows, small vessel, liquid above tubes).
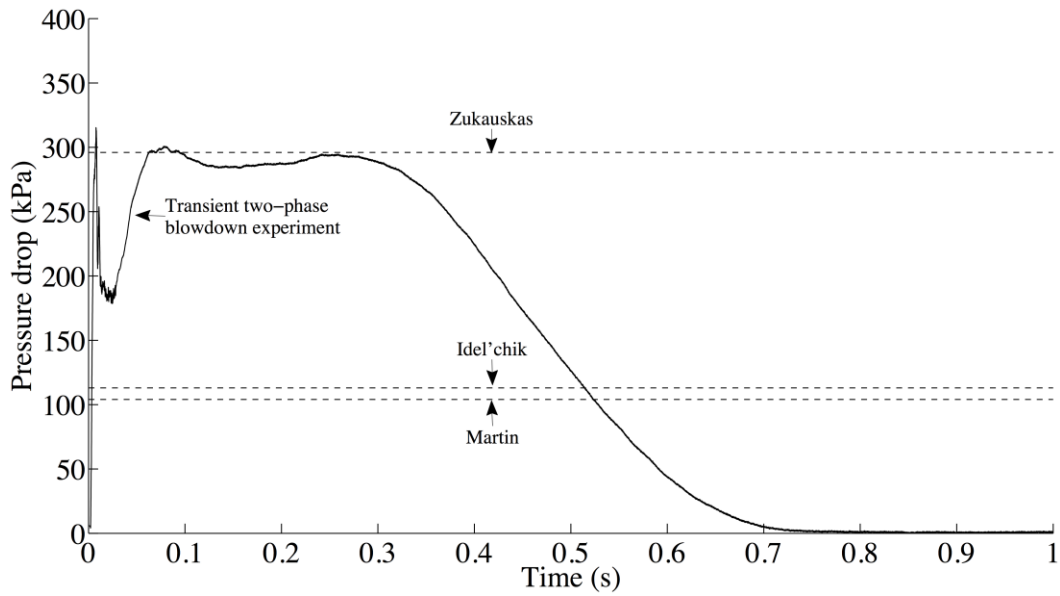
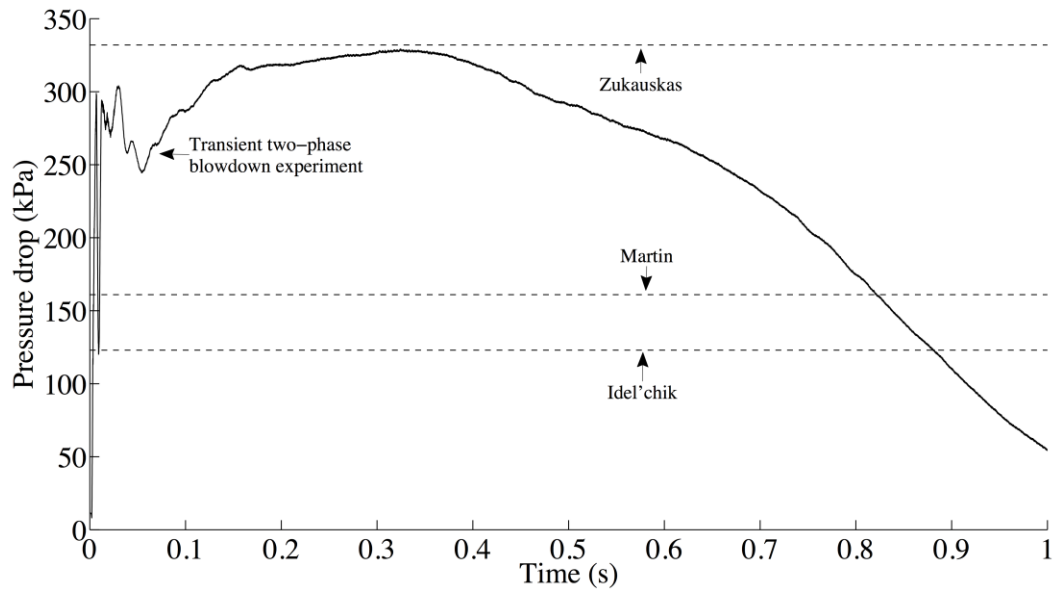Figure G-3. Test T06 pressure drop comparison (6 rows, small vessel, liquid below tubes).

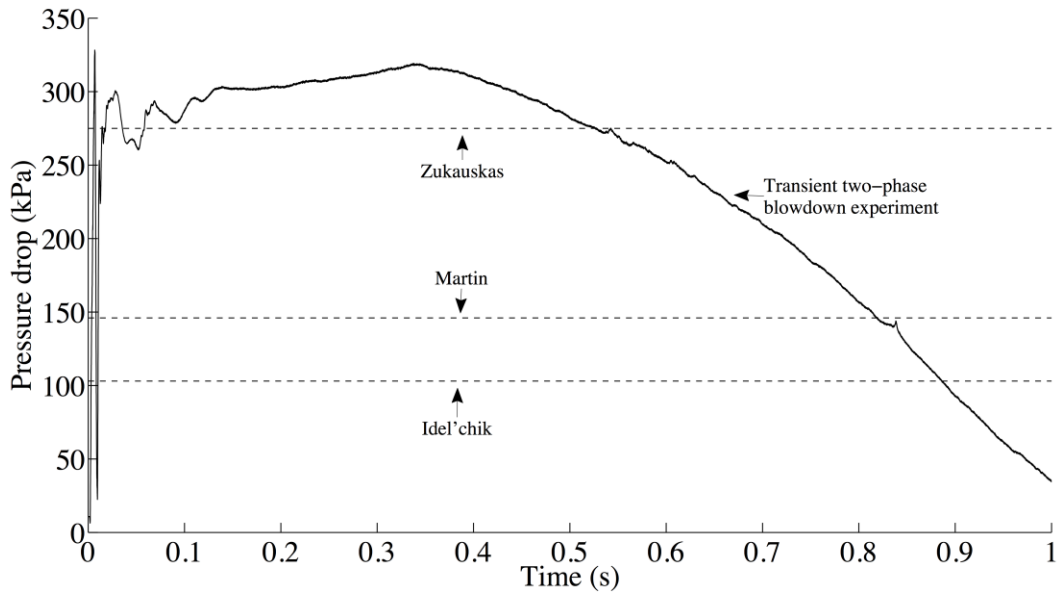Figure G-4. Test T08 pressure drop comparison (6 rows, large vessel).

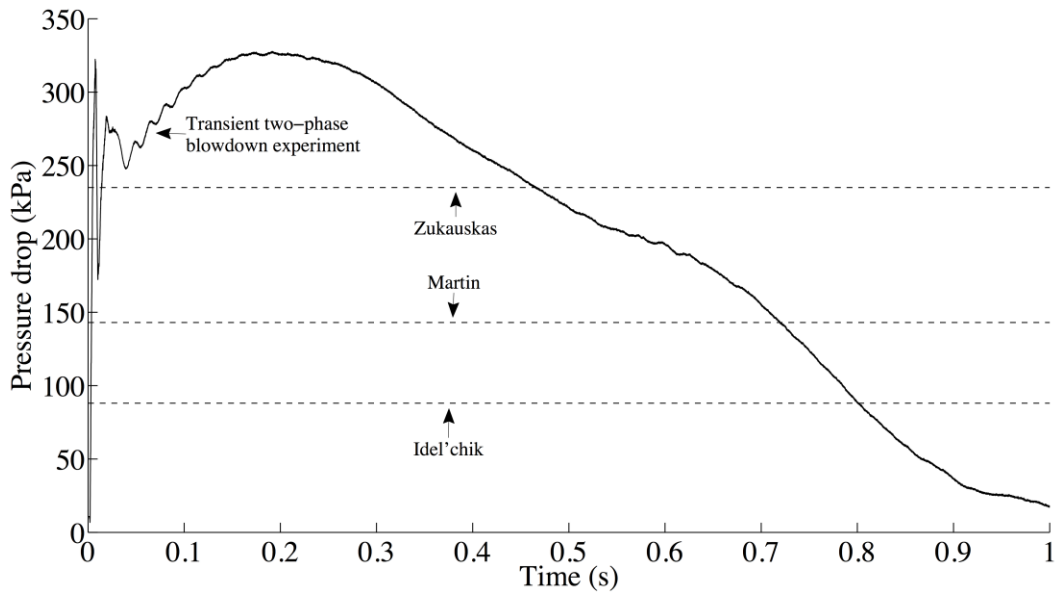Figure G-5. Test T09 pressure drop comparison (5 rows, large vessel).

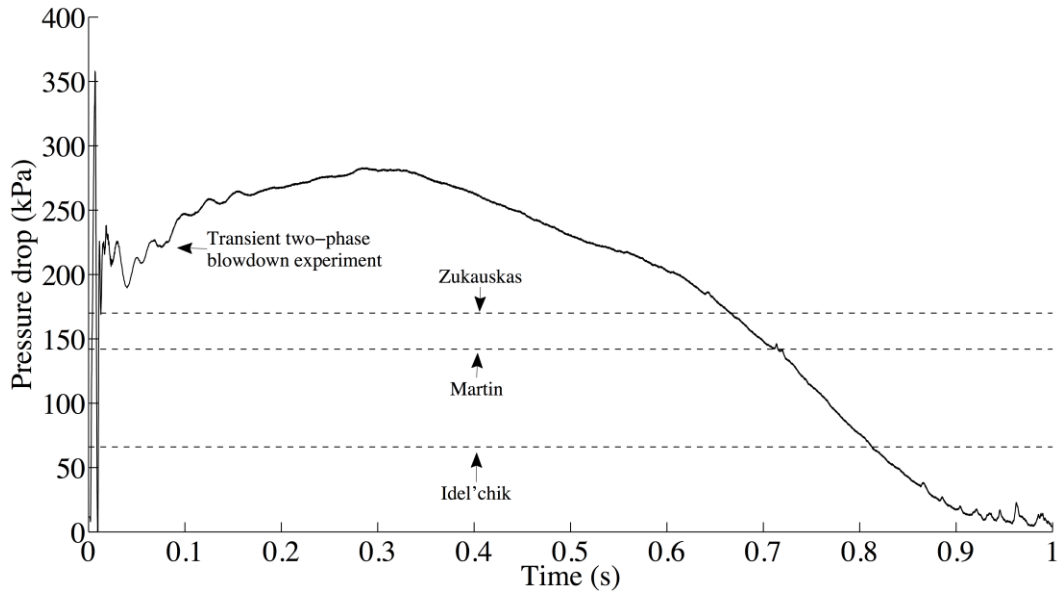Figure G-6. Test T10 pressure drop comparison (4 rows, large vessel).

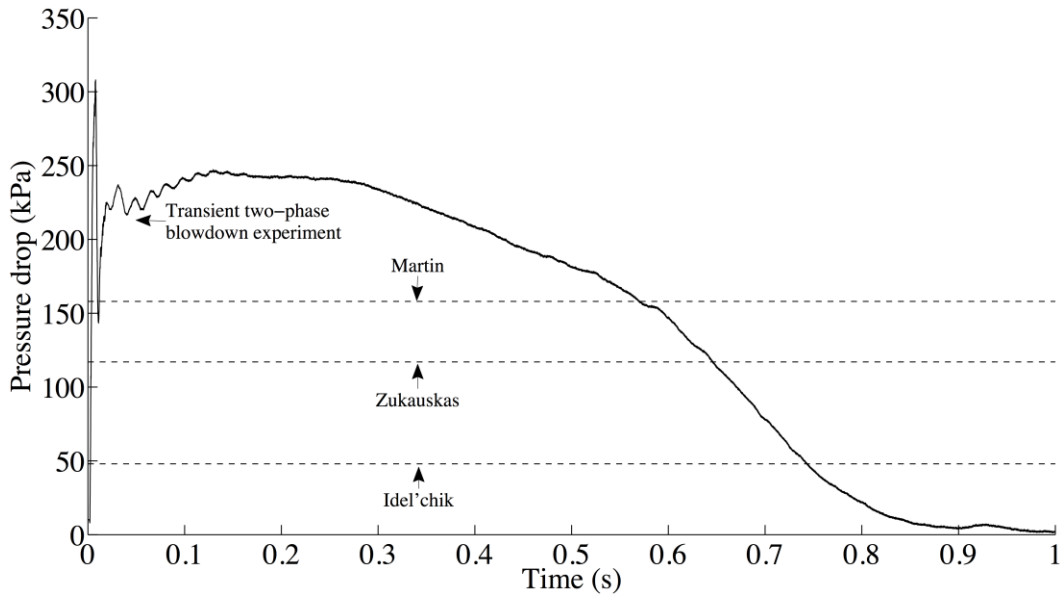Figure G-7. Test T11 pressure drop comparison (3 rows, large vessel).

Figure G-8. Test T12 pressure drop comparison (2 rows, large vessel).